Fluorinated Paramagnetic Probes for 19-F and 1-H MRS/ MRI

CHALMERS, KIRSTEN,HARDIE

Durham University

Department of Chemistry

Fluorinated Paramagnetic Probes for ^{19}F and ^{1}H MRS/ MRI

Kirsten Hardie Chalmers

A thesis submitted for the degree of Doctor of Philosophy

2011

Declaration

The work described herein was carried out in the Department of Chemistry, University of Durham between October 2007 and December 2010. All of the work is my own, except where specifically stated otherwise. No part has previously been submitted for a degree at this or any other university.

Statement of Copyright

Abstract

Novel CF_3-labelled lanthanide(III) complexes have been synthesised for use as probes for ^{19}F and ^{1}H magnetic resonance spectroscopy and imaging.

The syntheses and evaluation of two classes of fluorinated paramagnetic complexes are defined. Notably, the ^{19}F magnetic resonance relaxation processes for the complexes have been assessed, allowing for the analysis of the interplay between applied field, Ln^{3+} ion and rotational correlation time on relaxation properties.

Strategies employed to enhance signal intensity are discussed, examining a number of different of fluorinated mono- and di-amide cyclen ligands. Systems incorporating phosphinate pendant arms are of particular interest, resulting in complexes with favourable isomer distributions, faster longitudinal relaxation rates and narrower linewidths.

Finally, the synthesis of high molecular weight conjugates with paramagnetic fluorinated complexes is described. Three different classes of medium to high molecular adducts were considered, with the merits and limitations of each assessed. The desirable formation of one species in solution, ease of solubility and attractive ^{19}F and ^{1}H relaxometric properties render the chitosan conjugates promising candidates for future use as imaging probes.

Acknowledgements

I would like to thank the following people, without whom the work in this thesis would not have been possible:-

My supervisor, Prof. David Parker, who has been a constant source of encouragement, support and inspiration.

Dr. Alan Kenwright, Catherine Hefferman and Ian McKeag for their advice and assistance with NMR spectroscopy. Dr. Mike Jones, Lara Turner and Dr. Jackie Mosely for mass spectroscopy measurements. Judith Magee for elemental analysis. Dr. Ilya Kuprov for his advice and DFT calculations.

Prof. Andrew Blamire and Dr. Ian Wilson, at the Newcastle Magnetic Resonance Centre, for *in vivo* and phantom imaging experiments.

Prof. Mauro Botta, at the Universitá del Piemonte in Alessandria, for welcoming me into his lab and for all the relaxivity measurements.

All members of the DP group for making the lab a fun and happy place to work. I would particularly like to thank Liz, Dave, James and Pete for their friendship, and Kanthi for all our lovely chats. My friends in Durham and Glasgow, especially Laura, Katie, Jen, Dave, Fred, Ads, Jo and Jess for lots of fun nights out.

My sisters, and their gorgeous little girls, for always making me smile.

Andy, for his love, and for being such a wonderful husband.

A very special thanks to Mum and Dad for their continued love and support over the past 25 years, and for giving me the opportunity to achieve so much.

For Mum and Dad

Contents

List of Abbreviations

15C5 - perfluoro-15-crown-5-ether
5-FU - 5-fluorouracil
6-FPAM - 6-fluoropyridoxamine
6-FPOL - 2-fluoro-5-hydroxy-6-methyl-3,4-pyridinedimethanol
AP – alkaline phosphatase
APTRA - o-aminophenol-*N*,*N*,O-triacetic acid
BAPTA - 1,2-bis(o-amino-phenoxy)ethane-*N,N,N',N'*-tetraacetic acid
CA - contrast agent
CD - cytosine deaminase
CHO - chinese hamster ovary
CPG2 – carboxy peptidase
CSA - chemical shift anisotropy
CSI - chemical shift imaging
cyclen - 1,4,7,10-tetraazacyclododecane
d - doublet
DCM - dichloromethane
DD - dipole-dipole
dd - doublet of doublets
DFT - density functional theory
DHFU - 5,6-dihydrofluorouracil
DMF - *N,N*-dimethylformamide
DMSO - dimethyl sulfoxide
DO3A - 1,4,7,10-cyclododecane-1,4,7-triacetic acid
DOTA - 1,4,7,10-cyclododecane-1,4,7,10-tetraacetic acid
DOTP - 1,4,7,10-tetraazacyclododecane-1,4,7,10-tetrakis(methylene phosphonate)
DTPA - diethylenetriaminepentaacetic acid
EPR - enhanced permeability and retention
ESI/MS^- - electrospray ionisation with negative ion detection
ESI/MS^+ - electrospray ionisation with positive ion detection
FACS – Fluorescence activated cell sorting
FBAL - α-fluoro-β-alanine
FDG - fluorodeoxyglucose
FPOL- fluoropyridocol
F-POSS - perfluorinated cubic silsesquioxane
FSB - (E,E)-1-fluoro-2,5-bis(3-hydroxycarbonyl-4-hydroxy)styryl-benzene
GDEPT- gene directed pro-drug therapy
GPC - gel permeation chromatography

GS-MS - gas chromatography mass spectrometry
HFB - hexafluorobenzene
HPLC - high performance liquid chromatography
ICP-MS - inductively coupled plasma mass spectrometry
IQ - indolequinone
LIS - lanthanide induced shift
m - multiplet
MR - magnetic resonance
MRI - magnetic resonance imaging
MRS - magnetic resonance spectroscopy
MTT - 3-(4,5-dimethyl-2-thiazolyl)-2,5-diphenyl-2H-tetrazolium bromide
MW - molecular weight
MWCO - molecular weight cut off
NMM - *N*-methylmorpholine
NMR - nuclear magnetic resonance
NMRD - nuclear magnetic resonance dispersion
NOD – non-obese diabetic
NP – nanoparticle
NSC – neural stem cells
OFPNPG – 2-fluoro-4-nitrophenyl β-D-galactopyranoside
OFPNP - 2-fluoro-4-nitrophenol
PAMAM- polyamidoamine
PEG - polyethylene glycol
PET - positron emission tomography
PFC - perfluorocarbon
PFCE – emulsified perfluoro-15-crown-5-ether
PFOB - perfluorooctylbromide
PFONPG - 4-fluoro-2-nitrophenyl-β-D-galactopyranoside
PFPE - perfluoropolyether
PLE - pig liver esterase
q - quartet
RAFT – reversible addition-fragmentation chain transfer
RF - radio frequency
RNA - ribonucleic acid
s - singlet
SBM - Solomon-Bloembergen-Morgan
T1D – type 1 diabetes
t - triplet
TBTU - *O*-(benzotriazol-1-yl)-*N,N,N′,N*′-tetramethyluronium tetrafluoroborate
TFA - trifluoroacetic acid

tfm-Phe - trifluoromethyl-L-phenylalanine
THF - tetrahydrofurane
TPP - tetraphenyl iron(III)porphyrins
tri-BOC - *tert*-butoxycarbonyl
TSAP - twisted square-antiprismatic
UV - ultraviolet
Vis - visible
β-CD - poly-β-cyclodextrin

Chapter 1: Introduction

1.0 Introduction

1.1 Magnetic Resonance Imaging

Magnetic Resonance Imaging (MRI) is a powerful and non-invasive medical imaging modality that exploits the intense water signal present in living systems to generate high resolution, anatomical three dimensional images.[1] Proton MRI can establish the distribution of water protons in the body through examination of the water proton signal determined by the longitudinal relaxation time, T_1, and the transverse relaxation time, T_2. The particularly strong signal, which is sensitive to tissue status, provides indications of soft tissue anatomy. In clinical practice, it is possible to distinguish between malignant and normal tissue owing to the significantly longer T_1 value of malignant tissue (Table 1.1).[2]

Tissue	Tumour T_1(s)	Normal T_1(s)
Breast	1.08 ± 0.08	0.37 ± 0.08
Stomach	1.24 ± 0.11	0.76 ± 0.08
Skin	1.05 ± 0.11	0.62 ± 0.02
Muscle	1.41 ± 0.08	1.02 ± 0.03

Table 1.1: Longitudinal relaxation times (T_1) for malignant and normal human tissue.[2]

In MRI, the signal intensity increases with increasing longitudinal relaxation rate, R_1, and decreases with increasing transverse relaxation rate, R_2. The introduction of paramagnetic gadolinium(III) contrast agents dramatically increase the relaxation rates (R_1 and R_2) of nearby water protons, with the percentage change of R_1 in tissue being much greater than that of R_2. Consequently, this class of agents are best visualised using pulse sequences that emphasize changes in R_1, which are more commonly known as T_1 weighted images.[1] The resulting signal intensity increase enhances distinction between normal and malignant tissue, thereby making diagnosis easier. There are several paramagnetic gadolinium(III)-based contrast agents in clinical use, examples include [Gd(DO3A-butrol)(H_2O)] and [Gd(DOTA)(H_2O)]$^-$.

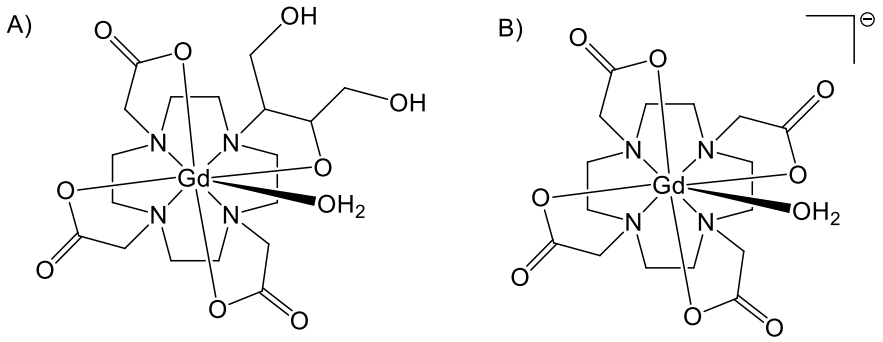

Figure 1.1*:* Stuctures of (A) Gadovist™ - [Gd(DO3A-butrol)(H_2O)] and (B) Dotarem™ - [Gd(DOTA)(H_2O)]$^-$.

In addition to gadolinium(III) contrast agents, an alternative class of agents based upon polysaccharide coated iron oxide particles are in clinical practice, however the most commonly utilized are those containing gadolinium.[3]

Whilst MRI has proved extremely successful and popular in the biomedical field, studies of magnetic resonance spectroscopy (MRS) can be hindered by the intense water signal, often requiring the need for water suppression. This is particularly a problem in the detection of metabolites other than water, which is made extremely difficult due to the relative signal intensity. In recent years, an alternative approach using heteronuclear magnetic resonance has been explored. The key benefit is that heteronuclei can provide physiological reporters and metabolic tracers while avoiding the intense water and lipid signals.[4,5] Although ^{13}C, ^{23}Na and ^{31}P nuclei are widely used in MRS, there is a significant loss of signal intensity owing to the considerably lower gyromagnetic ratio of these nuclei with respect to ^{1}H. Additionally, all of the aforementioned isotopes are naturally present in biological tissues which can result in background signal issues.

1.2 ^{19}F Magnetic Resonance Imaging and Spectroscopy

There are many merits of ^{19}F NMR spectroscopy that justify the high level of interest and current research in this field. ^{19}F has a nuclear spin of ½, is 100% abundant, has high NMR sensitivity (0.83 relative to ^{1}H NMR) and an impressively large chemical shift range (>300 ppm). This means there is the potential for multiple different fluorinated agents to be detected simultaneously with very little danger of signal

overlap. The high gyromagnetic ratio, 40.05 MHz/T (approximately 6% lower than ^{1}H), allows for the use of existing proton NMR instrumentation with minimal adjustment. Moreover, ^{19}F MRI can be used in conjunction with conventional ^{1}H MRI, providing high spatial resolution anatomy.

As with proton NMR spectroscopy, the various parameters such as signal intensity (SI), chemical shift (δ), R_1 and R_2, can be easily manipulated to extract potential information on the desired compound. Furthermore, quantitative measurements can be achieved through relative signal intensity measurements. Over the years, each of these parameters has been utilised in the development of ^{19}F NMR reporter molecules, for which a few examples are noted (Table 1.2).

Parameter	Fluorinated Molecule	NMR Parameter
pO_2	Perfluorocarbons	R_1 (R_2)
pH	FPOL	$\Delta\delta$, J
$[Mg]^{2+}$	5F-APTRA	δ, ρατιο
Gene Acitivity	5FC	$\Delta\delta$,
Glycolysis	FDG	Signal Intensity
Drug Metabolism	5FU	Signal Intensity

Table 1.2: Fluorinated reporter molecules FPOL (fluoropyridocol), 5F-APTRA (5-fluoro-2-aminophenol-N,N,O-triacetate), 5FU (5-fluorocytosine), FDG (fluorodeoxyglycose) and 5FU (5-fluorouracil).[6]

Another benefit in the use of ^{19}F NMR spectroscopy is that there is very little natural fluorine in the body and so there is a near-zero background signal. The small concentration of natural fluorine present occurs mostly in the form of solid fluorides in bones and teeth.[7] This, however, does not interfere with exogenously dispensed fluorine compounds as endogenous fluorine has extremely short T_2 relaxation and is therefore below the limits of NMR detection.[7] These factors combined render ^{19}F MRI and Magnetic Resonance Spectroscopy (MRS) extremely promising for use in biological studies.

Increasingly fluorine is being used as ^{18}F for Positron Emission Tomography (PET).[8, 9] One of the key strengths of PET is the ability to use only nano- to femto-molar concentrations, in comparison to the milli- to micro-molar concentrations required for NMR spectroscopy. That being said, ^{18}F has a short half-life ($t_{1/2}$ = 110 min) and all ^{18}F- containing probes simply detect radioactive decay, relaying no information on multiple substrates. Conversely, ^{19}F-containing molecules are generally very stable, have an infinite shelf life and, owing to the expansive chemical shift range, ^{19}F NMR spectroscopy can simultaneously provide information on a multitude of molecules.

The possibility of ^{19}F MRI was first reported by Holland *et al.*[10] just four years after the development of ^{1}H MRI by Lauterbur in 1973.[11] Numerous common drugs contain a fluorine atom and are therefore ideal for examination. One of the initial *in vivo* studies investigated the metabolic pathway of the anticancer chemotherapeutic agent 5-fluorouracil (Figure 1.2). This was firstly performed in animals by Griffiths *et al.* in 1984[12], followed by the first human study by Wolf *et al.* in 1987.[13]

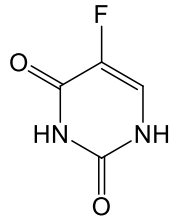

Figure 1.2: Anticancer chemotherapeutic agent 5-fluorouracil.

There have been many advances in ^{19}F NMR spectroscopy since the eighties, with many new and diverse applications now in practice. With the relatively large number of fluorine-containing compounds being studied for ^{19}F MRI/MRS, it is useful to categorise them based on their function. There are three major classes of compounds: active agents, whereby the compound experiences a modification following interaction with the local environment; passive agents, in which the compound discloses information regarding tissue property; and fluorine-containing drugs whose metabolic fate and biodistribution can, in principle, be monitored by ^{19}F NMR spectroscopy.

1.2.1 Active Agents

Active agents are intended to be transformed, reversibly or irreversibly, by a selective parameter *in vivo,* such as pH or enzyme activity. This modification can then be revealed by a detectable change in one or more NMR parameters, *e.g.* a variation in chemical shift, scalar coupling or relaxation time.

1.2.1.1 pO_2 Reporters

In cancer patients, it is essential to evaluate the levels of tumour oxygenation prior to treatment as it has been shown that hypoxic tumour cells are much less receptive to radiotherapy, and hypoxia appears to promote malignant progression and metastasis of tumours.[14] Furthermore, some chemotherapeutic drugs, such as streptonigrin and mitomycin, portray differing levels of efficiency depending on the degree of hypoxia (Figure 1.3).[15]

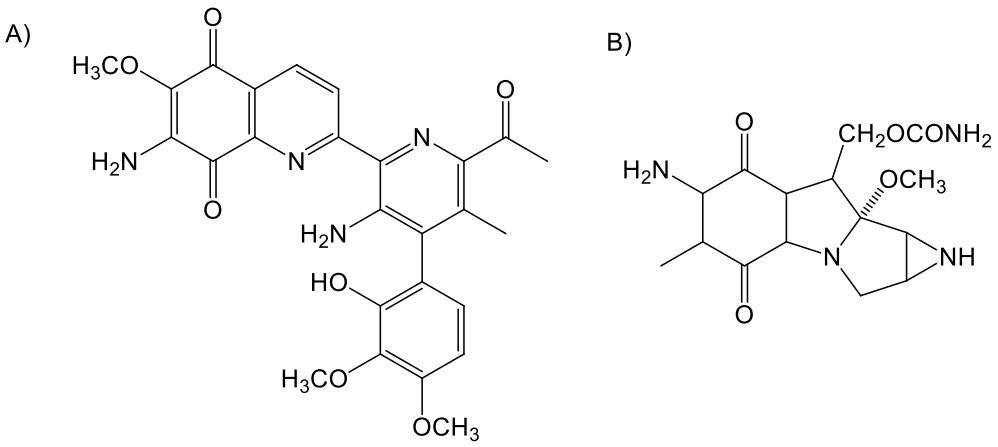

Figure 1.3: Streptonigrin (A) is 10 times more toxic to normally aerated cells than hypoxic cells, whereas mitomycin (B) is more efficient in hypoxic cells.[15]

The well-established linear relationship between the partial pressure of oxygen, pO_2, and the ^{19}F NMR spin lattice relaxation rate, R_1, allows for pO_2 measurement *in vivo* (Equation 1.1).[16] Quantitative evaluation of tissue oxygenation can be accomplished by monitoring the reduction in ^{19}F NMR spin lattice relaxation rate, which is caused by the paramagnetic effect of dissolved molecular oxygen.

$$R_1 = A + B\,pO_2 \qquad (1.1)$$

where A is the anoxic relaxation rate and B represents the sensitivity of the reporter molecule to the paramagnetic contribution of oxygen.

Perfluorocarbons are biocompatible in an emulsified form and when administered intravenously they are taken up in the well-perfused tumour regions.[17] The level of tumour oxygenation can then be determined in a non-invasive manner by monitoring the variation in relaxation rates (Figure 1.4).

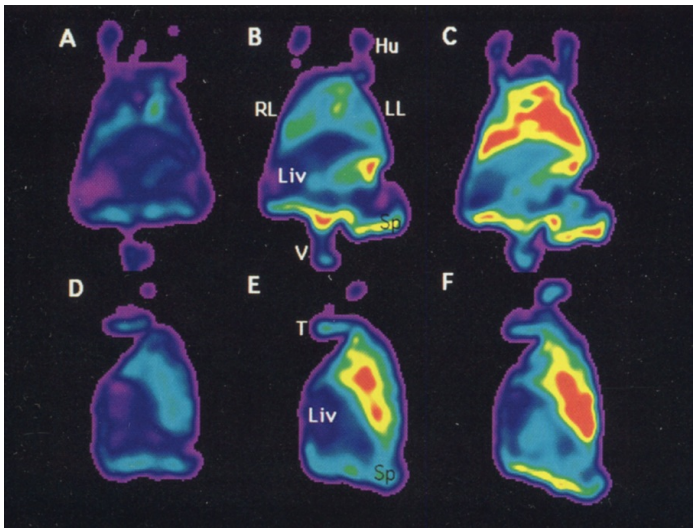

Figure 1.4: Pseudo colour calculated pO_2 images coronal (A-C) and sagital (D-F) projections in a pig. Three separate levels of inspired oxygen are shown: (A, D) ambient air breathing; (B, E) ~ 31min^{-1} supplemental oxygen; (C, F) ~ 61 min^{-1} supplemental oxygen. Areas of high pO_2 are highlighted red with the lower pO_2 regions shown in blue.[16]

There are numerous perfluorocarbons available and the decision on which is deemed most appropriate often comes down to cost and availability. There are however some practical considerations that should be made. Perfluorocarbons such as Therox^{TM}, which have multiple ^{19}F NMR spectroscopic resonances, can lead to experimental complexity, unreliable relaxation measurements and poor signal to noise ratio (Figure 1.5). Conversely, through clever experimental design the multiple resonances can be exploited to generate additional spectroscopic information.

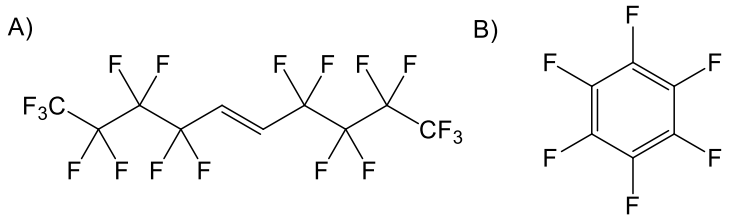
A)
B)
F
F
F

Initial studies by Aboage *et al*. found that the retention of SR-4554, quantified by ^{19}F MRS, related well to the reported radiobiological hypoxic fraction of mouse tumours.[20] Modulation of tumour oxygenation by the addition of hydralazine and carbogen was also detected, successfully demonstrating the exquisite sensitivity of ^{19}F MRS. Unfortunately, further studies within the same group could find no linear correlation between the ^{19}F retention index and pO_2 parameters.[21] This suggests that additional factors, such as blood flow/perfusion could be influencing the hypoxia marker retention. A Phase I clinical study by Seddon *et al.* demonstrated that SR-4554 was detectable in tumours of eight patients, with dosing concentrations of 400-1600 mg/m^2, prior to being rapidly cleared.[22] It was reported that SR-4554 was well tolerated however dosing at 1600 mg/m^2 induced nausea and vomiting in the patient. This clearly demonstrates that there is fine balance to be struck between the need to give a high dose to optimise ^{19}F signal to noise, and the need to avoid unacceptable toxicity.

In 2009, Tanabe *et al.* reported the development of a ^{19}F-labelled indolequinone derivative, consisting of a hypoxia-sensitive indolequinone parent unit and a nona-fluoro-tert-butyl reporter group.[23] Under hypoxic conditions, one-electron reduction of the fluorinated isoquinoline released the nona-fluoro-tert-butyl alcohol consituent, indicated by a ^{19}F NMR chemical shift change of ~5 ppm (Scheme 1.1). Conversely, the addition of O_2 suppressed the release of the alcohol substituent. Further optimization of the chemical structure is needed to increase solubility and intracellular retention. Nonetheless it is a promising initial result.

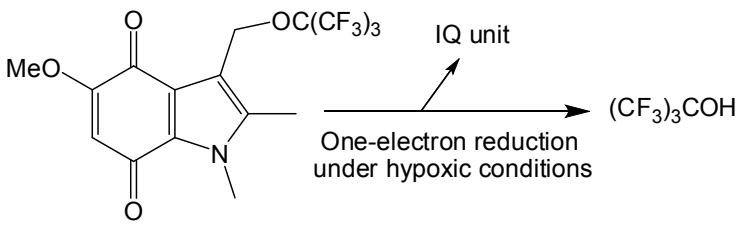

Scheme 1.1: Bioreduction of ^{19}F-labelled indoquinoline derivative under hypoxic conditions.

1.2.1.2 Gene Therapy Reporters

Gene therapy shows great potential for the treatment of various diseases. The main difficulty of this work is the ability to gauge the success of transgene activity *in situ*, in terms of gene expression, spatial extent and longevity of expression. However, by introducing a non-invasive reporter gene in conjunction with the therapeutic gene, assessment of transfection can be quantitatively measured. Much research has focused on reporter genes associated with optical imaging due to the low cost, ease of availability and high sensitivities.[24] Other strategies include radionuclide imaging and NMR spectroscopy.[25]

*Lac*Z, which encodes β-galcosidase, has historically been the reporter gene of choice for verifying effective transfection in biochemistry. Mason *et al.* devised a ^{19}F NMR approach that assesses the β-galactosidase activity *in vivo*.[26] The rapid cleavage of 2-fluoro-4-nitrophenyl β-D-galactopyranoside (OFPNPG), in response to the action of β-galcosidase, to form the aglycone 2-fluoro-4-nitrophenol (OFPNP), results in a pH-dependent ^{19}F chemical shift of Δδ= -4 to – 6 ppm, relative to the substrate. The signal of the aglycone is separated sufficiently from the substrate, thereby revealing distribution of each entity separately and allowing for chemical shift selective imaging at 4.7 T (Figure 1.7).[27] The reduced intensity of the product signal is due to the longer T_1 of the aglycone in comparison with the substrate. It may be possible to selectively determine the pH at the site of enzyme activity as the aglycone product is pH-sensitive and, importantly, the pK_a is in the physiological range.

In an attempt to further enhance sensitivity and reduce toxicity, the introduction of a trifluoromethyl group (CF_3), in place of the single fluorine atom, was undertaken. As expected, the signal to noise ratio was enhanced, however the chemical shift change was reduced (Δδ < 2 ppm), most likely due to the transmission of the electron density redistribution through an additional carbon-carbon bond.

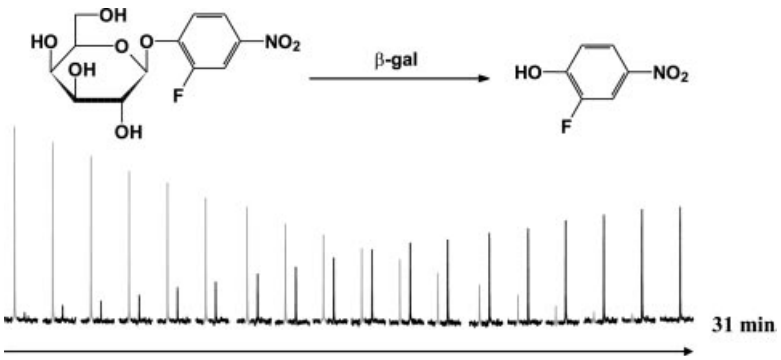

Figure 1.7: Stacked NMR plot demonstrating the conversion of OFPNPG (2.9 mg; 9 mmol) by PC3-lacZ prostate cancer cells (2 x 10^7 in PBS, pH=7.4 at 37°C) to the aglycone OFPNP by stably transfected PC3-*lac*Z cells. OFPNP resonates approximately 5 ppm upfield of the substrate (OFPNPG, grey traces, OFPNP black traces). Each spectrum was acquired in 102 s, and the conversion of OFPNPG to OFPNP was assessed over a period of 31 min. The resulting concentration of OFPNP was not reported. [27]

The success of many different types of anti-cancer therapies is limited by their toxicity to normal, healthy tissues. Gene directed enzyme prodrug therapy (GDEPT) is a method developed to address this problem. Firstly, tumour cells are transfected by a so-called 'suicide' gene. This gene can then selectively code an enzyme capable of converting a nontoxic prodrug into a highly potent chemotherapeutic agent, which in turn kills the cells expressing the gene. For the development of GDEPT, the ability to monitor the degree of targeted gene delivery, in addition to subsequent prodrug delivery and activation, would be of great value in both preclinical and clinical development and evaluation.

Cytosine deaminase (CD) is a microbial enzyme found in several bacteria and fungi, but not in mammalian cells. CD is able to deaminate the minimally toxic pyrimidine derivative 5-fluorocytosine (5-FC) to the cytotoxic 5-fluorouracil (5-FU). Ross *et al*. demonstrated the feasibility of GDEPT, utilising subcutaneous human colorectal carcinoma xenographs in nude mice transfected with yeast CD.[28] The conversion of 5-FC to 5-FU *in vivo* resulted in a ^{19}F chemical shift change of ~1.5 ppm, confirming gene activity (5-FC -49.6 ppm, 5-FU -48.5 ppm, at 7T). Several reports of similar systems *in vivo* have been reported in recent years. [29, 30]

More recently, Payne *et al*. reported a GDEPT strategy utilising another bacterial gene, carboxypeptidase G2 (CPG2).[31] This gene successfully activates the prodrug {4-[bis(2-chloroethyl)amino]-3,5-difluorobenzoyl}-L-glutamic acid to its toxic counterpart by cleavage of the glutamate group (Figure 1.8). The resulting 1 ppm ^{19}F chemical shift separation is adequate to allow for detection of prodrug activation *in vivo*, however the compound is readily hydrolysed and protein binding broadens the signal. To enhance the CPG2 substrate, hydroxyethyl groups were introduced, in place of the chloroethyl groups, resulting in a non-toxic and stable pro-drug. Upon cleavage by CPG2 there is a 1.1 ppm ^{19}F chemical shift separation and, importantly, the activated drug has a narrow MRS resonance in the presence of bovine and foetal bovine albumin. [31]

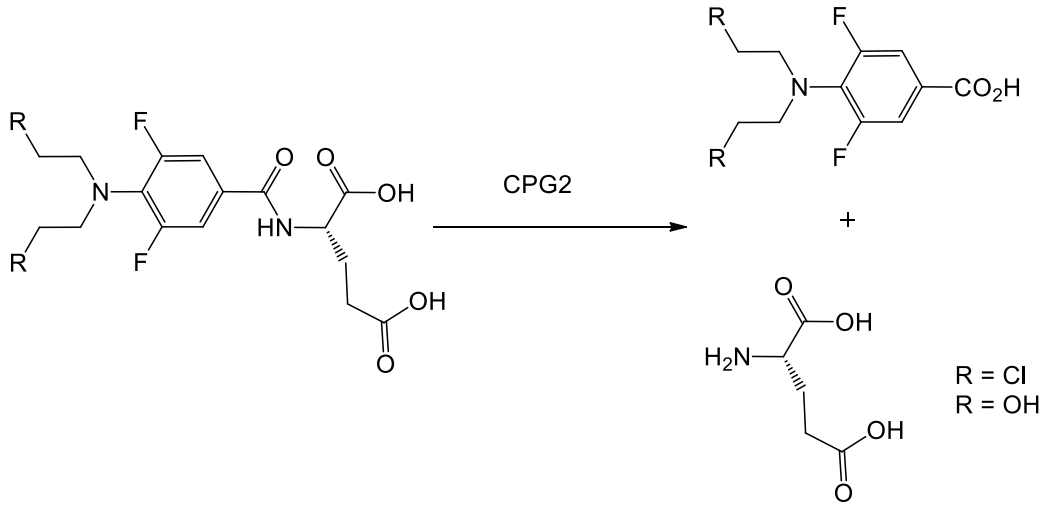

Figure 1.8: Activation of prodrug {4-[bis(2-chloroethyl)amino]-3,5-difluorobenzoyl}-L-glutamic acid.[31]

1.2.1.3 Enzyme Reporters

The use of fluorinated compounds in studies of enzyme activity is of great interest because of the possibility of carrying out the measurements non-invasively *in vivo*. Owing to steric and electrostatic considerations, a hydroxyl group can easily be replaced by a fluorine atom in a variety of sugars with very little overall structural disruption. As they still retain their enzyme substrate activity, they are ideal molecules to probe enzymatic activity, and many of the early examples utilised these .[32]

Mendz *et al*. focused their work on fluorinated compounds containing carboxylic ester groups to measure carboxylesterase activities in two different cellular systems: erythrocytes and in the bacterium *Helicobacter pylori*.[33] Ethyl fluoroactetate and diethyl fluoromalonate penetrated through the cell membrane where they were subsequently converted to the corresponding acid *via* the carboxylesterases, revealed by a shift in ^{19}F MR signal (Table 1.3)

Probe	δ_F Free Acid (ppm)	δ_F Ester (ppm)
Ethyl fluoroacetate	-58.8	-45.9
Diethyl fluoromalonate	-63.2	-72.8

Table 1.3: ^{19}F Chemical shifts to the free acid and ester forms of the different probes incubated with rabbit liver esterase at 310 K in Hepes/Phosphate buffer, 282 MHz. Initial substrate concentration was 8 mM. Chemical shifts are quoted relative to an external 6-Fluoro-Tryptophan reference at 0.0 ppm. [33]

Cubic octameric polyhedral oligomeric silsesquioxanes (POSS) are an excellent scaffold for the accumulation of equivalent fluorine atoms. Chujo *et al*. reported a highly fluorinated POSS (F-POSS), employing trifluoroacetyl groups as the ^{19}F MR signal moiety, covalently linked to silica nanoparticles (NPs) *via* a phosphordiamidate linker.[34] The limited rotation of the linked F-POSS results in significant loss of signal intensity, owing to the extreme broadening of the ^{19}F MR signal. However, in the presence of alkaline phosphatase (AP) the phosphordiamidate linker is cleaved by enzymatic digestion, indicated by an enhancement of ^{19}F MR signal. Two different sizes of NPs, 280 nm and 150 nm diameter, were investigated. The resulting rate of signal intensity increase was shown to be essentially independent of size of NPs ($t_{1/2}$ = 6.2 h and 6.0 h, respectively). While there remains room to improve on signal sensitivity and solubility, there is also the exciting possibility of developing this system further. For example, through modification of the linker the sensing of other various enzymes and proteases could be possible. Moreover, it could have the potential to probe pH *via* hydrolysis.

Kikuchi *et al.* have examined the possibility of *in vitro* real time imaging of enzyme activities, which could potentially offer a vast quantity of information on living systems.[35] This is based on the ability of protease activities to modulate the transverse relaxation time, T_2. The probe consists of three sections; a Gd^{3+} complex, a ^{19}F-containing group, and a short peptide linker, which acts as a substrate for the enzyme caspase-3 (Figure 1.9). Caspase-3 is used in the evaluation of cancer agents as it is an effective marker enzyme of apoptosis. Upon cleavage of the C-terminal peptide bond by caspase-3, the paramagnetic effect felt by the ^{19}F nucleus is reduced and therefore the signal intensity increases as the ^{19}F linewidth narrows. However, the high concentrations required for the detection of protease activity (1 mM, 37 ^{0}C, 70 min, 7 T), due to sensitivity limitations, suggest that this method will only be of interest for *in vitro* approaches. Such a system is also inherently difficult to calibrate.

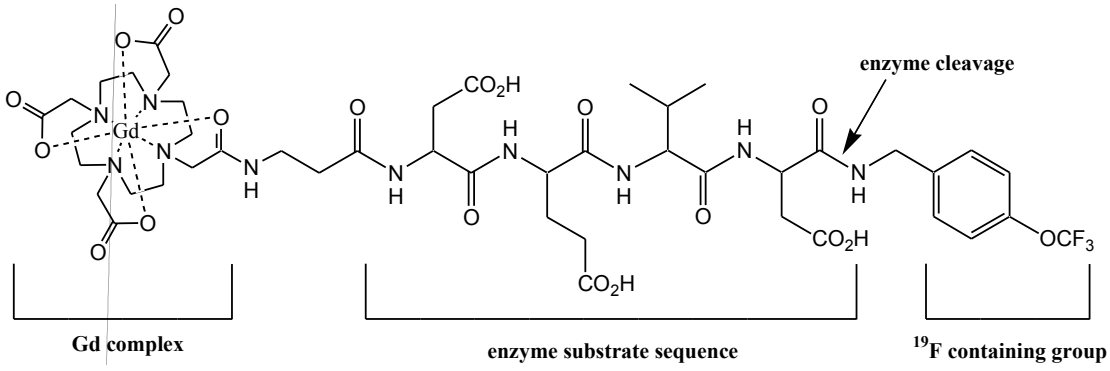

Figure 1.9: The design principle of a ^{19}F MRI conjugate probe.

1.2.1.4 pH Reporters

The pH of biological systems plays an important role in many physiological processes, therefore a great deal of research has focused on optimising methods for measuring intracellular pH. Owing to the high sensitivity of the ^{19}F NMR chemical shift in relation to the microenvironment, many pH indicators incorporating a fluorine atom (or fluorine-containing group) have been investigated. In several cases the fluorinated molecules exploit the chemical shift differences of their protonated and deprotonated moieties. If they are in fast exchange generally only one signal is

observed, as the weighted mean shift of the acid and base forms. The pH can then be measured using the Henderson-Hasselbalch equation:

$$pH = pKa + \log10\ [(\delta_{obs} - \delta_{acid})/ (\delta_{base} - \delta_{obs})] \qquad \text{(Equation 1.2)}$$

where δ_{acid} and δ_{base} is the limiting chemical shift in acid and base, respectively, and δ_{obs} is the chemical shift observed at a given pH. Greatest sensitivity is found close to the pK_a due to the non linear form of the equation. If the exchange is slow on the NMR time scale, both the protonated and deprotonated forms will appear as separate signals. The pH can then be calculated by measuring the ratio of the two observed peaks.

The pioneering work by Deutsch *et al*. presented a series of mono-, di-, and tri-fluoro- α-methylalanines, capable of measuring intracellular pH in human peripheral blood lymphocytes by ^{19}F NMR.[36] After crossing the cellular membrane into the cytoplasm, they are subsequently hydrolysed to give the free amino acid, generating the pH-sensitive moiety. Tandem experiments with both the di- and trifluoromethylalanine methyl esters showed that intracellular pH measurements from the two probes in the same cell suspension agreed to within 0.05 pH units (Figure 1.10).

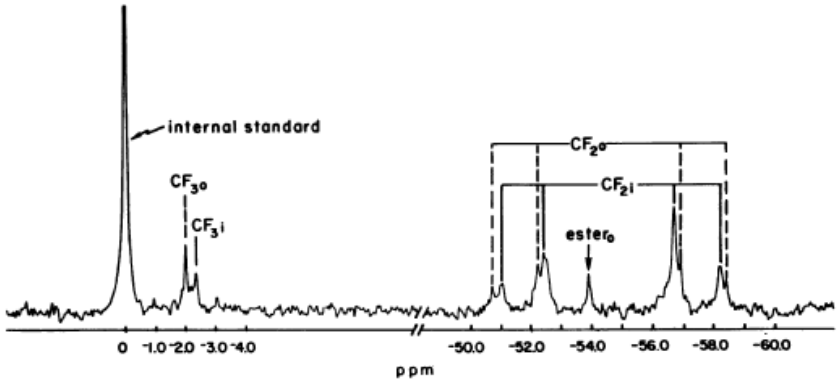

Figure 1.10: *In vitro* ^{19}F NMR spectroscopic study of human lymphocytes with difluoromethylalanine methyl ester (1 mM, labelled CF_2) and trifluoromethylalanine methyl ester (0.17 mM, labelled CF_3) added at 25°C, 200 MHz. Spectra were taken at 6 min intervals (1000 scans, 4.2 μs pulse, acquisition time 0.35 s). The resonances marked o arise from extracellular species, while those marked *i* arise from intracellular species.[36]

A major drawback of this system is the associated error in determining accurate chemical shift values, as illustrated in Figure 1.10. The early work by Deutsch *et al*. did however lead the way for the development of subsequent non-toxic, ^{19}F NMR indicators capable of measuring intracellular pH.

An interesting example of a reporter capable of both intra- and extracellular pH measurement in blood cells is 6-fluoropyridoxamine (6-FPAM).[37] The structure is based on the pyridine vitamin B6 core, with the introduction of a fluorine atom para to the 3 phenolic group and modification of the 4- and 5-position hydroxymethyl moieties (Figure 1.11). 6-FPAM is readily transported across the cell membrane, exhibits a pK_a of 7.05, provides well resolved resonances and has a chemical shift independent of environment, obviously excluding pH. 6-FPAM shows a single resonance in solution, indicative of fast exchange between acid and base forms, and titration in plasma and blood cells showed no change in results. The chemical shift range is 10 ppm, associated with the protonation and deprotonation of the 3-phenolic OH group. Unfortunately, the anaesthetic gas isoflurane also appears in the same spectral region, thereby causing complexity in the interpretation of data. This could be prevented by using a different anaesthetic, or alternatively the introduction of a CF_3 group in place of the fluorine atom would shift the reporter signal so that there is no longer any interference. This could however alter the water solubility and the chemical shift range would be likely to decline.

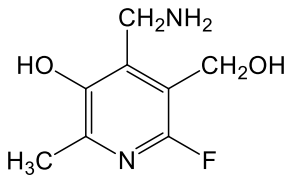

Figure 1.11: Structure of 6-FPAM.

In 2009, Fahmy *et al.* reported a new class of fluorinated polyamidoamine (PAMAM) dendrimers that exhibit a stimulus-induced response to low external pH, which triggers the dendrimers to irreversibly break down into their corresponding

dendrons.[38] ^{19}F MRI experiments were performed with chemical shift imaging focused on the CF_3 resonance. The particulates were surface-modified with poly(ethylene glycol) (PEG), to enhance circulation and transportation in blood, prior to intravenous injection into female B6 mice. The disassembly of the dendrimers *in vivo* was revealed by a reduction in signal intensity, caused by the decrease in ^{19}F longitudinal relaxation rate at lower pH. Additionally, the ^{19}F signal linewidths narrowed and became significantly sharper with altering the external microenvironment from physiological pH to low pH (pH=7.5, $\omega_{1/2}$ = 300 Hz, pH=2, $\omega_{1/2}$ = ~100 Hz, 4.0 T). Scanning electron micrography (SEM) confirmed the break-down of the dendrimers. The amphiphilic nature and easily modifiable surface of the PAMAM dendrimer opens up many possibilities for future development, targeted drug delivery and responsive molecular imaging.

Nanosized particles (< 100 nm) have been shown to accumulate in solid tumours through enhanced permeability and retention (EPR) effects.[39] As such, Nagasaki *et al.* have recently focused their research on the development of pH-responsive PEGylated ^{19}F nanoprobes.[40] The probe consists of two sections; a polyamine gel core cross-linked with trifluoromethyl containing groups, and an external matrix of PEG chains that support acetal groups to enable linkage to tumour-specific molecules (Figure 1.12).

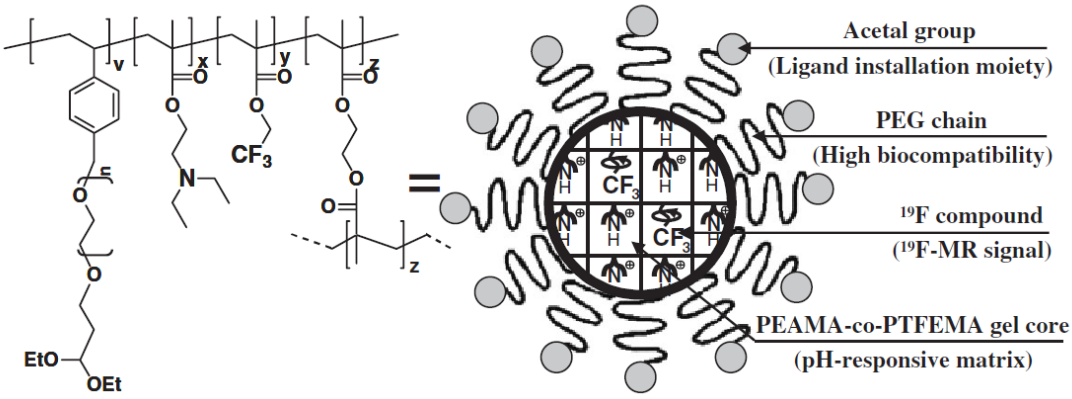

Figure 1.12: Schematic illustration of tumour-specific nanoprobe.[40]

The fluorinated PEGylated nanogels have been designed to observe changes in pH values between pH 6.5 and 7.4, signified by a change in ^{19}F signal intensity. This

result is attributed to the unique ability of the gel core to swell at acidic pH and shrink in basic media, thereby altering the molecular motion of the ^{19}F atoms and, in turn, affecting the transverse relaxation time T_2. At lower pH, the amino groups are protonated, resulting in an 8.7 fold larger hydrodynamic volume in comparison to that at the physiological pH, in addition to an increase in the ion osmotic pressure. (Table 1.4)

pH	Diameter (nm)	T_1 (ms)	T_2 (ms)	S/N
7.4	52	<30	<1	0.0
6.5	107	280	56.8	7.6
5.5	109	304	53.2	5.8

Table 1.4: Changes in PEGylated nanogel parameters with varying pH. [40]

As the extracellular pH of the tumour environment is typically 0.4 to 1.0 pH units lower than physiological pH,[41] the probe should intensify signal inside the tumour and essentially 'turn-off' the signal outside of the tumour. While phantom ^{19}F and ^{1}H MR images yielded promising results, *in vivo* experiments need to be performed to determine if the 'on-off' switch regulation successfully works in tumour environments.

1.2.1.5 Metal Ion Reporters

Metal ions, such as Ca^{2+} and Mg^{2+}, are present in many cells. Changes in their local concentration occurs during many cellular processes, driving the desire for specific reporter molecules. In the late 1980s, fluorinated derivatives of the chelator *o*-aminophenol-N,N,O-triacetic acid (APTRA) were exploited for the determination of cytosolic, ionized magnesium levels by ^{19}F NMR spectroscopy.[42] The magnesium ions are in slow exchange with the 5F-APTRA and MF-APTRA (Figure 1.13), as shown by the presence of both free and bound chelates. The relatively large chemical shift change exhibited ($\Delta\delta \approx 10$ ppm) allows for the distribution of each entity separately. Although complexation of the fluorinated APTRA derivatives with Ca^{2+} ions

generated similar chemical shifts to that of complexed magnesium, previous determinations in these cells proved that cytosolic free calcium is present at too low a level to complex the indicator. Subsequent studies on APTRA derivatives include the determination of changes in cystosolic free magnesium ion concentration during myocardial ischemia by ^{19}F NMR spectroscopy in a perfused rat heart.[43]

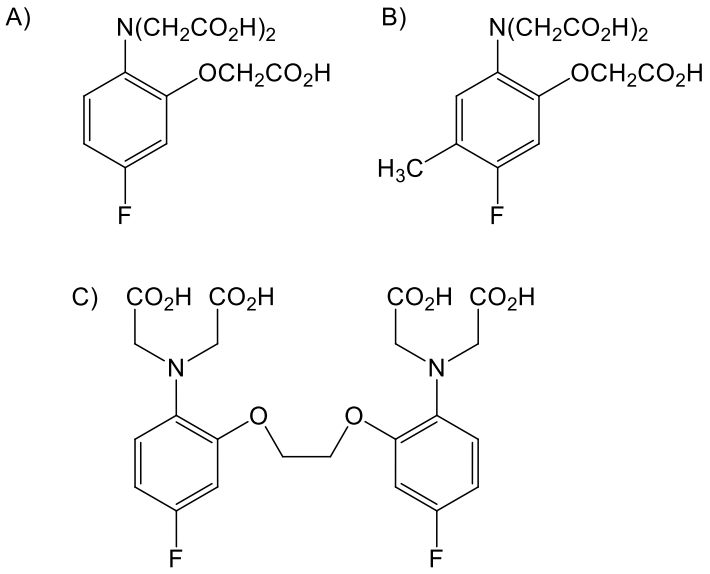

Figure 1.13: Structure of A) 5F-APTRA, B) MF-APTRA and C) 5FBAPTA.

A reporter molecule capable of detecting many different divalent metal ions, including Zn^{2+}, Pb^{2+}, Fe^{2+} and Ca^{2+} is 5,5,-difluoro-1,2-bis(o-aminophenoxy)ethane-N,N,N',N'-tetraacetic acetic acid, more commonly known as 5FBAPTA (Figure 1.13).[44] There is no need for an external reference with 5FBAPTA, because the free and bound moieties are in slow exchange on the NMR timescale, and appear as two separate resonances. The metal ion concentration can then be calculated from the signal integrals (Equation 1.3).

$$[M^{2+}] = K_D \frac{[M^{2+} - 5FBAPTA]}{[5FBAPTA]} \qquad \text{(Equation 1.3)}$$

where K_D is the dissociation constant and [M^{2+}-5FBAPTA] and [5FBAPTA] are the peak integrals of the metal bound and free chelator signals, respectively. It is

important to note that K_D depends on ionic strength, pH and concentration of free Mg, all of which need to be evaluated independently for the above equation to hold true.

Schanne *et al.* cleverly used 5FBAPTA to probe the effect of lead on intracellular free Ca^{2+} concentration in the rat osteoblastic bone cell line ROS 17/ 2.8.[45] Ca-5FBAPTA and Pb-FBAPTA resonances occur at δ_F 5.8 and 4.9 ppm, respectively, from the free reporter molecule. Addition of 5 and 25 μM of Pb^{2+} resulted in a 50 % and 120 % increase in [Ca^{2+}] over a time period of 5 h. This simple experiment successfully demonstrated the unique ability of 5FBAPTA to quantitatively measure multiple ion concentrations in tandem.

Plenio and Diodone synthesised a series of fluoro-cryptands, capable of forming complexes with a number of different group I and II metal ions (Figure 1.14).[46]

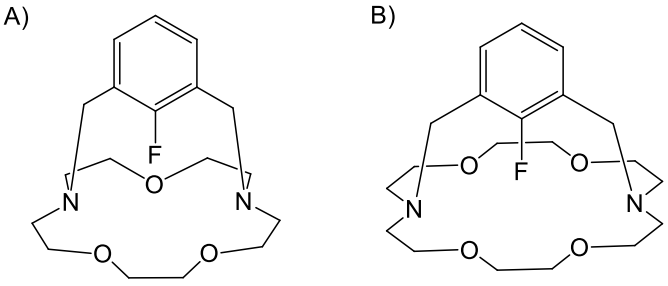

Figure 1.14: Structure of A) FN_2O_3 and B) FN_2O_4.

The change in ^{19}F NMR shift of FN_2O_4 complexes correlates well with the ionic radii of the metal ions, as does the $^1J_{CF}$ coupling constants which range from 253.0 Hz for FN_2O_4 to 238.5 Hz for [Li.FN_2O_4] (Table 1.5). These values give an indication of the strength of metal-fluorine interactions, suggesting that the smaller metals ions migrate into the cavity and interact with the C-F unit with less difficulty than the larger ions. While this system benefits from multiple ions being able to be detected simultaneously, it lacks capability for quantitative analysis.

	δ_F/ FN_2O_3	δ_F/ FN_2O_4
Ligand	-109.1	-114.4
Li^+	-18.2	-12.8
Na^+	-5.1	-11
K^+	N/A	-4.5
Rb^+	N/A	-1.7
Cs^+	Several Species	-4.6
Ca^{2+}	-9.2	-11.9
Sr^{2+}	-3.1	-9.5
Ba^{2+}	N/A	-5.1

Table 1.5: ^{19}F NMR shifts of Fluoro Cryptands, FN_2O_3 and FN_2O_4, and their metal complexes [53]

1.2.2 Passive Agents

Passive agents do not interact with the local environment, they merely occupy a space in tissue or organs. Such agents, as discussed in detail below, are extremely useful in disclosing information on anatomical properties, such as vascular volume or blood flow.

1.2.2.1 Marker for Alzheimers Disease

Alzheimers disease is the principal cause of senile dementia, characterised by amyloidosis and tauopathy.[47] Accumulation of plaques composed of amyloid β peptide in human brains can be found many years before the launch of the disease, thus detection of such plaques is vital in diagnosis of pre-symptomatic patients. Highuchi *et al*. intraveneously administered a ^{19}F-containing amyloidophilic compound (FSB, 20 mg kg^{-1}) to amyloid precursor protein transgenic mice (Figure 1.15).[48] The FSB, capable of crossing the blood-brain barrier, specifically labelled the amyloid β plaques and allowed them to be visualised *in vivo* by ^{19}F and ^{1}H MRI. The drawback of the system was the low sensitivity of the ^{19}F MRI method.

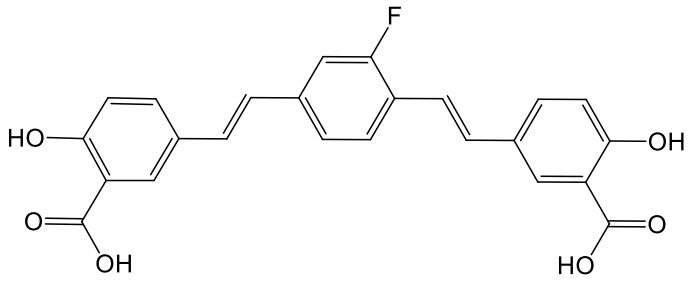

Figure 1.15: Structure of FSB

The toxicity profile of FSB, examined as part of the study, indicated that administrations > 40 mg kg^{-1} could be nephrotoxic. Thus, it was not possible to increase the dosage in an attempt to enhance sensitivity. Flaherty *et al.* tackled this problem by modifying the structure to include multiple equivalent fluorine atoms in the form of a tetrafluorophenyl core or symmetrical trifluoromethyl groups (Figure 1.16).[49] Aside from the increase in signal, it was found that the more electropositive tetrafluorophenyl core provided a stronger interaction with the amyloid β plaques than FSB. This observation was tentatively attributed to the ability of the fluorine atoms to form hydrogen bonds and interact with cations. The former is plausible, the latter is very unlikely.

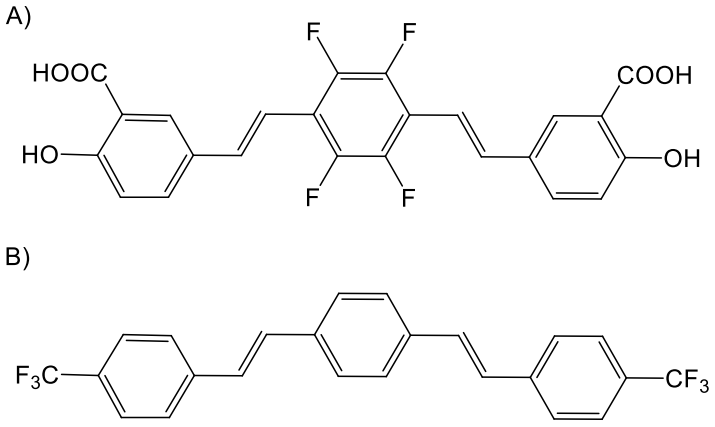

Figure 1.16: Structures of A) tetraphenyl core derivative and B) trifluoromethyl derivative

1.2.2.2 Volume Reporters

The significant gas solubility and strong ability for transportation of oxygen and carbon dioxide renders perfluorocarbons ideal candidates as synthetic blood

substitutes.[50] Perfluorocarbons in their biocompatible emulsified form are utilised in the measurement of lung filling by ^{19}F NMR spectroscopy. Relaxation measurements are examined to gauge the regional pO_2 values in the lungs, which subsequently leads to the determination of lung volume. The perfluorocarbons are often administered to the lungs in the form of aerosols despite this being a rather stressful approach for the test subjects. An alternative, less aggressive, method is to use an inert gas and initial studies utilising CF_4, C_2F_6 and SF_6 have been explored. In particular, SF_6 has shown potential for detection of diseases, including emphysema and lung cancer (Figure 1.17).[51] However, specialised instrumentation is required for SF_6 detection, owing to its extremely short ^{19}F relaxation time (T_1 = 5.9 ± 0.2 ms). The use of hyperpolarized gases, such as helium for this application, has increased dramatically in recent years, reducing the demand for ^{19}F MRI of the lungs.[52]

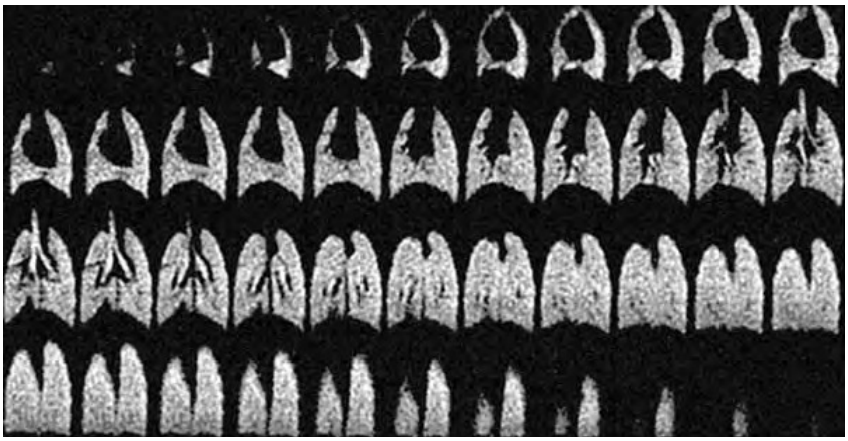

Figure 1.17: Three dimensional ^{19}F NMR spectra of SF_6 in the lungs of a large rat. Spectra obtained in 30 min. Frames, from top left to bottom right are successive planes of the image from chest to back. In the lungs 25 % of the volume is occupied by tissue. Therefore, the lungs are not as bright as the large airways, where the spin density of pure gas is higher. [51]

In cancer patients the growth of new blood cells, termed angiogenesis, is necessary for cancerous cells to grow and spread. Therefore, it is vital to be able to monitor tumour blood volume. Proton MRI contrast agents are capable of indicating perfusion, an approach based on first pass kinetic analysis, however the interpretation of results is very complex.[53] An alternative approach, in conjunction with ^{19}F NMR spectroscopy, utilises intravenous biocompatible perfluorocarbon emulsions, which are retained in the vasculature for a period of hours, to provide an

indication of vascular volume in a non-invasive manner.[54] Fluorinated gases, such as trifluoromethane, have been used for the measurement of cerebral blood flow, a method based on inflow and outflow kinetics.[55]

Inflammation is linked with a number of human diseases, including brain trauma, transplant rejection and heart disease. Precise diagnosis is extremely difficult and therapy is often limited to symptomatic treatment. In 2008, Flogel *et al*. demonstrated the feasibility of monitoring inflammation processes *in vivo* with a 'positive contrast' at high local resolution using ^{19}F MRI.[56] Emulsified perfluoro-15-crown-5-ether (PFCE), chosen because of the 20 equivalent fluorine nuclei, was intravenously injected into two separate murine models of acute cardiac and cerebral ischemia. The merging of ^{1}H and ^{19}F MR images, simultaneously collected at 9.4 T, enabled an exact anatomic localisation of PFCE after injection (Figure 1.18). Repetitive imaging (5 times within a 7 day period) revealed penetration of the PFCE into the border zone of infracted areas in both models, showing a tremendous degree of specificity.

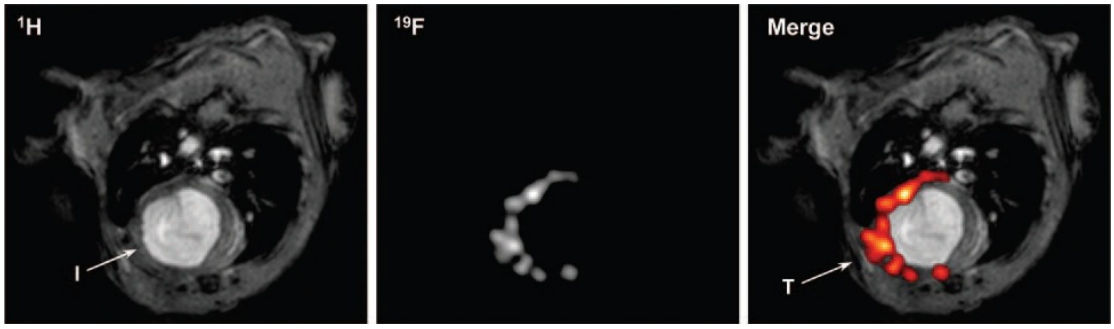

Figure 1.18: ^{19}F MRI *in vivo* demonstrating infiltration of PFCE after myocardial infarction. ^{1}H and ^{19}F images from the mouse thorax recorded 4 days after ligation of the LAD show accumulation of ^{19}F signal near the infarcted region (I) and at the location of surgery where the thorax was opened (T). PFCE was injected at day 0 (2 hours after infarction) *via* the tail vein.[56]

1.2.2.3 Cellular Therapeutics

When cells are transferred to a patient to treat a specific disease this is known as cellular therapeutics. A significant amount of research has focused on stem cell transfers to help restore function to damaged tissues. For successful cellular therapy

it is critical that transferred cells are quantitatively monitored, post-transplant, in a non-invasive manner. Traditionally, *in vitro* cultured stem cells are incubated with contrast agents, such as Gadolinium diethylenetriamine penta-acetic acid [Gd.DTPA(H_2O)], allowing the cells to serve as imaging agents and enabling monitoring by ^{1}H MRI.[57]

Alternatively, Chen *et al.* demonstrated that stem cells labelled with liquid perfluorocarbon (PFC) nanoparticles produce sensitive cell markers, suitable for ^{19}F MRI detection at 11.7 T (research) and 1.5 T (clinical) scanners. Two PFC cores were examined, perfluorooctylbromide (PFOB) and perfluoropolyether (PFPE). Mononuclear cells, harvested from human umbilical cord blood, internalized the PFC nanoparticles readily whilst retaining their functionality. This enabled spatial cell localization and detection of multiple fluorine signals. (Figure 1.19).[58]

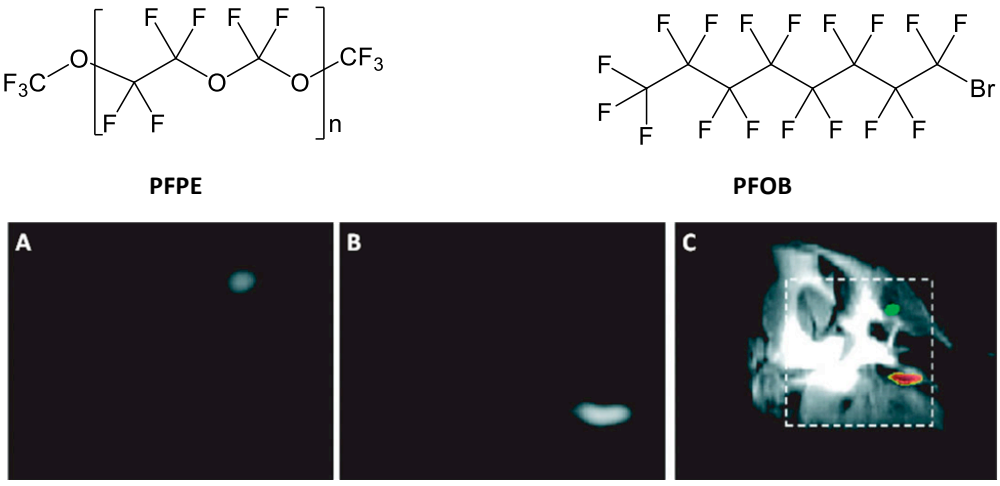

Figure 1.19: Localisation of labelled cells after *in situ* injection into the skeletal mouse thigh. At 11.7 T, spectral discrimination permits imaging the fluorine signal attributable to 10^6 FBOB-loaded (A) or PFPE-loaded (B) individually, which when overlaid onto a ^{1}H MRI image of the site (C) reveals FPOB and PFPE labelled cells localized to the left and right leg, respectively.[58]

Ruiz-Cabello *et al.* reported the synthesis and evaluation of cationic PFCE labelled neural stem cells (NSCs). Following injection into the stratium of mouse brain, the labelled cells were identified *in vivo*, retaining a constant ^{19}F signal over a 2 week period, consistent with low toxicity and high stability.[59] The MR sensitivity of 140 pmol of PFCE per cell (at 5 mins of acquisition) is more than adequate to monitor cell

therapy of neurodegenerative diseases in the central nervous system, based on the current injected cell doses in practice (of the order of 1 x 10^5 cells or more).

Whilst it is vital to be able to track stem cells, as described above, it is of equal importance to be able to quantify a specific cell population. Lymphoid cells, including T cells, infiltrate the islets of Langerhans in the early stages of type 1 diabetes (T1D), eventually destroying the insulin-producing β cells of the islets.[60] In 2007, Ahrens *et al.* labelled T cells *ex vivo* with a PFPE nanoparticle tracer agent and administered them into the nonobese diabetic mouse, a widely established model of human T1D.[61] Quantitative cell migration was monitored using spin density-weighted ^{19}F MRI in conjunction with ^{1}H MRI to provide anatomical context, and a computational algorithim provided cell counts. Approximately 2 % of the injected diabetogenic T cells homes to the pancreas after 48 h.

In a subsequent report from the same group, a common fluorescent dye (BODIPy-TR) was conjugated to the PFPE nanoparticle tracer, allowing for studies of the cells post-imaging.[62] Naïve mouse T cells were labelled *ex vivo* and then injected to a simple BALB/c mouse model (Figure 1.20).

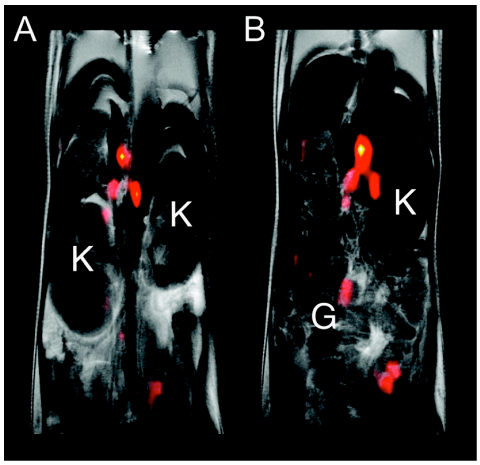

Figure 1.20: *In vivo* MRI of labelled T cells in a BALB/c mouse model. The ^{19}F image (pseudo-colour) shows a localized accumulation of T cells labeled with PFPE nanoemulsion in lymph nodes and the grayscale underlay is an anatomical ^{1}H image. (A) and (B) display two consecutive 2 mm thick slices through the torso, and for anatomical orientation the kidneys (K) and gut (G) are noted.[62]

The lymph nodes displaying the strongest ^{19}F MRI signal *in vivo* were surgically extracted after imaging. Fluorescence activated cell sorting (FACS) was then used to quantify the presence of the T cells and confirm the localisation information from the ^{1}H and ^{19}F MRI results. This approach was subsequently applied to a murine inflammation model using antigen-specific T cells. The main difference with this study is the clever exploitation of the fluorescent section of the labelled cells, enabling the use of *in vivo* optical imaging to corroborate the ^{19}F MRI T-cell trafficking patterns and eliminating the need for post-imaging biopsies.[63]

1.2.2.4 Highly Fluorinated ^{19}F MR agents

Whilst PFCs have numerous advantages, such as low toxicity and high stability, they also have limitations due to their low solubility, long T_1 relaxation times, split ^{19}F signals and excessive retention in internal organs. As such, there is a growing interest in the development of stable, hydrophilic molecules capable of emitting a single ^{19}F signal from multiple fluorine atoms.

Yu *et al.* reported the synthesis of a water soluble bispherical fluorocarbon molecule, consisting of 27 equivalent fluorine atoms (Figure 1.21).[64] *In vivo* studies on BALB/c male mice (60 mmol kg^{-1} ^{19}F) showed a single ^{19}F peak with no evidence of prolonged organ retention ($t_{1/2}$ = 12 h) or degradation. The main advantage of spherical cones is the ability to modify the structure at the cone without disrupting the symmetry of the molecule. However, to increase ^{19}F MR sensitivity more equivalent fluorine atoms would need to be added to the cone, and this approach can only go so far (~ 100 fluorine atoms).

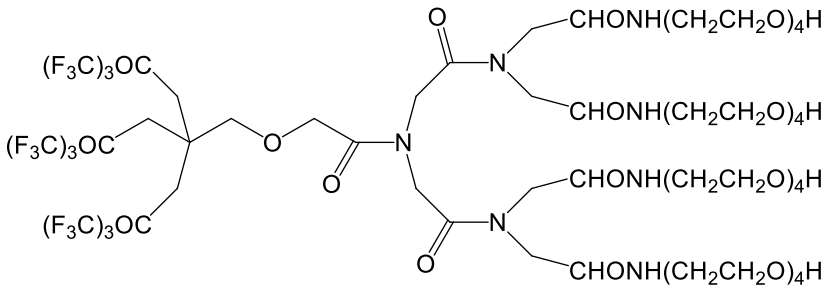

Figure 1.21: Structure of water soluble bispherical fluorocarbon

Wooley *et al.* developed a series of fluorinated polymeric micelles, self assembled from co-polymers with high fluorine content, as potential ^{19}F MR agents.[65] The nanomaterials were designed to have a hydrophobic core, to enable therapeutic loading, and a hydrophilic shell (owing to the incorporation of acrylic acid groups) to ensure water solubility. All micelles gave a single resonance by ^{19}F NMR spectroscopy ($\omega_{1/2}$ = 130 Hz, T_1 = 500 ms, T_2 = 50 ms, 11.7 T) and the relaxation times were not affected by size or composition of structure. While the ^{19}F phantom imaging studies showed good SNR for all micelles, in the region of 11-32, this was only after extremely long scan times (1024 scans, 13 h).

An alternative approach involves the use of diblock coploymers consisting of hydrophilic blocks of poly-acrylic acid and hydrophobic blocks of fluorinated acrylate and methyacrylate.[66] In water/DMF mixtures they undergo spontaneous self-assembly to form stable micelles, ranging in size from 20-45 nm, with a single peak observed in the ^{19}F NMR spectra. Two distinct T_2 values were recorded for each micelle; the shorter T_2 is caused by restricted movement of the fluorine nuclei in chain segments (resulting in broader signals with poorer signal intensity), while the longer T_2 is caused by large amplitude molecular motion. The acrylate system revealed a sharper fluorine resonance, a shorter T_1 ($\omega_{1/2}$ = 231 Hz, T_1 = 511 ms vs $\omega_{1/2}$ = 280 Hz, T_1 = 676 ms at 7 T for the methylacrylate) and superior MRI image intensity, owing to the greater chain flexibility.

It has long been known that fluorinated groups in polymeric structures are prone to aggregate in water, which can lead to a reduction in molecular mobility. To combat this problem, Whittaker *et al*. synthesised partially fluorinated polyelectrolytes.[67] By exploiting the electrostatic repulsion between the different monomer units, aggregation in water could be prevented, maintaining sufficient mobility and obtaining images of high intensity (Figure 1.22).

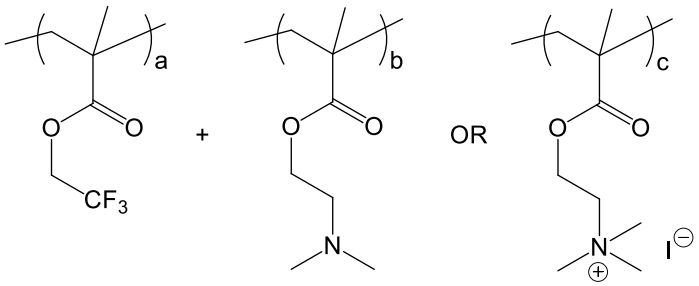

Figure 1.22: Structures of the different monomer units

In 2010, Whittaker *et al*. also reported a new class of hyper-branched polymers that are capable of controlled functionality, achieved through reversible addition-fragmentation chain transfer (RAFT) chemistry.[68] Four different hyper-branched polymers, incorporating acid (P1), alkyne (P2) and mannose (P4) end groups, were investigated. Although P1 exhibited significant toxicity in comparison to a control polymer (PEG-400) it was chosen for preliminary *in vivo* studies owing to its non-targeting properties (Figure 1.23). Unfortunately results show minimal ^{19}F signal immediately after injection into mouse tail vein (20 mg/ mL, 100 µL). This could be due to the vast distribution of P1 in the vasculature. While it is clear the system requires many improvements, most notably in terms of reducing toxicity and increasing signal intensity, there is huge potential for hyper-branched polymers if they can be successfully adapted to a variety of biological targets.

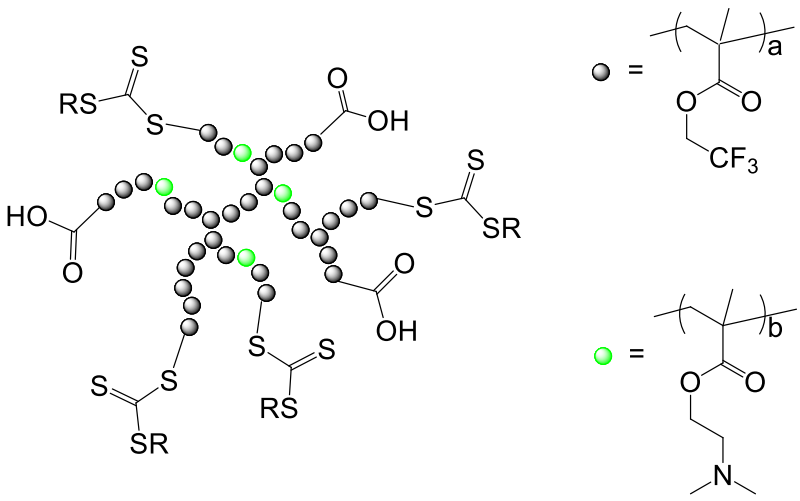

Figure 1.23: Structure of Polymer P1

1.2.3 Fluorinated Drugs

Fluorine atoms can be selectively incorporated into pharmaceuticals to alter biological activity, lipophilicity, pK_a and, or *in vivo* retention times. As such, there are a vast number of fluorinated pharmaceuticals and industrial agents, ranging from chemotherapeutics for cancer such as gefitinib, to antifungals such as fluconazole. The diverse range of applications for fluorinated compounds render them ideal for use in ^{19}F NMR spectroscopic analysis.

Most studies to date have focused on the metabolic pathway of anticancer chemotherapeutic agent 5-fluorouracil (5FU). The investigation into the uptake, biodistribution and metabolism of 5FU is required due to its restricted efficiency and possible toxicity.[69] Ideally, all 5FU should be converted to nucleosides and nucleotides for cytostatic activity, requiring the activity of various kineases and phosphorylases. However competing catabolic reactions convert 5FU to 5,6-dihydrofluorouracil (DHFU) and α- fluoro β-alanine (FBAL) in the liver, offering very little toxicity. More troubling is the conversion of FBAL in the kidneys to generate fluoride ions, which are cardio- and neuro-toxic.[70] ^{19}F NMR spectroscopy studies analysing the chemical shift and relaxation properties of side products have been used to monitor the metabolic pathway of 5FU.[71, 72]

Owing to the restrictive toxicity profile of 5-FU a great deal of research has focused on developing new anticancer drugs. Gemcitabine is one such drug, incorporating both sugar and pyrimidine moieties (Figure 1.24). Gemcitabine, once in cells, requires conversion to a triphosphate derivative by phosphorylation. Once in its active form, it is incorporated into DNA where it can inhibit DNA polymerases. It was hypothesised that the rate limiting enzyme in this phosphorylation was the kinase dCK. Blackstock *et al.* examined Gemcitabine uptake and clearance in two different models of HT-29 human colon carcinoma xeonographs (160 mg kg^{-1}); a control model and a model infected with the dCK gene.[73] *In vivo* ^{19}F MRI results showed a 2.5 fold greater accumulation of Gemicatabine in the dCK xenograph in comparison with the control model. Unlike most compounds studied by ^{19}F MRI/S, which give rise to a

singlet, the two diastereotopic fluorine atoms on Gemcitabine give rise to a quartet at -42 ppm.

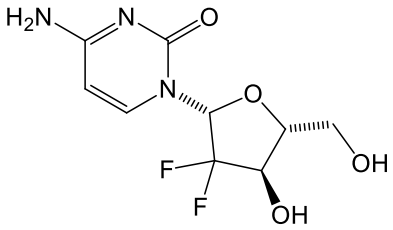

Figure 1.24: Structure of Gemcitabine

3-Aminobenzamide (3-ABA) is an inhibitor of poly(AD-ribo) polymerase 1, a key enzyme for the early repair of spontaneous and stimulated DNA strand breaks. Brix *et al*. evaluated the biodistribution and pharmacokinetics of a trifluoromethylated derivative of 3-ABA, named 3-ABA-TFE, in Copenhagen rats with Dunning prostate adenocarcinoma (Figure 1.25).[74] Full body *in vivo* ^{19}F MRS sampling of all nine rats (400 mg kg^{-1}) showed 3-ABA-TFE signal intensities in tumours much weaker than in the muscular and liver system, suggesting that intra-tumoral uptake could be low in comparison with normal tissue. There was no evidence of contamination, degradation or formation of by-products up to 8 days post-injection. This provides a good example of how MRS can be used to monitor the biodistribution of a drug in a non-invasive, longitudinal manner.

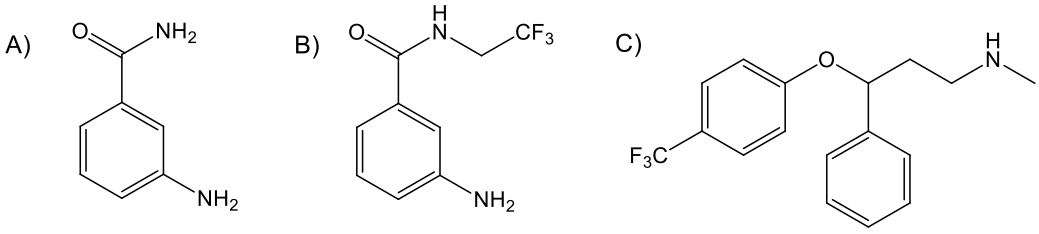

Figure 1.25: Chemical Structure of A) 3-ABA, B) ^{19}F-labelled derivative 3-ABA-TFE and C) (±)-fluoxetine.

There have been many reports of fluorinated psychiatric agents being investigated by ^{19}F MRS, including the antidepressant drug (±)-fluoxetine (Prozac). In an interesting report, Bolo *et al.* investigated the withdrawal kinetics in humans treated with fluoxetine.[75] Six subjects, who had been receiving daily doses of 100-300 mg for a period of 1-12 months, were studied. *In vivo* ^{19}F MRS of the brain and lower

extremities, in conjunction with blood plasma sampling, confirmed the presence of the drug in both areas (δ_F = -61.6 ppm, $\omega_{1/2}$ = 54 Hz, 2.7 T). Surprisingly, 84 days post withdrawal from the drug, a ^{19}F MRS signal was still being detected after complete disappearance from plasma and brain (Table 1.6). The enduring signal is most likely from the drug, or a metabolite of the drug, which is accumulated in the bone marrow. This study is an excellent example of the unique capabilities of MRS, in comparison with more traditional techniques.

Last day signal was detected	SNR of last detected signal
13	1.4 µM
40	2.2
Still present at 84 days	7

Table 1.6: Comparison of late post-withdrawal ^{19}F MRS signal characteristics from different tissues.[75]

1.3 Paramagnetic NMR

There are many applications which utilise lanthanide complexes as NMR shift and relaxation reagents, ranging from molecular stereochemistry investigations to the previously mentioned contrast agents for MRI.

When in solution, the most stable oxidation state of the lanthanides is +3, giving an electronic configuration of [Xe] $4f^n$, with *n* varying from 0 (La^{3+}) to 14 (Lu^{3+}) (Table 1.7). Obvious exceptions to this are when the ion achieves an empty (f^0), half filled (f^7) or full (f^{14}) *f* orbital, examples include Eu^{2+} and Ce^{4+}.

When a Ln^{3+} ion interacts with a Lewis base, the presence of unpaired 4*f* electrons influences all NMR active nuclei within close proximity. This can lead to perturbation of NMR parameters such as increased relaxation, resonance broadening, and alterations in chemical shift values. The Gd^{3+} ion is unique in that it has an isotropic spatial distribution of unpaired *f* electrons. Each of the remaining Ln^{3+} ions have an anisotropic spatial distribution of unpaired *f* electrons, and are therefore able to

create a dipolar lanthanide-induced shift in solution, more commonly known as a pseudocontact shift.

1.3.1 Chemical Shift

The lanthanide induced shift for a nucleus of a ligand coordinated to a Ln^{3+} ion can be expressed as the sum of three terms: the diamagnetic (Δ_d), the contact (Δ_c), and the pseudocontact shift (Δ_p) (Equation 1.4).

$$\Delta = \Delta_d + \Delta_c + \Delta_p \qquad (1.4)$$

The diamagnetic shift, which stems from inductive and electrical field effects, in addition to conformational changes, is generally insignificant. However, in cases where the nuclei under investigation is directly coordinated to the Ln^{3+} ion, the diamagnetic shift plays a more important role. The contact shift originates from through-bond transmission of unpaired electron spin density to the nucleus from the lanthanide 4f orbital (Equation 1.5). The Ln unpaired spin density can be transferred to the nucleus of the ligand by direct spin delocalisation through weak covalent bonding using the 6s metal orbital or through spin polarisation from 4f orbitals. As the number of bonds between Ln^{3+} and the nucleus under investigation increases, the magnitude of the shift decreases, allowing for identification of ligand donor sites.[76]

$$\Delta c = < S_Z > F = < S_Z > \frac{-A}{h\gamma_I B_0} 10^6 \qquad (1.5)$$

Where, $<S_z>$ is the calculated spin expectation value for a calculated paramagnetic ion (Table 1.7), γ_I is the gyromagnetic ratio of the nucleus, and A/h is the hyperfine coupling constant of the nucleus under study. The large lanthanide induced shift of the donor nucleus is associated with considerable line broadening. Consequently, if the exchange between the bound and free state is slow on the NMR timescale, it is unlikely there will be a detectable signal for the bound state.

The pseudocontact shift originates from the local magnetic field induced by the anisotropy of the magnetic moment of the lanthanide ion in the nucleus under study. If the principal magnetic axes system is used, the pseudocontact shift can be expressed by equation 1.6:

$$\Delta p = \frac{C_J \mu_B^{\ 2}}{60k^2T^2}\left[\frac{\langle r^2\rangle A(3\cos^2\theta - 1)}{r^3} + \frac{\langle r^2\rangle A'\sin^2\theta\cos 2\phi}{r^3}\right] \qquad (1.6)$$

Where, C_J is the Bleaney's constant characteristic of the Ln^{3+} ion (Table 1.7), $\langle r^2\rangle A$ and $\langle r^2\rangle A'$ are ligand field coefficients, μ_B is the Bohr magneton and r, θ and ϕ are the spherical coordinates which describe the position of the nucleus under study. For a given series of isostructural complexes, it is assumed that the ligand field coefficients are invariant amongst the lanthanides.

Ln^{3+}	Electronic Configuration	$^{2S+1}L_J$	C_J[a]	$\langle S_z\rangle$[b]	μ_{eff}[c]	^{1}H shift/ aqua[d]
Ce	[Xe] $4f^1$	$^2F_{5/2}$	-6.3	-0.98	2.56	----
Pr	[Xe] $4f^2$	$^3H_4$	-11	-2.97	3.62	0.27
Nd	[Xe] $4f^3$	$^4I_{9/2}$	-4.2	-4.49	3.68	0.32
Pm	[Xe] $4f^4$	$^5I_4$	2	4.01	-----	----
Sm	[Xe] $4f^5$	$^6H_{5/2}$	-0.7	0.06	1.55- 1.65	----
Eu	[Xe] $4f^6$	$^7F_0$	4	10.68	3.40- 3.51	----
Gd	[Xe] $4f^7$	$^8S_{7/2}$	0	31.5	7.94	3.01
Tb	[Xe] $4f^8$	$^7F_6$	-86	31.82	9.7	-10.53
Dy	[Xe] $4f^9$	$^6H_{15/2}$	-100	28.55	10.6	-6.95
Ho	[Xe] $4f^{10}$	$^5I_8$	-39	22.63	10.6	-4.88
Er	[Xe] $4f^{11}$	$^4I_{15/2}$	33	15.37	9.6	3.83
Tm	[Xe] $4f^{12}$	$^3H_6$	53	8.21	7.6	9.29
Yb	[Xe] $4f^{13}$	$^2F_{7/2}$	22	2.59	4.5	2.52

Table 1.7: Various NMR parameters for paramagnetic lanthanide ions: [a] Normalised to 100 for Dy[77]; [b] Calculated Values[78]; [c, 77]; [d] Values in ppm[78].

The interpretation of lanthanide induced shift values is relatively simple when the exchange of nuclei of the ligand between the bound and free state is slow on the NMR timescale. However, complications can arise due to the effect of the Curie relaxation mechanism (refer to 1.3.2) and extreme line broadening, especially with

complexes of the later lanthanides (*eg.* Tb, Dy, Ho). In an attempt to minimise the Curie relaxation mechanism, measurements can be taken at high temperatures and low magnetic field strengths.

1.3.2 Relaxation Theory

As mentioned previously, the coordination of a paramagnetic lanthanide ion to a ligand results in an increase in both the longitudinal, R_1, and transverse, R_2, relaxation rates. The observed relaxation rate can be expressed as the sum of two terms; the diamagnetic contribution, R_{id}, and the paramagnetic contribution, R_{iM} (Equation 1.7).

$$R_{iobs} = R_{id} + R_{iM} \tag{1.7}$$

R_{id} corresponds to the relaxation rate of solvent nuclei in the absence of a paramagnetic solute, and is often measured with diamagnetic (*i.e.* utilising Y^{3+}, Lu^{3+}, or La^{3+}) complexes. R_{iM} originates from the electron-nuclear interaction between the nuclear spin of the nucleus under investigation, and the magnetic field generated by the presence of unpaired 4f electrons. Electron spin relaxation, molecular tumbling and chemical exchange all modulate the electron-nuclear interaction. The dominant relaxation mechanisms for paramagnetic systems can be described in terms of the contact contribution, R_{icon}, the dipole-dipole contribution, R_{idip}, and the Curie contribution, $R_{i\chi}$ (Equation 1.8).

$$R_{iM} = R_{icon} + R_{idip} + R_{i\chi} \tag{1.8}$$

The contact contribution, R_{icon}, is negligible for all Ln^{3+} ions, with the exception of gadolinium. For Ln^{3+} ions (excluding gadolinium) with short electronic relaxation times, (T_{1e}), the dipolar contribution can be expressed by the simplified Solomon-Bloembergen equation:

$$R_{1dip} = R_{2dip} = \frac{4}{3}\left(\frac{\mu_0}{4\pi}\right)^2 \frac{\gamma_I^2 \mu_{eff}^2}{r^6} T_{1e} \quad (1.9)$$

where, $\mu_0/4\pi$ is the magnetic permeability of a vacuum, r is the Ln-nucleus distance and μ_{eff} is the effective magnetic moment. The dipole-dipole contributions to longitudinal and transverse relaxation rates are approximately equal. Conversely, the Curie spin contribution is more significant to the transverse relaxation rate, $R_{2\chi}$, as opposed to the longitudinal relaxation rate, $R_{1\chi}$ (Equations 1.10 and 1.11). This effect is most apparent with Ln^{3+} ions with high μ_{eff} and long rotational correlation times.[79]

$$R_{1\chi} = \frac{6}{5}\left(\frac{\mu_0}{4\pi}\right)^2 \frac{\gamma_I^2 B_0^2 \mu_{eff}^4}{(3kT)^2 r^6}\left(\frac{\tau_r}{1+\omega_I^2\tau_r^2}\right) \quad (1.10)$$

$$R_{2\chi} = \frac{1}{5}\left(\frac{\mu_0}{4\pi}\right)^2 \frac{\gamma_I^2 B_0^2 \mu_{eff}^4}{(3kT)^2 r^6}\left(4\tau_r + \frac{3\tau_r}{1+\omega_I^2\tau_r^2}\right) \quad (1.11)$$

where, ω_I is the Larmor frequency of the nucleus and τ_R is the rotational correlation time of the complex. Relaxation data generated at different field strengths can be employed, using the above two equations, to allow an estimate of the Ln-nucleus distance.[80, 81]

1.3.3 Relaxivity Theory

The effectiveness of a paramagnetic substance to enhance the relaxation rates of nearby nuclei is termed its relaxivity (r_1), typically expressed in $mM^{-1}s^{-1}$. It is most commonly utilised when assessing the ability of a contrast agent to increase the relaxation rate of bulk water, defined as the increase in $1/T_1$ and $1/T_2$, proportional to the concentration of paramagnetic species, [Gd]:

$$1/T_{1,obs} = 1/T_{1,d} + r_1[Gd] \quad (1.12)$$

The relaxation mechanism derived from the interaction between electron spins and the water protons in the first coordination sphere of the gadolinium is termed the inner sphere contribution. Additionally, the paramagnetic effect experienced by the bulk solvent molecules diffusing around the paramagnetic complex can also increase relaxivity, termed the outer-sphere contribution. While the inner-sphere and outer-sphere mechanisms are the most evident for increasing relaxivity, a third type of water association should be taken in to consideration. When there is hydrogen bonding, or alternative interactions, between the ligand and inner-sphere water molecules, a loose layer of water molecules between the inner- and outer- sphere can arise. The contribution from such molecules is termed 'second sphere' (Figure 1.26). The total paramagnetic relaxation rate enhancement due to the presence of the paramagnetic species is therefore given by:

$$r_i = r_i^{IS} + r_i^{OS} + r_i^{SS} \qquad (1.13)$$

where, the superscripts IS, OS and SS refer to inner-sphere, outer-sphere and second-sphere respectively, and i= 1 for longitudinal, and i= 2 for transverse relaxation.[79]

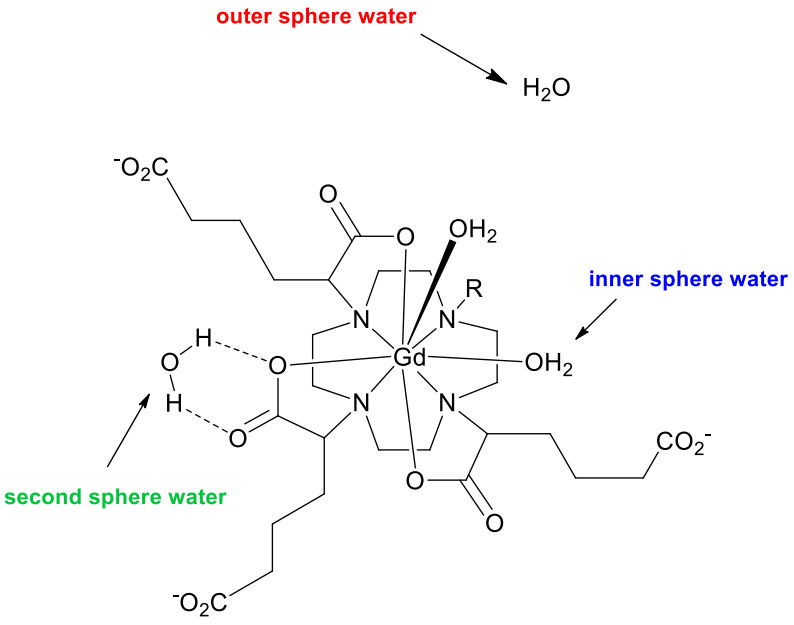

Figure 1.26: Illustration of inner –sphere, outer-sphere and second-sphere water molecules.

The longitudinal relaxation time of bound water protons, T_1, in the magnetic field range of 0.2 to 2 T, is controlled by the rotational correlation time of the complex, τ_R. Therefore, by developing contrast agents which possess a high correlation time, τ_R, relaxation times will be faster, leading to increased relaxivity.

1.4 Fluorinated Probes

Fluorinated paramagnetic probes offer significant opportunities for use in biological studies, as illustrated by the diverse range of applications discussed previously (section 1.2). While there have been many advances in utilising ^{19}F NMR spectroscopy, there are still many issues currently unresolved.

1.4.1 Key Difficulties with Fluorinated Probes

The key issue with this work is the slow longitudinal relaxation rate, R_1, of the ^{19}F nucleus, which hinders the use of fluorinated probes in magnetic resonance. This is particularly a problem with CF_3 groups, where R_1 values are typically of the order of 0.5 to 1 s^{-1}. One approach to increase the signal intensity is to increase the number of scans. Unfortunately, in MRS, this also results in an increase in spectral acquisition time, as it is necessary to wait for a delay of 3 to 5 times T_1 to allow for full relaxation of the nucleus prior to the next scan. This equates to an approximate repetition time of 3 to 6 seconds.[82] The signal to noise ratio varies with the square root of the number of scans acquired, therefore at least an order of magnitude increase in R_1 is required.

Currently, high concentrations of fluorinated compounds (~ 50 mM) are required to obtain reasonable signal intensities in high field ^{19}F MRI studies in biosystems.[83, 84] Consequently, the development of kinetically stable probes, with high sensitivity and the ability to generate increased signal intensity in a short acquisition time is desired.

1.4.2 Fluorinated Lanthanide Probes

The introduction of a paramagnetic lanthanide ion in close proximity (within 7.5 Å) to the ^{19}F nucleus, in a kinetically stable complex or conjugate, leads to much shorter T_1 and T_2 relaxation times (as discussed in 1.3.2). The enhancement in relaxation rates of the ^{19}F nucleus has been shown to be approximately two orders of magnitude, predominantly *via* dipolar mechanisms.[82] This results in a much faster acquisition time and hence increased signal intensity per unit complex concentration.

The pseudocontact shift, generated by the paramagnetic Ln^{3+} ion (as discussed in 1.3.1), increases the sensitivity of the ^{19}F chemical shift to variations in the microenvironment and structural changes. The introduction of Eu, which is a weakly relaxing ion, results in a large dipolar shift but does not have much effect on relaxation. Conversely, Dy is a strongly relaxing ion, and the dipolar and Curie relaxation mechanisms follow an r^{-6} dependence. Therefore, the unique features of each Ln^{3+} ion can be exploited in the design and development of fluorinated lanthanide probes.

It must be appreciated, however, that the benefits of shorter relaxation times can be outweighed by the reduced sensitivity associated with the broader signal linewidth. Therefore, there is a fine balance to be struck in optimising the conditions.

1.4.3 Review of ^{19}F NMR in Lanthanide Systems

While lanthanide shift reagents are often utilised for simplifying the interpretation of spectra, there are very few examples on the relaxation and dipolar shift effects of lanthanide ions on ^{19}F NMR spectroscopic parameters. A recent example of a paramagnetic relaxation based fluorinated MRI probe to detect protease activity was discussed in section 1.2.1.3.

One of the earliest examples reported is from Sherry *et al.* who examined a series of $Ln(F\text{-}DOTPME)^-$ complexes and assigned several resolved ^{19}F NMR resonances to

specific diastereomers. This approach is based upon the comparison of resonance integrals, assuming pendant arm interactions, and the magnitude and direction of pseudocontact shifts. The addition of cationic detergents resulted in increased selectivity for the Δ-SSSS isomer, whereas introduction of neutral polyethylene glycol showed variation in the chemical shift values but not the distribution of isomers.[85] While the work is of much interest, it is limited not only by the similarity of the chemical shift values of some of the isomers, but also by the fact that there are several isomeric species present in solution (Figure 1.27).

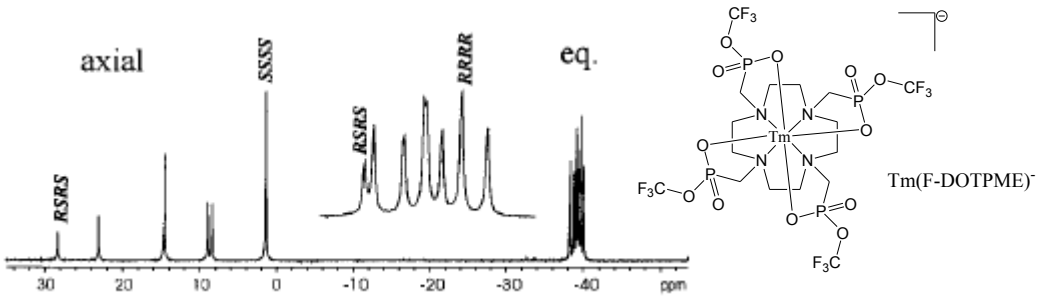

Figure 1.27: ^{19}F NMR spectra of 40 mM Tm(F-DOTPME)$^-$ at 25 ^{o}C. The inset at the middle of the spectrum is an expansion of the low frequency group of resonances. The labelled resonances are assigned to the indicated isomer.[85]

In 2004, Aime *et al.* probed the relaxation enhancement obtained following reversible binding of trifluorolactate to [GdDO3A(H_2O)].[86] The two coordinated inner sphere water molecules of the [GdDO3A(H_2O)] can be replaced by the trifluorolactate, forming a fairly weak ternary complex. Thus, the fluorine nuclei in the anion are in close proximity to the paramagnetic Gd centre, leading to an increase in relaxation (trifluorolactate T_1 = 4500 ms, [trifluorolactate-GdDO3A] T_1 = 23 ms at 7T). This study was an excellent proof of principle to demonstrate that Gd-based probes could offer the opportunity to enhance relaxation of molecules other than water.

Atherosclerotic plaques, which exhibit micro-deposits of fibrin, can accumulate in the arterial system leading to a heart attack or stroke. It is therefore vital to be able to screen such lesions. Wickline *et al.* developed fluorinated fibrin-targeted perfluorocarbons that incorporate chelated gadolinium atoms (> 50000) to enhance

the R_1.[87] Results from *in vitro* ^{19}F MRI studies at 4.7 T, utilising a diseased human carotid artery segment, reveal that the nanoparticles show a high degree of specificity for the fibrin (Figure 1.28). Moreover the nanoparticle-fibrin binding can be quantified by clever manipulation of integral measurements, which is then corroborated with ^{1}H T_1 measurements (1.5 T) and elemental (% gadolinium) analysis. To properly assess the viability of this approach *in vivo* studies are needed. However, the chelating agent, DTPA, can undergo metal dissociation *in vivo* so a more stable analogue would be required for such experiments.

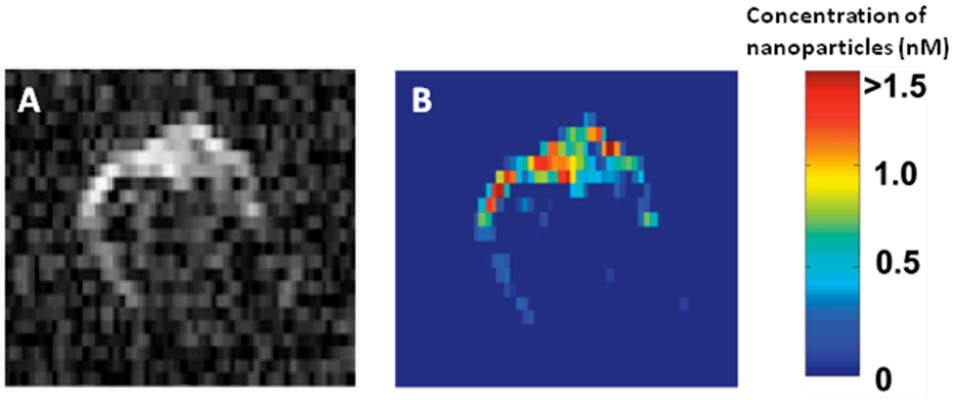

Figure 1.28: A) ^{19}F projection image acquired at 4.7 T through the entire carotid artery sample which shows high signal along the lumen due to nanoparticles bound to fibrin. B) Concentration map of bound nanoparticles in the carotid sample.[87]

An example of a paramagnetic relaxation-based fluorinated MRI probe to detect protease activity was discussed in section 1.2.1.3. In 2009, this concept was developed further through incorporation of a reporter fluorophore that is active in both ^{19}F MRI and fluorescence measurements, allowing for dual studies. The probe, when enzymatically cleaved by caspase-3, releases the fluorophore from the [GdDOTA(H_2O)] complex instigating an increase in both ^{19}F MRI signal and fluorescence. There are many drawbacks to this system, particularly the fact that the [GdDOTA(H_2O)] remains in solution with the fluorophore after cleavage causing paramagnetic broadening and hampering of the ^{19}F signal.[88]

When using MRI to detect changes in pH it is essential to be able to accurately determine the local concentration of the probe otherwise any variations in the reporter signal cannot be accurately ascribed to an alteration in pH. In an attempt to

solve this problem a ratiometric $^{1}H/\ ^{19}F$ MRI method for pH mapping was developed in 2009.[89] The Gd and ^{19}F moieties are hosted by a poly-β-cyclodextrin carrier, thereby guaranteeing the fluorine and gadolinium nuclei are sufficiently separated to prevent broadening of the ^{19}F signal (Figure 1.29). The pH responsiveness arises from the sulphonamide arm on the Gd(III)-chelate which has a pKa of 6.7. Upon formation of the supramolecular adduct, under acidic conditions, the increase in molecular reorientation time results in a significant increase in relaxivity. The ^{19}F signal intensity measurement can then be used to normalise the relaxation enhancement values. As discussed earlier, it would be possible for the two coordinated inner sphere water molecules of the Gd chelate to be replaced by protein or a number of anions which would definitely hinder the pH response. Furthermore, the affinity constants have been used to gauge the ratio of the three components. A more accurate means of characterisation is needed.

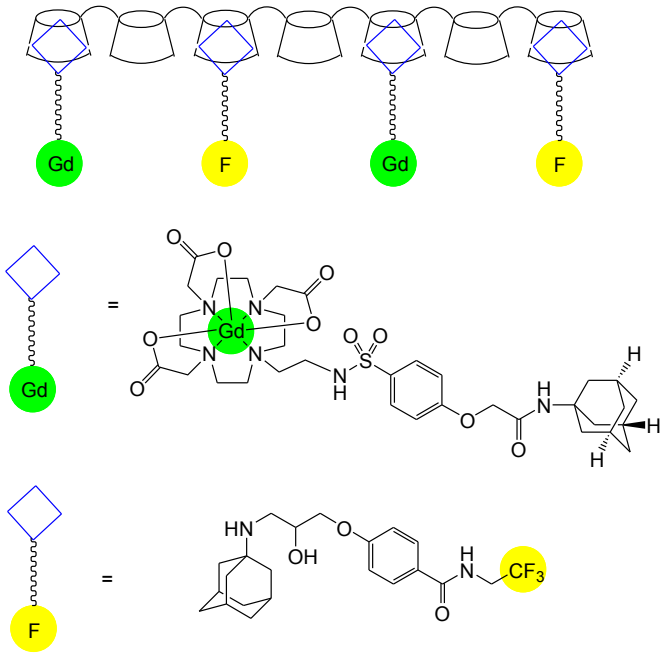

Figure 1.29: Schematic representation of the supramolecular adduct between poly-β-cyclodextrin, the Gd complex and the ^{19}F reporting molecule.

1.5 Project Aims

The main aim of this work is to develop multi-disciplinary fluorinated lanthanide probes, capable of use in both ^{19}F and ^{1}H magnetic resonance imaging and spectroscopy. There are numerous cyclen-based lanthanide complexes commercially available for ^{1}H MRI studies, and previous work in Durham has demonstrated the feasibility of introducing a CF_3 group into these structures.[82] The resulting stable paramagnetic fluorinated complexes present faster relaxation rates and increased signal intensity per unit complex concentration.

The research detailed in this thesis builds on related recent work, focussing on the synthesis and evaluation of novel fluorinated lanthanide(III) complexes. Many parameters, such as the number of the fluorine atoms and the choice of Ln^{3+} ion, have been investigated, with the aim of optimising the ^{1}H and ^{19}F relaxation parameters. Strategies are explored to promote the formation of one stable isomer in solution, and increase signal intensity, with the results of each discussed in detail.

1.6 References

1) P. Caravan, J. J. Ellison, T. J. McMurry, R. B. Lauffer, *Chem. Rev.*, **1999**, *99*, 2293
2) R. Damadian, K. Zaner, D. Hor, T. DiMaio, *Proc. Natl. Acad. Sci. USA*, **1974**, *71*, 1471
3) S. Aime, M. Botta, M. Fasano, E. Terreno, *Chem. Soc. Rev.*, **1998**, *27*, 19
4) M. Stubbs, L. Rodrigues, F. A. Howe, J. Wang, K. S. Jeong, R. L. Veech, J. R. Griffiths, *Cancer Res.*, **1994**, *54*, 4011
5) N. Bansal, M. J. Germann, V. Seshan, G. T. Shires, C. R. Malloy, A. D. Sherry, *Biochem.*, **1993**, *32*, 5638
6) A. Tressaud, G. Haufe, *Fluorine and Health: Molecular Imaging, Biomedical Materials and Pharmaceuticals*, Elsevier, **2008**
7) R. F. Code, J. E. Harrison, K. G. McNeill, M. Szyjkowski*, Magn. Reson. Med.,* **1990**, *13*, 358
8) M. J. Adam, D. S. Wilbur, *Chem. Soc. Rev.*, **2005**, *34*, 153
9) O. Couturier, A. Luxen, J. F. Chatal, J. P. Vuillez, P. Rigo, R. Hustinx, *Eur. J. Nucl. Med. Mol. Imaging*, **2004**, *31*, 1182
10) G. N. Holland, P. A. Bottomley, W. S. Hinshaw, *J. Magn. Reson.*, **1977**, *28*, 133
11) P. C. Lauterbur, *Nature*, **1973**, *242*, 190
12) A. N. Stevens, P. G. Morris, R. A. Illes, P. W. Sheldon, J. R. Griffiths, *Br. J. Cancer*, **1984**, *50*, 113
13) W. Wolf, M. J. Albright, M. S. Silver, H. Weber, U. Reichadt, R. Sauer, *Magn. Reson. Imag.,* **1987**, *5*, 165
14) L. Gray, A. Conger, M. Ebert, S. Hornsey, O. Scott, *Br. J. Radiol.*, **1953**, *26*, 638
15) B. A. Teicher, J. S. Lazo, A. C. Sartorelli, *Cancer Res.*, **1981**, *41*, 73
16) S. R. Thomas, R. G. Pratt, R. W. Millard, C. R. Samaratunga, Y. Shiferaw, A. J. McGoron, K. K. Tan, *Magn. Reson. Imag*., **1996**, *14*, 103
17) J. X. Yu, V. D. Kodibagkar, W. Cui, R. P. Mason, *Curr. Med. Chem.,* **2005**, *12*, 819
18) L. W. Hall, S. R. K. Jackson, G. M. Massey, *Hexafluorobenzene in veterinary anaesthesia*, Oxford, **1975**
19) R. J. Maxwell, P. Workman, J. R. Griffiths, *Int. J. Radiat. Oncol. Biol. Phys.*, **1989**, *16*, 925
20) E. O. Aboagye, R. J. Maxwell, A. B. Kelson, Cancer Res., **1997**, *57*, 3314

21) E. O. Aboagye, R. J. Maxwell, M. R. Horsman, A. D. Lewis, P. Workman, M. Tracy, J. R. Griffiths, *Br. J. Cancer*, **1998**, *77*, 65

22) B. M. Seddon, G. S. Payne, L. Simmons, *Clin. Cancer. Res.*, **2003**, *9*, 5101

23) K. Tanabe, H. Harada, M. Narazaki, K. Tanaka, K. Inafuku, H. Komatsu, T. Ito, H. Yamada, Y. Chujo, T. Matsuda, M. Hiraoka, S. Nishimoto, *J. Am. Chem. Soc.*, **2009**, *131*, 15982

24) C. H. Contag, B. D. Ross, *Magn. Reson. Imag.*, **2002**, *16*, 378

25) U. Haberkorn, W. Mier, M. Eisenhut, *Curr. Med. Chem.*, **2005**, *12*, 779.

26) W. Cui, P. Otten, L. Yingming, S. Koeneman, Y. Jianxin, R. P. Mason, *Magn. Reson. Med.*, **2004**, *51*, 616.

27) L. Liu, D. Kodibagkar, J. Yu, R. P. Mason, *FASEB J.*, **2007**, *21*, 2014.

28) L. D. Stegman, A. Rehemtulla, B. Beattie, E. Kievit, T. S. Lawrence, R. G. Blasberg, J. G. Tjuvajev, B. D. Ross, *Proc. Natl. Acad. Sci. USA*, **1999**, *96*, 9821.

29) L. D. Stegman, A. Rehemtulla, D. A. Hamstra, D. J. Rice, S. J. Jonas, K. L. Stout, T. L. Chenevert, B. D. Ross, *Gene Ther.*, **2000**, *7*, 1005.

30) H. Corben-Wilhelm, W. E. Hull, G. Becker, U. Bauder-Wüst, D. Greulich, J. Debus, *Gene Ther.*, **2002**, *9*, 1564.

31) L. Mancine, L. Davies, F. Fredos, M. Falck-Miniotis, A. S. Dzik-Jurasz, C. J. Springer, M. O. Leach, G. S. Payne, *NMR Biomed.*, **2009**, *22*, 561.

32) F. Millett, M. A. Raftery, *Biochemistry.*, **1972**, *11*, 1639.

33) G. L. Mendz, T. N. Lim, S. L. Hazell, *Arch. Biochem. Biophys.*, **1993**, *305*, 252.

34) K. Tanaka, N. Kitamura, K. Naka, Y. Chujo, *Chem. Commun.*, **2008**, 6176.

35) S. Mizukami, R. Takikawa, F. Sugihara, Y. Hori, H. Tochio, M. Walchli, M. Shirakawa, K. Kikuchi, *J. Am. Chem. Soc.*, **2008**, *130*, 794.

36) J. S. Taylor, C. Deutsch, *Biophys. J.*, **1983**, *43*, 261.

37) S. He, R. P. Mason, S. Hunjan, V. D. Mehta, V. Arora, R. Katipally, P. V. Kulkarni, P. P. Antich, *Bioorg. Med. Chem.*, **1998**, *6*, 1631.

38) J. M Criscione, B. L. Le, E. Stern, M. Brennan, C. Rahner, X. Papademetris, T. M. Fahmy, *Biomaterials*, **2009**, *30*, 3496.

39) Y. Matsumura and H. Maeda, *Cancer Res.*, **1986**, *46*, 6387.

40) M. Oishi, S. Sumitani, T. K. Bronich, A. V. Kabanov, M. D. Boska, Y. Nagasaki, *Chem. Lett.*, **2009**, *38*, 128.

41) L. E. Gerweck, K. Seetharaman, *Cancer Res.,* **1996**, *56*, 1194.

42) L. A. Levy, E. Murphy, B. Raju, R. E. London, *Biochem.,* **1988**, *27*, 4041.

43) E. Murphy, C. Steenbergen, L. A. Levy, B. Raju, R.E. London, *J. Biol. Chem.*, **1989**, *264*, 5622.

44) G. A. Smith, R. T. Hesketh, J. C. Metcalfe, J. Feeney, P. G. Morris, *Proc. Natl. Acad. Sci. USA.*, **1983**, *80*, 7178.

45) F. A. Schanne, T. L. Dowd, R. K. Gupta, J. F. Rosen, *Proc. Natl. Acad. Sci. USA.*, **1989**, *86*, 5133.

46) H. Plenio, R. Diodone, *J. Am. Chem. Soc.*, **1996**, *118*, 356.

47) D. J. Selkoe, *J. Neuropathol. Exp. Neurol.*, **1994**, *53*, 438.

48) M. Higuchi, N. Iwata, Y. Matsuba, K. Satu, K. Sasamoto, T. C. Saido, *Nat. Neurosci.*, **2005**, *8*, 527.

49) D. P. Flaherty, S. M. Walsh, T. Kiyota, Y. Dong, T. Ikezu, J. L. Vennerstrom, *J. Med. Chem.*, **2007**, *50*, 4986.

50) J. G. Riess, *Chem. Rev.*, **2001**, *101*, 2797.

51) D. O. Kuethe, V. C. Behr, S. Begay, *Magn. Reson. Med.*, **2002**, *48*, 547.

52) H. U. Kauczor, X. J. Chen, E. J. Van Beek, W. G. Schreiber, *Eur. Respir. J.,* **2001**, *17*, 1008.

53) P. S. Tofts, G. Brix, D. L. Buckley, J. L. Evelhoch, E. Henderson, M. V. Knopp, H. B. Larsson, T. Y. Lee, N. A. Mayr, G. J. Parker, R. E. Port, J. Taylor, R. M. Weisskoff, *Magn. Reson. Imag*., **1999**, *10*, 223.

54) N. J. Baldwin, Y. Wang, T. C Ng, *Magn. Reson. Imag.*, **1996**, *14*, 275.

55) S. M. Eleff, M. D. Schnall, L. Ligetti, M. Osbakken, V. H. Subramanian, B. Chance, J. S. Leigh, *Magn. Reson. Med.*, **1988**, *7*, 412.

56) U. Flogel, Z. Ding, H. Hardung, S. Jander, G. Reichmann, C. Jacoby, R. Schubert, J. Schrader, *Circulation*, **2008**, *118*, 140.

57) E. M. Shapiro, K. Sharer, S. Skrtic, A. P. Koretsky, *Magn. Reson. Med.*, **2006**, *55*, 242.

58) K. C. Partlow, J. Chen, J. A. Brant, A. M. Neubauer, T. E. Meyerrose, M. H. Creer, J. A. Nolta, S. D. Caruthers, G. M. Lanza, S. A. Wickline, *FASEB J.*, **2007**, *21*, 1647.

59) J. Ruiz-Cabello, P. Walczak, D. A. Kedziorek, V. P. Chacko, A. H. Schmieder, S. A. Wicklone, G. M. Lanza, J. W. M. Bulte, *Magn. Reson. Med.*, **2008**, *60*, 1506.

60) A. Miyazaki, T. Hanafusa, K. Yamada, J. Miyagawa, H. Fujino-Kurihara, H. Nagajima, K. Nonaka, S. Tarui, *Clin. Exp. Immunol.*, **1985**, *60*, 622.

61) M. Srinivas, P. A. Morel, L. A. Ernst, D. H. Laidlaw, E. T. Ahrens, *Magn. Reson. Med.*, **2007**, *58*, 725.

62) M. Jelena, M. Srinivas, D. K. Kadayakkara, E. T. Ahrens, *J. Am. Chem. Soc.*, **2008**, *130*, 2832.

63) M. Srinivas, M. S. Turner, J. M. Janjic, P. A. Morel, D. H. Laidlaw, E. T. Ahrens, *Magn. Reson. Med.*, **2009**, *62*, 747.

64) Z. X. Jiang, X. Liu, E. K. Jeong, Y. B. Yu, *Angew. Chem.-Int. Edit.*, **2009**, *48*, 4755.

65) W. J. Du, A. M. Nystrom, L. Zhang, K. T. Powell, Y. L. Li, C. Cheng, S. A. Wickline, K. L. Wooley, *Biomacromolecules*, **2008**, *9*, 2826.

66) H. Peng, I. Blakey, B. Dargaville, F. Rasoul, S. Rose, A. K. Whittaker, *Biomacromolecules*, **2009**, *10*, 374.

67) L. Nurmi, H. Peng, J. Seppälä, D. M. Haddleton, I. Blakey, A. K. Whittaker, *Polym. Chem.*, **2010**, *1*, 1039.

68) K. J. Thurecht, I. Blakey, H. Peng, O. Squires, S. Hsu, C. Alexander, A. K. Whittaker, *J. Am. Chem. Soc.*, **2010**, *132*, 5336.

69) I. Chukweumeka, D. O'Hagan, *J. Fluor. Chem.*, **2006**, *127*, 303.

70) W. E. Hull, R. E. Port, R. Herrmann, B. Britsch, W. Kunz, *Cancer Res.*, **1988**, *48*, 1680.

71) G. Brix, M. E. Bellemann, U. Haberkorn, L. Gerlach, W. J. Lorenz, *Nucl. Med. Biol.*, **1996**, *23*, 897.

72) G. Brix, M. E. Bellemann, L. Gerlach, U. Haberkorn, *Magn. Reson. Imag.*, **1999**, *17*, 151.

73) S. W. Ng, M. Tsao, T. Nicklee, D. W. Hedley, *Clin. Cancer Res.*, **2001**, *7*, 3263.

74) G. Brix, A. Schlicker, W. Mier, P. Pesche, M. E. Bellemann, *Magn. Reson. Imag.*, **2005**, *23*, 967.

75) N. R. Bolo, Y. Hode, J. P. Macher, *MAGMA*, **2004**, *16*, 268.

76) C. C. Bryden, C. C. Reilley, J. F. Desreuz, *Anal. Chem.*, **1981**, *53*, 1418.

77) E. Bovens, *PhD Thesis*, Delft University of Technology, **2001**.

78) J. A. G. Williams, *PhD Thesis*, University of Durham, **1995**.

79) A. Sigel, H. Sigel, *The Lanthanides and Their Interrelations with Biosystems Vol. 40*, Chapter 14, Marcel Dekker, University of Basel, Switzerland, **2003**.

80) I. Bertini, F. Capozzi, C. Luchinat, G. Nicastro, Z. C. Xia, *J. Phys. Chem.*, **1993**, *97*, 6351.

81) I. Bertini, C. Luchinat, G. Pangi, *Prog. Nucl. Mag. Reson. Spec.*, **2002**, *40*, 249.

82) P. K. Senanayake, A. M. Kenwright, D. Parker, S. K. van der Hoorn, *Chem. Commun.*, **2007**, 2923.

83) V. D. Kodibagkar, J. X. Yu, L. Liu, H. P. Hetherington, R. P. Mason, *Magn. Reson. Imag.*, **2006**, *24*, 959.

84) J. X. Yu, V. D. Kodibagkar, W. N. Cui, R. P. Mason, *Bioorg. Med. Chem.*, **2006**, *14*, 326.

85) W. D. Kim, G. E. Kiefer, J. Huskens, A. D. Sherry, *Inorg. Chem.,* **1997**, *36*, 4128.

86) E. Terreno, M. Botta, W. Dastru, S. Aime, *Contrast Media Mol. Imaging*, **2006**, *1*, 101.

87) A. M. Neubauer, J. Myerson, S. D. Caruthers, F. D. Hockett, P. M. Winter, J. J. Chen, P. J. Gaffney, J. D. Robertson, G. M. Lanza, S. A. Wickline, *Magn. Reson. Med.*, **2008**, *60*, 1066.

88) S. Mizukami, R. Takikawa, F. Sugihara, M. Shirkawa, K. Kikuchi, *Angew. Chem. Int. Ed.*, **2009**, *48*, 3461-3463.

89) E. Gianolio, R. Napolitano, F. Fedeli, F. Arena, S. Aime, *Chem. Commun.*, **2009**, 6044.

Chapter 2: Spectroscopic and Relaxation Properties

2.0 Spectroscopic and Relaxation Properties

2.1 Introduction

As discussed in Chapter one, fluorinated paramagnetic probes offer significant opportunities for use in biological studies owing to the high sensitivity of ^{19}F NMR, the large chemical shift range and the absence of a background signal. The introduction of a paramagnetic centre within 7 Å to the ^{19}F nucleus can significantly increase the longitudinal and transverse relaxation rates, allowing for a much faster acquisition time and hence increased signal intensity per unit complex concentration.[1,2] However, the benefits of shorter relaxation times can be outweighed by the reduced sensitivity associated with the broader signal linewidth. Therefore, there is a fine balance to be struck in optimising the signal aquisition conditions. This balance is a function of the field chosen, the nature of the Ln^{3+} ion, and its average distance from the ^{19}F nucleus.

The work contained in this chapter builds on the above theory through the introduction of CF_3 groups in close proximity to lanthanide (Ln^{3+}) ions in stable macrocyclic complexes. Two different classes of Ln^{3+} complexes (Figure 2.1) have been synthesised, with the aim of exploring their ^{19}F chemical shift and relaxation properties, in addition to the ^{1}H relaxometric properties of the Gd^{3+} analogues.

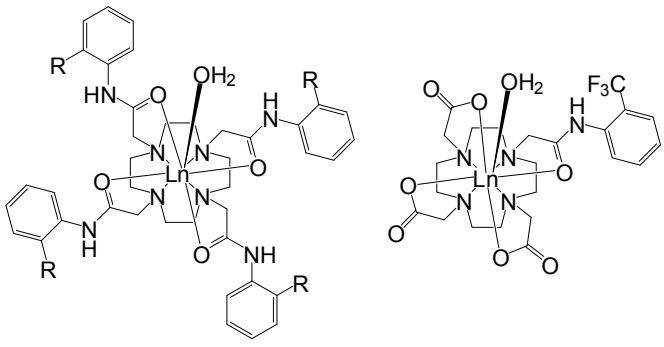

L^1 *(R= CF_3)*, **L^2** *(R= CH_3)* **L^3**

Figure 2.1: Structures of $[Ln.L^1(H_2O)]^{3+}$, $[Ln.L^2(H_2O)]^{3+}$ and $[Ln.L^3(H_2O)]$

Ligand **L^2** was prepared as an analogue of **L^1**, replacing the trifluoromethyl group by a methyl group to assess the impact on relative stability, and to compare the behaviour of the Gd^{3+} complexes.

2.2 Synthesis and Characterisation of Complexes

2.2.1 L^1 and L^2 Synthesis

The tetra-amide ligands, **L^1** and **L^2**, were prepared *via* the same method. The first step involved the acylation of the *ortho*-substituted aniline with chloroacetyl chloride, with subsequent purification by silica gel column chromatography to yield the desired α-chloroamide arm, **1** or **2** (Scheme 2.1).

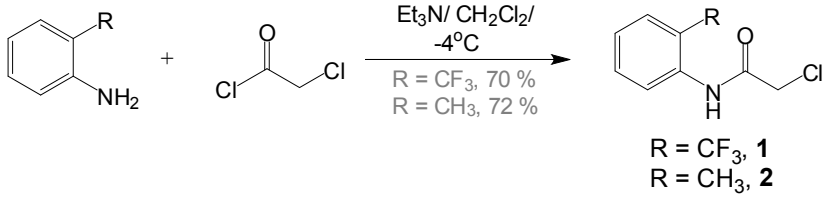

Scheme 2.1

The subsequent tetra-alkylation of 1,4,7,10-tetraazacyclododecane (cyclen), proved more difficult (Scheme 2.2). Even when using a large excess of the α-chloroamide arm (6 equivalents), the mono-, di-, tri- and tetra-amide ligands could all be identified in the crude mixture by electrospray mass spectrometry (ESMS). The isolation of the desired tetra-amide ligand was achieved by silica gel column chromatography. However, due to the similar R_f values of the products formed, the overall yield was moderately low for both **L^1** and **L^2**. The slightly higher yield of **L^2** could be attributed to the smaller size of the methyl group, and hence a lesser steric effect in the formation of the desired ligand.

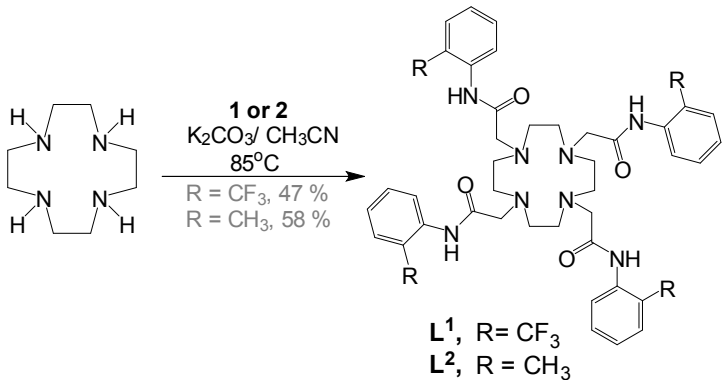

Scheme 2.2

The final step involved the complexation of the ligand with the appropriate Ln^{3+} ion (Scheme 2.3). This was achieved *via* two different methods. The first approach involved reaction of the ligand with $LnCl_3$ in a H_2O/CH_3OH mixture. The purification was simple: the crude product, dissolved in CH_3CN, was added dropwise into cold Et_2O, thereby removing any unreacted lanthanide salts. The benefit of this procedure is that the complex can be used immediately as the chloride salt.

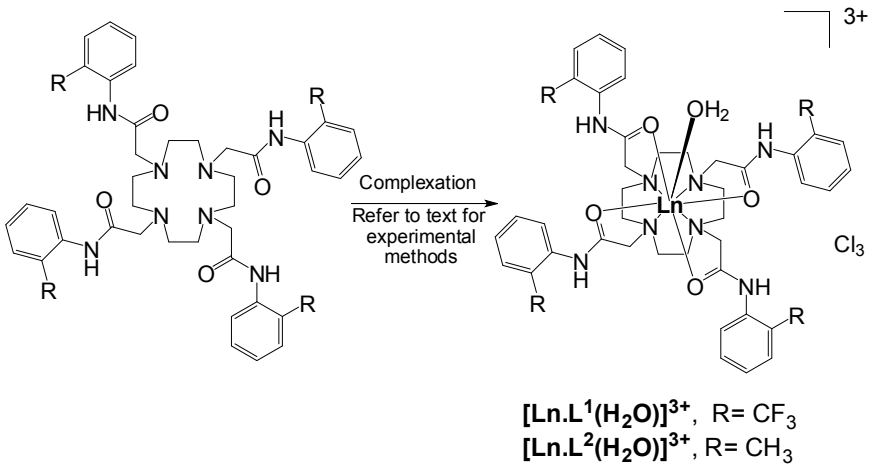

Scheme 2.3

The second approach involved the reaction of the ligand with $Ln(OTf)_3$ in CH_3CN. The complex was subsequently converted to the chloride salt using a chloride anion exchange resin. In addition to the removal of the unwanted triflate signal in the ^{19}F NMR spectrum, the chloride salt also increased the water solubility of the complex.

2.2.2 L^3 Synthesis

The preparation of $\mathbf{L^3}$ begins with the alkylation of cyclen with *tert*-butyl bromoacetate, under mildly basic conditions, following a literature method (Scheme 2.4).[3] The desired tri-ester was purified by silica gel chromatography, thereby eliminating any traces of the tetra-substituted analogue.

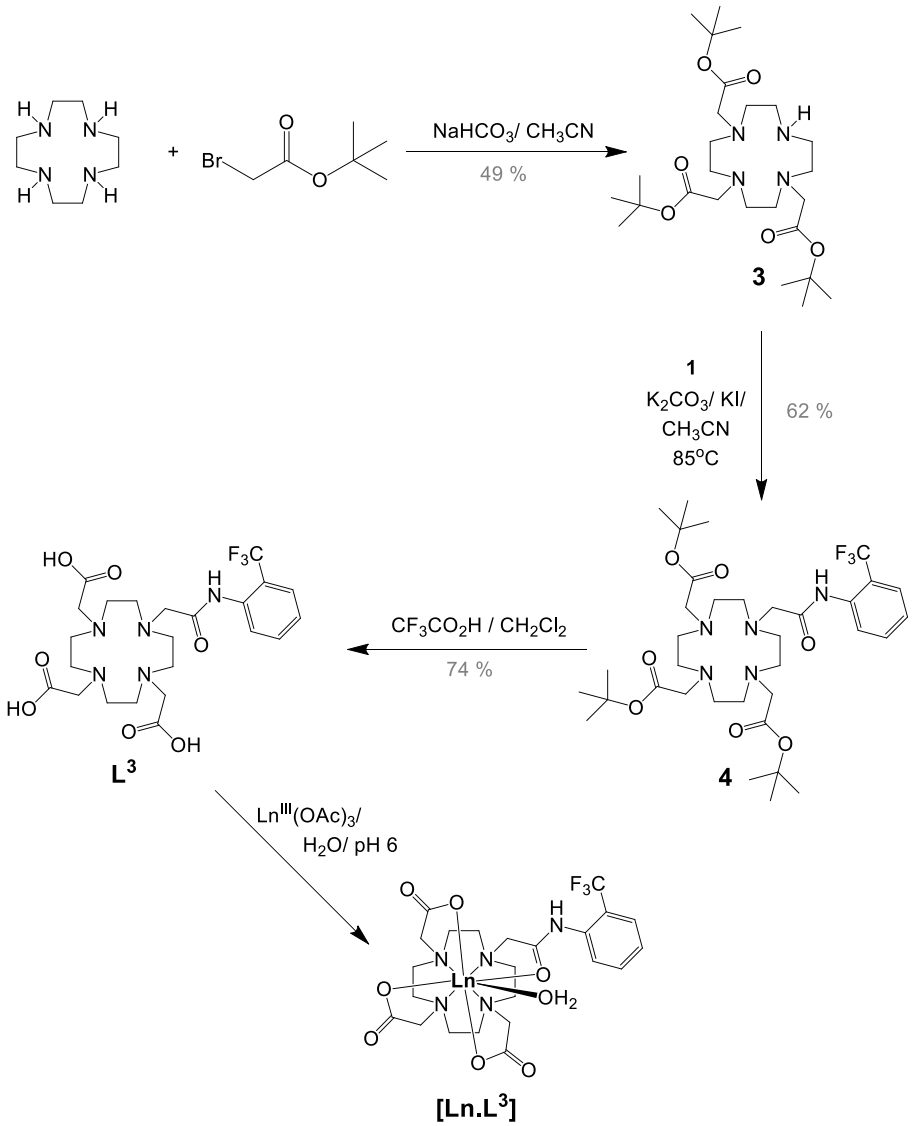

Scheme 2.4: Synthetic route to [Ln.L^3]

The subsequent mono-alkylation of the tri-ester with **1** was achieved under basic conditions, utilising KI as a catalyst. The removal of the *tert*-butyl protecting groups was accomplished by treatment with trifluoroacetic acid in CH_2Cl_2, yielding the

desired ligand as a trifluoroacetate salt. Conversion to the chloride salt was achieved using an anion exchange resin.

The final step in the synthesis involved reaction of the $\mathbf{L^3}$ with the appropriate $Ln(OAc)_3$ salt in water, adjusting the pH to approximately 6. The complex was subsequently purified by alumina column chromatography, thereby ensuring the removal of any unreacted lanthanide salts.

2.3 Characterisation of Complexes

In ESMS, a characteristic isotope pattern is observed for each complex, associated with isotope distribution of each Ln^{3+} ion. This can be utilised to confirm the presence of the desired complex (Figure 2.2). In each case, the calculated and experimental isotope patterns showed very good correspondence.

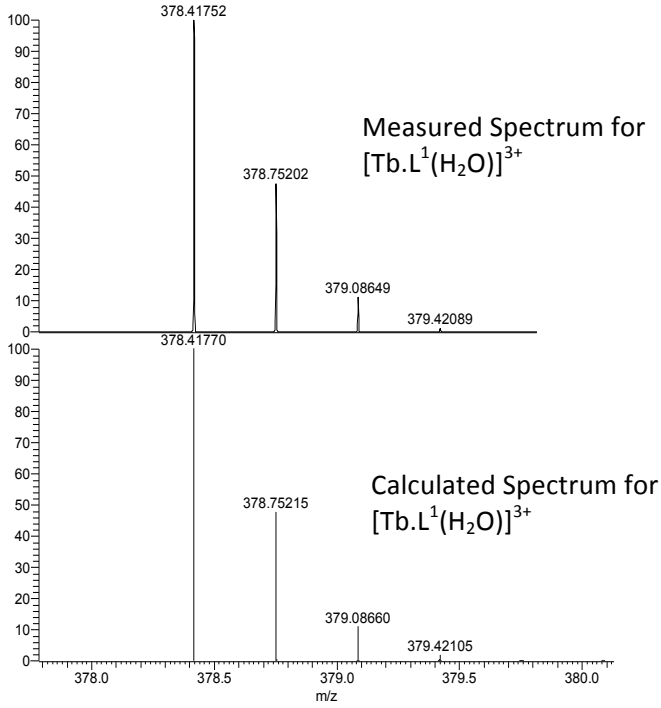

Figure 2.2: Electrospray Mass Spectrum of $[Tb.L^1(H_2O)]^{3+}$, showing measured and calculated values. Accurate masses to seven significant figures were considered.

For each class of complex, the ^1H and ^{19}F NMR properties were examined, and the purity assessed by HPLC.

2.3.1 Estimation of Complex Hydration State

Lanthanide ions in their emissive state are sensitive to quenching by vibrational energy transfer. Many different quenching pathways contribute to the rate constant for the depopulation of the lanthanide excited state in water (Equation 2.1).

$$k_{H2O} = k_{nr} + \sum k_{XH} + \sum k_{C=O} \quad (2.1)$$

where, k_{nr} is the non-radiative constant, $\sum k_{XH}$ is the energy transfer to nearby XH oscillators, and $\sum k_{C=O}$ is the energy transfer to nearby C=O matched oscillators

In D_2O, it is assumed that all exchangeable XH oscillators do not contribute to the quenching. However, in aqueous media, quenching by OH groups is the most prominent and therefore, the number of bound water molecules can be calculated from the difference in the rate of quenching in H_2O and D_2O (Equation 2.2).[4, 5]

$$q = A(k_{H2O} - k_{D2O} + corr_{Ln}) \quad (2.2)$$

where, A is a proportionality constant giving the sensitivity of the lanthanide ion to vibronic quenching by OH oscillators, and the $corr_{Ln}$ term allows for the effect of closely diffusing OH oscillators. The equation is modified slightly to make it specific for terbium based complexes (Equation 2.3).[6]

$$q'_{Tb} = 5[(k_{H2O} - k_{D2O} - 0.06)] \quad (2.3)$$

The lifetime measurements of $[Ln.L^1(H_2O)]^{3+}$, $[Ln.L^2(H_2O)]^{3+}$ and $[Ln.L^3(H_2O)]$ in H_2O and D_2O, indicate that there is one bound water molecule in each case (Table 2.1). As the geometry of the complex does not change significantly between the series of lanthanides, it can be assumed that the Eu^{3+}, Gd^{3+} and Tb^{3+} complexes of the same ligand will also have the same hydration number.

Complex	k_{H2O} (ms^{-1})	k_{D2O} (ms^{-1})	q'
$[Tb.L^1(H_2O)]^{3+}$	0.56	0.31	0.97
$[Tb.L^2(H_2O)]^{3+}$	0.60	0.36	0.90
$[Tb.L^3(H_2O)]$	0.57	0.36	0.75

Table 2.1: Lifetime measurements of $[Ln.L^1(H_2O)]^{3+}$, $[Ln.L^2(H_2O)]^{3+}$ and $[Ln.L^3(H_2O)]$ in H_2O and D_2O, including calculation of hydration number (± 20 %)

2.4 ^{19}F NMR Spectroscopic Properties

The Tb, Ho, Er and Tm complexes of **L^1** each formed one major species as revealed by ^{19}F NMR spectroscopy (Figure 2.3), with the percentage fraction falling in a sequence that mirrors the change in ionic radius: Tm > Er > Ho > Tb. In each case, a second species lacking C_4 symmetry is evident, existing either as four resonances in a 1:1:1:1 ratio, or as two resonances in a 1:1 ratio where C_2 symmetry is retained. In contrast, the diamagnetic complex, $[Y.L^1(H_2O)]Cl_3$ gave rise to only one resolved resonance, although at 656 MHz, a minor species could be discerned as a shoulder to the major resonance. Earlier crystallographic studies of structurally related tetra-amide complexes have verified the existence of 9-coordinate systems with one coordinated water molecule that adopt a mono-capped C_4 symmetric antiprismatic geometry.[7,8]

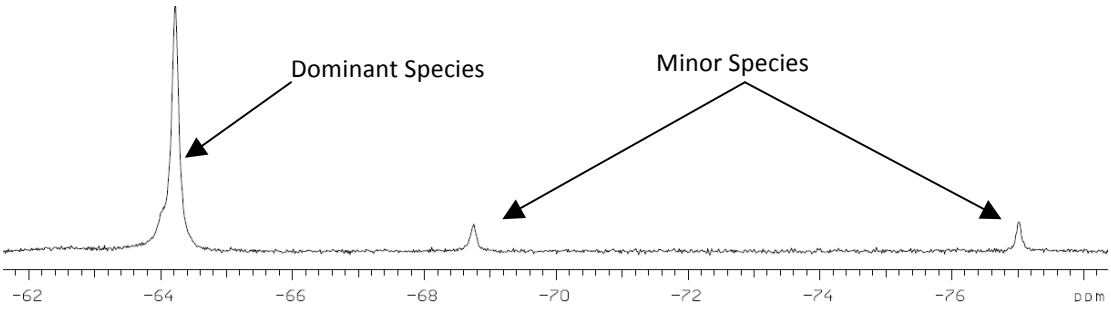

Figure 2.3: ^{19}F NMR spectra of $[Tm.L^1(H_2O)]^{3+}$ (2 mM, D_2O:CD_3OD (20 %), 295 K, 4.7 T) showing the presence of one major species

Immediately following dissolution of the Tb, Ho, Er and Tm complexes of **L^3** in water, comparable spectral features were noted. One major species was observed by ^{19}F

NMR spectroscopy, in addition to minor species that varied in number and proportion, according to the nature of the Ln^{3+} ion (Table 2.2). For the discussions contained in this thesis, the chemical shift value quoted refers to the dominant isomer. The sign of the ^{19}F pseudo-contact shift follows the sign of the Bleaney coefficients in each case; these are negative for Tb and Ho, and positive for Er and Tm.[9] Therefore the fluorine resonances of Ho and Tb complexes are shifted to higher frequency, whereas the Tm and Tm are shifted to lower frequency, with respect to the diamagnetic Y complex. This is consistent with the adoption of a common solution structure across the series, with each CF_3 group at a similar angle to the main axis of the complex and a comparable distance from the metal ion.

Complex	δ_F / ppm	Bleaney's coefficient, C_j	% Major species	No. of minor species
$[Tb.L^3(H_2O)]$	-51.9	-39	68	5
$[Ho.L^3(H_2O)]$	-56.9	-86	85	3
$[Er.L^3(H_2O)]$	-64.8	+33	82	8
$[Tm.L^3(H_2O)]$	-77.4	+53	74	6
$[Y.L^3(H_2O)]$	-62.0	N/A	92	1

Table 2.2: ^{19}F NMR chemical shift data for $[Ln.L^3(H_2O)]$ (2 mM, D_2O, 295 K, pD 5.4, Ln = Tb, Ho, Er, Tm and Y)

The ^{19}F resonance observed in the corresponding Gd^{3+} complexes of **L^1** and **L^3** was extremely broad, with a chemical shift very close to the corresponding diamagnetic Y complex ($[Gd.L^3(H_2O)]$ δ_F = 62.3 ppm, $\omega_{1/2}$ = 1240 MHz (2 mM, D_2O, pD 5.4, 295K, 9.4 T)).

2.5 ^{19}F Relaxation Parameters

2.5.1 ^{19}F NMR Relaxation Theory

The introduction of a paramagnetic centre close to the ^{19}F nucleus can significantly increase the longitudinal and transverse relaxation rates, R_1 and R_2. There are five main spin relaxation process for ^{19}F nuclei in non-viscous solutions of paramagnetic

molecules that, in principle, can contribute to this enhancement; chemical shift anisotropy (CSA), inter-nuclear dipole-dipole (DD) interaction, electron-nucleus contact interaction, electron-nucleus dipole-dipole interaction and a special case known as Curie relaxation.[10-13]

In the specific case of the fluorinated cyclen-based systems under review, the CSA and inter-nuclear interactions can be discounted. This is because the CSA contribution for a trifluoromethyl group is fairly small,[14] and the inter-nuclear dipole-dipole (DD) interaction is insignificant in comparison to the much larger electron-nuclear interactions. The experimentally measured ^{19}F T_1 in diamagnetic Y^{3+} and La^{3+} complexes is approximately 1 s, thus the combined CSA and inter-nuclear DD cannot account for more than 1 Hz in the measured paramagnetic relaxation rates; these are normally of the order ~10-1000 Hz. Furthermore, the contact mechanism may also be ignored, because DFT calculations for a ^{19}F nucleus positioned more than 5 Å from the metal shows an expected zero value for this term.[15]

The two remaining mechanisms, electron nucleus DD and Curie relaxation, do contribute significantly. Their independent contributions to R_1 and R_2 are described, respectively, in equations 2.4 to 2.7:[16, 17]

$$R_1 = \frac{2}{15}\left(\frac{\mu_0}{4\pi}\right)^2 \frac{\gamma_F^2 g_e^2 \mu_B^2 S(S+1)}{r^6}\left(\frac{3\tau_{R+e}}{1+\omega_F^2\tau_{R+e}^2} + \frac{7\tau_{R+e}}{1+\omega_e^2\tau_{R+e}^2}\right) \qquad (2.4)$$

$$R_2 = \frac{1}{15}\left(\frac{\mu_0}{4\pi}\right)^2 \frac{\gamma_F^2 g_e^2 \mu_B^2 S(S+1)}{r^6}\left(4\tau_{R+e} + \frac{3\tau_{R+e}}{1+\omega_F^2\tau_{R+e}^2} + \frac{13\tau_{R+e}}{1+\omega_e^2\tau_{R+e}^2}\right) \qquad (2.5)$$

$$R_1 = \frac{2}{5}\left(\frac{\mu_0}{4\pi}\right)^2 \frac{\omega_F^2 g_e^4 S^2 (S+1)^2}{(3kT)^2 r^6} \frac{3\tau_R}{1+\omega_F^2\tau_R^2} \qquad (2.6)$$

$$R_2 = \frac{1}{5}\left(\frac{\mu_0}{4\pi}\right)^2 \frac{\omega_F^2 g_e^4 S^2 (S+1)^2}{(3kT)^2 r^6}\left(4\tau_R + \frac{3\tau_R}{1+\omega_F^2\tau_R^2}\right) \qquad (2.7)$$

in which $T_{1e} = T_{2e}$ is assumed, $\tau_{R+e} = (\tau_R^{-1} + T_{1e}^{-1})$, τ_R is the rotational correlation time, $T_{1,2}$ are the electronic relaxation rates, ω_F is the fluorine Zeeman frequency, γ_F is the magnetogyric ratio of the ^{19}F nuclei, μ_B is the Bohr magneton, k is the the Boltzmann constant, g_e is the electron g-factor, $\mu_0/4\pi$ is the magnetic permeability of a vacuum, $S(S+1)$ is the total electron angular momentum and r is the Ln-^{19}F distance.

The resulting total relaxation rates, R_1 and R_2, are given as a combination of the electron-nucleus DD and Curie relaxation mechanisms (Equations 2.8 and 2.9).

$$R_1 = \frac{2}{15}\left(\frac{\mu_0}{4\pi}\right)^2 \frac{\gamma_F^2 \mu_{eff}^2}{r^6}\left(\frac{7\tau_{R+e}}{1+\omega_e^2\tau_{R+e}^2} + \frac{3\tau_{R+e}}{1+\omega_F^2\tau_{R+e}^2}\right) + \frac{2}{5}\left(\frac{\mu_0}{4\pi}\right)^2 \frac{\omega_F^2 \mu_{eff}^4}{(3kT)^2 r^6}\frac{3\tau_R}{1+\omega_F^2\tau_R^2} \qquad (2.8)$$

$$R_2 = \frac{1}{15}\left(\frac{\mu_0}{4\pi}\right)^2 \frac{\gamma_F^2 \mu_{eff}^2}{r^6}\left(4\tau_{R+e} + \frac{3\tau_{R+e}}{1+\omega_e^2\tau_{R+e}^2} + \frac{13\tau_{R+e}}{1+\omega_F^2\tau_{R+e}^2}\right) + \frac{1}{5}\left(\frac{\mu_0}{4\pi}\right)^2 \frac{\omega_F^2 \mu_{eff}^4}{(3kT)^2 r^6}\left(4\tau_R + \frac{3\tau_R}{1+\omega_F^2\tau_R^2}\right) \qquad (2.9)$$

in which $\mu_{eff}^2 = g_e^2 \mu_B^2 \langle S^2 \rangle$ is the effective magnetic moment of the Ln^{3+} ion and ω_e is the electron Larmor frequency.

2.5.2 ^{19}F Relaxation Analysis

As the relaxing lanthanide centre and the fluorine nuclei are in the same molecule, the ^{19}F relaxation properties are independent of concentration. This was proven by measuring the R_1/ R_2 values for $[Ho.L^1(H_2O)]^{3+}$ at 1, 2, 4, 6 and 8 mM (D_2O:CH_3OH (20 %), 295 K, 4.7 T). No significant changes in the measured values were found.

The Ln-^{19}F nucleus distance can be calculated by measuring the paramagnetic rate of relaxation as a function of magnetic field (Equations 2.8 and 2.9). The ^{19}F longitudinal relaxation rates, R_1, were measured using the inversion recovery technique, without proton decoupling, at 295 K. The inversion-recovery type function was fitted to the resulting data using Levenberg-Marquardt minimization of the non-linear least squares error functional.

The variation of the observed linewidths ($\omega_{1/2}$) of the ^{19}F resonances, defined as the peak width at half-height, was used to calculate the ^{19}F transverse relaxation rates, R_2 (Equation 2.10).

$$R_2 = \pi \times \omega_{1/2} \qquad (2.10)$$

To extract the Ln-^{19}F nucleus distance for complexes of **L^1**, R_1 and R_2 values were measured for a series of Ln^{3+} ions at four different field strengths (Table 2.3 and 2.4).

	R_1/ Hz			
Complex	4.7 T	9.4 T	11.7 T	16.5 T
$[Tb.L^1(H_2O)]^{3+}$	115	218	250	341
$[Ho.L^1(H_2O)]^{3+}$	84	192	224	282
$[Er.L^1(H_2O)]^{3+}$	46	109	143	200
$[Tm.L^1(H_2O)]^{3+}$	33	60	76	102

Table 2.3: ^{19}F Longitudinal relaxation data for $[Ln.L^1(H_2O)]^{3+}$ (2 mM, D_2O:CH_3OD (20 %), 295 K, Ln= Tb, Ho, Er and Tm)

	R_2/ Hz			
Complex	4.7 T	9.4 T	11.7 T	16.5 T
$[Tb.L^1(H_2O)]^{3+}$	261	243	287	328
$[Ho.L^1(H_2O)]^{3+}$	97	207	259	356
$[Er.L^1(H_2O)]^{3+}$	79	124	169	197
$[Tm.L^1(H_2O)]^{3+}$	62	94	102	158

Table 2.4: ^{19}F Transverse relaxation data for $[Ln.L^1(H_2O)]^{3+}$ (2 mM, D_2O:CH_3OD (20 %), 295 K, Ln= Tb, Ho, Er and Tm)

While further simplifications to equations 2.8 and 2.9 can be made, sufficient data has been collected to avoid further approximations and to perform a direct global fit of experimental relaxation data to the equations. As the geometry does not appreciably change between the different lanthanides, the Ln-^{19}F distance and the rotational correlation time can be set to be global between the Ho, Tm and Er data sets of **L^{1}** complexes. While the Tb set is analysable, the rather large linewidth results in huge point scatter, and therefore was excluded from the fitting. This approach does not utilise the set values of μ_{eff} and τ_{r+e} published in the literature. Instead, it allows the computer to calculate the values based on a least-squares fitting of the experimental data, with the values of μ_{eff} and τ_{r+e} kept local for every lanthanide data set.

When utilising a linear correlation, it is apparent that the point related to the highest field is lower than expected (Figure 2.4). However, when the full equation (Equation 2.8) is exploited, the fit is not linear and therefore the associated error is less significant. The analysis was performed by Dr. Ilya Kuprov at the University of Oxford, with a result of $r_{Ln\text{-}F}$ = 6.1 ± 0.2 Å and τ_r = 255 ± 20 ps. These values are in keeping with distances calculated for other complexes utilising similar amide arms.[15]

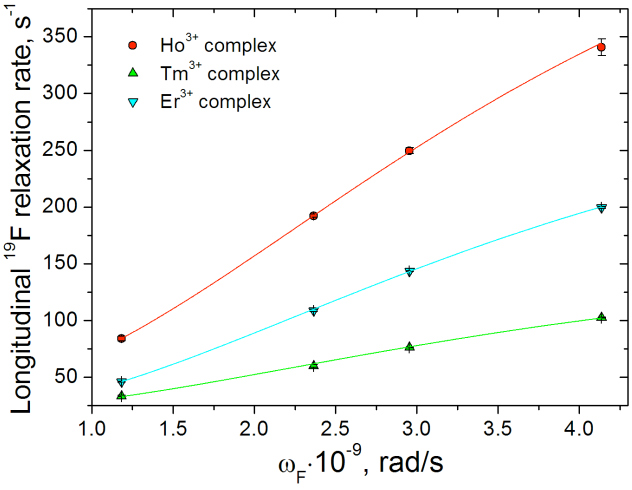

Figure 2.4: Longitudinal relaxation rates at different magnetic fields for [Ln.L^{1}(H$_2$O)]$^{3+}$ (2 mM, D$_2$O:CH$_3$OD (20 %), 295 K, Ln= Ho, Er and Tm). The steeper rise of the Ho curve as a function of magnetic field is due to its shorter electron relaxation time in comparison with the other lanthanides.

For the complexes of **L^3**, the ^{19}F chemical shifts, R_1 and R_2 values have been measured for a series of Ln^{3+} ions at two different field strengths (Table 2.5).

	R_1 / Hz		R_2 / Hz	
Complex	4.7 T	9.4 T	4.7 T	9.4 T
[Tb.L^3(H_2O)]	72	116	61	119
[Dy.L^3(H_2O)]	75	139	116	220
[Ho.L^3(H_2O)]	48	109	69	151
[Er.L^3(H_2O)]	29	65	75	157
[Tm.L^3(H_2O)]	26	51	79	91

Table 2.5: ^{19}F Longitudinal and transverse relaxation data for [Ln.L^3(H_2O)] (2mM, D_2O, pD 5.4, 295K)

For each of the Ln^{3+} ions, it can be seen that as the magnetic field is increased the relaxation rate decreases, allowing for faster acquisition time. However, the R_2 values demonstrate that this faster relaxation is also accompanied by broadening of the signal peak. Consequently, there needs to be a compromise between the two factors to enable optimisation.

For the complexes of **L^1** and **L^3**, the longitudinal and transverse relaxation rates follow the order of Tb > Ho > Er > Tm, consistent with the presence of μ^2_{eff} and μ^4_{eff} terms (Equations 2.8 and 2.9). Assessing which Ln^{3+} ion is most suitable for further development is a difficult task, as each has advantages and shortcomings. With the Tb^{3+} complexes, there is a vast relaxation enhancement. However, this is coupled with a linewidth so large it can inhibit accurate interpretation of results. Conversely, the linewidth of Tm^{3+} is more favourable but the lesser longitudinal relaxation rate enhancement could mitigate against the use of this lanthanide, at lower fields especially. Based on the above data, it could be tentatively suggested that Tb^{3+} and Ho^{3+} complexes are best suited for further development at higher fields. However, this preliminary assessment does not take into account the effect of minor species, and how the Ln^{3+} ions would perform in an imaging experiment (rather than spectroscopy).

Volumetric plots of the ^{19}F relaxation rates, resulting from equations 2.8 and 2.9, have been generated, calculating the ^{19}F longitudinal and transverse relaxation rates, R_1 and R_2, as a function of the applied magnetic field (B_0), the rotational correlation time (τ_R) and the distance between the ^{19}F nucleus and the paramagnetic centre (r). These are based on an idealised Ln^{3+} ion with a magnetic moment μ_{eff} of 10.0 Bohr magnetons (*viz.* Tb: 9.7; Dy and Ho 10.6; Er 9.6; Tm 7.6 BM) and an electronic relaxation time of 0.20 ps (Figure 2.5). Values for the electronic spin relaxation time, τ_R, have been estimated to be in the range 0.15 to 0.4 ps for both the aqua ions (Tb, Dy, Ho, Er and Tm) and their complexes with [Ln.DTPA(H_2O)].[18, 19]

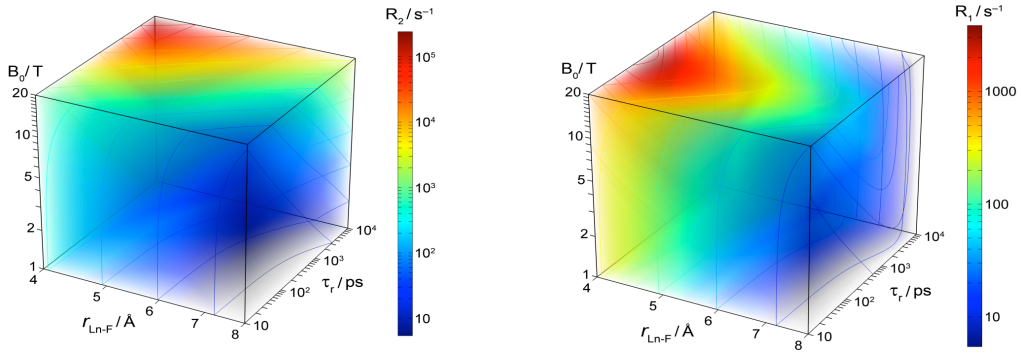

Figure 2.5: Volumetric plots showing the variation of R_1 (left) and R_2 (right) with applied field, B_o, mean distance, r, between the paramagnetic centre and the effective rotational correlation time, τ_R; the analysis is based on equations 2.8 and 2.9, assuming μ_{eff}=10.0 BM and τ_e = 0.20 ps.

The nuclear relaxation rates decrease relatively quickly, as the ^{19}F-Ln^{3+} distance is increased due to the steep distance dependence of both dipolar and Curie terms. In the ^{19}F-Ln^{3+} distance range predicted for **L^1**-**L^3** complexes (5.5 – 6.5 Å), and at a field of 3.0 Tesla, R_1 and R_2 values of ~100 Hz are expected. When moving to higher field strengths, greater line broadening is predicted for complexes of Dy, Ho, Tb and to a lesser extent, Er and Tm.

2.6 Proton Relaxation Parameters

The main aim of this project is to design multidisciplinary probes, capable of use in both ^{19}F and ^{1}H magnetic resonance imaging and spectroscopy. Consequently, the

Gd^{3+} analogue of each ligand has also been synthesised, and the corresponding ^1H MR relaxometric properties assessed.

2.6.1 Proton Relaxation Theory

Proton relaxivity directly refers to the efficiency of a paramagnetic substance to enhance the relaxation rate of water protons. As discussed in section 1.3.3, the paramagnetic contribution to total relaxivity consists of inner-sphere, second-sphere and outer-sphere contributions (Equation 2.11):

$$r_i = r_i^{IS} + r_i^{OS} + r_i^{SS} \tag{2.11}$$

The inner-sphere contribution relates to the interaction between electron spins and the water protons in the first coordination sphere of the Gd^{3+}, given by equation 2.12:

$$R_{1p}^{is} = \frac{Cq}{55.5}\left(\frac{1}{T_{1m} + \tau_m}\right) \tag{2.12}$$

in which C is the concentration in mM, q is the number of bound water molecules per Gd^{3+} (hydration number), T_{1m} is the longitudinal relaxation time of the coordinated water protons and τ_m is the water residence lifetime at the Gd^{3+} centre.[20] The longitudinal relaxation time of bound water protons is governed by the dipole-dipole (DD) and scalar (SC) mechanisms, where both are dependent on magnetic field. The relaxation rate, $1/T_{1m}$, is generally described by the modified Solomon-Bloembergen equation:

$$\frac{1}{T_{1m}} = \frac{2}{15}\left(\frac{\mu_0}{4\pi}\right)^2 \frac{\gamma_H^2 g^2 \mu_B^2 S(S+1)}{r_{GdH}^6}\left(\frac{3\tau_{c1}}{1+\omega_H^2\tau_{c1}^2} + \frac{7\tau_{c2}}{1+\omega_s^2\tau_{c2}^2}\right) \tag{2.13}$$

where γ_H is the nuclear gyromagnetic ratio for proton, g is the electron g-factor, μ_B is the Bohr magneton, r_{GdH} is the electron spin – proton distance, ω_H and ω_S are the nuclear and electron Larmor frequencies, respectively ($\omega = \gamma B$, where B is the

magnetic field), and μ_{ci} (i = 1, 2) are the correlation times relative to the electron-proton dipolar coupling.[20] The correlation times which are characteristic of the relaxation processes are described by equation 2.14:

$$\frac{1}{\tau_{ci}} = \frac{1}{\tau_R} + \frac{1}{T_{ie}} + \frac{1}{\tau_m} \tag{2.14}$$

in which τ_R is the rotational correlation time, T_{ie} (i= 1 or 2) are the electron spin relaxation times of the metal ion and τ_m is the water residence lifetime at the Gd^{3+} centre (or ion).[20]

The relaxation rates, $1/T_{1e}$ and $1/T_{2e}$, also depend on magnetic field. It is common for Gd^{3+} complexes to be interpreted in terms of zero field splitting (ZFS) interaction, given by equations 2.15 and 2.16:

$$\left(\frac{1}{T_{1e}}\right)^{ZFS} = \frac{2\Delta^2\tau_v\left\{4S(S+1)-3\right\}}{50}\left(\frac{1}{1+\omega_s^2\tau_v^2} + \frac{4}{1+4\omega_s^2\tau_v^2}\right) \tag{2.15}$$

$$\left(\frac{1}{T_{2e}}\right)^{ZFS} = \frac{\Delta^2\tau_v\left\{4S(S+1)-3\right\}}{50}\left(3 + \frac{5}{1+\omega_s^2\tau_v^2} + \frac{2}{1+4\omega_s^2\tau_v^2}\right) \tag{2.16}$$

in which Δ^2 is the mean-square ZFS energy and τ_v is the correlation time for the ZFS modulation (resulting from the transient distortions of the complex). The combination of equations 2.13, 2.15 and 2.16 represent the Solomon-Bloembergen-Morgan (SBM) theory.

The second-sphere term relates to a loose layer of water molecules between the inner- and outer-sphere. They are not directly bound, but arise from other interactions, such as hydrogen bonding, allowing them to remain in proximity to the Gd^{3+} ion for a relatively long time. Often this term is neglected or its effect is taken into account in the outer-sphere term.

The outer-sphere term is related to the paramagnetic effect experienced by the bulk solvent molecules diffusing around the Gd^{3+} complex. For low molecular weight molecules, the outer sphere contribution can be given in a simplified form (Equation 2.17).

$$R_{1p}^{os} = C^{os}\left(\frac{1}{aD}\right)\left[7J(\omega_S) + 3J(\omega_H)\right] \qquad (2.17)$$

in which C^{os} is a constant (5.8×10^{-13} $s^{-2}M^{-1}$), a is the minimum distance between the Gd^{3+} and the water molecules, D is the diffusion coefficient, and $J(\omega_i)$ is the dependence on the electronic relaxation times.

For the low molecular weight Gd^{3+} complexes studied within this thesis, the most significant contribution is usually from the inner sphere term.[20]

2.6.2 Proton Relaxation Properties of Gd^{3+} Complexes

For the measurement of relaxivity, the obvious solvent of choice is water. However, due to the high number of fluorine atoms present in $[Gd.L^1(H_2O)]^{3+}$, water solubility was limited and therefore 20 % methanol was added for the experiments. As a control, ^1H relaxivity measurements were made in a 10, 15, 20 and 25 % CD_3OD/ H_2O mixture. No significant changes in the measured values were found (2 mM, 295 K, 1.4 T).

The solubility issues encountered with $[Gd.L^1(H_2O)]^{3+}$ prevented accurate measurements of the temperature dependence of the transverse relaxation rate of the ^{17}O water signal. Consequently, information on the water exchange rate, τ_m, was obtained from the analysis of the temperature dependence of r_{1p} in association with standard analyses of the field dependence of relaxivity (0.01 to 70 MHz) (Figure 2.6). This analysis is based upon the Solomon-Bloembergen-Morgan equations that rationalise the time-dependence of the water proton-Gd^{3+} dipolar coupling, in addition to considering the contribution from the second sphere.[21, 22]

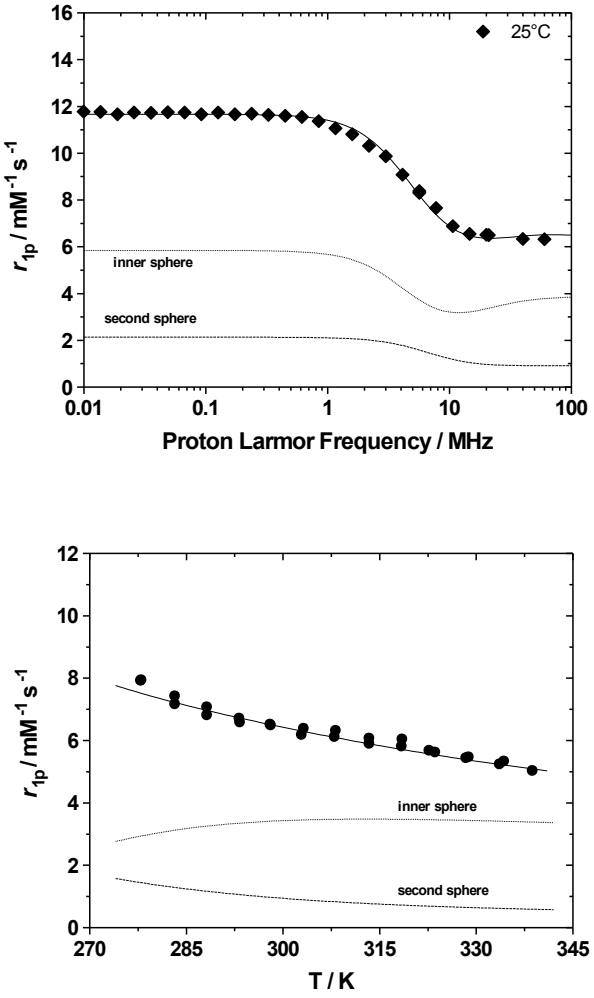

Figure 2.6: Variation of relaxivity, r_{1p}, with a) field and b) temperature, showing the estimated contributions of inner and second sphere waters for $[Gd.L^1(H_2O)]^{3+}$ (0.6 mM, 298 K, pH 6.5)

For $[Gd.L^1(H_2O)]^{3+}$, the relaxivity decreases as a function of temperature, consistent with a relatively fast water exchange (τ_m = 3.5 μs) at the Gd^{3+} centre (Figure 2.6). The proton relaxivity of $[Gd.L^1(H_2O)]^{3+}$ was calculated to be 6.5 $mM^{-1}s^{-1}$ (20 MHz, 298 K) which is significantly higher than expected. Conversely, the tetra-methyl analogue, $[Gd.L^2(H_2O)]^{3+}$, has a measured proton relaxivity value of 3.8 $mM^{-1}s^{-1}$ (20 MHz, 298 K), which is comfortably in the region expected of tetra-amides.[23] While the relaxivity of $[Gd.L^2(H_2O)]^{3+}$ does decrease as a function of temperature, the profile is significantly different from that of $[Gd.L^1(H_2O)]^{3+}$ (Figure 2.7).

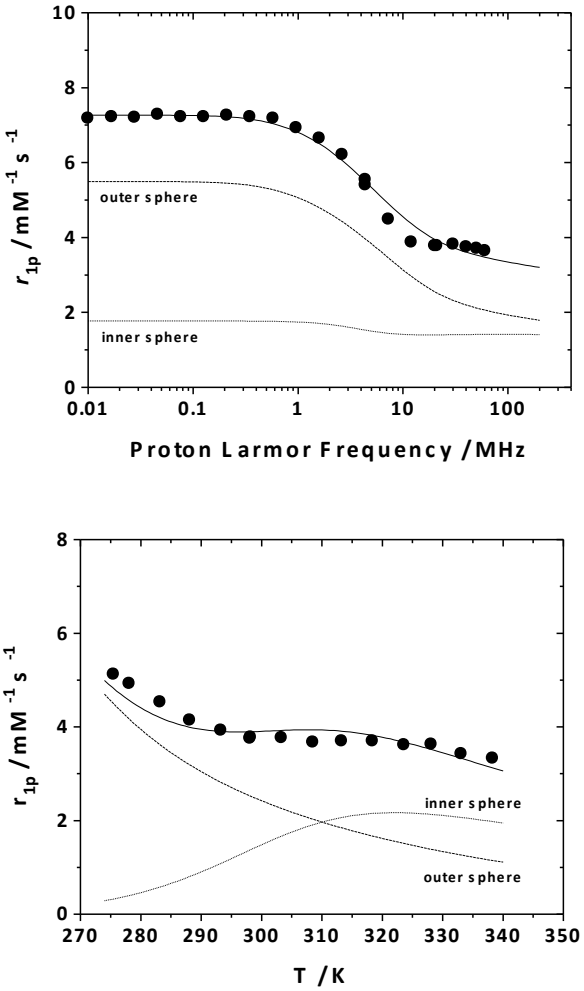

Figure 2.7: Variation of relaxivity, r_{1p}, with a) field and b) temperature, showing the estimated contributions of inner and second sphere waters for $[Gd.L^2(H_2O)]^{3+}$ (0.4 mM, 298 K, pH 6.5)

Analysis of the NMRD profile and the temperature dependence of the proton relaxivity demonstrated a markedly slower rate of water exchange (τ_m = 9 μs) for $[Gd.L^2(H_2O)]^{3+}$. Further differences were apparent when examining the pH-dependence of the complexes. For $[Gd.L^1(H_2O)]^{3+}$ the relaxivity remained constant over the pH range of 4-10, consistent with high kinetic stability. But with $[Gd.L^2(H_2O)]^{3+}$ the relaxivity increased at high pH, most likely due to the onset of base-catalysed prototopic exchange.

The presence of a larger contribution of the second sphere of hydration for $[Gd.L^1(H_2O)]^{3+}$, presumably associated with the presence of the CF_3 groups, helps to rationalise the increased relaxivity in comparison with $[Gd.L^2(H_2O)]^{3+}$. It is presumed

there is well-defined second sphere of hydration that assists the water exchange at gadolinium, causing an increase in relaxivity. This is also evident from consideration of the different enthalpy of activation of the two complexes (Figure 2.8).

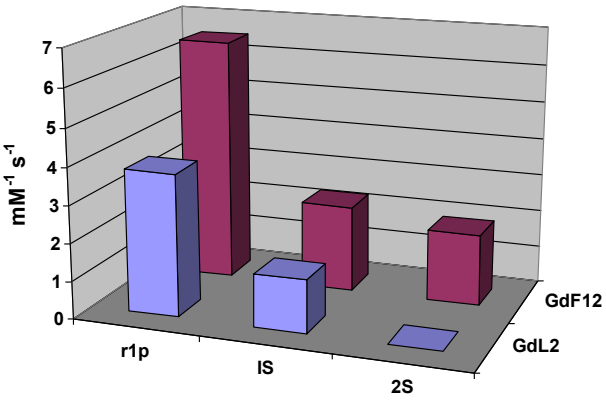

	[L²Gd]	[L¹Gd]
r_{1p}^{20} (mM^{-1} s^{-1})	3.8	6.5
Δ^2 (s^{-2};×10^{19})	1.5	4.0
τ_V (ps)	8.5	13
ΔH_v (*k*J/mol)	5.0	2.0
τ_R (ps)	120	118
ΔH_R (*k*J/mol)	15	16
τ_M (μs)	9.0	3.5
ΔH_M (*k*J/mol)	51.0	30.1
q	1	1
r (Å)	3.0	3.0
a (Å)	4.0	4.0
D (cm^{2}s^{-1};×10^{-5})	2.24	2.24
ΔH_d (*k*J/mol)	-28	-22
q'	0	8
r' (Å)	/	4.4

Figure 2.7: Summary of selected relaxation parameters for [Gd.L^1(H$_2$O)]$^{3+}$ and [Gd.L^2(H$_2$O)]$^{3+}$ derived from analysis of VT ^{1}H NMR relaxivity and fitting of NMRD profiles. *Note: Parameters denoted with prime refer to second sphere relaxivity*

As discussed, the high relaxivity value for [Gd.L^1(H$_2$O)]$^{3+}$ is somewhat unusual for this type of tetra-amide complex. To further our understanding of this result, a DFT calculated structure of [Y.L^1(H$_2$O)]$^{3+}$ was generated, as a model for the related lanthanide paramagnetic complexes, in collaboration with Dr Ilya Kuprov (Figure 2.9).

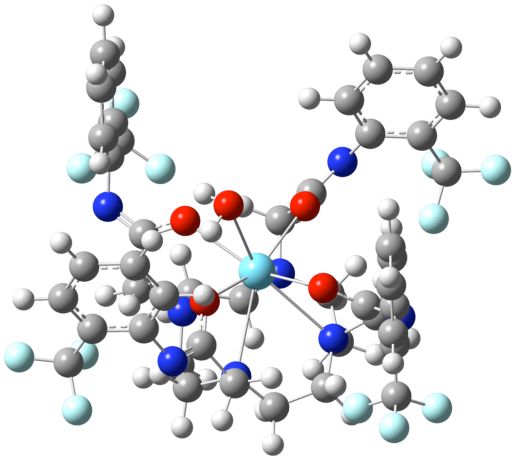

Figure 2.9: DFT calculated structure of $[L^1Ln]^{3+}Cl_3$. Colour code: grey= carbon; white= hydrogen; dark blue= nitrogen; red= oxygen; light blue= fluorine; turquoise= Ln.

The DFT calculated structure identifies two possible hydrogen bonding sites for water molecules; to the amide N-H and to the relatively acidic C-H proton. The latter is encountered rather infrequently, and may be attributed to the positive charge on the hydrogen of the CH_2 groups on the cyclen cage (owing to the close proximity of the other electronegative groups). The most important hydrogen bond interaction is between the amide NH and a water molecule. This interaction is enhanced by the higher acidity of the amide proton, due to the proximity of the trifluoromethyl group. Consequently, this results in these second sphere water molecules spending longer time, on average, in the immediate vicinity of the paramagnetic ion. Additionally, while the water molecules are bonded to the complex, they share the same rotational correlation time with the complex. As discussed previously, the relaxivity is proportional to both the time spent near the complex and the rotational correlation time. Both parameters are increased in $[Gd.L^1(H_2O)]^{3+}$ and therefore could contribute to the increased relaxivity value. The DFT structure calculated the Ln-^{19}F nucleus distance to be 6.2 Å. This is in good agreement with the value of 6.1 Å calculated from the relaxation rates measured at different field strengths (Section 2.5.2).

The relaxivity of $[Gd.L^3(H_2O)]$ was independent of pH (± 7 %) over the pH range 2.5 to 11.5, consistent with high kinetic stability with respect to acid-catalysed or base-promoted dissociation pathways. The temperature dependence of the transverse

relaxation rate of the ^{17}O water signal, in addition to the analysis of the temperature and field dependence of r_{1p}, allowed an estimate of the water exchange lifetime, τ_m, based on standard 'Swift-Connick' methodology (Figure 2.10).[22]

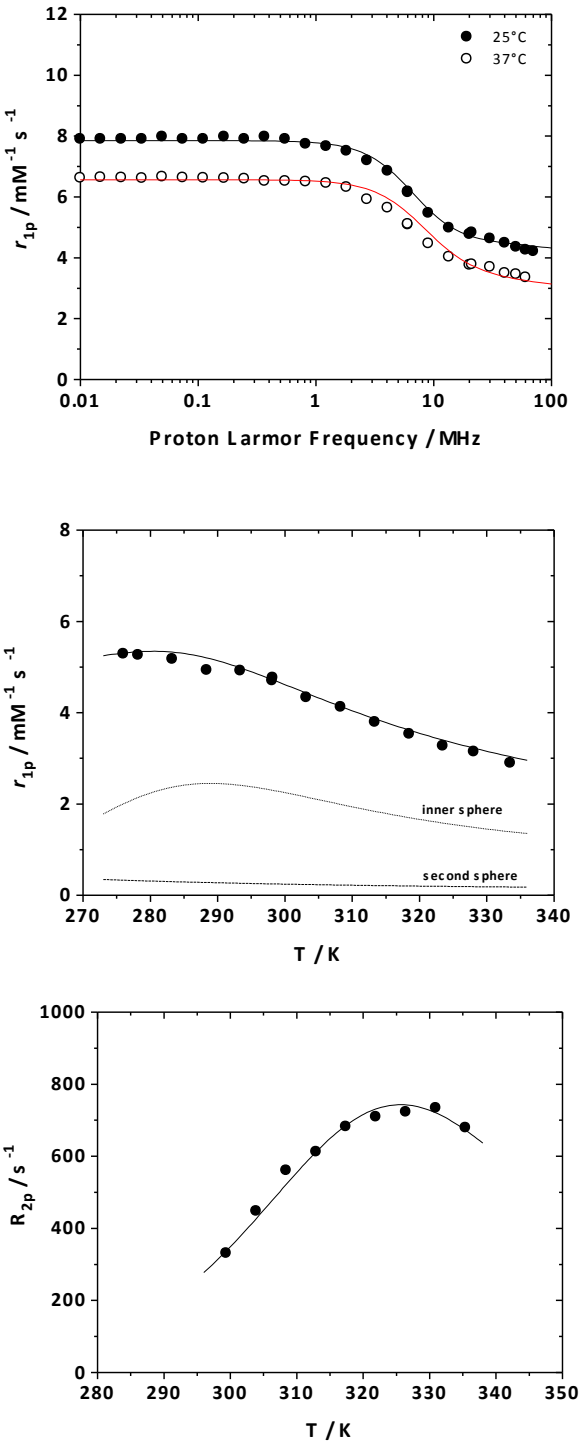

Figure 2.9: Variation of relaxivity, r_{1p}, with a) field and b) temperature, showing the estimated contributions of inner and second sphere waters. c) ^{17}O NMR - variation of R_{2p} with temperature for [Gd.L^3(H_2O)] (0.6 mM, 298 K, pH 6.5).

The proton relaxivity of [Gd.L^3(H_2O)] was found to be 5.5 $mM^{-1}s^{-1}$ (20 MHz, 298 K), and the water exchange lifetime estimated to be 0.9 μs. Both values are typical of a variety of related monoamide derivatives of [Gd.DO3A(H_2O)].[17]

2.7 Sensitivity Enhancement in Spectroscopic and ^{19}F MR Imaging Studies

A comparative study was undertaken to assess the gain in signal intensity for the Tb, Ho, Er and Tm complexes of **L^1** and **L^3** over the diamagnetic yttrium analogue. Equimolar (2 mM) solutions were used and spectral signal intensity recorded at 4.7 T, using an acquisition time of three times the measured T_1 value, acquiring spectral data for 20 min in each case. In spectral processing, the line broadening was set to 50 % of the observed linewidth and the relative signal intensity only took into account the signal from the major species. The values obtained reveal the expected gains in signal intensity, which are of the order of a factor of 10 (Table 2.6).

Complex	Relative signal intensity	Complex	Relative signal intensity
[Y.L^1(H_2O)]$^{3+}$	1.0	[Y.L^3(H_2O)]	1.0
[Tb.L^1(H_2O)]$^{3+}$	14.8	[Tb.L^3(H_2O)]	11.1
[Ho.L^1(H_2O)]$^{3+}$	9.2	[Ho.L^3(H_2O)]	5.5
[Er.L^1(H_2O)]$^{3+}$	8.6	[Er.L^3(H_2O)]	4.8
[Tm.L^1(H_2O)]$^{3+}$	5.7	[Tm.L^3(H_2O)]	4.8

Table 2.6: Assessment of ^{19}F NMR spectroscopic sensitivity for a) [Ln.L^1(H_2O)]$^{3+}$ (2 mM, D_2O:CH_3OH (20 %), 295 K, Ln=Y, Tb, Ho, Er and Tm) and b) [Ln.L^3(H_2O)] (2 mM, D_2O, 295 K, pD 5.4). The acquisition time was set as 3 x T_1, with no delay time; total acquisition time was 20 min; in spectral processing the line broadening was set as 50 % of the observed linewidth.

From the results it can be seen that complexes of **L^1** are superior to those of **L^3** for relative signal intensity gain, in comparison to the corresponding diamagnetic Y^{3+} complex. Complexes of **L^1** incorporate 12 fluorines whereas complexes of **L^3** have only 3. Moreover, complexes of **L^1** have one major resonance by ^{19}F NMR spectroscopy which is ≥ 70 % of the overall observed signal intensity, whereas complexes of **L^3** have additional species present that limit the effective signal intensity gain.

Preliminary imaging studies were carried out at 7 T by Prof. Andrew Blamire at the Newcastle Magnetic Resonance Centre. R_1 values were estimated to be 46.4 s^{-1} and 2.2 s^{-1} for the Er and Y complexes of **L^3**, leading to calculated Ernst angles of 72^o and 19^o, respectively, for a repetition rate, T_R, of 25 ms. Equimolar solutions of [Y.L^3(H_2O)] and [Er.L^3(H_2O)] were prepared, and fluorine MR images of were collected over 34 min. The measured signal to noise ratio in [Er.L^3(H_2O)] was 16.7, compared to 7.2 in [Y.L^3(H_2O)], yielding a sensitivity enhancement of 2.3 (Figure 2.11). This is lower than the theoretical calculated sensitivity difference for Ernst angle imaging, under these conditions, of 4.4. Some loss of sensitivity is expected due to R_2 decay during the echo time. Although the minimum repetition time could be reduced further, the theoretical sensitivity increase in moving to an even shorter T_R is small. Scans were therefore collected with T_R=25 ms as a typical value that could be used for multi-slice measurements *in vivo*.

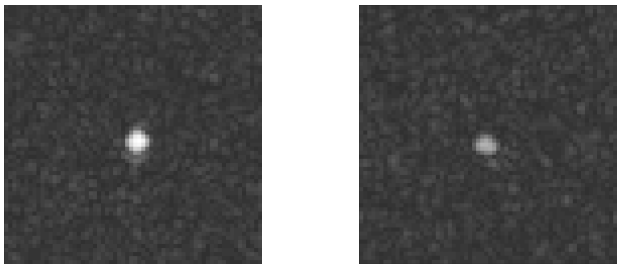

Figure 2.10: Gradient echo ^{19}F images of [Er.L^3(H_2O)] (left) and [Y.L^3(H_2O)] (right) samples. Samples contained 5mM solution and were imaged using a Ernst angle excitation of a 6 mm thick slice, in-plane resolution of 1.5×1.5 mm, T_E=0.88 ms, T_R=25 ms and 2560 averages.

2.8 Cytotoxicity

As with all compounds that are designed for *in vivo* applications, the cytotoxicity has to be evaluated to determine whether or not the application will be viable. IC_{50} values were determined using the MTT assay, as described by Carmichael *et al.,* which makes use of the conversion of MTT (3-(4,5-dimethylthiazol-2-yl)-2,5-diphenyltetrazolium bromide) to a purple formazan product by the mitochondrial succinate dehydrogenase of viable cells (Scheme 2.5).[24] This insoluble formazan

product was quantified spectrophotometrically upon dissolution in DMSO. IC_{50} values were determined as the drug concentration required to reduce the absorbance to 50% of that in the untreated, control wells, and represent the mean for data from at least three independent experiments.

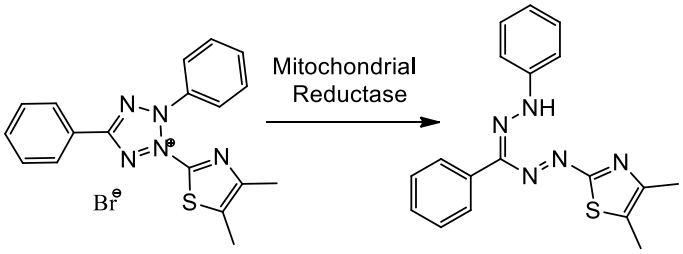

Scheme 2.5: Conversion of MTT (3-(4,5-dimethylthiazol-2-yl)-2,5- diphenyltetrazolium) to a purple formazan product by the mitochondrial dehydrogenase of viable cells.

The cytotoxicity of the complexes of **L^1**- **L^3** was assessed using the NIH 3T3 cell line, with an incubation time of 24 h (Table 2.7).

Complex	IC_{50} (μM)
$[Gd.L^1(H_2O)]^{3+}$	> 200
$[Tb.L^2(H_2O)]^{3+}$	>500
$[Gd.L^2(H_2O)]^{3+}$	>500
$[Gd.L^3(H_2O)]^{3+}$	>500

Table 2.7: Cyctotoxicity results for complexes of **L^1** – **L^3** in NIH 3T3 cells, following 24 h incubation, determined by the MTT assay.

The limited solubility of $[Gd.L^1(H_2O)]^{3+}$ resulted in the complexes being tested at lower concentrations which accounts for the lower IC_{50} value in comparison complexes of **L^2** and **L^3**. A control experiment, testing both the Gd^{3+} and Tb^{3+} complexes of **L^2**, demonstrated that the IC_{50} value measured is independent of Ln^{3+} ion (within a given ligand set). All complexes of **L^1**-**L^3** exhibit IC_{50} values sufficiently high to be considered non-toxic. This is most likely to be due to their poor ability to enter this cell type, under the experimental conditions.

2.9 Preliminary *In vivo* Studies

The Ln^{3+} complexes of monoamide derivatives of DO3A exhibit high kinetic and thermodynamic stability with respect to metal dissociation and are very water soluble. Hence, they are appropriate systems for consideration for use *in vivo*. Preliminary *in vivo* studies were performed by Dr. Ian Wilson, at the Newcastle Magnetic Resonance Centre, on SCID male mice (25 g) with HT29 tumours (human colorectal carcinoma). Measurements were taken 10-14 days after inoculation when the tumours were ~10 mm in diameter. Mice had their tail vein cannulated and restrained within a 39 mm volume coil, and were anaesthetized with isofluorane inhalation and kept warm using a warm air feedback system. Scout images were acquired and slices selected for our region of interest (ROI), including tumour, muscle and bladder. A dynamic gradient echo multi-slice sequence was used for imaging. The performance of $[Gd.L^3(H_2O)]$ was compared to that of the commercial contrast agent, Prohance (0.1 mM kg^{-1}). Images were collected 30 seconds pre- and 10 minutes post-injection for $[Gd.L^3(H_2O)]$ and Prohance (Figure 2.12).

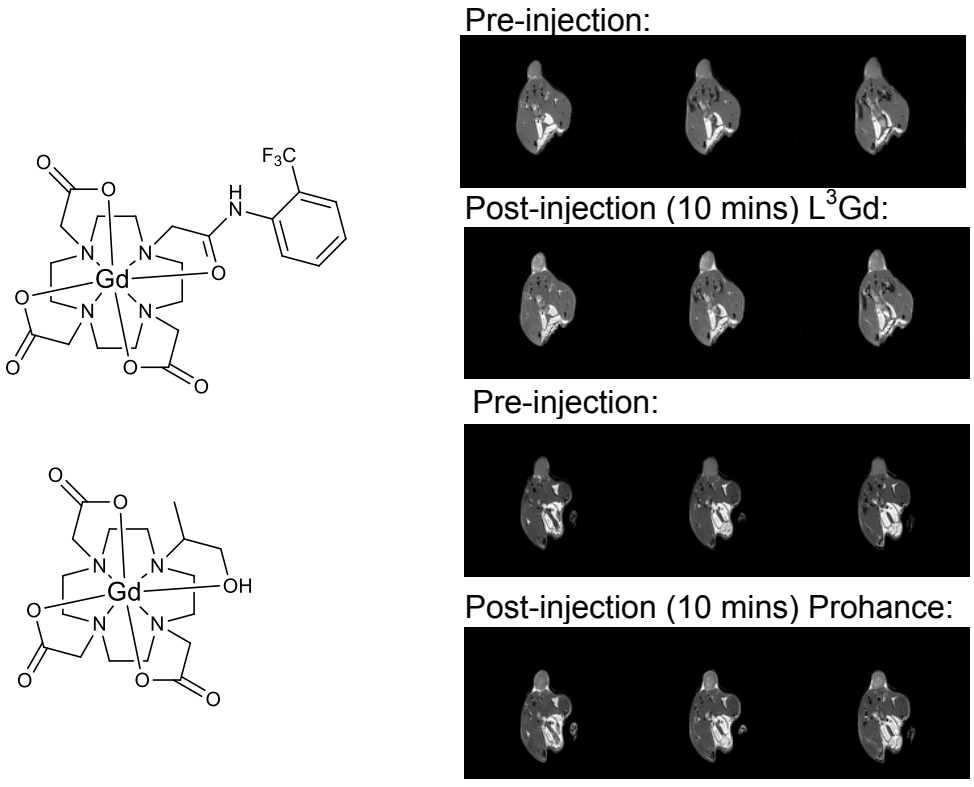

Figure 2.12: ^1H MRI images of SCID male mice collected at 30 secs pre and 10 mins post injection: $[Gd.L^3(H_2O)]$ (upper) and Prohance (lower)

The tumour area was analysed to measure the mean signal intensity profile as a function of time. The increase of the mean signal intensity reached 1.19 (± 0.02) for [Gd.L^3(H_2O)] and 1.22 (± 0.02) for Prohance. There was rapid uptake of [Gd.L^3(H_2O)] observed in the tumour, which was subsequently released into the bladder, indicative of renal excretion. These findings were very promising owing to the similarity in results with the commercially available Prohance. As such, a complimentary ^{19}F MRI study was performed using [Ho.L^3(H_2O)] (0.1 mM kg^{-1}). Disappointingly no fluorine image was recorded. This could be due to the presence of multiple species in the ^{19}F NMR spectra, limiting the observed signal intensity, or it could be that there are simply too few fluorines in complexes of **L^3**, leading to insufficient signal intensity in the observed region.

2.10 Stability of L^3 complexes

As discussed in section 2.4, the complexes of **L^3** give rise to one major species in solution, with many other minor species that vary in number and proportion according to the nature of the Ln^{3+} ion. However, if left in solution for more than 48 h, the number and, more significantly, the proportion of major to minor species was altered (Table 2.8).

	% Major species		No. of minor species	
Complex	0 h	48 h	0 h	48 h
[Tb.L^3(H_2O)]	68	43	5	8
[Ho.L^3(H_2O)]	85	62	3	7
[Er.L^3(H_2O)]	82	47	8	10
[Tm.L^3(H_2O)]	74	74	6	9
[Y.L^3(H_2O)]	92	92	1	1

Table 2.8: ^{19}F NMR spectroscopic data for [Ln.L^3(H_2O)] (2 mM, D_2O, 295 K, pD 5.4, Ln = Tb, Ho, Er, Tm and Y) at 0 and 48 h.

This is most apparent for [Er.L^3(H_2O)] where the major species comprised > 80 % of the observed signal immediately following dissolution, but reduced to ~ 47 % after 48 h in D_2O (Figure 2.13).

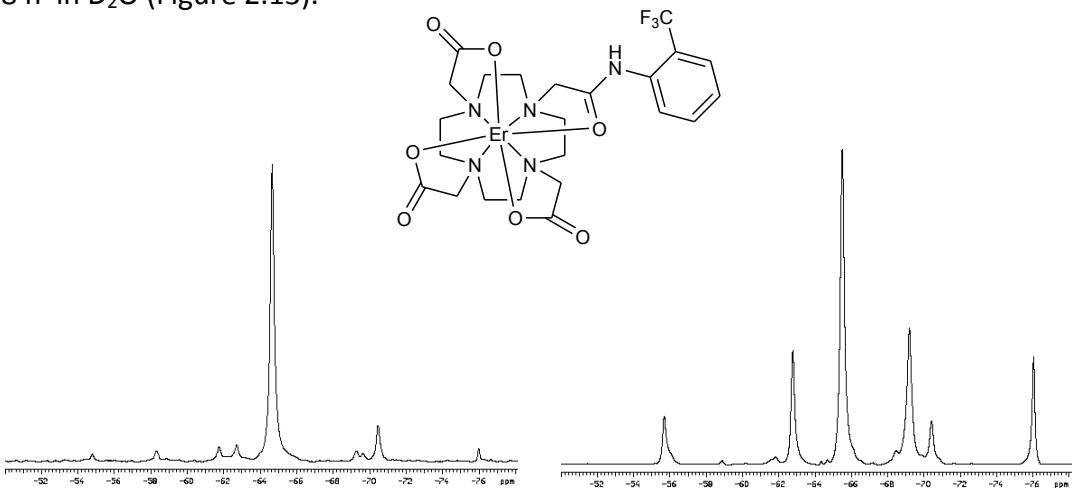

Figure 2.12: ^{19}F NMR spectra of [Er.L^3(H_2O)] at a) 0 h and b) 48 h (2mM, D_2O, 295K, pD 5.4, 4.7 T)

The isomeric species observed in these ^{19}F NMR spectra relate to the presence of diastereoisomeric species. These may be ascribed to two differing elements of chirality associated with the NCCN and NCCO metal chelate rings. There are a number of different conformations that complexes of **L^3**, or any cyclen-based system, can adopt (Figure 2.14).

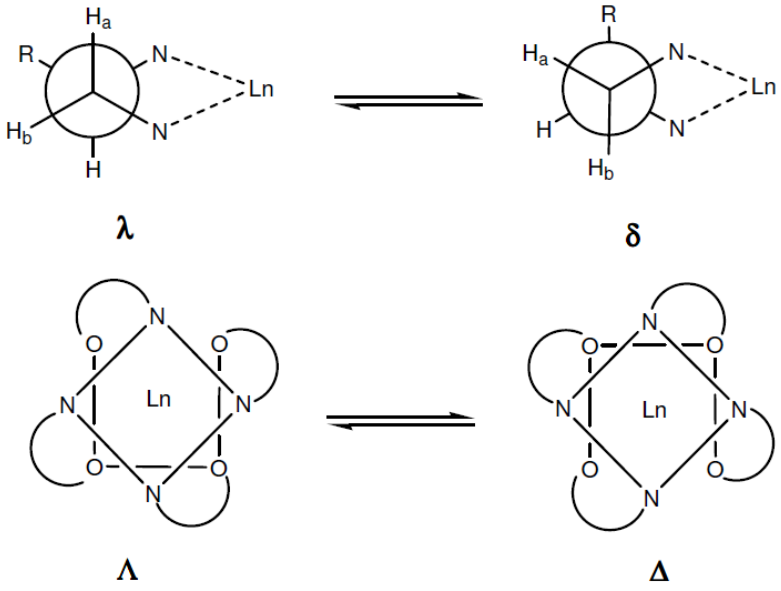

Figure 2.14: Conformations of the Ln^{3+} complexes of DOTA showing the orientation of the cyclen ring and acetate arms

Each NCCN chelate ring is characterised by a torsion angle of +60° or -60° (δ or λ), and in a similar fashion, the NCCO torsion angle of the acetate arms can be +30° or -30° (Δ or Δ). This gives rise to four stereoisomers, exisiting as a pair of enantiomers. A common configuration is favoured – giving δδδδ/ λλλλ pairs of isomers that are observed crystallographically. There are other possible conformations, such as λδδδ, but they are usually higher in energy and have not previously been observed in crystallographic studies of Ln^{3+} cyclen-based complexes.[26,27]

A third element of chirality relates to the dissymmetry presented by the ortho-substituted aryl substituent on the coordinated amide N. This can be thought of in terms of placing the CF_3 group '*cis*' or '*trans*' with respect to the coordinated amide oxygen.

Evidently, the formation of new resonances in the ^{19}F NMR spectra over time will reduce signal intensity. Thus, it is vital to be able to develop a fluorinated probe that is water soluble, exists as one main species in solution and that is stable over time.

2.11 Conclusions

Two model fluorinated macrocyclic lanthanide (III) complexes have been synthesised, and their spectroscopic and relaxation properties discussed. Analysis of the interplay between applied field, Ln^{3+} ion and rotational correlation time has demonstrated that complexes of Tb and Ho are most favourable at lower field (3 to 7 T), yielding large increases in R_1 without experiencing excessive line broadening of the resonances. Conversely, complexes of Er and Tm have been shown to be worthy of consideration of use at fields greater than 7 T.

The field dependence of the Curie contribution to the R_1 values has allowed the distance between the Ln^{3+} ion and the trifluoromethyl group to be estimated, which has been confirmed by DFT calculations.

Using complexes of Tb, Ho, Er and Tm, longitudinal relaxation rate enhancements, versus diamagnetic analogues, can be achieved. This results in the faster acquisition of data in a given time period, leading to signal intensity enhancements in both spectroscopic and imaging studies.

The possibility of ^{1}H / ^{19}F dual imaging studies has been explored, using complexes of the Gd^{3+} for the proton MRI work. Finally, the importance of achieving one preferred, and stable, species in solution has been discussed. Strategies to achieve this will be addressed in chapter 3.

2.12 References

1) P.K. Senanayake, A. M. Kenwright, D. Parker, S. van der Hoorn, *Chem. Commun.*, **2007**, 2923.

2) A. M. Kenwright, I. Kuprov, E. De Luca, D. Parker, S. U. Pandya, P. K. Senanayake, D. G. Smith, *Chem. Commun.*, **2008**, 2514.

3) O. Reany, T. Gunnlaugsson, D. Parker, *J. Chem. Soc., Perkin Trans. 2*, **2000**, 1819.

4) W. DeW. Horrocks, D. R. Sudnick, *J. Am. Chem. Soc.,* **1979**, *101*, 334.

5) W. DeW. Horrocks, D. R. Sudnick, *Acc. Chem. Res.*, **1981**, *14*, 384.

6) R. S. Dickins, D. Parker, A. S. de Sousa, J. A. G. Williams, *Chem. Commun.,* **1996**, 697.

7) S. Aime, A. Barge, M. Botta, J. A. K. Howard, J. M. Moloney, D. Parker, A. S. de Sousa, M. Woods, *J. Am. Chem. Soc.*, **1999**, *121*, 5762.

8) S. Aime, M. Botta, D. Parker, J. A. G. Williams, *J. Chem. Soc. Dalton Trans.*, **1995**, 2259.

9) B. Bleaney, *J. Magn. Reson.*, **1972**, *8*, 91.

10) L. Helm, *Progr. NMR Spec.* **2006**, *49*, 45.

11) R. Sharp, L. Lohr, J. Miller, *Progr. NMR Spec.* **2001**, *38*, 115.

12) M. Gueron, *J. Magn. Reson.* **1975**, *19*, 58.

13) J. Kowalewski, C. Luchinat, T. Nilsson, G. Parigi, *Journal of Physical Chemistry A,* **2002**, *106*, 7376.

14) S. L. Grage, U. H. N. Durr, S. Afonin, P. K. Mikhailiuk, I. V. Komarov, A. S. Ulrich, *J. Magn. Reson.* **2008**, *191*, 16.

15) K. H. Chalmers, E. De Luca, N. H. M. Hogg, A. M. Kenwright, I. Kuprov, D. Parker, M. Botta, J. I. Wilson, A. M. Blamire, *Chem. Eur. J.*, **2010**, *16*, 134.

16) I. Bertini, F. Capozzi, C. Luchinat, G. Nicastro, Z. Xia, *J. Phys. Chem.*, **1993**, *97*, 6351.

17) I. Bertini, C. Luchinat, G. Parigi, *Prog. Nucl. Mag. Res. Sp.*, **2002**, *40*, 249.

18) B. M. Alsaadi, F. J. C. Rossotti, R. J. P. Williams, *J. Chem. Soc. Dalton Trans.*, **1980**, 2151.

19) S. Aime, L. Barbero, M. Botta, G. Ermondi, *J. Chem. Soc. Dalton Trans.*, **1992**, 225.

20) A. Sigel, H. Sigel, *The Lanthanides and Their Interrelations with Biosystems Vol. 40*, Chapter 14, Marcel Dekker, University of Basel, Switzerland, **2003**.

21) A. E. Merbach, E. Toth, *The Chemistry of Contrast Agents in Medical Magnetic Resonance Imaging*, Wiley, New York, **2001.**

22) T. J. Swift, R. E. Connick, *J. Chem. Phys.*, **1962**, *37*, 307.

23) A. L. Thompson, D. Parker, D. A. Fulton, J. A. K. Howard, S. U. Pandya, H. Puschmann, P. K. Senanayake, P. A. Stenson, A. Badari, M. Botta, S. Avedano, S. Aime, *Dalton Trans.,* **2006**, 5606.

24) J. Carmichael, W. G. DeGraff, A. F. Gazdar, J. D. Minna, J. B. Mitchell, *Cancer Res.*, **1987**, *47*, 936.

25) J. R. Morrow, S. Amin, C. H. Lake, M. R. Churchill, *Inorg. Chem.*, **1993**, *32*, 4566.

26) K. O. A. Chin, J. R. Morrow, C. H. Lake, M. R. Churchill, *Inorg. Chem.,* **1994**, *33*, 656.

27) D. Parker, R. S. Dickins, H. Puschmann, C. Crossland, J. A. K. Howard, *Chem Rev.*, **2002**, *102*, 1977.

Chapter 3: Strategies to Enhance Signal Intensity

3.0 Strategies to Enhance Signal Intensity
3.1 Introduction

The initial work discussed in chapter two focussed on the behaviour of lanthanide complexes of a CF_3-labelled mono-amide derivative of DO3A, $[Ln.L^3(H_2O)]$ (Figure 3.1). Unfortunately there were limitations to this system, most notably the number of isomeric species present in solution, which varied from one Ln to another and gave rise to a changing distribution over time. Furthermore, the observed linewidths were significantly broader than expected, owing to dynamic intramolecular conformational processes. Previous studies have shown that by introducing a substituent at the α- position to the ring nitrogen,[1,2] or by replacing the carboxylate group with a more sterically demanding group, these dynamic processes can be slowed down.[3,4]

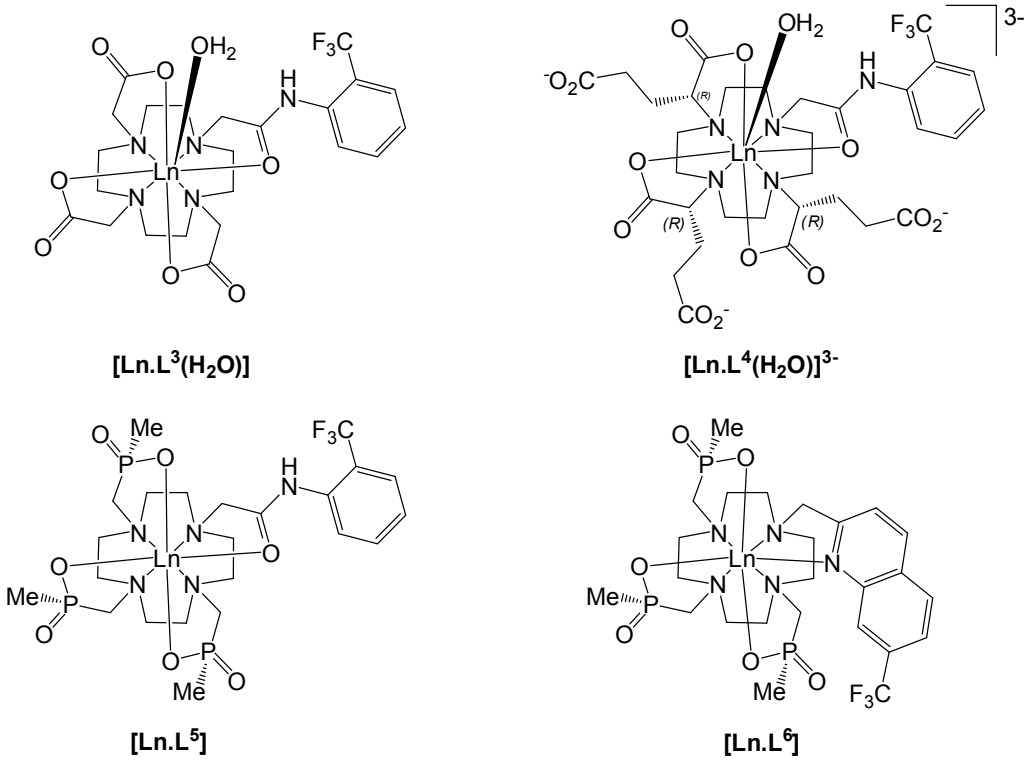

Figure 3.1: Structures of $[Ln.L^3(H_2O)]$, $[Ln.L^4(H_2O)]^{3-}$, $[Ln.L^5]$ and $[Ln.L^6]$

Consequently, two main strategies were employed in an attempt to reduce the number of isomeric species and minimise exchange broadening (Figure 3.1). Firstly, the development of chiral lanthanide complexes was investigated, through the

introduction of glutarate and phosphinate pendant arms ($[Ln.L^4(H_2O)]^{3-}$ and $[Ln.L^5]$ respectively). Secondly, a CF_3 quinoline was synthesised to prevent arm rotation and to increase the local rigidity of the trifluoromethyl moiety ($[Ln.L^6]$).

The disappointing preliminary ^{19}F MRI *in vivo* studies with $[Ho.L^3(H_2O)]$, as discussed in chapter two, demonstrated that there was insufficient signal intensity in the observed region. The simplest way to increase signal intensity is the incorporation of more fluorine atoms in to the complex. Importantly the fluorine atoms must be chemically and magnetically equivalent to ensure a single ^{19}F resonance. Therefore, three further complexes were synthesised, each based on DO2A and possessing two C_2-related CF_3 groups in each amide moiety (Figure 3.2). The α-substituent in **L^{7b}** is derived from (*S*)-glutaric acid, leading to an enantiopure ligand, and **L^{7a}** is the corresponding racemic ligand.

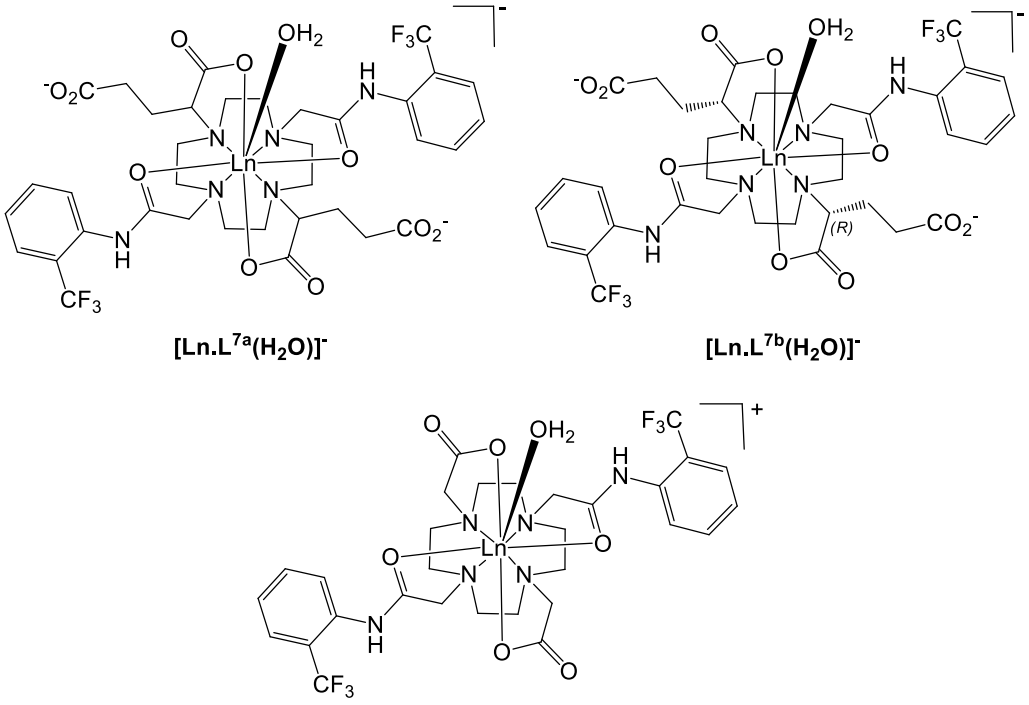

$[Ln.L^{7a}(H_2O)]^-$ **$[Ln.L^{7b}(H_2O)]^-$**

$[Ln.L^8(H_2O)]^+$

Figure 3.2: Stuctures of $[Ln.L^{7a}(H_2O)]^-$, $[Ln.L^{7b}(H_2O)]^-$ and $[Ln.L^8(H_2O)]^+$

3.2 Synthesis and Characterisation of Complexes

3.2.1 Synthesis of $[Ln.L^4(H_2O)]^{3-}$

The first step in the synthesis of $\mathbf{L^4}$ involved the alkylation of tri-BOC protected cyclen with the α- chloroamide arm, **1** (Scheme 3.1). Surprisingly, even under fairly harsh reaction conditions, utilising 5 equivalents of Cs_2CO_3 and DMF as the solvent, the yield was very low (11 %). The BOC protecting groups were subsequently removed by treatment with trifluoroacetic acid in CH_2Cl_2. This reaction was also low yielding at 23 %, and therefore it was decided to explore an alternative synthetic pathway to achieve selective mono-alkylation.

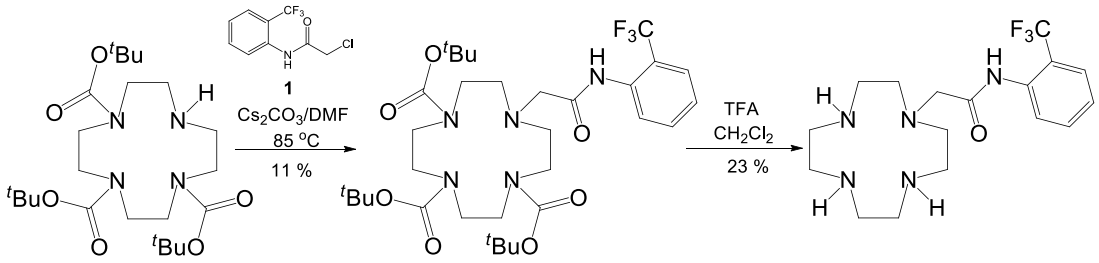

Scheme 3.1

The second approach involved selective alkylation of cyclen with **1**, without the use of any protecting groups (Scheme 3.2). To ensure only mono-alkylation occurred, cyclen was used in a 10 fold excess and mild reaction conditions were employed. The purification was very simple; the crude product was extracted into CH_2Cl_2 and then washed repeatedly with water to remove the unreacted cyclen.

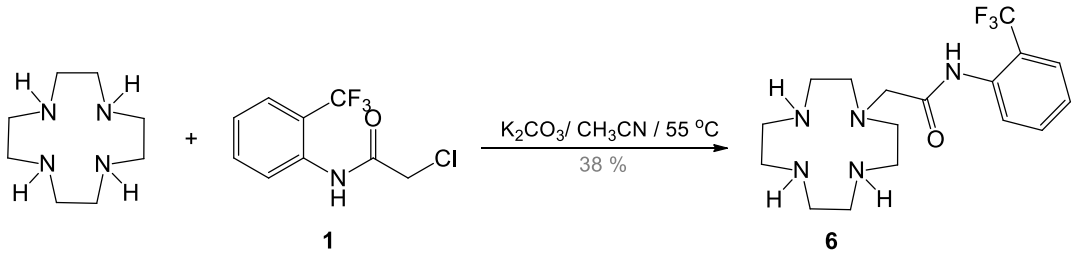

Scheme 3.2

The bromination and subsequent esterification of (*S*)-glutaric acid monomethyl ester was achieved *in situ* (Scheme 3.3).

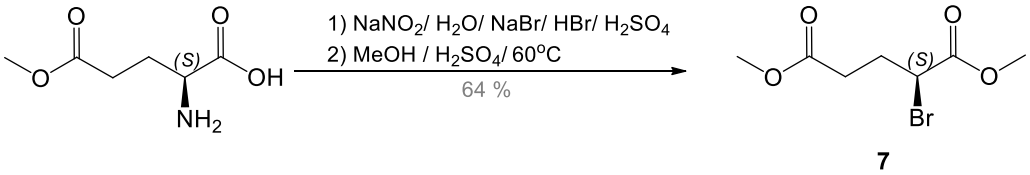

Scheme 3.3

Firstly, the diazotization of the amino group was accomplished by reaction with sodium nitrite, followed by treatment with hydrobromic acid in the presence of sodium bromide at -5 °C. It is hypothesized that the diazonium salt undergoes an intramolecular S_N2 reaction immediately after formation. This entails nucleophilic attack of the oxygen of the carboxylic acid onto the electrophilic carbon, followed by loss of a dinitrogen leaving group to yield a strained lactone ion (Scheme 3.4).

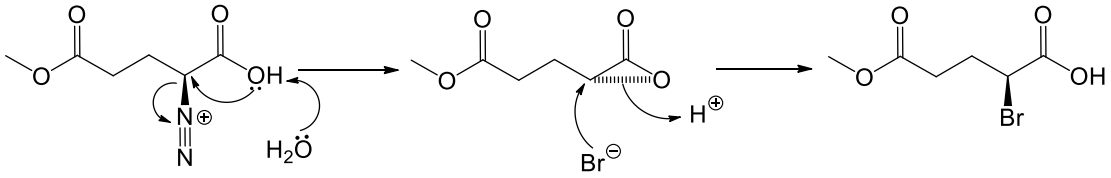

Scheme 3.4: Proposed double inversion mechanism in the bromination of (*S*)-glutaric acid monomethyl ester

Subsequent nucleophilic attack by bromide opens the ring resulting in the formation of the α-bromoacid, wherein the α-carbon possesses the same configuration as the starting material. The crude product was then stirred in anhydrous CH_3OH, in the presence of a catalytic amount of H_2SO_4, to yield the desired diester, **7**, in 64 % yield.

The subsequent alkylation of the three remaining secondary nitrogen atoms of the cyclen ring, **6**, with enantiomerically pure diester, **7**, was achieved under basic conditions, utilising KI as a catalyst (Scheme 3.5). The removal of the methyl ester groups was accomplished by treatment with KOD, thereby allowing for the reaction to be monitored by ^1H NMR. The crude product was purified by cation exchange column chromatography (DOWEX 50-W, 12 % NH_4OH dilution) to afford the desired ligand as its ammonium salt, $\mathbf{L^4}$.

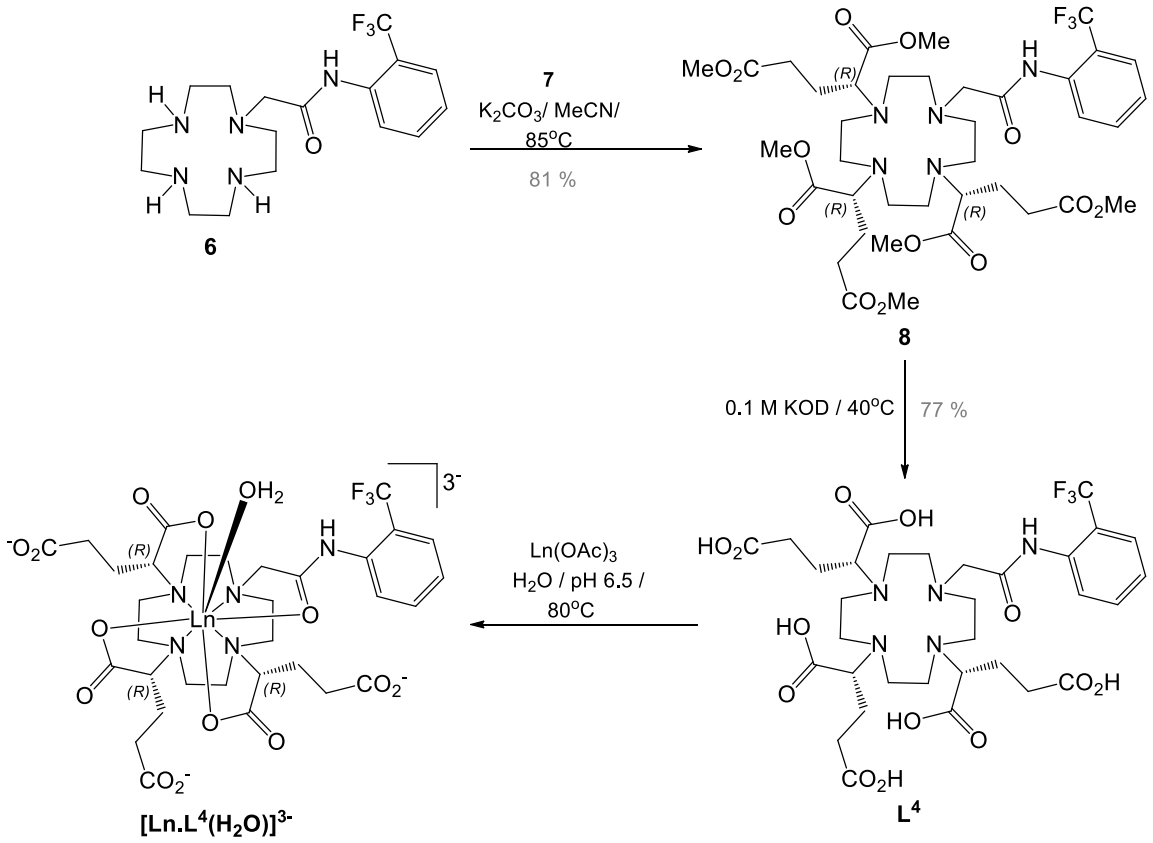

Scheme 3.5: Synthetic pathway to **[Ln.L^4(H$_2$O)]$^{3-}$**

The corresponding complexes, **[Ln.L^4(H$_2$O)]$^{3-}$**, were prepared using an aqueous solution of the appropriate metal acetate (pH 6.5, 85 ^{o}C), and purified as potassium salts by dialysis.

3.2.2 Synthesis of [Ln.L^5]

The preparation of **L^5** began with the condensation of the mono-alkylated macrocyle, **6**, with paraformaldehyde to yield an imine which was trapped by reaction with diethoxymethylphoshine (Scheme 3.6). An Arbuzov rearrangement gave the triethylphosphinate ester, **9**, as a mixture of stereoisomers differing in configuration at each stereogenic P centre. Subsequent base hydrolysis afforded the chiral ligand, **L^5**.

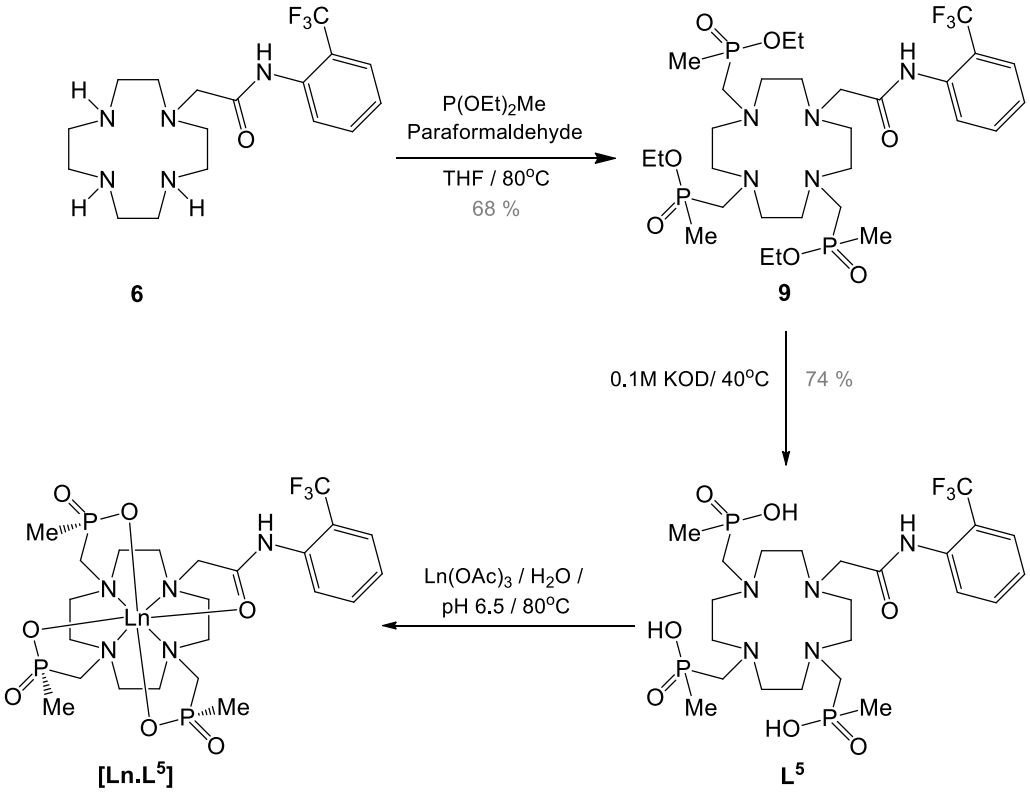

Scheme 3.6: Synthetic Pathway to **[Ln.L^5]**

Metal complexation was achieved using an aqueous solution of the appropriate metal acetate (pH 6.5, 85 ^{o}C), and the resultant complex purified by short-path chromatography on neutral alumina.

3.2.3 Synthesis of [Ln.L^6]

The formation of the desired fluorinated quinoline, **10**, was achieved *via* a classic Skraup synthesis of the *meta*-substituted aniline with crotonaldehyde, with the resulting product purified by silica gel column chromatography (Scheme 3.7). Subsequent bromination was accomplished by reaction of **10** with *N*-bromosuccinimide in carbon tetrachloride, utilising benzoyl peroxide as the radical initiator. Unfortunately, both the mono- and di-brominated products, **11** and **12**, were formed (2:1 respectively). However, separation of the desired product was readily achieved *via* silica gel column chromatography. Moreover, **12** can easily be transformed back to the mono-brominated compound, **11,** in a high yielding reaction (89 %).

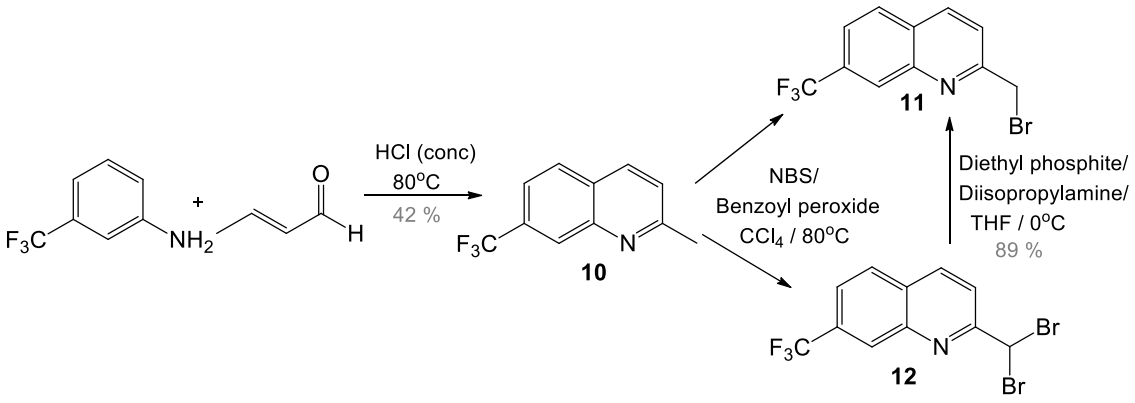

Scheme 3.7

Selective mono-alkylation of cyclen with the fluorinated quinoline, **11**, was first attempted under basic conditions (K_2CO_3, CH_3CN, 55 °C). Unfortunately di- and tri-alkylation also occurred, even when using cyclen in a 15 fold excess and maintaining the reaction temperature at 20 °C (Scheme 3.8). Purification at this stage was not possible. Thus, co-condensation of the mixture of amines with paraformaldehyde and diethoxymethylphosphine in THF afforded the corresponding phosphinate esters.

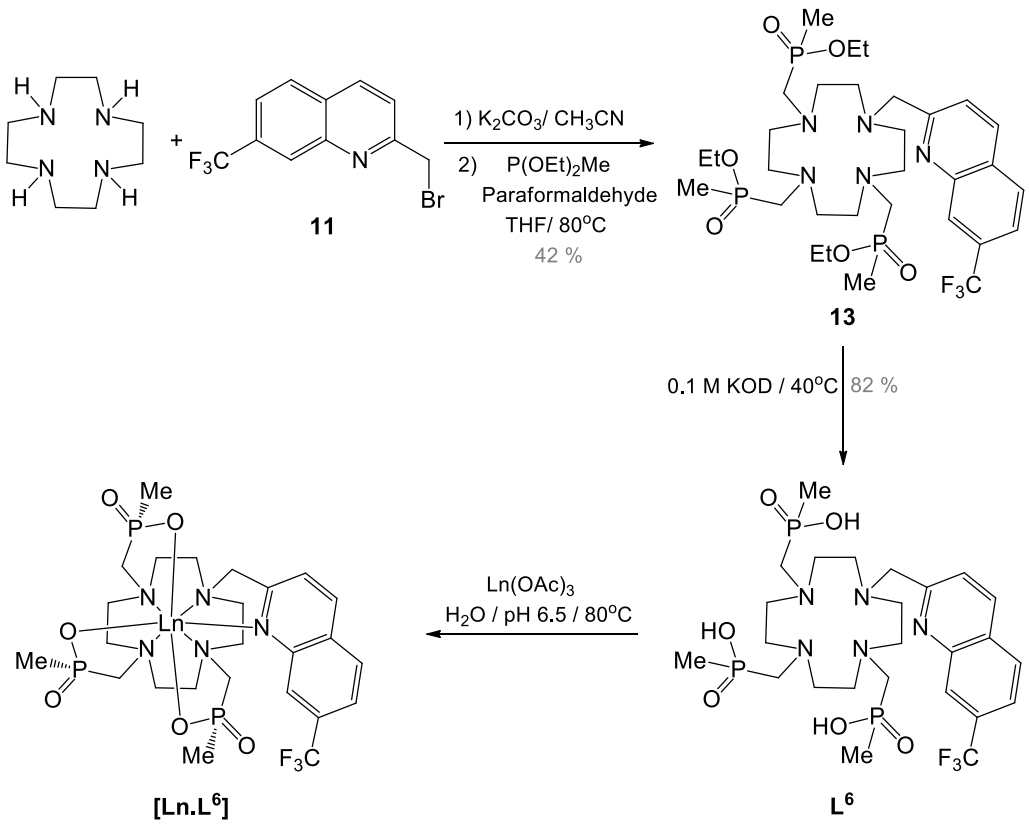

Scheme 3.8: Synthetic Pathway to [Ln.L^6]

Isolation of the desired triphosphinate ester **13**, as a mixture of stereoisomers, was achieved by silica gel column chromatography in 42 % overall yield. Subsequent base hydrolysis and complexation followed the same procedure as described for [Ln.L^5].

3.2.4 Synthesis of [Ln.$L^{7a}(H_2O)]^-$

The initial step in the preparation of L^{7a} involved the preparation of the racemic dimethyl α-bromoglutarate, **14**, *via* a Hell-Volhardt-Zelinski reaction (Scheme 3.9). Molecular bromine was added dropwise to a solution of the acid chloride, derived from the starting (±) glutaric acid mono-methyl ester, and after 3 hours the reaction was quenched by the addition of methanol at 0°C.[5] The product was separated from the undesired 2,4-dibromodimethylglutarate by distillation under reduced pressure, using a long Vigreux column.

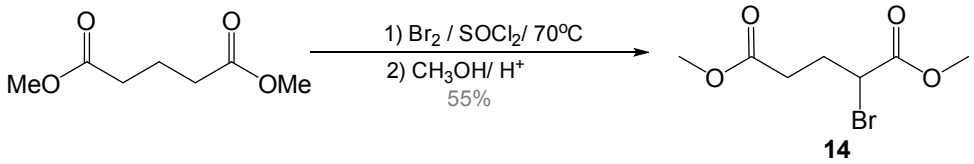

Scheme 3.9

Subsequent alkylation of cyclen with the racemic dimethyl-α-bromoglutarate, **14**, under mildly basic conditions, gave a combination of the di- and tri-substituted products (Scheme 3.10). The di-alkylated macrocyle, **15**, purified by silica gel chromatography, was isolated as a mixture of diastereoisomers.[6] The low yield achieved (29 %) could possibly be increased by lowering the reaction temperature and reducing the quantity and strength of base added, thereby reducing the amount of tri-alkylated species formed.

The alkylation, base hydrolysis and complexation, was achieved in a similar fashion to that described for L^4.

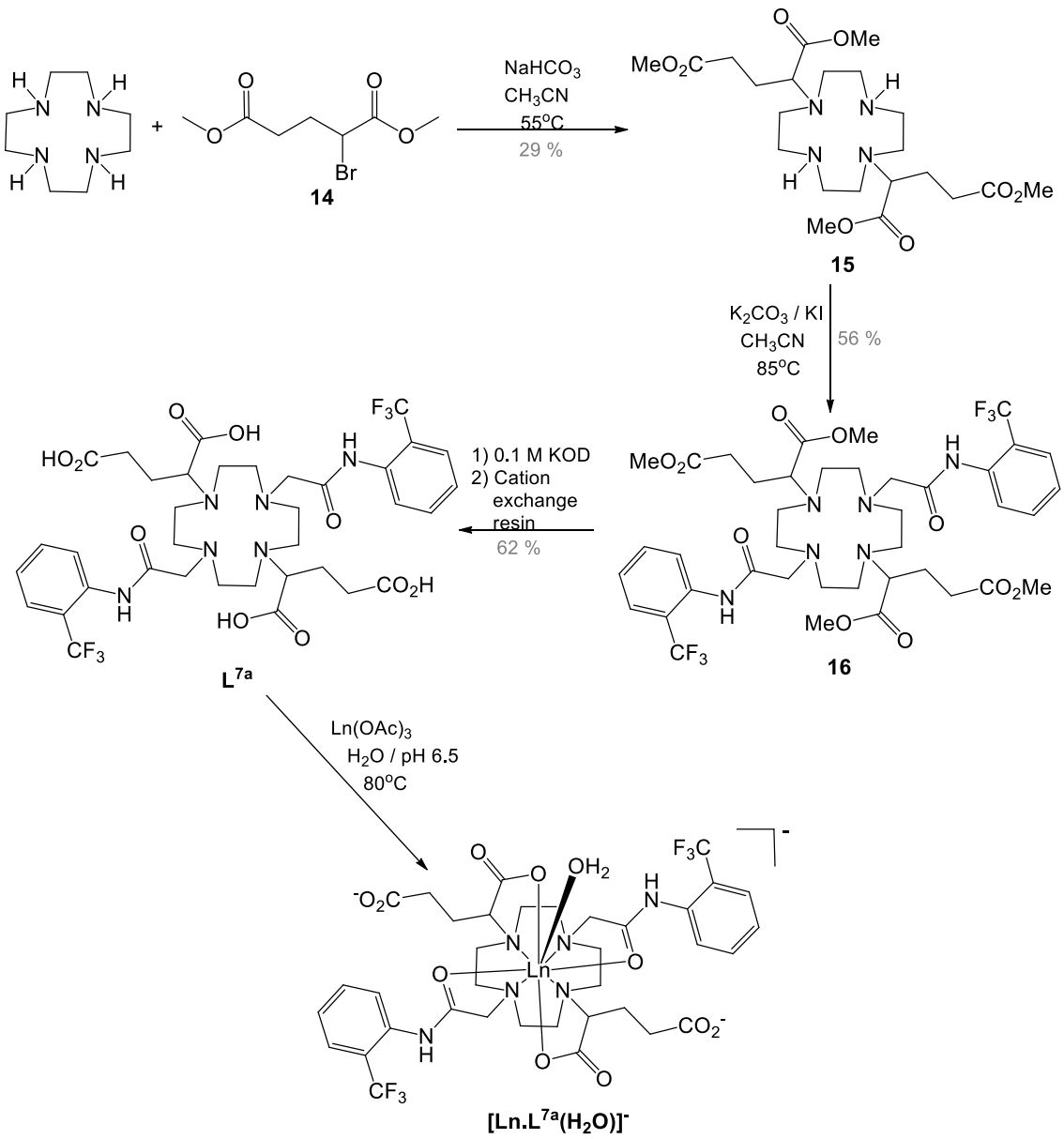

Scheme 3.10: Synthetic Pathway to **[Ln.L^{7a}(H$_2$O)]$^-$**

3.2.5 Synthesis of [Ln.L^{7b}(H$_2$O)]$^-$

Owing to the low yield achieved in the synthesis of the bis-alkylated cyclen **15**, in the preparation of **L^{7a}**, a different approach was taken in the synthesis of **L^{8a}**. Direct alkylation of cyclen with **1**, under anhydrous conditions, allowed the isolation of the 1,7-disubstituted fluorinated diamine **17**, in 37 % yield (Scheme 3.11). The constitution of the C_2 symmetry was verified by ^{13}C NMR spectroscopic analysis as only two cyclen ring CH_2N resonances were observed (δ_c 45.1 and 51.9 ppm).

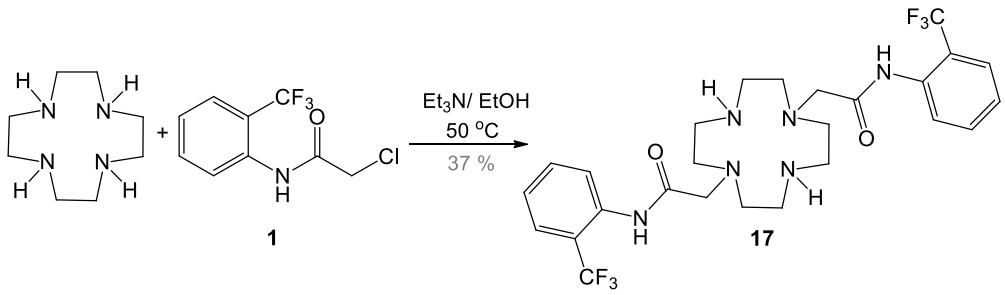

Scheme 3.11

Alkylation of **17** with dimethyl (*S*)-2-bromoglutarate, **7**, under basic conditions gave the corresponding diester, **18** (Scheme 3.12). Removal of the methyl ester groups yielded the ligand $\mathbf{L^{7b}}$, following treatment with cation exchange resin. ^{1}H, ^{13}C and ^{19}F NMR spectroscopic analysis confirmed the presence of the (*RR*)-enantiomeric product (δ_F = - 62.0 ppm, pD 5.4, D_2O). Conversely, analysis of the ligand $\mathbf{L^{7a}}$ by ^{19}F NMR spectroscopy gave spectral data consistent with a mixture of diastereoisomers (δ_F = - 61.4 and – 61.1 ppm, pD 5.4, D_2O).

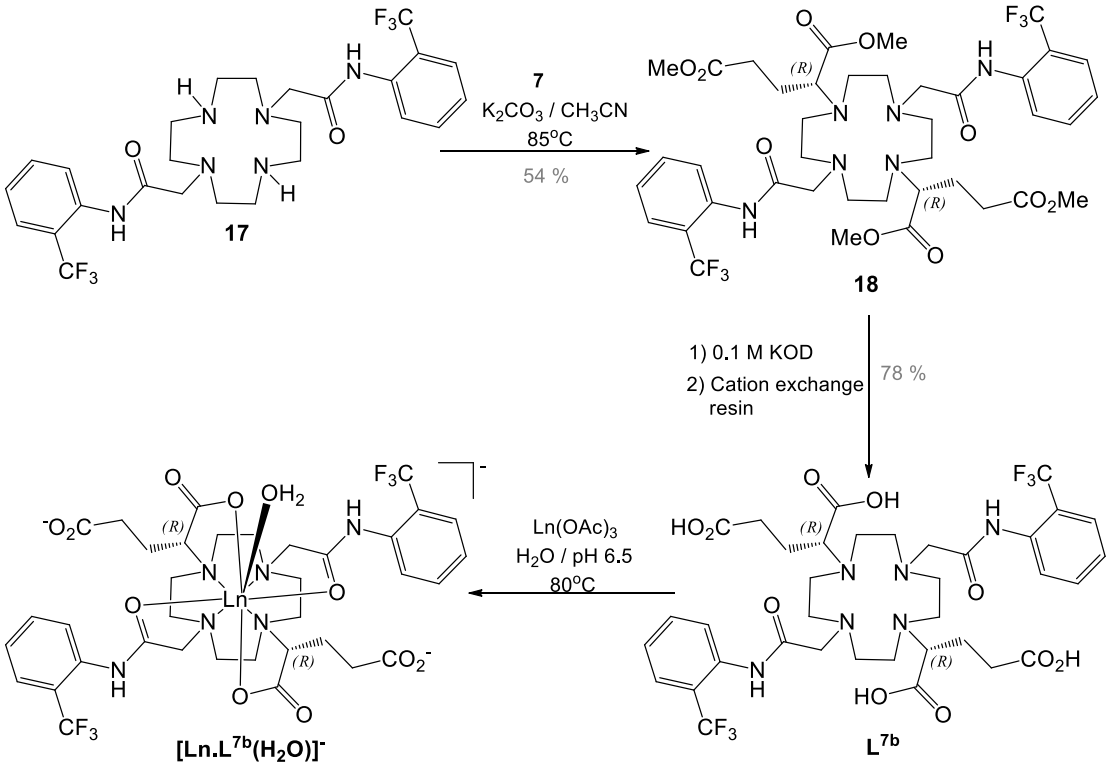

Scheme 3.12

3.2.6 Synthesis of $[Ln.L^8(H_2O)]^+$

Firstly, the *trans*-protected cyclen, **19**, was formed following the literature method *via* the reaction of benzylchloroformate with cyclen (Scheme 3.13).[7] The following alkylation reaction at each secondary nitrogen atom of the cyclen ring with *tert*-butyl bromoacetate proceeded in good yield.[8]

The removal of the carbamate protecting groups was achieved *via* hydrogenation, utilising $Pd(OH)_2/C$ as the catalyst.[8] The synthesis of the *trans*-ester was not attempted in one step because mono- and tri-ester derivatives would also be formed, and the mixture of products would not be amenable to purification by chromatography. Moreover, it would be extremely difficult to ensure that the reaction yielded no *cis*-ester.

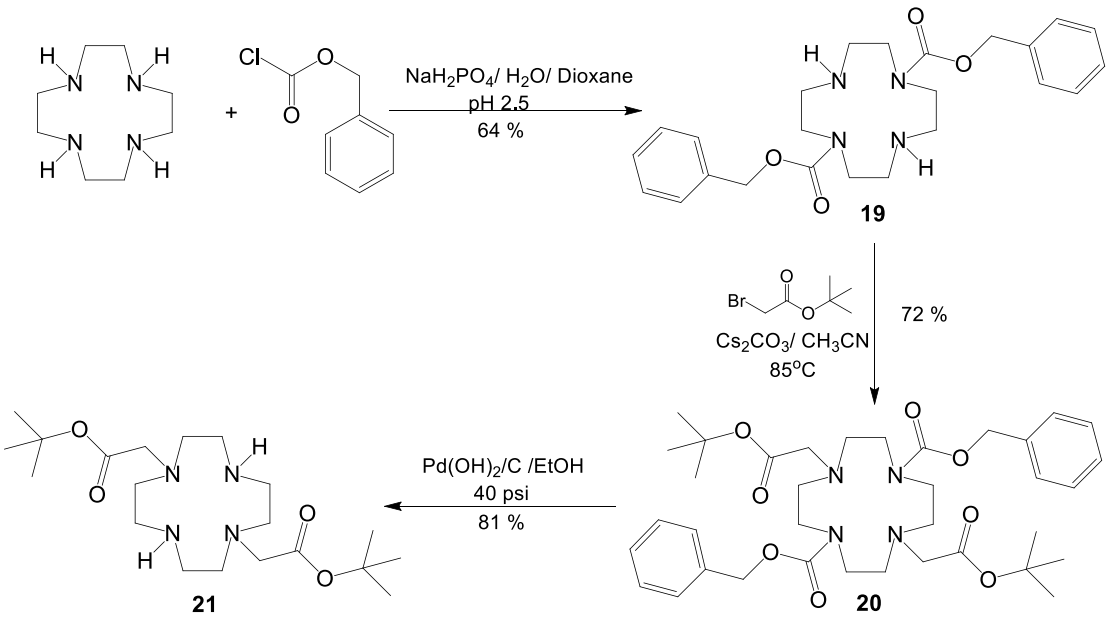

Scheme 3.13

The dialkylation of the cyclen ring, **21**, followed the procedure noted for $\mathbf{L^4}$ (Scheme 3.14). Subsequent treatment with trifluoroacetic acid in CH_2Cl_2 afforded the protonated ligand, $\mathbf{L^8}$, which was then mixed with a slight excess of the appropriate $Ln(OAc)_3$ salt in water (pH 6.5) to yield the crude complex. The desired monocationic complexes, $\mathbf{[Ln.L^8(H_2O)]^+}$, were isolated as chloride salts, following anion exchange chromatography (DOWEX, pre-treated with 1M HCl).

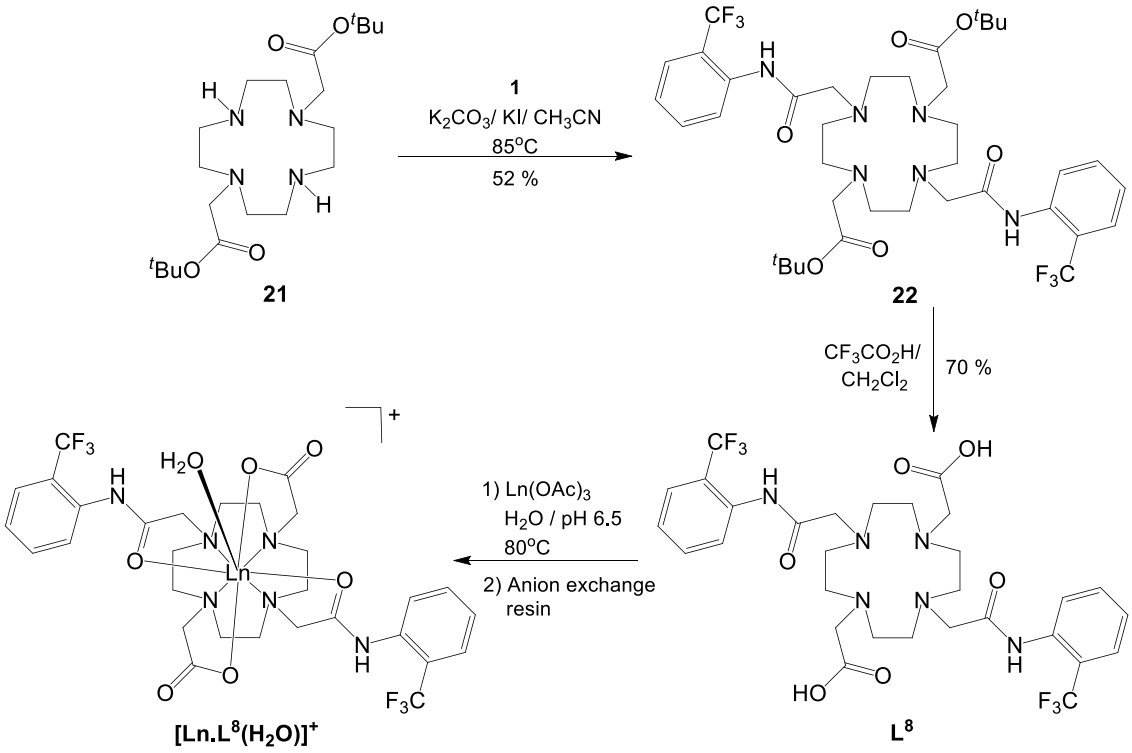

Scheme 3.14

3.2.7 Estimation of Complex Hydration State

For each Tb complex of $\mathbf{L^4}$- $\mathbf{L^8}$ the hydration state, q, was measured by a luminescence method, examining the radiative rate constants in H_2O and D_2O associated with the decay of the ΔJ = -1 transition at 545 nm (theory explained in section 2.3.1).

Complex	k_{H2O}	k_{D2O}	q'
$[Tb.L^4(H_2O)]^{3-}$	0.59	0.35	0.90
$[Tb.L^5]$	0.32	0.28	0
$[Tb.L^6]$	0.37	0.28	0.15
$[Tb.L^{7a}(H_2O)]^-$	0.58	0.34	0.90
$[Tb.L^{7b}(H_2O)]^-$	0.56	0.31	0.95
$[Tb.L^8(H_2O)]^+$	0.56	0.32	0.90

Table 3.1: Lifetime measurements of Tb complexes of $\mathbf{L^4}$-$\mathbf{L^8}$ in H_2O and D_2O, including calculation of hydration number; k values have a 10% error and values of q are ± 20 %.

Results show that all complexes incorporating carboxylate or glutarate donor pendant arms possess one coordinated water molecule (Table 3.1). Conversely, phosphinate complexes each have a q value of zero, owing to the more sterically demanding nature of these pendant arms.

3.3 ^{19}F Spectroscopic Properties

For each complex incorporating glutarate donor pendant arms (*i.e* complexes of **L^{4}**, **L^{7a}** and **L^{7b}**), ^{19}F NMR spectroscopy revealed the presence of a mixture of species, whose relative abundance varied from one Ln to another (Table 3.2). In contrast with complexes of **L^{3}**, the relative composition of isomeric species in solution changed neither with time, nor with pH over the range 4 to 8.

Complex	δ_F / ppm	% Major species	No. of minor species
$[Tb.L^{4}(H_2O)]^{3-}$	-59.1	41	7
$[Er.L^{4}(H_2O)]^{3-}$	-63.5	59	3
$[Tm.L^{4}(H_2O)]^{3-}$	-73.9	60	4
$[Tb.L^{7a}(H_2O)]^{-}$	-58.9	58	3
$[Tm.L^{7a}(H_2O)]^{-}$	-76.4	52	4
$[Tb.L^{7b}(H_2O)]^{-}$	-62.1	88	1
$[Er.L^{7b}(H_2O)]^{-}$	-64.3	63	4
$[Tm.L^{7b}(H_2O)]^{-}$	-78.4	40	5

Table 3.2: ^{19}F NMR chemical shift data for selected complexes of L^{4}, L^{7a} and L^{7b} (2 mM, D_2O, 295 K, pD = 5.4, 4.7 T).

With $[Tm.L^{7b}(H_2O)]^{-}$, six different resonances were observed, with the major species comprising only 42 % of the total signal intensity, whereas with $[Tb.L^{7b}(H_2O)]^{-}$ only two resonances were observed, and the dominant species comprised 88% of the observed signal intensity. Interestingly, the major resonance observed by ^{19}F NMR spectroscopy for $[Tb.L^{7b}(H_2O)]^{-}$ was only minimally shifted with respect to the hydrolysed ligand, **L^{7b}**(< 1 ppm). Initially, this was assumed to be unreacted ligand. However ^{1}H NMR spectroscopic studies showed the presence of paramagnetically

shifted macrocyclic ring protons. Furthermore, HPLC analysis revealed the absence of any free ligand, and $ESMS^+$ data clearly demonstrated that the complex had formed. From equation 3.1, it is apparent that it is not only the Bleaney constant, C_J, and the distance of the fluorine nuclei to the metal centre, r, which determines the dipolar shift but also the angle of the fluorine nuclei with respect to the principal axis, θ. If this angle is close to 54^o then the $((3\cos^2\theta - 1) / r^3)$ term tends to zero and the resulting dipolar shift is noticeably reduced. This could suggest a reason for the unexpectedly small shifted resonance observed by ^{19}F NMR spectroscopy for $[Tb.L^{7b}(H_2O)]^-$ with respect to **L^{7b}**.

$$\delta_{dip} = C_J \frac{\beta^2}{60(kT)^2} \frac{(3\cos^2\theta - 1)}{r^3} B_0^2 \qquad (3.1)$$

As suggested earlier, replacing the carboxylate donor group in **L^3** with a more sterically demanding group, such as a phosphinate, could slow down the dynamic processes that lead to exchange broadening in solution. Such complexes have an additional element of chirality introduced upon complexation, giving rise to the possibility of differing configurations at each phosphorus centre (Figure 3.3).

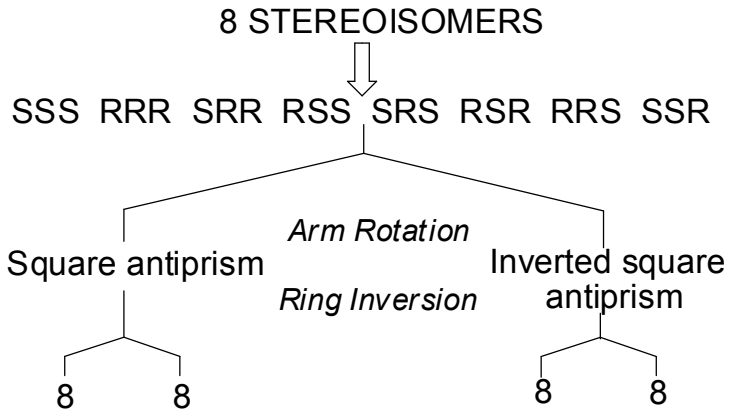

Figure 3.3: Stereoisomers of **[Ln.L^5]** and **[LnL^6]**

This results in the possible formation of 32 isomers, 16 of which will be enantiomeric pairs. Previous studies have shown that a low-energy common configuration is favoured in solution, wherein the configuration at P is the same, *i.e.* the (*RRR*) or (*SSS*) configuration.[4, 9] With complexes of **L^5** there is an added element of chirality

introduced by the dissymmetry presented by the *ortho*-substituted aryl substituent on the coordinated amide N. This can be thought of as placing the CF_3 moiety '*cis*' or '*trans*' with respect to the coordinated amide oxygen (Figure 3.4). Consequently this results in the possible formation of two isomers, arising from the rotation around the CN bond, and yields the feasibility of 64 isomers overall.

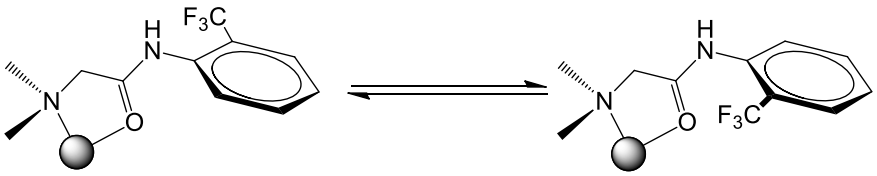

Figure 3.4: Schematic representation of the two isomers of **[Ln.L^5]** arising from the rotation of the aromatic ring around the CN bond.

Evidently, with complexes of **L^5** one low-energy conformation is preferred, as demonstrated by ^{19}F NMR spectroscopy; no pH or time variation in the spectrum was observed (Figure 3.5).

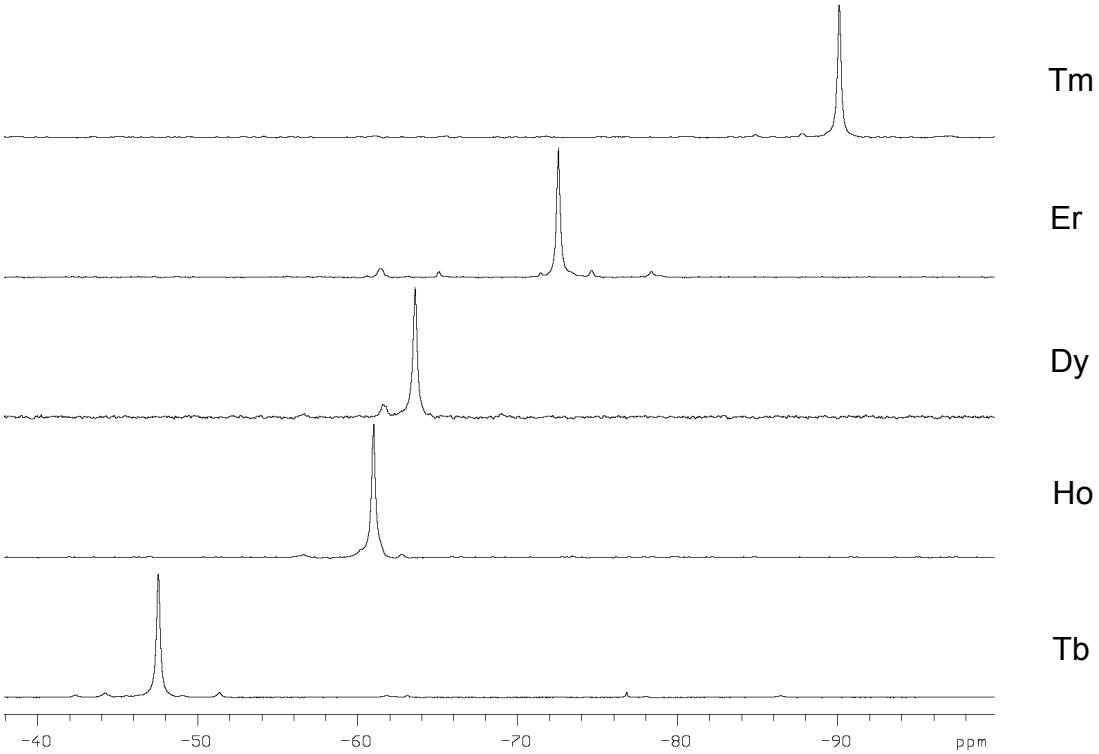

Figure 3.5: ^{19}F NMR spectra of [Ln.L^5] (2 mM, D_2O, 295 K, pD = 5.4, 9.4 T, where Ln = Tb, Dy, Ho, Er and Tm), showing the presence of one major species in each case.

It is thought that line-broadening associated with dynamic intramolecular conformational exchange processes is minimised, owing to the bulkiness of the phosphinate moiety, which inhibits cooperative arm rotation in this system. To probe this aspect further, variable temperature ^{19}F NMR spectroscopic analyses were undertaken, comparing the behaviour of the Tm and Ho complexes of **L^3** and **L^5**, over the temperature range of 278- 323 K (2mM, D_2O, pD 5.4, 11.7 T).

$$\Delta_p = \frac{C_J \mu_B{}^2}{60k^2T^2}\left[\frac{\langle r^2\rangle A(3\cos^2\theta - 1)}{r^3} + \frac{\langle r^2\rangle A'\sin^2\theta\cos 2\varphi}{r^3}\right] \qquad (3.2)$$

As expected, from equation 3.2, each complex displayed a linear variation of the ^{19}F chemical shift with the inverse of the second power of the absolute temperature (Figure 3.6).

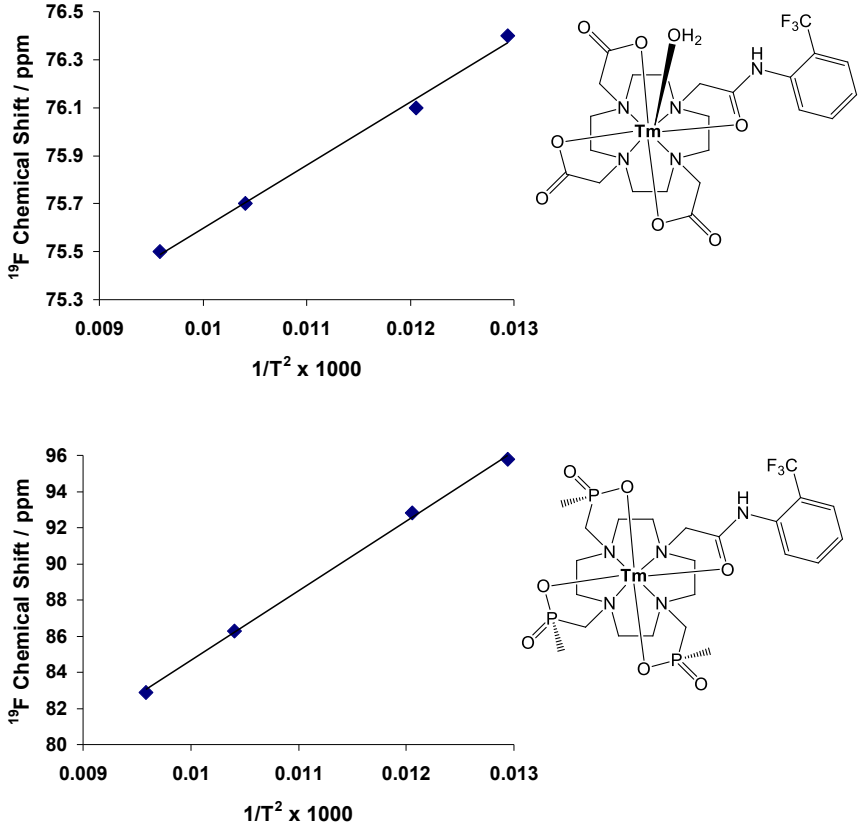

Figure 3.6: Linear variation of the observed ^{19}F shift of [Tm.L^3(H_2O)] and [Tm.L^5] as a function of T^2 from 278 to 328 K (2 mM, D_2O, pD 5.4, 11.7 T).

The measured linewidth of [Ho.L^5] was 80 Hz at 288 K, which increased to 120 Hz at both 310 and 323 K. In contrast, the measured linewidth of [Ho.$L^3(H_2O)$] was 260 Hz, which increased to 700 and then 1000 Hz at 310 and 323 K respectively. The resonances of the minor species in [Ho.$L^3(H_2O)$] were also broadened and shifted towards the major resonance, although they did not reach coalescence. This behaviour suggests that the excessive broadening observed in complexes of L^3 may be ascribed, at least in part, to dynamic exchange associated with stereoisomer interconversion. Furthermore, the data indicates that the complexes of L^5 have enhanced stereochemical rigidity on the NMR timescale, in comparison to their carboxylate counterparts.

The Tb and Tm complexes of **L^6** gave rather different behaviour to each other. Both complexes formed predominantly one species in solution, as confirmed by ^{19}F and ^{1}H NMR analysis. Whilst the ^{19}F resonance of the Tb complex was considerably shifted with respect to the hydrolysed ligand ([Tb.L^6] δ_F = -180.2 ppm and L^6 δ_F = -62.3 ppm, pD 5.4, 295 K) the Tm complex was hardly shifted at all ([Tm.L^6] δ_F = -62.8 ppm). This suggests either that the N atom on the fluorinated quinoline is coordinated to the Ln^{3+} ion in the Tb complex but is not bound in the Tm analogue, or that there is a different coordination environment present in the Tm complex that places the CF_3 moiety at a very different angle with respect to the principal axis from that observed with Tb analogue. This yields two separate structures, in which each is characterised by the differing positions of the CF_3 moiety with respect to the principal axis, presumably caused by the small differences in ionic radii of the two lanthanides.

The Tb, Dy, Ho, Er and Tm complexes of **L^8** each formed one predominant species (75 – 85 %) in aqueous solution, as indicated by ^{19}F NMR spectroscopic analysis. In each case, pH and time-dependent variation of the relative composition of isomeric species was not observed. Again, the major species of [Tb.$L^8(H_2O)]^+$ was only marginally shifted with respect to the hydrolysed ligand ([Tb.$L^8(H_2O)]^+$ δ_F = -62.0 ppm and L^8 δ_F = -61.3 ppm, pD 5.4, 295 K). To further our understanding of this

result, calculated DFT structures of $[Tb.L^{8}(H_2O)]^{+}$ were generated, in collaboration with Dr Ilya Kuprov of Oxford University (Figure 3.7).

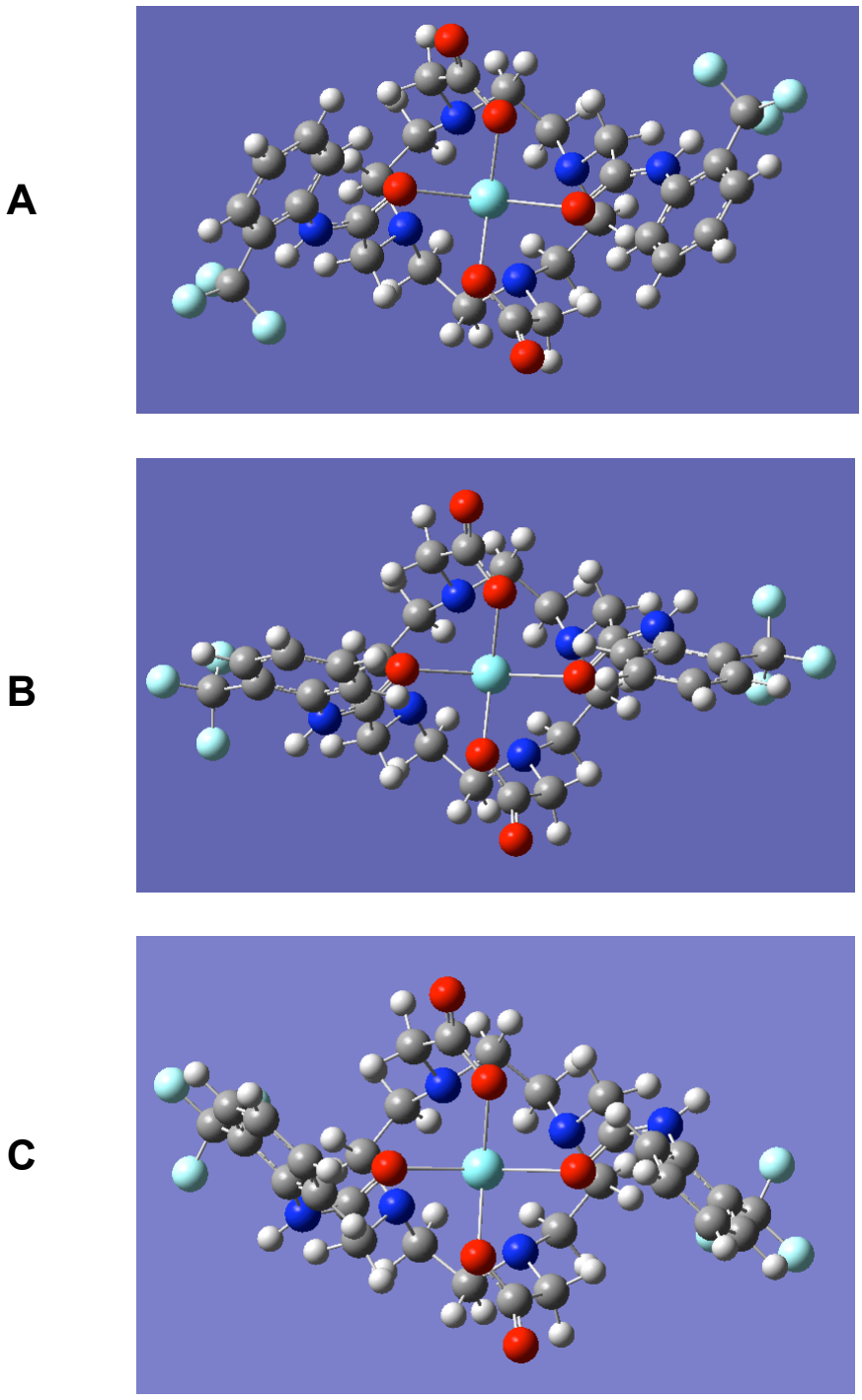

Figure 3.7: DFT calculated structures of $[Tb.L^{8}(H_2O)]^{+}$ with three different phenyl ring arrangements. Calculated distances between the metal and the CF_3 group A) r_{Ln-F} = 6.32 Å, B) r_{Ln-F} = 7.07 Å and C) r_{Ln-F} = 7.14 Å

Three different phenyl ring arrangements were identified in low energy structures, resulting in Tb to fluorine distances, $r_{Ln\text{-}F,}$ of 6.32, 7.07 and 7.14 Å. Interestingly, each arrangement had near identical energies. The calculated structures illustrate the possibility of differing positions of the CF_3 group with respect to Tb^{3+} ion, each of which will have a profound effect on the observed ^{19}F chemical shift.

Whilst there is an obvious improvement in spectral features when compared with complexes of **L^3**, the most suitable system for suppression of dynamic processes is that based on **L^5**, as illustrated in figure 3.8.

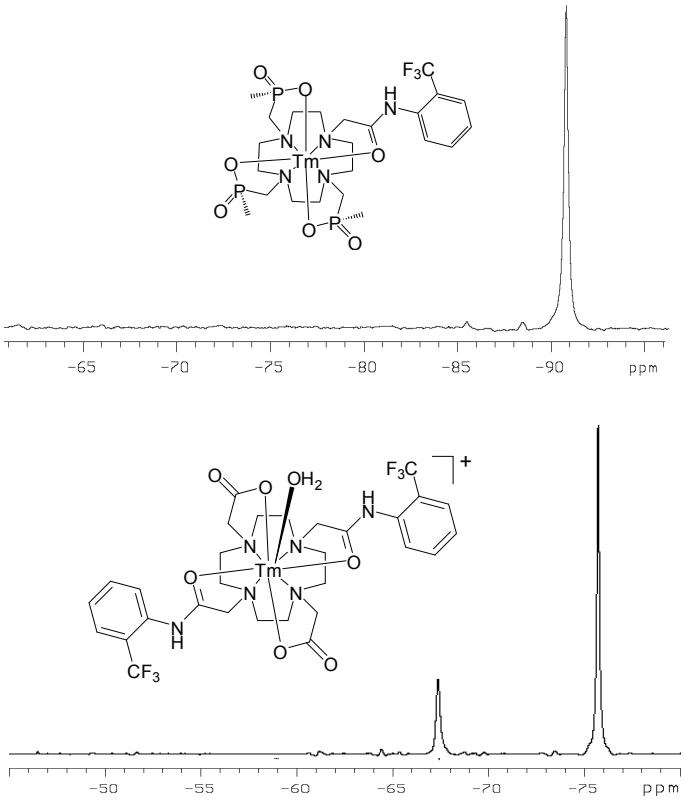

Figure 3.8: ^{19}F NMR spectra of **[Tm.L^5]** (upper) and **[Tm.L^8(H$_2$O)]$^+$** (lower) (2mM, D_2O, pD 5.4, 295 K, 9.4 T).

3.4 ^{19}F Relaxation Analysis

In accordance with the ^{19}F relaxation theory discussed in chapter two, the relaxation rates measured for the series of complexes of **L^4** broadly follow the order of Tb> Er> Tm, consistent with the dependence on μ_{eff} and τ_{1e} terms (Table 3.3).

	R_1/ Hz		R_2 / Hz	
Complex	4.7 T	9.4 T	4.7 T	9.4 T
$[Tb.L^4(H_2O)]^{3-}$	64	98	104	283
$[Er.L^4(H_2O)]^{3-}$	45	80	87	109
$[Tm.L^4(H_2O)]^{3-}$	28	72	72	98

Table 3.3: ^{19}F Longitudinal and transverse relaxation data for $[Ln.L^4(H_2O)]^{3-}$ at 4.7 and 9.4 T (2 mM, D_2O, pD 5.4, 295 K).

A similar account is true for complexes of **L^{7a}** and **L^{7b}** (Table 3.4). The only exception to this is the markedly lower R_1 and R_2 value measured for the most dominant isomer of $[Ln.L^{7b}(H_2O)]^-$. In contrast, the minor isomer, which accounts for approximately 12% of the total signal intensity, has a much higher R_1 value (R_1 of 94/168 Hz at 4.7/ 9.4 T respectively). This could possibly be attributed to the two differing positions of the CF_3 moiety with respect to the principle axis, as discussed in section 3.3.

	R_1/ Hz		R_2 / Hz	
Complex	4.7 T	9.4 T	4.7 T	9.4 T
$[Tb.L^{7a}(H_2O)]^-$	70	101	75	153
$[Tm.L^{7a}(H_2O)]^-$	22	67	72	98
$[Tb.L^{7b}(H_2O)]^-$	9.4	12.2	19	34
$[Er.L^{7b}(H_2O)]^-$	38	76	92	151
$[Tm.L^{7b}(H_2O)]^-$	27	65	82	96

Table 3.4: ^{19}F Longitudinal and transverse relaxation data for $[Ln.L^{7a}(H_2O)]^-$ and $[Ln.L^{7b}(H_2O)]^-$ at 4.7 and 9.4 T (2 mM, D_2O, pD 5.4, 295 K).

The Tm and Tb complexes of **L^6** give rather different behaviour to each other, as expected by their differing structures (section 3.3). The Tb complex reveals very fast relaxation coupled with a relatively narrow line (Tables 3.5). This suggests that incorporation of the quinoline group has helped to prevent arm rotation, in addition to the shortening of the mean distance, r, between the Tb^{3+} ion and the CF_3 moiety (with respect to $[Tb.L^3(H_2O)]$). Conversely, with $[Tm.L^6]$, where the fluorine nuclei must be at a differing angle to the principal axis than with the Tb analogue,

relaxation rates similar to [Tm.L^3(H_2O)] are observed and so the mean distance, r, must also be similar.

	[Tb.L^6]		[Tm.L^6]	
Complex	R_1/ Hz	R_2/ Hz	R_1/ Hz	R_2/ Hz
4.7 T	112	162	23	52
9.4 T	142	186	48	74
11.7 T	181	248	59	89
16.5 T	238	309	72	107

Table 3.5: ^{19}F Longitudinal and transverse relaxation data for [Ln.L^6] at 4.7, 9.4, 11.7 and 16.5 T (2 mM, D_2O, pD 5.4, 295 K).

When comparing the complexes of **L^8** and **L^3**, the R_1 and R_2 data measured were generally very similar for a given Ln^{3+} ion (Table 3.6). This is indicative of a mean similar distance, r_{Ln-F}, between the Ln^{3+} centre and the CF_3 group. The exception to this is with [Tb.L^8(H_2O)]$^+$, where the r_{Ln-F} must be greater (section 3.3) and thus R_1 and R_2 values are significantly smaller.

	R_1/ Hz		R_2 / Hz	
Complex	4.7 T	9.4 T	4.7 T	9.4 T
[Tb.L^8(H_2O)]$^+$	1.7	2.8	41	132
[Dy.L^8(H_2O)]$^+$	92	1158	96	213
[Ho.L^8(H_2O)]$^+$	47	91	72	159
[Er.L^8(H_2O)]$^+$	33	81	78	164
[Tm.L^8(H_2O)]$^+$	24	56	84	102
[Y.L^8(H_2O)]$^+$	1.4	1.4	3.2	3.1

Table 3.6: ^{19}F Longitudinal and transverse relaxation data for [Ln.L^8(H_2O)]$^+$ at 4.7 and 9.4 T (2 mM, D_2O, pD 5.4, 295 K).

Faster rates of longitudinal relaxation were measured for [Ln.L^5] in comparison with [Ln.L^3(H_2O)] which is consistent with a shorter r_{Ln-F}. As discussed in section 2.6.2, the variation of R with r follows an r^{-6} relationship, and so this distance can be calculated by measuring the paramagnetic rate of relaxation as a function of field (calculated to

be 6.3 Å for [Ln.L^3(H_2O)]). If it is assumed that the difference in R_1 values is solely due to a variation in r_{Ln-F} then the distance for [Ln.L^5] can also be estimated. A mean value for r_{Ln-F} of 6.0 Å (± 0.1) was calculated from the R_1 data measured for each complex of L^5 (Table 3.7). It is unsurprising that the 8-coordinate phosphinate complexes are more compact than their 9-coodinate carboxylate counterparts, and this is consistent with the reported X-ray structural analyses of related systems. [3, 4, 10]

	R_1/ Hz		R_2 / Hz	
Complex	4.7 T	9.4 T	4.7 T	9.4 T
[Tb.L^5]	84	146	102	267
[Dy.L^5]	104	185	135	251
[Ho.L^5]	58	120	74	143
[Er.L^5]	71	109	67	138
[Tm.L^5]	46	63	60	84
[Y.L^5]*	1.2	1.3	10	16

Table 3.7: ^{19}F Longitudinal and transverse relaxation data for [Ln.L^5] at 4.7 and 9.4 T (2mM, D_2O, pD 5.4, 295 K). **Note: For [Y.L^5], the T^2 values quoted are T^2* data, as there is evidence for dynamic exchange broadening , leading to an increased linewidth at higher T (323K) and the onset of appearance of more than one species.*

3.5 Proton Relaxation Properties of Gd^{3+} Complexes

Complexes of **L^5** and **L^6** have a q value of zero, as determined by analysis of the Tb emission decay lifetimes in H_2O and D_2O (section 3.2). From previous proton relaxometric studies of structurally related Gd^{3+} phosphinate systems, it can be safely be assumed that the relaxivity of both **L^5** and **L^6** systems will be inherently low (in the region of ~ 2 $mM^{-1}s^{-1}$) owing to the lack of an inner-sphere contribution.[9] For this reason, the Gd^{3+} complexes of L^5 and L^6 were not synthesised.

The proton relaxivity of [Gd.L^4(H_2O)]$^{3-}$ was found to be 5.9 $mM^{-1}s^{-1}$ (60 MHz, 310 K), and independent of pH (± 9 %) over the pH range 3.5 to 10.5. This is consistent with high kinetic stability with respect to acid-catalysed or base-promoted dissociation pathways.

For both $[Gd.L^{7b}(H_2O)]^-$ and $[Gd.L^{8}(H_2O)]^+$ variable temperature R_2/ ^{17}O measurements were undertaken, with Dr Mauro Botta, with 10 to 20 mM solutions of each complex in ^{17}O-enriched water, allowing for an estimate of the water exchange lifetime, τ_m, based on standard 'Swift-Connick' methodology (Figure 3.9).[11]

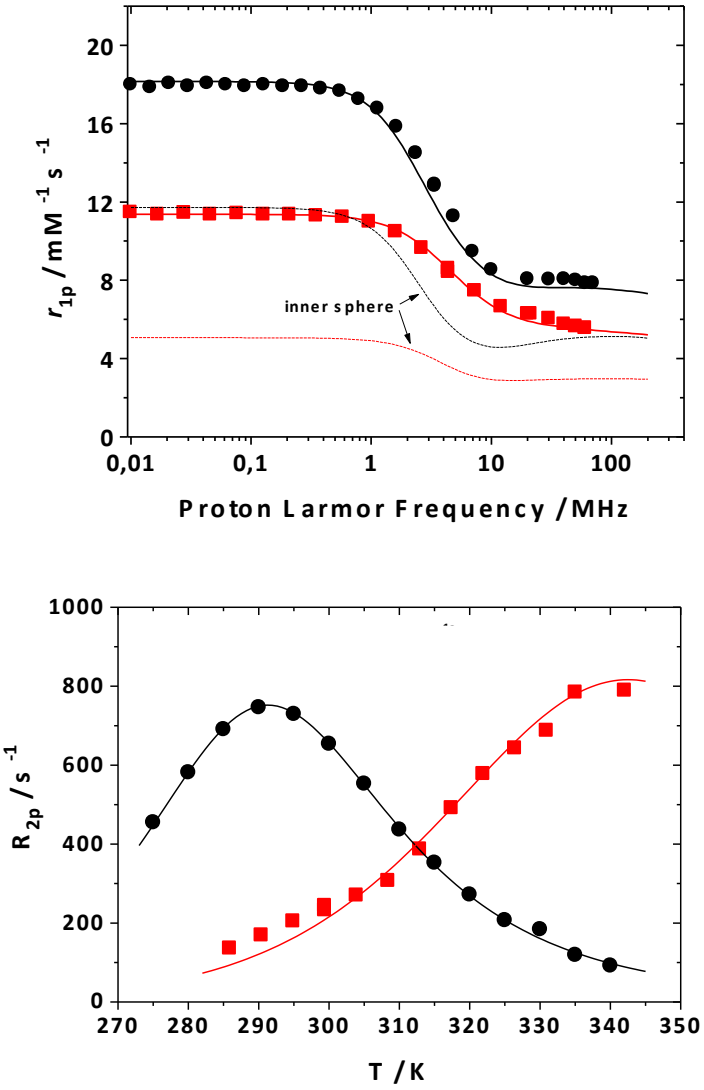

Figure 3.9: a) Upper: NMRD profiles (298K), showing the estimated inner sphere contributions; b) Lower: variation of the transverse ^{17}O relaxation rate R_{2p}, with temperature for $[Gd.L^{8}(H_2O)]^+$ in red (9.4 T) and $[Gd.L^{7b}(H_2O)]^-$ in black (11.7 T), scaled to 20 mM concentration.

The significantly longer τ_m value found for $[Gd.L^{8}(H_2O)]^+$ (1.7 µs versus 0.1 µs for $[Gd.L^{7b}(H_2O)]^-$) is attributed to the differing overall charge of the two ionic complexes, *i.e.* +1 (long τ_m) and -1 (short τ_m). This is also indicated in the different

values of the enthalpy ($\Delta H_m^{\#}$ = 42.0 and 50.3 kJ mol^{-1}) and entropy of activation associated with the water exchange process ($\Delta S_m^{\#}$ = +6.3 and +58.2 J mol^{-1} K^{-1}). The small value of ΔS_m found for [Gd.L^{8}(H$_2$O)]$^+$ is consistent with an interchange exchange mechanism, while the larger value calculated [Gd.L^{7b}(H$_2$O)]$^-$ is a sign of a dissociatively activated mechanism.[12]

Further information on both complexes was extracted by analysing the temperature dependence of r_{1p}, in addition to the classical analyses of the field dependence of relaxivity (0.01 to 70 MHz (Figure 3.9)). These analyses are based upon the Solomon-Bloembergen-Morgan equations which rationalise the time-dependence of the water proton-Gd^{3+} dipolar coupling, in addition to considering the contribution from the second sphere.[13]

The measured proton relaxivity of [Gd.L^{7b}(H$_2$O)]$^-$ and [Gd.L^{8}(H$_2$O)]$^+$ was 8.1 and 6.3 mM^{-1}s^{-1} respectively (298 K, 20 MHz). The higher relaxivity value for [Gd.L^{7b}(H$_2$O)]$^-$ correlates well with its longer rotational correlation time, its faster water exchange rate and the presence of a significant second sphere term. It is hypothesised that the presence of the proximate carboxylate groups may help to promote water exchange between inner and second sphere water molecules.

The variation of r_{1p} with pH was also undertaken for both complexes (60 MHz, 310 K (Figure 3.10)).

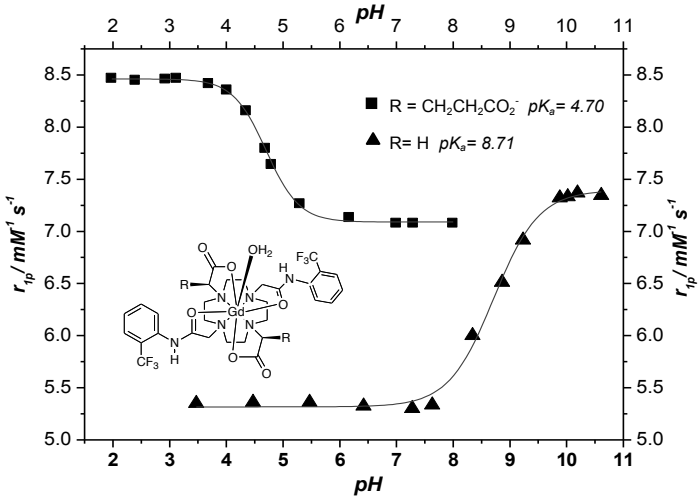

Figure 3.10: pH dependence of the ^{1}H relaxivity, r_{1p}, of [Gd.L^{8}(H$_2$O)]$^+$ and [Gd.L^{7b}(H$_2$O)]$^-$ showing the fit to the measured data, with p*Ka* = 4.70 (± 0.05) and 8.71 (± 0.05) (310K, 60 MHz, H$_2$O)

With $[Gd.L^{8}(H_2O)]^{+}$ the relaxivity increases by 30 % over the pH range 8 to 10. This can be ascribed to base catalysed prototopic exchange, associated with the deprotonation of the amide proton (p*K*a = 8.71 (± 0.05), as depicted in Figure 3.11.[14] It appears that the lanthanide ion acts as a charge sink, enhancing the acidity of the amide proton in the monocationic complex.

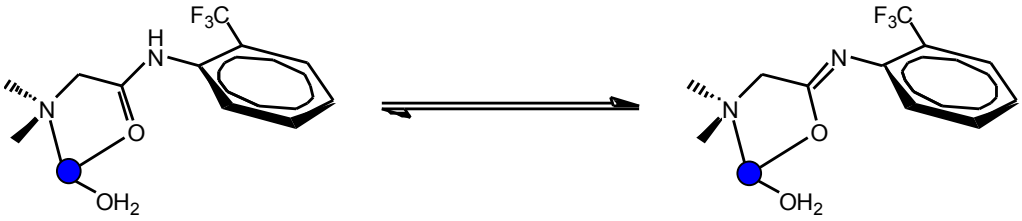

Figure 3.11: Acid-Base equilibrium between the protonated and non-protonated form of $[Gd.L^{8}(H_2O)]^{+}$.

With $[Gd.L^{7b}(H_2O)]^{-}$, a pH dependence of the measured r_{1p} was observed over the range of pH 4 to 5.5, resulting in an 18 % change in relaxivity (p*Ka* = 4.70 (±0.05), 310 K). At low pH, the carboxylate arm is protonated and therefore the second sphere contribution to relaxivity is high; the opposite is true at higher pH (Figure 3.12). Interestingly, such well-defined pH-modulation has not been reported previously for related complexes with pendant glutarate donors, such as $[Gd.gDOTA(H_2O)]^{5-}$.[2]

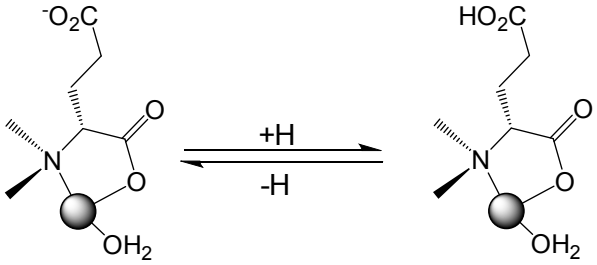

Figure 3.12: Acid-Base equilibrium between the protonated and non-protonated form of $[Gd.L^{7b}(H_2O)]^{-}$

Some general observations can be made for the series of Gd^{3+} complexes of **L^{1}**, **L^{2}**, **L^{3}**, **L^{7b}** and **L^{8}** when comparing selected ^{1}H NMR relaxation parameters (Figure 3.13, Table 3.8).

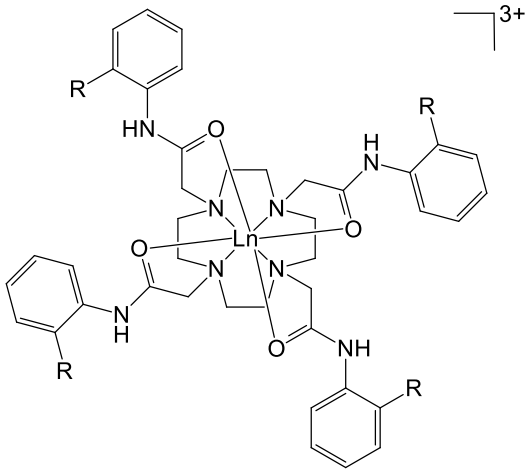

[Ln.L^{1}(H$_2$O)]$^{3+}$, where R = CF$_3$
[Ln.L^{2}(H$_2$O)]$^{3+}$, where R = CH$_3$

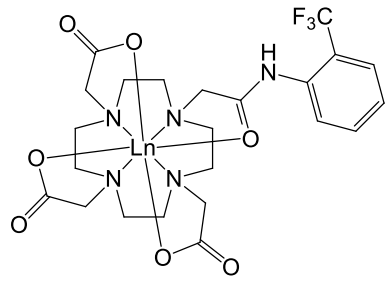

[Ln.L^{3}(H$_2$O)]

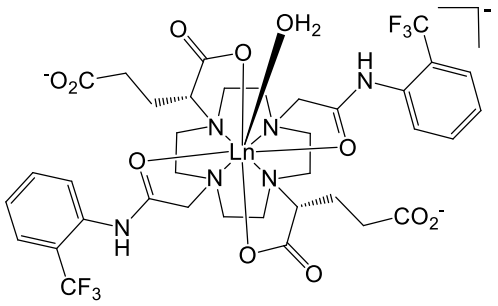

[Ln.L^{7b}(H$_2$O)]$^{-}$

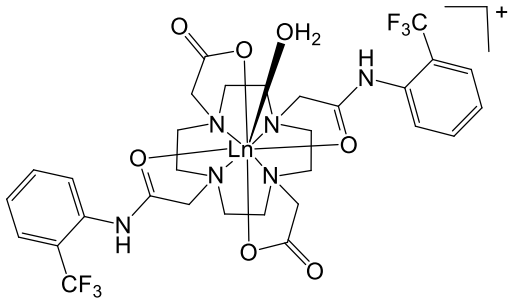

[Ln.L^{8}(H$_2$O)]$^{+}$

Figure 3.13: Structures of [Ln.L^{1}(H$_2$O)]$^{3+}$, [Ln.L^{2}(H$_2$O)]$^{3+}$, [Ln.L^{3}(H$_2$O)], [Ln.L^{7b}(H$_2$O)]$^{-}$ and [L^{8}(H$_2$O)]$^{+}$.

Firstly, the water exchange lifetime, τ_m, increases with increasing charge. While this is not unusual behaviour, the τ_m values are notably lower than those of structurally related complexes that do not include CF_3 groups (*i.e.* τ_m= 3.5 μs for [Gd.L^{1}(H$_2$O)]$^{3+}$ while τ_m= 9 μs for the methyl analogue [Gd.L^{1}(H$_2$O)]$^{3+}$). Furthermore, the enthalpy of activation decreases with increasing charge, and in the case of the carboxylate systems, decreases with increasing number of CF_3 groups.

Parameter	$[Gd.L^1(H_2O)]^{3+}$	$[Gd.L^2(H_2O)]^{3+}$	$[Gd.L^3(H_2O)]$	$[Gd.L^{7a}(H_2O)]^{-}$	$[Gd.L^8(H_2O)]^{+}$
r_{1p}^{20} (mM^{-1} s^{-1})	6.5	3.8	5.5	8.1	6.3
τ_M (μs)	3.5	9	0.9	0.11	1.7
τ_R (ps)	118	120	88	140	106
τ_V (ps)	13	8.5	14	10	14
Δ^2 ($s^{-2};\times10^{19}$)	4	1.5	5.9	2.8	2.4
$\Delta H_m^{\#}$ (kJ/mol)	30.1	51	48	50.3	42
$\Delta H_s^{\#}$ (kJ/mol)	/	/	32.4	58.2	6.3
E_r (kJ/mol)	16	15	18	18	15
E_v (kJ/mol)	2	5	2	1	1
q	1	1	1	1	1
$A/2\pi h$ ($x10^6$)rad s^{-1}	-22	-28	-2.9	-2.6	-2.6
q”	8	0	2	4	4
r' (Å)	4.4	/	4.4	4.4	4.3

Table 3.9: Summary of selected ^{1}H NMR relaxation parameters, derived from analyses of variable temperature ^{1}H relaxivity, ^{17}O NMR spectroscopy and fitting of the NMRD profiles (298K). *Note: The Gd-H distances for the coordinated water molecule, r, and the outer-sphere water molecules, a, were fixed at 3.0 and 4.0Å respectively; the relative diffusion coefficient, D, was fixed at 2.24 x 10^{-5} cm^2s^{-1}.*

3.6 Lipophilicity

The biodistribution of a complex can depend largely on its relative lipophilicity and/or its hydrophilic properties. For this reason, it is sometimes useful to determine the lipophilicity of a complex prior to any *in vivo* studies.

To enable measurement of logP, it is necessary to have a method of calculating the relative concentration of a complex in both octanol and water. For this study, lanthanide luminescence was used. Water was saturated with 1-octanol, and 1-octanol was saturated with water to ensure any miscibility effects were constant throughout the experiment. Complexes were prepared as 100 µM solutions in water and mixed with 1-octanol in 1:2, 1:1 and 2:1 water:octanol ratios. Mixtures were agitated for twelve hours, after which emission spectra of the water and octanol layers were measured. For the Tb complexes of L^1- L^8, the logP value was calculated according to Equation 3.5:

$$\log P = \log_{10} \frac{[X]_{\text{1-octanol}}}{[X]_{\text{water}}} \tag{3.5}$$

Final logP values were calculated as the average of at least two replicates for the three solvent mixtures (Table 3.9).

Complex	Log P_{oct}	SD
$[Tb.L^1(H_2O)]^{3+}Cl_3$	-0.16	0.04
$[Tb.L^2(H_2O)]^{3+}(OTf)_3$	-0.91	0.11
$[Tb.L^2(H_2O)]^{3+}Cl_3$	-2.10	0.23
$[Tb.L^3(H_2O)]$	0.63	0.09
$[Tb.L^4(H_2O)]^{3-}$	-2.03	0.12
$[Tb.L^5]$	0.12	0.06
$[Tb.L^6]$	-0.04	0.04
$[Tb.L^{7b}(H_2O)]^{-}$	-1.42	0.10
$[Tb.L^8(H_2O)]^{+}$	-1.23	0.02

Table 3.9: LogP values for Tb complexes of L^1-L^8

Some general observations can be made. Firstly, in a control experiment with $[Tb.L^2(H_2O)]^{3+}$ the counterion was varied, with results indicating that the triflate complex is more lipophilic than the chloride salt. This is consistent with the enhanced hydrophobicity of triflate salts.[15] The charged complexes have a more negative value of logP than the neutral complexes, which is consistent with their greater water solubility. It is interesting to note that the Tb complexes of L^5 and L^6 are slightly more hydrophilic compared to $[Tb.L^3(H_2O)]$.

3.7 Sensitivity Enhancement in ^{19}F Spectroscopic Studies

Of all the complexes studies thus far, the most promising system for applications in ^{19}F MRS and MRI is that based on the complexes of the triphosphinate ligand, L^5. They possess faster longitudinal relaxation rates and, in general, have narrower linewidths owing to the suppression of dynamic exchange processes. Most importantly, they exist in solution as one preferred species (> 86 %) and are stable as a function of time. Thus, they are ideal complexes to assess ^{19}F signal intensity enhancement. The diamagnetic analogue, $[Y.L^5]$ was used as a control, because it has essentially zero effect on the relaxation of the CF_3 moiety.

The experiment was set up in an analogous fashion to that undertaken for the complexes of L^1 and L^3, discussed in section 2.8. Equimolar solutions were used (2mM) and spectra was acquired at both 4.7 and 9.4 T. The acquisition time was set to be three times the measured T_1 value and spectral data were aquired over 15 minutes. In spectral processing, the line-broadening function was set to be 50 % of the observed linewidth, and the relative signal intensity was normalised to that found for the diamagnetic yttrium complex analogue (Table 3.10).

The results follow the order expected (Tb> Dy> Ho> Er> Tm) on the basis of R_1 enhancement, offset by R_2 'loss' of signal. The values obtained show an increased signal intensity enhancement compared with the complexes of L^3 (30, 20 and 14 % increase for Tb, Ho and Tm respectively at 4.7 T), which is consistent with the lower R_2 values associated with the more rigid and stable structure of the phosphinate

complexes. Analysis of the above data strongly suggests that Dy and Tb complexes of L^5 are the most promising for ^{19}F MRS studies, over the field range of 3.0 to 9.4 T.

	Relative Signal Intensity	
Complex	4.7 T	9.4 T
[Tb.L^5]	14.4	15.2
[Dy.L^5]	12.5	14.9
[Ho.L^5]	6.6	9.3
[Er.L^5]	5.5	8.9
[Tm.L^5]	4.8	7.2
[Y.L^5]	1	1

Table 3.10: Assessment of ^{19}F spectroscopic sensitivity for a) [Ln.L^5] (2 mM, D_2O, pD 5.4, 295 K, Ln=Tb, Ho, Er, Tm and Y) at 4.7 and 9.4 T. The acquisition time was set as 3 x T_1, with no delay time; total acquisition time was 15 min; in spectral processing, the line broadening function was set as 50 % of the observed linewidth. Values quoted are ± 6 %.

3.8 Sensitivity Enhancement in ^{19}F Imaging Studies

A comparative imaging study was undertaken, in collaboration Prof. Andrew Blamire, with the aim of addressing the gain in signal intensity for Tb, Dy, Ho, Er and Tm complexes of L^5, compared to the diamagnetic analogue [Y.L^5]. Images were collected at 7 T, running data acquisition at the Ernst angle to optimise signal to noise ratio (SNR), with a total acquisition time of 6 minutes per complex (Figure 3.14).

Results show that [Dy.L^5] produces the highest SNR, with [Ho.L^5] and [Er.L^5] providing the next best sensitivity enhancement. This is consistent with the predicted theoretical imaging enhancement values, which takes into account both the signal enhancement by R_1 (from rapid pulsing and flip angle adjustment) and signal loss by R_2 during the echo time.

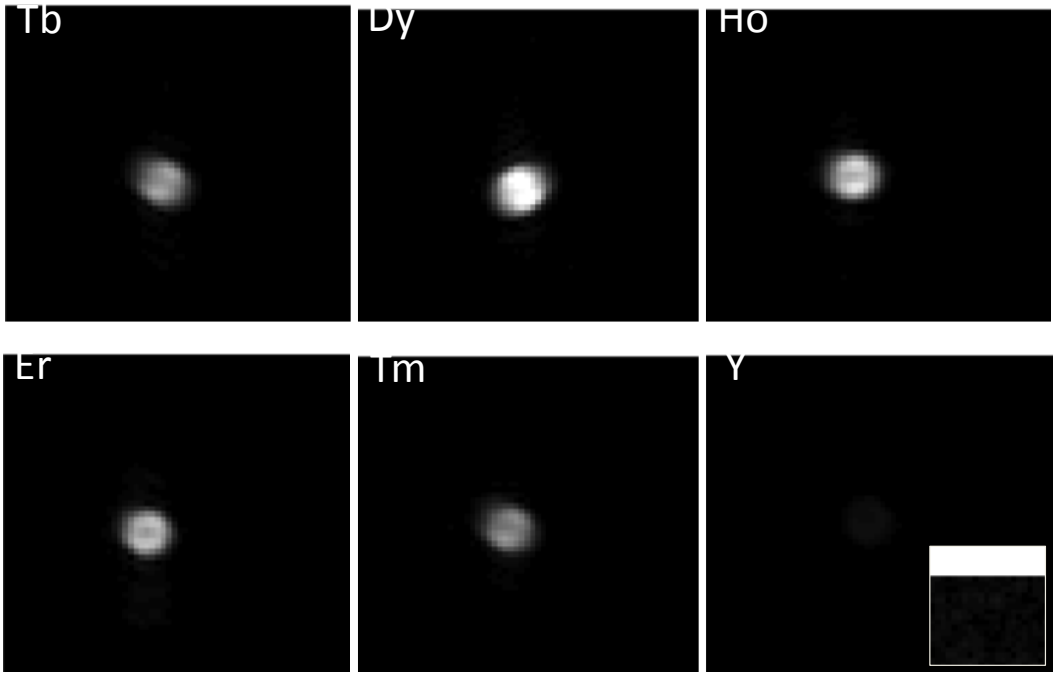

Figure 3.14: *In vitro* imaging data of [Ln.L^5] (2mM, 295 K, 7 T). All images intensity scaled to the same value. Experimental SNR: Tb- 135, Dy – 211, Ho – 175, Er – 150, Tm- 132. *Note: Inset Y image is scaled by factor of 10.*

3.9 Conclusions

Strategies employed to minimise dynamic chemical exchange processes, and promote the formation of one stable, preferred species in solution have been detailed and discussed.

The lanthanide(III) complexes of the triphosphinate ligand, L^5, have shown the most promise for use as probes for ^{19}F MRS and MRI versus their carboxylate analogues, [Ln.L^3(H_2O)]. They exist in solution as one preferred species, and are stable over time. In general, a faster longitudinal relaxation rate is observed and yet they still possess narrower linewidths, owing to the suppression of dynamic chemical exchange processes. These factors combined led to enhanced sensitivity of detection in ^{19}F NMR, and phantom imaging, experiments versus a diamagnetic Y^{3+} analogue.

Comparison of selected ^1H relaxation parameters across the series of Gd^{3+} complexes highlighted that the water exchange lifetime increases with increasing charge, whilst

the enthalpy of activation decreases. Interestingly, in the case of the carboxylate systems, the enthalpy of activation increases with increasing number of CF_3 groups.

In Chapter 4, the favourable characteristics displayed with the complexes of L^5 will be optimised further in an attempt to fine tune the biodistribution properties of the complexes, and further enhance signal intensity.

3.10 References

1) F. Mani, R. Morassi, P. Stoppini, A. Vacca, *J. Chem. Soc. Perkin Trans.*, **2001**, *2*, 2116.
2) M. Woods, S. Aime, M. Botta, J. A. K. Howard, J. M. Moloney, M. Navet, D. Parker, M. Port, O. Rousseaux, *J. Am. Chem. Soc.*, **2000**, *122*, 9781.
3) S. Aime, M. Botta, D. Parker, K. Senanayake, J. A. G. Williams, A. S. Batsanov, J. A. K. Howard, *Inorg. Chem.*, **1994**, *33*, 4696.
4) S. Aime, A. S. Batsanov, M. Botta, R. S. Dickins, S. Faulkner, C. E. Foster, A. Harrison, J. A. K. Howard, J. M. Moloney, T. J. Norman, D. Parker, L. Royle, J. A. G. Williams, *J. Chem. Soc., Dalton Trans.*, **1996**, 3623.
5) H. Reinheckel, *Alfa-Bromo Esters*, **1965**
6) M. P. Lowe, D. Parker, *Inorg. Chim. Acta.*, **2001**, *317*, 163.
7) Z. Kovacs, A. D. Sherry, *J. Chem. Soc., Chem. Commun*., **1995**, *2*, 185.
8) Z. Kovacs, A. D. Sherry, *Synthesis*, **1997**, *7*, 759.
9) S. Aime, M. Botta, D. Parker, J. A. G. Williams, *J. Chem. Soc., Dalton Trans.*, **1995**, 2259.
10) D. Parker, R. S. Dickins, H. Puschmann, C. Crossland, J. A. K. Howard, *Chem. Rev.*, **2002**, *102*, 1977.
11) T. J. Swift, R. J. Connick, *J. Chem. Phys.*, **1962**, *37*, 307.
12) S. Aime, A. Barge, J. I. Bruce, M. Botta, J. A. K. Howard, J. M. Moloney, D. Parker, A. S. de Sousa, M. Woods*, J. Am. Chem. Soc.*, **1999**, *121*, 5762.
13) L. Helm, A. E. Merbach, *Chem. Rev.*, **2005**, *105*, 1923.
14) J. C. Blazejewski, E. Anselmi, C. Wakselman, *J. Org. Chem.*, **2001**, *66*, 106.

Chapter 4: High Molecular Weight Fluorinated Conjugates

4.0 High Molecular Weight Fluorinated Conjugates

4.1 Introduction

Low sensitivity is one of the key difficulties with ^{19}F MRI, as discussed in chapters one, two and three. The signal to noise ratio can be improved by introducing more fluorine atoms into the molecule, however there are limitations in applying this strategy to the cyclen-based systems under review. Another possible solution would be to covalently link the complexes to a medium or high molecular weight adduct, which would result in the number of fluorine atoms being significantly increased. Moreover, the increase in molecular weight could also improve retention times *in vivo*.

4.2 Potential Platforms for Paramagnetic Probes

There are many desirable characteristics that a medium to high molecular weight molecule (1,000 to 6,500 D) should possess to successfully act as a platform for the development of fluorinated probes. Ideally, the molecule should have a number of repeating functional groups capable of forming stable bonds with the desired complexes. Also of great importance is water solubility and non-toxicity in the final conjugate. Bearing this in mind, three different classes of adducts were considered for our studies; β-cyclodextrin, silsesquioxane and chitosan. The merits and limitations of each will be discussed in more detail below.

4.2.1 β- Cyclodextrin

Natural cyclodextrins are cyclic oligosaccharides composed of 6, 7 or 8 α- 1, 4- linked D-(+)- glucopyranose units, more commonly known as α-, β-, and θ- cyclodextrin respectively. They are best known for forming inclusion complexes in the hydrophobic cavity of the cyclodextrin, and there are numerous practical applications in engineering and pharmacy.[1,2] Owing to their good binding ability towards aromatic units, coupled with the ease of availability, β-cyclodextrin has the most commercial potential. However, the downfall with β-cyclodextrin is its inherently low aqueous water solubility (18.5 gL^{-1}).[3] Consequently, a chemically modified β–cyclodextrin was used in our studies, whereby methoxy and amino

groups were incorporated into the structure to increase aqueous solubility and allow for facile linkage to complexes (Figure 4.1).

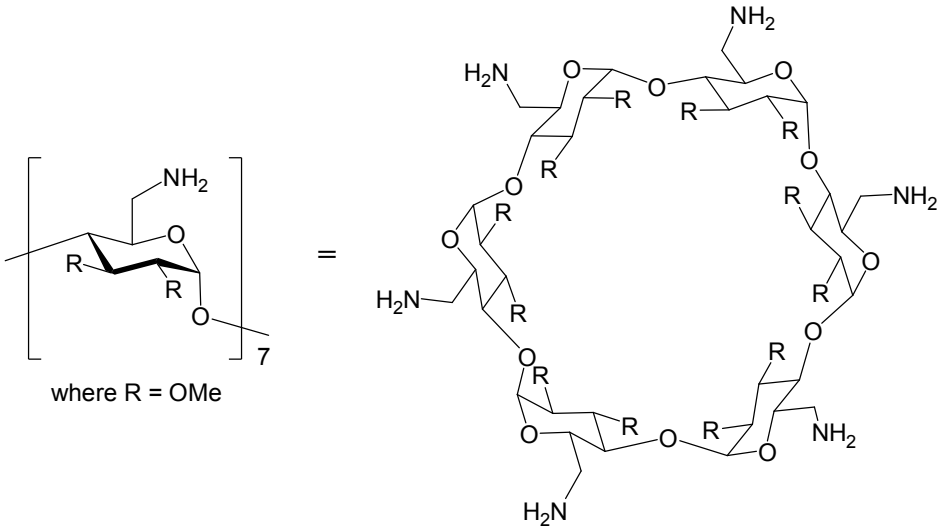

Figure 4.1

4.2.2 Silsesquioxane

Another potential medium molecular weight adduct for the development of highly fluorinated probes is the symmetric octa(3-aminopropyl)silsesquioxane (Figure 4.2). Owing to its precisely defined architecture, the T_8-silsesquioxane core leads to compact globular contrast agents, of which there are numerous examples.[4] When considering the design of such conjugates it is important to note that hydrolysis of the silsesquioxane core can occur in aqueous media. This is particularly important with Gd^{3+} -based conjugates whereby hydrolysis can break the conjugate down into smaller fragments, ultimately leading to a decrease in relaxivity. However, Mayer *et al.* have studied the hydrolysis of structurally related T_8-silsesquioxane conjugates, with very promising results. At pH 7.4, in serum at 37^{o}C, a half life of 15 hours was observed for the T_8-silsesquioxane core, with no change in relaxivity within the first 3 hours. The first step of the hydrolysis pathway is rate limiting and so the major species *in vivo* will be the starting silsesqiuoxane and the monomeric product, thereby avoiding the build up of intermediate molecular weight species.[5]

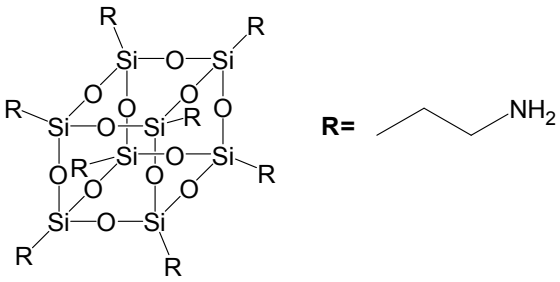

Figure 4.2

4.2.3 Chitosan

Chitosan is a linear polysaccharide composed of randomly distributed β-(1-4)-linked D-glucosamine and *N*-acetyl-D-glucosamine (Figure 4.3). Importantly, it is non-toxic, biodegradable and tolerated well *in vivo*. It is produced *via* the de-*N*-acetylation of chitin and so it is a cost efficient and readily available high molecular weight platform for our conjugation work. However, the main limitation of linear polymers is their poorly defined architecture and random morphology, which can lead to unpredictable and inconsistent results.

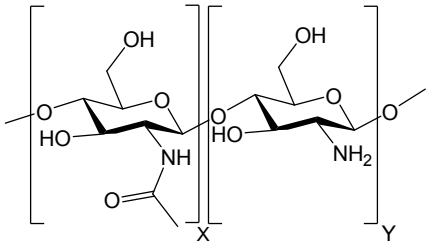

Figure 4.3

To ensure adequate water solubility, a chitosan sample with an average molecular weight of approximately 6,500 D was chosen for the development of our fluorinated conjugated contrast agents.

4.3 Fluorinated Complexes for Linkage to Macromolecules

As discussed in chapter three, the most promising system that we have developed thus far is that based on the complexes of the triphosphinate ligand, **L**^{5} (Figure 4.4). This is due to the faster longitudinal relaxation rates and narrower linewidths

observed, in comparison to the other cyclen-based systems examined (*i.e* **L^1 – L^4** and **L^6-L^8**). Consequently, complexes of **L^5** were the obvious choice for linkage to the macromolecules. Each of the carrier molecules include amino moieties, therefore by slightly modifying the structure of **L^5** to include a carboxyl group, linkage becomes feasible *via* the formation of stable amide bonds (Figure 4.4).

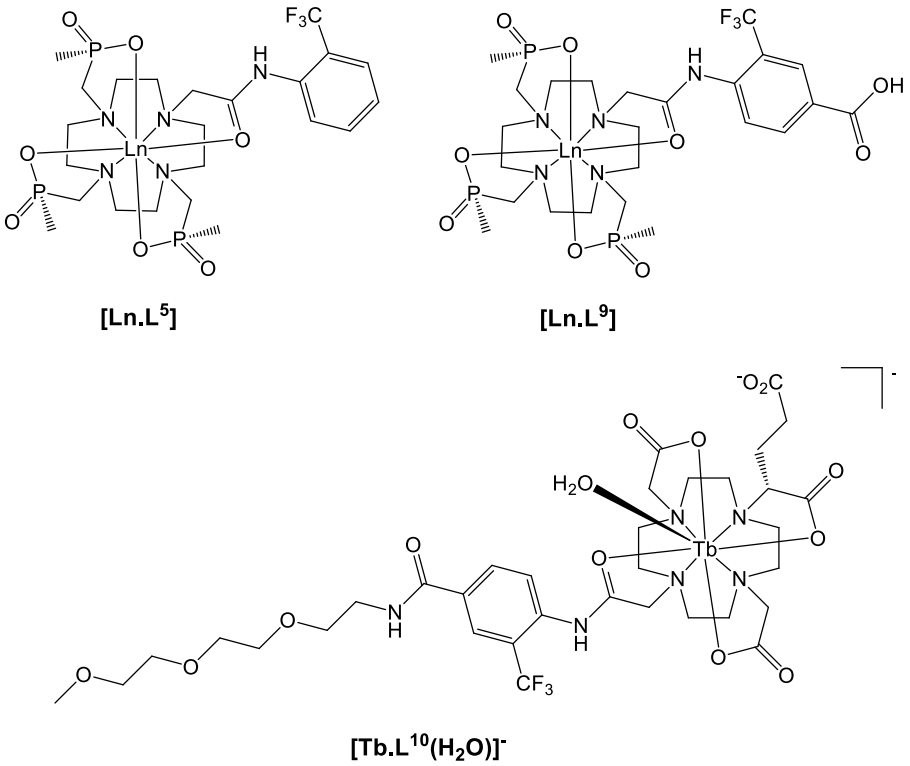

Figure 4.4: Structures of [Ln.L^5], [Ln.L^9] and [Tb.L^{10}(H$_2$O)]$^-$

Solubility can be a problem with high molecular weight conjugates, as discussed briefly above, therefore an additional complex was developed to specifically tackle this issue (Figure 4.4). Based on DO2A, the complex includes a methyl triethylene glycol derivative, at the *ortho* position of the aromatic ring, to increase solubility. A glutarate pendant arm is utilised to provide the necessary carboxyl moiety for linkage ([Tb.L^{10}(H$_2$O)]$^-$).

4.4 Synthesis

4.4.1 Synthesis of [Ln.L^9]

The first step in the synthesis of **L^9** involved the esterification of the nitrile precursor, by treatment with sulphuric acid in ethanol, to give **23** in a 64 % yield (Scheme 4.1). The alternative methyl ester was also attempted, however a low yield and lack of stability deemed it unsuitable for further use. Subsequent acetlyation of **23**, utilising chloroacetyl chloride in CH_2Cl_2 with triethylamine, gave the corresponding α-haloamide, **24**.

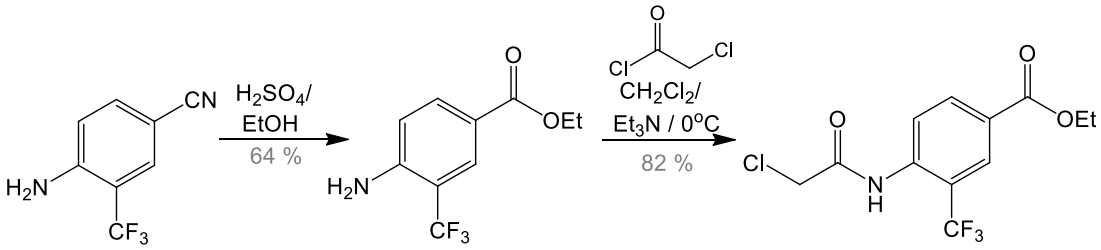

23 **24**

Scheme 4.1

Selective mono-alkylation with cyclen was achieved under very mild reaction conditions (no base, CH_2Cl_2, 40°C, Scheme 4.2). Co-condensation of the amine, **25**, with paraformaldehyde and diethoxymethylphosphine in THF afforded the corresponding triethylphosphinate ester, **26**. Subsequent base hydrolysis and complexation followed the same procedure as described previously for [Ln.L^5] in chapter three.

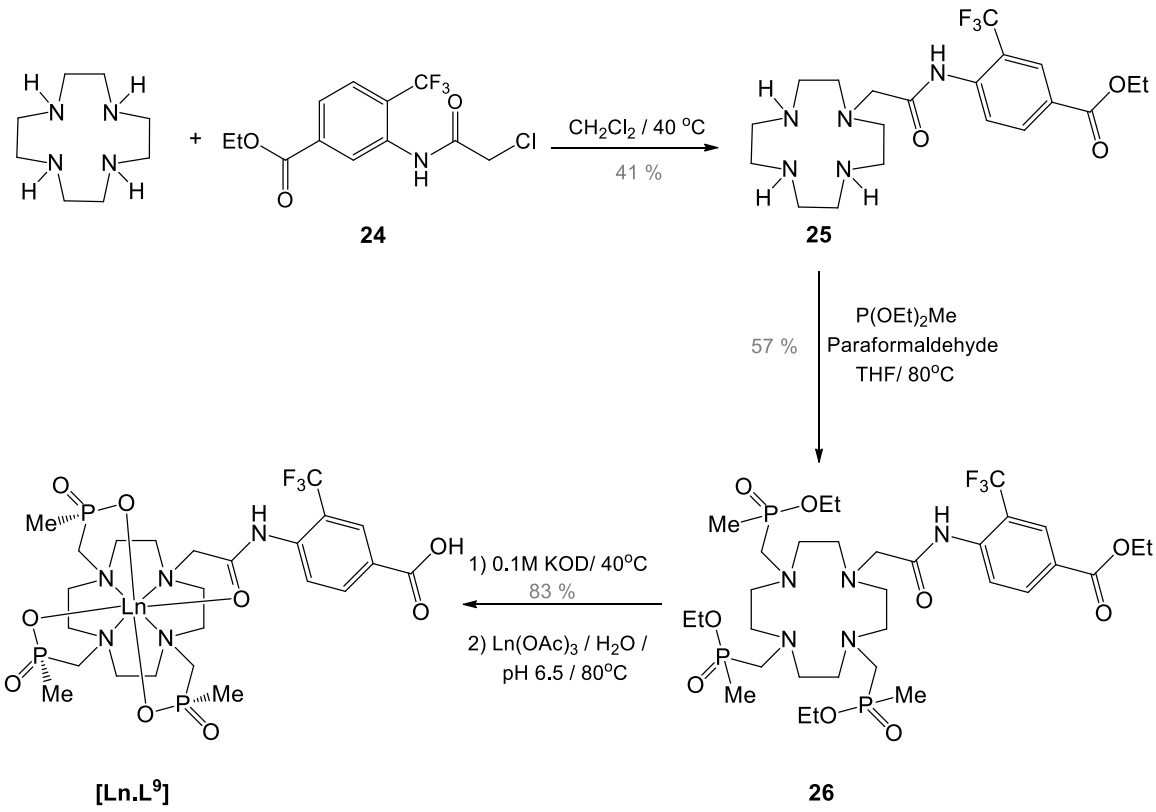

Scheme 4.2: Synthesis of [Ln.L[9]]

4.4.2 Synthesis of $[Tb.L^{10}(H_2O)]^-$

The mitsunobu reaction of triethylene glycol monomethyl ether with phthalimide, DIAD and PPh_3 afforded the desired product, **27**, after purification by silica gel chromatography. Subsequent hydrazinolysis of the phthalimide to give **28** was achieved as described by Dombi *et al.* [6]

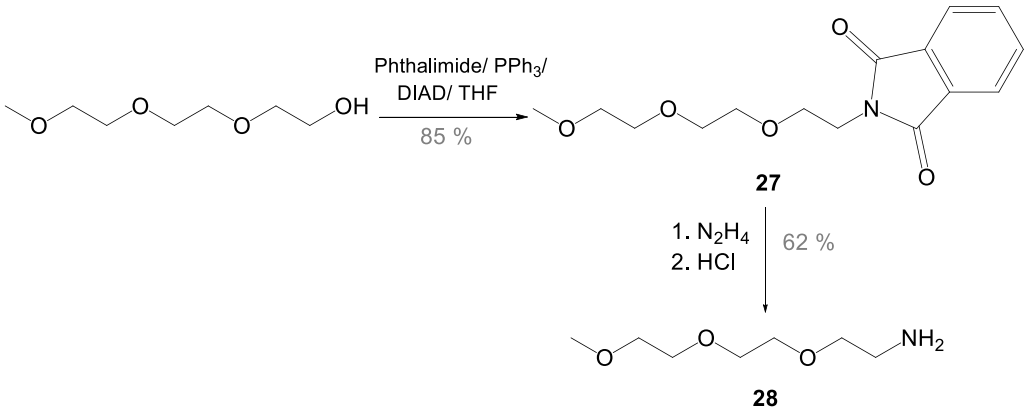

Scheme 4.3

Base hydrolysis of the ester, **24**, using potassium hydroxide gave the corresponding acid, **29**, in 86 % yield (Scheme 4.4). The active ester, **30**, was then prepared by reaction of **29** with TBTU in DMF, utilising N-methylmorphiline (NMM) as the base. Subsequent reaction of the amino moiety on the methyl triethylene glycol derivative **28**, with the active ester, **30**, afforded the desired product, **31**, in an excellent yield (91 %). Actylation of **31** was achieved by treatment with chloroacetylchloride and triethylamine in CH_2Cl_2.

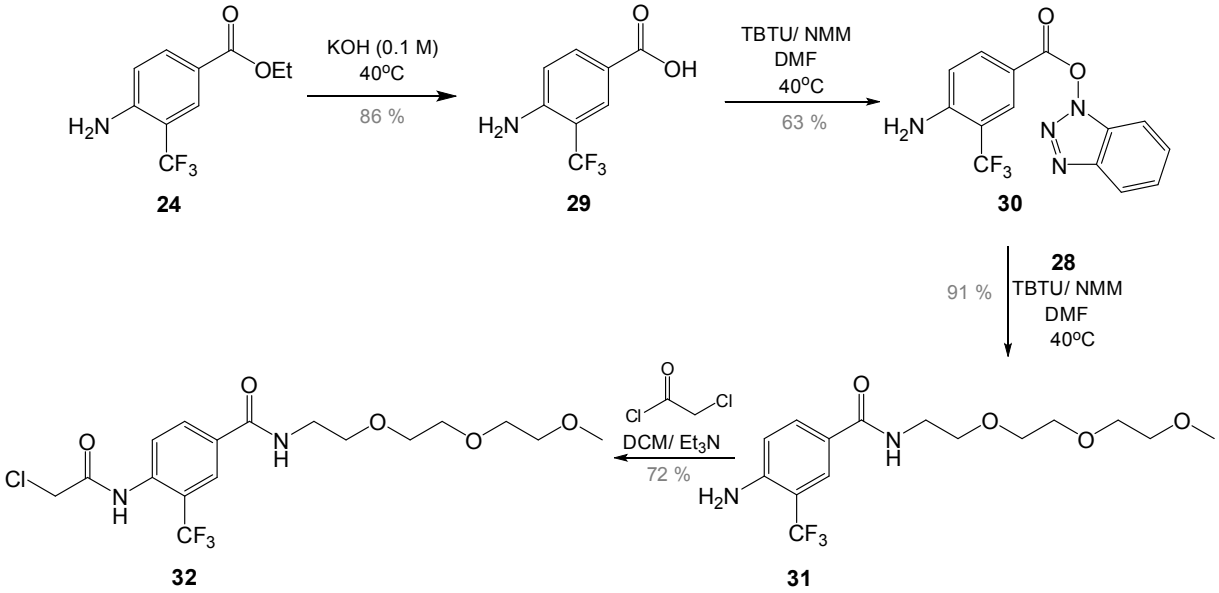

Scheme 4.4

The enantiopure 2-bromo amino acid diester, **34**, was prepared in two steps from the commercially available L-glutamic acid 5-benzyl ester (Scheme 4.5). The bromination step, to yield **33**, was achieved in an analogous fashion to that described in the synthesis of (*S*)-2-bromoglutarate, **7** (section 3.2.1). The transesterification of **33** with ^{t}BuOAc, in the presence of a catalytic amount of $HClO_4$ (70 %), afforded the enantiopure diester product, **34**, in good yield (81 %).

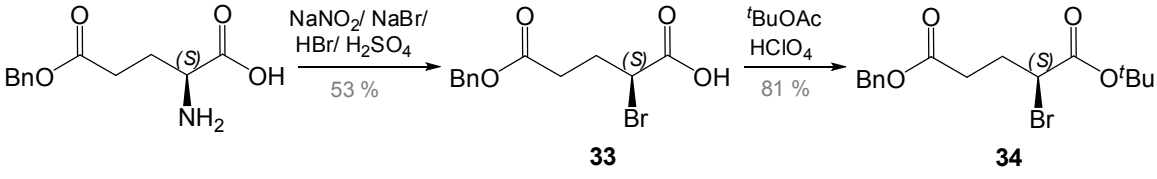

Scheme 4.5

Mono-alkylation of DO2A, **21**, with the enantiopure diester, **34**, was achieved under mildly basic conditions ($NaHCO_3$). The desired product, **35**, was separated from the small quantity of di-alkylated product by silica gel column chromatography (Scheme 4.6).

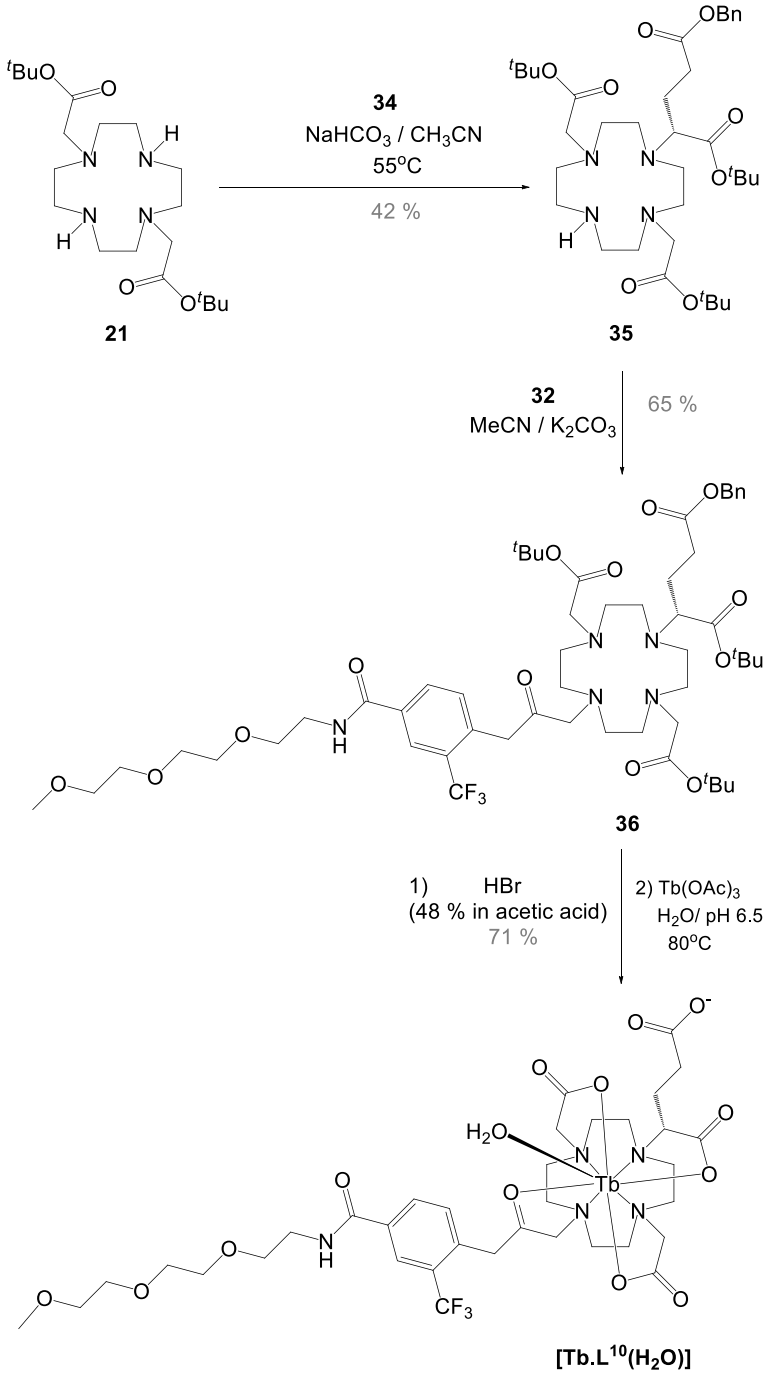

Scheme 4.6: Synthetic Pathway to $[Ln.L^{10}(H_2O)]^-$

Alkylation on the remaining secondary nitrogen atom of the cyclen ring, with **32**, proceeded with a reasonable yield (65 %). Removal of the benzyl and *tert*-butyl protecting groups was achieved *in situ*, by treatment with HBr in acetic acid at room temperature. Purification by dialysis (MWCO 500 D) afforded the hydrolysed ligand, which was then complexed with $Tb(OAc)_3$ as described for **L^7** (section 3.2.5).

4.4.3 Synthesis of β–Cyclodextrin Conjugates

In comparison with the complexes of [Ln.L^9], broader linewidths were expected in all of the corresponding conjugates detailed in this chapter. This is owing to the restricted mobility of the macromolecule carriers. As such, initial conjugation studies were attempted with [Tm.L^9] due to the narrower linewidth ($\omega_{1/2}$ = 21 Hz, D_2O, pD 5.5, 4.7 T) observed in the ^{19}F NMR spectroscopic analysis in comparison with [Tb.L^9] ($\omega_{1/2}$ = 27 Hz, D_2O, pD 5.5, 4.7 T).

Firstly, to enable conjugation, the carboxyl group of [Tm.L^9] was converted into an active ester form, by reaction with TBTU and NMM in anhydrous DMF (Scheme 4.7). The β–cyclodextrin derivative, dissolved in the minimum volume of water, was immediately added to the reaction mixture once the active ester was formed. The crude reaction mixture was purified by dialysis (MWCO 1000 D) over a 48 hour period, thereby removing unreacted coupling reagents and excess complex.

Analysis by MALDI$^+$ revealed that only one complex had conjugated, leaving six free unreacted amino groups on the β-cyclodextrin. In an attempt to achieve further conjugation, the crude product was re-reacted with [Tm.L^9], this time utilising harsher conditions (12 eq. [Tm.L^9], 15 eq. NMM) to try and drive the reaction to completion. However, following purification, both the analysis by MALDI$^+$, and the determination of the percentage of Tm present in the sample, revealed no further conjugation.

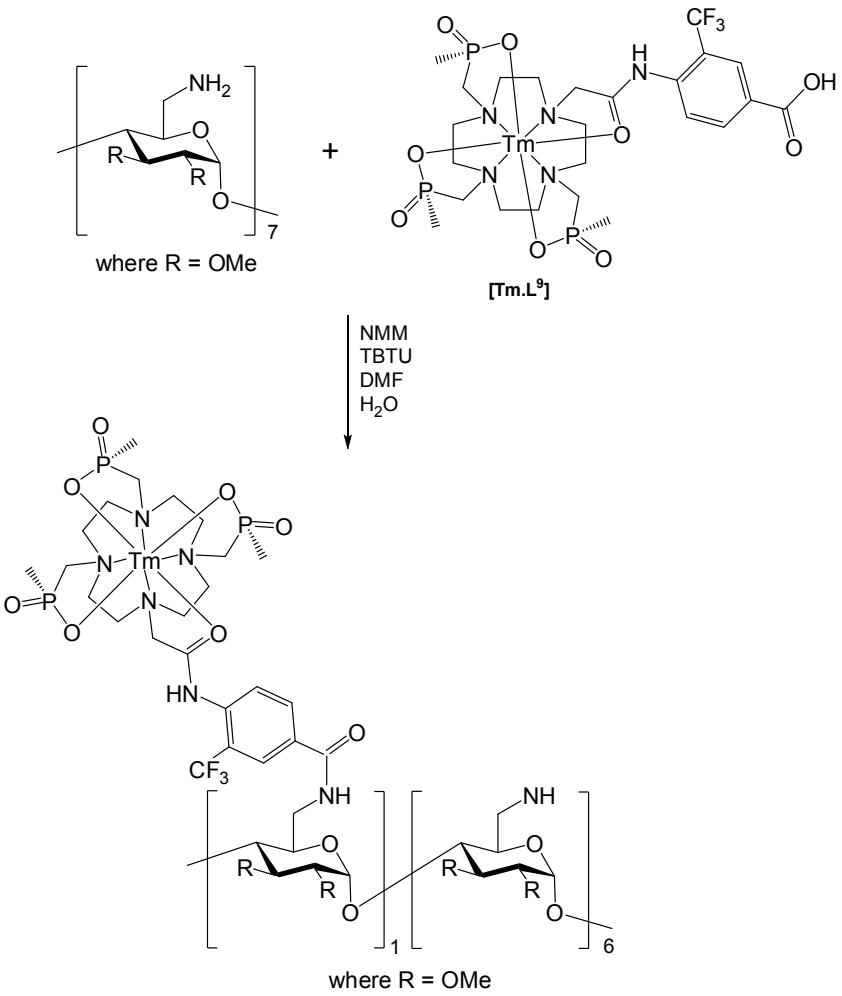

Scheme 4.7: Synthetic scheme for the preparation of the β-cyclodextrin complex conjugate

As discussed in section 4.2.1, these molecules are well known for forming inclusion complexes in the hydrophobic cavity of the cyclodextrin core. This could greatly hinder the extent of conjugation in our system. Consequently, the reaction was repeated in the presence of cumene. It was hoped that the cumene would preferentially become included, leaving the complex available to react with the amino groups on the β-cyclodextrin derivative. Unfortunately there was no change in the level of conjugation.

The possibility of steric effects was then considered. To probe this idea further, a second β-cyclodextrin derivative, with the incorporation of a linear linker chain, was explored (Figure 4.5). Furthermore, it was hoped that the added linker would increase the mobility of the conjugate, resulting in narrower linewidths in the ^{19}F

spectrum. An analogous reaction to that described above was undertaken but, again, analysis showed that only one complex had conjugated. Final purity of each conjugate was confirmed by reverse phase HPLC.

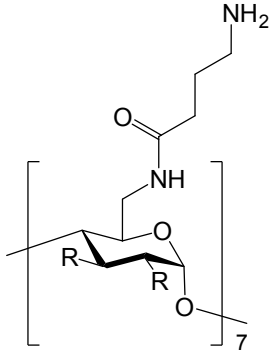

Figure 4.5

4.4.4 Synthesis of Silsesquioxane Conjugates

The poor solubility of the starting silsesquioxane material required the coupling reaction with [Tm.L[9]] to be carried out in DMSO, utilising TBTU and N,N-diisopropylethylamine (DIPEA) (Scheme 4.8). The reaction mixture was added dropwise into cold diethyl ether and the precipitate collected. Purification of the crude product was achieved by dialysis over a 48 hour period.

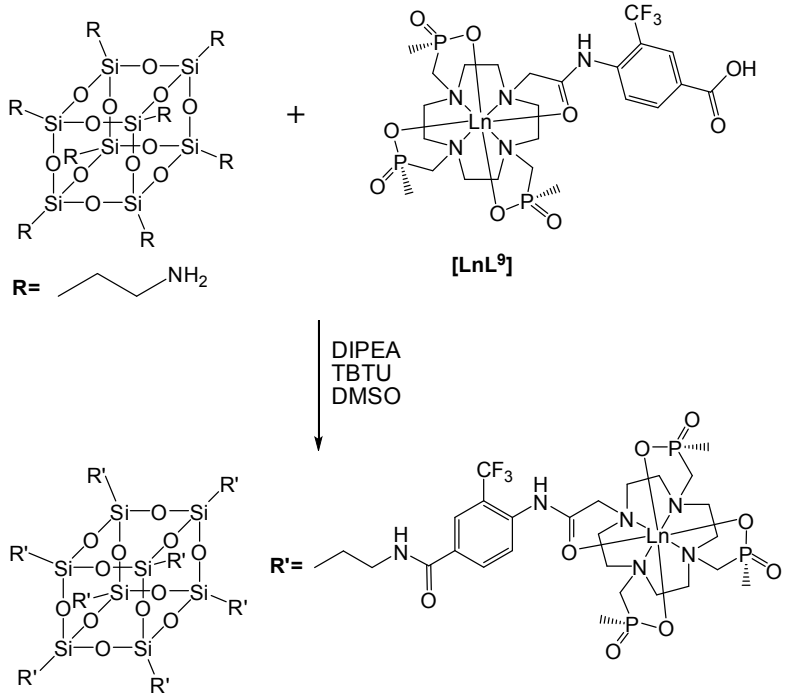

Scheme 4.8: Synthetic scheme for the preparation of the silsesquioxane complex conjugate

Mass spectra data was unable to be obtained, however HPLC analysis, ^{29}Si NMR measurements and the determination of the percentage of Tm suggested complete conjugation (Table 4.1).

	t_r (min)	^{29}Si Shift (ppm)	% Tm
Silsesquioxane	9.64	-64.1	0
[(Tm.L^9).Silsesquioxane]	4.83	-65.8	17.4

Table 4.1: HPLC (Method A in experimental section), ^{29}Si NMR and % Tm (Evans method[7]) results for the starting silsesquioxane and [(Tm.L^9).Silsesquioxane]

The poor solubility of the silsesquioxane conjugate dictated that all experiments be carried out in a H_2O:CH_3OH mix (50:50). Whilst these conditions are acceptable for the running of NMR spectroscopy experiments, they are unacceptable for *in vivo* studies.

To overcome this solubility problem, [Ln.L^{10}] was coupled with the silsesquioxane starting material under the same conditions as described above. Interestingly, in comparison with the [(Tm.L^9).Silsesquioxane], HPLC and ^{19}F NMR spectroscopic analysis revealed a mixture of products after purification. Analysis of the percentage of Tm in the purified product corresponded to a degree conjugation of only 27.4 %. This could be attributed to the differing carboxyl moieties in the two monomeric complexes. The solubility of the final conjugate was increased; however a H_2O:CH_3OH (80:20) mixture was still required for all experiments.

4.4.5 Synthesis of Chitosan Conjugates

The coupling reaction of [Ln.L^9] (where Ln= Gd and Tb) with chitosan (Scheme 4.9) was achieved in an analogous fashion to that described for the β-cyclodextrin conjugate (Section 4.3.3).

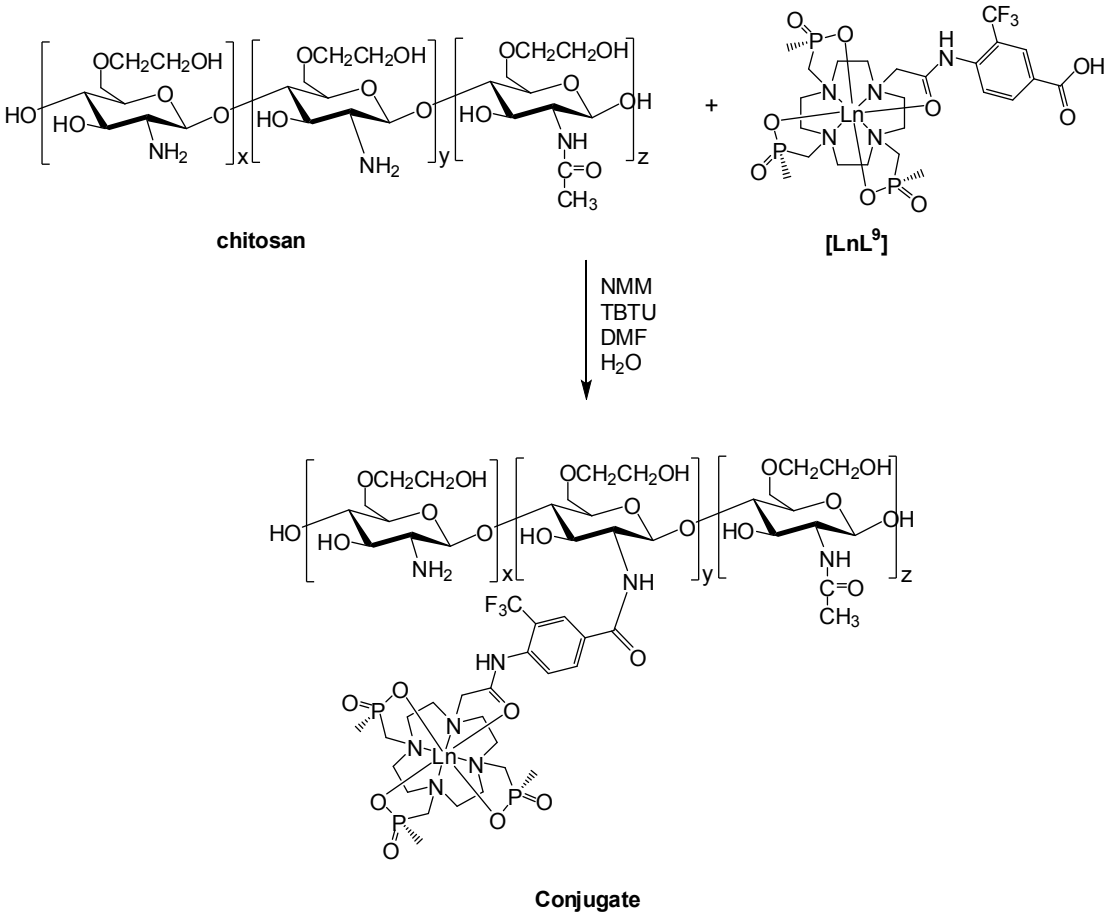

Scheme 4.9: Synthetic scheme for the preparation of the chitosan complex conjugates

Following purification, the conjugates were analysed by gel permeation chromatography (GPC). Results indicated an increase in the molecular weight of the conjugates, with respect to the unreacted polymer (Table 4.2). This data, in conjunction with elemental analysis of the metal content, confirmed the formation of covalently linked conjugates.

Sample	M_w [a]	M_n [b]	PDI [c]
Chitosan	6,590	2,250	2.9
[(Gd.L^9).Chitosan]	16,500	8,565	1.9
[(Tb.L^9).Chitosan]	16,300	8,615	1.9

Table 4.2: Gel permeation chromatography (GPC) data for the starting glycol chitosan sample and the corresponding Tb and Gd conjugates. Mean values obtained from two successive scans. [a] calculated molecular weight averages expressed as the pullulan polysaccaride equivalent molecular weights; [b] number average molecular weights; [c] polydispersity (Mw/Mn).

4.5 pH Dependent Spectroscopic Behaviour

The introduction of the carboxylate moiety in [Ln.L^9] alters the acidity of the amide NH. In general, the amide deprotonation equilibrium gives rise to a pK_a value greater than 9.5. However, the introduction of an electron-withdrawing group, capable of delocalising the negative charge in the conjugate base, can lower this value (Figure 4.6).

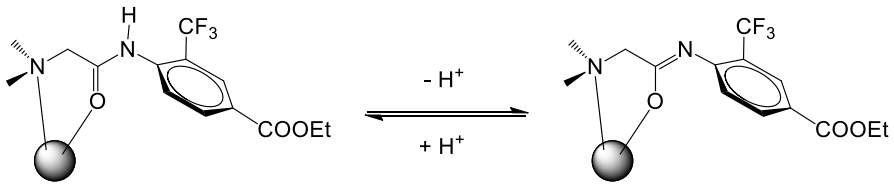

Figure 4.6: Acid-Base equilibrium between the protonated and non-protonated form of **[Ln.L^9]**

The amide deprotonation is indicated by a change in the chemical shift of the CF_3 group. From pH 5.4 to pH 10.1, a change in 10.9 ppm was detected for [Tm.L^9] (-88.9 ppm to -99.8 ppm) and a change in 8.6 ppm for [Tb.L^9] (-48.4 ppm to –57.0 ppm). Only one ^{19}F NMR spectroscopic resonance is observed in each case because the acid-base equilibrium is fast on the NMR timescale, whereby the signal is indicative of the mean acid and base form.

A pH titration was performed for [Tm.L^9] using a dilute solution of the complex in 0.1 M NaCl (298 K, 188 MHz). The NaCl was added to ensure a constant ionic strength was maintained throughout the experiment, and a D_2O coaxial was used to lock the instrument. The resulting data shows a continuous change in ^{19}F chemical shift as a function of pH. A pK_a value of was 8.62 calculated for [Tm.L^9].

Examination of the ^{19}F NMR spectroscopic resonance linewidth variation with pH reveals a maximum value at pH 8.5. This corresponds well with the calculated pKa. It is hypothesised that this exchange broadening is caused by the chemical exchange

between the protonated amide and its conjugate base. This is further supported by the fact that the linewidth decreases in more basic and acidic media.

4.6 ^{19}F Spectroscopic and Relaxation Analysis

The Tb and Tm complexes of **L^{9}** each formed one predominant ^{19}F resonance in solution (>85 %) and were stable over time. Conversely, in the ^{19}F NMR spectra of [Tb.L^{10}], a mixture of species was observed (7 resonances), with the dominant species comprising only 56 % of the total observed signal intensity. Interestingly, the [Ln.L^{9}] and [Ln.L^{10}] conjugates of cyclodextrin, silsesquioxane and chitosan all exhibited improved spectral features in comparison with their corresponding complexes (>90 % one species). In each case, a single peak was observed in the ^{19}F spectra, displaying the same chemical shift as the parent complex.

The longitudinal and transverse relaxation rates, R_1 and R_2, were measured as a function of field in each case (Table 4.3).

	^{19}F Shift/ ppm	R_1/ Hz		R_2 / Hz	
		4.7 T	9.4 T	4.7 T	9.4 T
[Tb.L^{9}]	-48.5	86	148	147	263
[Tm.L^{9}]	-89.1	48	73	83	109
[Tb.L^{10}(H_2O)]$^{-}$	-45.1	85	133	120	198
[(Tm.L^{9}).Cyclodextrin]	-48.5	45	79	136	190
[(Tm.L^{9}).Silsesquioxane]^{a}	-89.2	44	74	103	204
[(Tb.L^{10}(H_2O)).Silsesquioxane]^{b}	-45.4	80	122	196	322
[(Tb.L^{9}).Chitosan]	-48.5	81	131	182	407

Table 4.3: ^{19}F Longitudinal and transverse relaxation data for complexes of L^{9} and L^{10} , and their corresponding conjugates, at 4.7 and 9.4 T (2 mM, D_2O, pD 5.4, 295 K); ^{a}(2mM, CD_3OD:D_2O (50: 50), pD 5.4, 295 K); ^{b}(2 mM, CD_3OD:D_2O (20: 80), pD 5.4, 295 K).

The R_1 value does not appear to significantly change between the complexes and their corresponding conjugates. As expected, broader linewidths are displayed for the conjugates, owing to the limited mobility experienced by the macromolecule carrier. However there is still some local motion, as depicted in figure 4.8, due to the

local motion of the aromatic ring and of the complex with respect to the macromolecule.

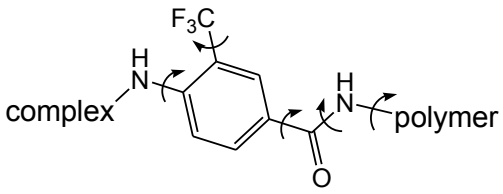

Figure 4.7: Representation of the possible rotations around the bond of the amide linker.

Owing to the limited conjugation achieved for [(Tm.L^9).Cyclodextrin], and the solubility issues encountered with both [(Tm.L^9).Silsesquioxane] and [(Tb.L^{10}(H_2O)).Silsesquioxane], these conjugates were not examined any further. The highly fluorinated, water soluble [(Tb.L^9).Chitosan] was therefore chosen to be analysed further as a potential contrast agent for *in vivo* studies.

4.7 Proton Relaxation Properties of Gd^{3+} Complexes

The relaxivity profiles of [Gd.L^9], as a function of temperature and magnetic field, were analysed to allow for an estimate of the rotational correlation time, τ_r, and other associated proton relaxation parameters (Figure 4.8, Table 4.4).

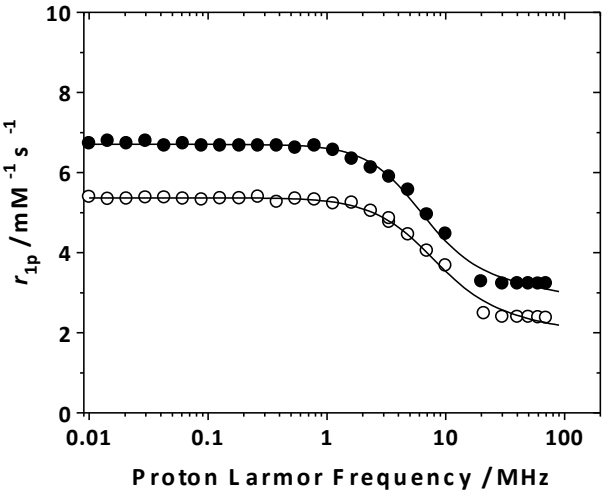

Figure 4.8: Variation of the observed relaxivity, r_{1obs}, with field for [Gd.L^9] (0.4 mM) at 298 K (filled circles) and 310 K (open circles).

Complexes of **L^9** do not have a coordinated water, as determined by analysis of the Tb emission decay lifetimes in H_2O and D_2O ($\tau_{(H2O)}$ 2.78 ms, $\tau_{(D2O)}$ 3.84 ms; q= 0.2). Thus, the measured relaxivity of the Gd analogue is low (3.3 $mM^{-1}s^{-1}$, 60 MHz, 298 K), owing to the lack of inner sphere contribution.

Parameter	298 K	310 K
$r_{1p}/mM^{-1}\,s^{-1}$	3.3	2.5
τ_V/ps	22.9	18.1
$\Delta^2(s^{-2} \times 10^{19})$	2.6	2.6
$E_V/kJ\,mol^{-1}$	1	1
q	0	0
q”	3	3
$r''/Å$	4	4
τ_R'/ps	60	40

Table 4.4: Summary of selected relaxation parameters for [Gd.L^9] fitting of NMRD profile. r_{1p} is the proton relaxivity; τ_V is the correlation time for the ZFS modulation; τ_R is the rotational correlation time; Δ^2 is the mean-square zero field splitting energy; q is the number of inner sphere water molecules; q” is the number of second sphere water molecules and r'' their distance from Gd.

The relaxivity of [(Gd.L^9).Chitosan] was measured to be 12.4 $mM^{-1}s^{-1}$ (60 MHz, 298 K). This significant increase in relaxivity, in comparison with the monomeric complex, [L^{9}Gd], is associated with a slower rotation of the Gd complex in the conjugate. This results in a longer rotational correlation time and, hence a higher relaxivity value. The variation of relaxivity with pH was also undertaken for [(Gd.L^9).Chitosan], with results showing an increase in relaxivity over the pH range 7-12 (Figure 4.9). This is consistent with base-catalysed prototopic exchange, related to the deprotonation of the amide proton.

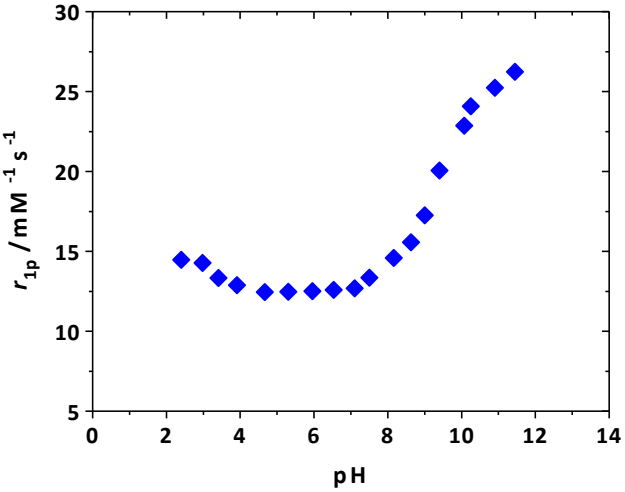

Figure 4.9: pH dependence of the ^{1}H relaxivity, r_{1p}, of [(Gd.L^{9}).Chitosan] (0.6 mM, 60 MHz, 298 K)

The higher relaxivity value of [(Gd.L^{9}).Chitosan] should allow for increased signal intensity per unit concentration, versus low molecular weight Gd complexes. Furthermore, high molecular weight molecules, such as [(Gd.L^{9}).Chitosan], often show enhanced permeability and retention (EPR) in tumour studies, resulting in favourable slow release profiles.

4.8 Conclusions and Future Work

Three different potential platforms, for conjugation with fluorinated paramagnetic probes, have been synthesised and their spectral properties assessed. The desirable formation of one species in solution, the ease of solubility and attractive ^{19}F and ^{1}H relaxometric properties render the chitosan conjugates, [(Ln.L^{9}).Chitosan], the most promising candidates for use as imaging probes.

More work is required to further examine and assess the full benefits of the chitosan conjugates. Short term goals should include the *in vivo* testing of [(Gd.L^{9}).Chitosan], with the aim of assessing the distribution and tumour uptake of the conjugate. Following this, the analogous ^{19}F MRI *in vivo* experiment should be undertaken to determine if sufficient signal is being achieved from the Tb conjugate.

Throughout this thesis, the effects of field, choice of lanthanide ion, design of macrocyclic ligand and carrier system, have been documented and discussed. Additionally, a number of strategies have been investigated with the aim of increasing the signal intensity in ^{19}F imaging experiments, with much progress made. While these systems still require optimisation, it is clear that structurally related ^{1}H / ^{19}F dual imaging probes are a strong possibility for the future.

4.9 References

1) J. Carranzana, A. Jover, F. Meijide, V. H. Soto, J. V. Tato, *J. Phys. Chem. B.*, **2005**, *109*, 9719.

2) W. Saegner, J. Jacob, K. Gessler, T. Steiner, D. Hoffmann, H. Sanbe, K. Koizumi, S. M. Smith, T. Takaha, *Chem. Rev.*, **1998**, *98*, 1787.

3) D. French, M. L. Levine, J. H. Pazur, E. Norberg, *J. Am. Chem. Soc.*, **1949**, *71*, 353.

4) T. L. Kaneshiro, E-K. Jeong, G. Morrel, D. L. Parker, Z-R. Lu, *Biomacromolecules*, **2008**, *9*, 2742.

5) J. Henig, E. Toth, J. Englemann, S. Gottschalk, H. A. Mayer, *Inorg. Chem.*, **2010**, *49*, 6124.

6) K. L. Dombi, N. Griesang, C. Richert, *Synthesis*, **2002**, 816.

7) D. M. Corsi, C. Plataas-Iglesias, H. V. Bekkum, J. A. Peters, *Mag. Reson. Chem.*, **2001**, *39*, 723.

Chapter 5: Experimental Procedures

5.0 Experimental Procedures

5.1 General Procedures

Reaction Conditions

All solvents used were laboratory grade and were dried over the appropriate drying agents when required. All reagents were used as supplied by commercial sources, unless otherwise stated. Water refers to high purity water obtained from the "PuriteSTILL Plus" purification system, with conductivity of 0.04 μS cm^{-1}. Reactions requiring anhydrous conditions were carried out using Schlenk-line techniques under an atmosphere of dry argon.

Purification Procedures

Thin layer chromatography was performed using silica plates (Merck Art 5554) or neutral aluminium oxide plates (Merck Art 5550), each of which are fluorescent under UV irradiation (254 nm). Preparative column chromatography was performed using silica (Merck Silica Gel 60, 230–400 mesh) or neutral aluminium oxide (Merck Aluminium Oxide 90, activity II–III, 70–230 mesh), which had been pre-washed in ethyl acetate. Anion exchange chromatography was performed using anion exchange resin DOWEX 1X8 200-400 MESH Cl (Sigma-Aldrich), pre-treated with a solution of 1M HCl or 1M KOH in Purite water, or cation exchange resin DOWEX 50WX4-100 (Sigma-Aldrich) pre-treated with 1M KOH in Purite water. Dialysis was performed with Dialysis Tubing Cellulose Membrane MWCO 500D and 12,000D (Sigma-Aldrich) or Spectra/Por Dialysis Membrane MWCO 1,000D (Spectrum Laboratories, Inc).

Mass Spectrometry

Electrospray mass spectra were recorded on a Fisons VG Platform II, Waters Micromass LCT or Thermo-Finnigan LTQ FT instrument operating in positive or negative ion mode as stated, with methanol as the carrier solvent. Accurate mass spectra were recorded using the Thermo-Finnigan LTQ FT mass spectrometer. GC-MS were acquired on a GSMS Thermo-Finnigan instrument.

NMR Spectroscopic Characterisation

^{1}H, ^{13}C and ^{19}F NMR spectra were recorded in commercially-available deuteriated solvents on a Varian Mercury-200 (^{1}H at 199.975 MHz, ^{13}C at 50.289 MHz, ^{19}F at 188.179 MHz), Varian Mercury-400 (^{1}H at 399.960 MHz, ^{13}C at 100.572 MHz, ^{19}F at 376.338 MHz), Varian Inova-500 (^{1}H at 499.772 MHz, ^{13}C at 125.671 MHz, ^{19}F at 470.253 MHz) or Varian VNMRS-700 (^{1}H at 699.731 MHz, ^{13}C at 176.034 MHz, ^{19}F at 658.407 MHz) spectrometer. All chemical shifts are given in ppm and coupling constants are reported in Hz.

^{19}F NMR Relaxation Analysis

^{19}F NMR longitudinal relaxation times were measured in dilute D_2O or CD_3OD solutions (typically 2mM) at 295 K using the inversion-recovery technique, without proton decoupling, on Varian spectrometers operating at magnetic inductions corresponding to fluorine frequencies of 188, 376, 470 and 658 MHz (Mercury-200, Mercury-400, Inova-500, VNMRS-700). The resulting free induction decays were subjected to backward linear prediction, optimal exponential weighting, zero filling, Fourier transform, phasing and baseline correction (by polynomial fitting to signal-free spectrum areas). The signals were integrated by Lorentzian line fitting. Inversion-recovery type function was fitted to the resulting data using Levenberg-Marquardt minimization of the non-linear least squares error functional.

Proton Relaxometric Studies

The water proton $1/T_1$ longitudinal relaxation rates (20 MHz, 298 K) were measured on a Stela Spinmaster Spectrometer (University of Piemonte Orientale in Alessandria, Italy) on 0.5-2 mM aqueous solutions of the complexes. For the T_1 determinations, the standard inversion-recovery method was used with a typical 90^{o} pulse width of 3.5μs with 16 experiments of 4 scans. The reproducibility of the T_1 data was estimated to be ± 1%. The temperature was controlled with a Stelar VTC-91 air-flow heater equipped with a copper-constantan thermocouple (uncertainty of 0.1 $\pm^{o}C$). The proton $1/T_1$ NMRD profiles were measured on a fast field-cycling Stelar Spinmaster FFC relaxometer over a continuum of magnetic field strengths from 0.00024 to 0.5 T (corresponding to 0.01-20 MHz proton Larmor frequencies). The

relaxometer operates under computer control with an absolute uncertainty in $1/T_1$ of ± 1%. Data points from 0.47 (20 MHz) to 1.7 T (70 MHz) were collected in a Stelar Spinmaster spectrometer operating at variable fields.

^{17}O NMR Relaxation Studies

Variable temperature ^{17}O NMR spectroscopic measurements were recorded on a JEOL ECP-400 (9.4T) spectrometer equipped with a 5 mm probe and a standard temperature control unit. Aqueous solutions of the complexes (~ 20-30 mM) containing 2.8% of the ^{17}O isotope (Cambridge Isotope) were used. The observed tranverse relaxation rates (R_2) were calculated from the signal width at half-height ($\Delta_{1/2}$): $R_2 = \pi\Delta_{1/2}$.

^{19}F MRI Phantom Studies

^{19}F phantom imaging data were collected at Newcastle Maagnetic Resonance Centre using a 7T Varian Unity Inova microimaging system (Varian Inc., Palo Alto, California, USA) equipped with broadband capability, actively shielded gradients and a purpose-built two turn circular ^{19}F surface coil (i.d. 12 mm, 281 MHz ^{19}F frequency) which was used for both excitation and reception of the signal. Dilute aqueous samples (~ 2 – 5 mM) were placed in 5 mm NMR tubes and positioned on the axis of the coil. Conventional proton MRI was used to localise and shim the samples based on the proton water signal. Following ^{19}F pulse calibration, R_1 values were determined for each sample using a saturation recovery sequence in order to calculate Ernst angle pulses for optimal imaging sensitivity. Fluorine MR images were then collected using a RF spoiled, gradient echo imaging sequence with repetition time (T_R) 10 ms, echo time (T_E) 0.88 ms, a 0.5 ms sinc pulse for selection of a 6 mm thick slice, 48 x 48 mm field of view, 32 x 32 matrix and 50 kHz receiver bandwidth. Relative imaging sensitivity for the complexes was determined by 'region of interest analysis' of the signal to noise ratio in each image.

^{19}F MRI *In Vivo* Studies

MRI *in vivo* studies were performed in the Newcastle Magnetic Resonance Centre using a Varian 7 T Unity Inova Pre-Clinical system equipped with a ^{1}H 39 mm-

diameter transmit/receive birdcage coil for proton images and a ^{19}F circular surface coil for fluorine images (12 mm diameter, 281 MHz ^{19}F frequency). Nude mice bearing an HT29 colorectal tumour xenograft were anaesthesised with oxygen/ 1-2% isoflurane and placed in the coil. A dynamic sequence was used in which 5 background images were collected (30 s) before the endovenous administration of the contrast agent during the 6th image. The remaining 94 images were dynamic images for a total of 100 over a 10 min acquisition period.

pH Measurements

All pH measurements were performed using a Jenway 3320 pH meter attached to an Aldrich micro–pH combination electrode, calibrated using pH 4.00 ±0.02, 7.00 ±0.02 and 10.00 ±0.02 buffer solutions by Aldrich. Diluted aqueous solutions of NaOH and HCl (or where required NaOD and DCl in D_2O) were used for pH adjustements. For measurements in D_2O the pD was calculated as pD = pH + 0.41, where pH is the meter reading.

Melting Point Measurements

Melting points were recorded using a Gallenkamp apparatus (Sanyo) and are uncorrected.

Gel Permeation Chromatography

Gel permeation chromatography was undertaken at Smithers Rapra UK using a Viscotek Model 301 TDA instrument with associated pump, autosampler and refractive index detector (with differential pressure and light scattering). PLaquagel-OH guard plus 2 x PLaquagel-OH Mixed-H, 30 cm, 8 µm columns were used with an eluent composed of 0.5 M $NaNO_3$, 0.01 M NaH_2PO_4 at pH 2 at a flow rate of 1.0 ml/min at 30˚C. The GPC system was calibrated using pullulan polysaccharides and the data were analysed using Malvern/Viscotek 'OmniSec' software.

HPLC

Reverse phase HPLC traces were recorded at 298 K using a Perkin Elmer system equipped with a Perkin Elmer Series 200 Pump, a Perkin Elmer Series 200

Autosampler and a Perkin Elmer Series 200 Diode array detector (operated at 254 nm). A 4.6 x 150 mm 4μm Phenomenex Synergi Fusion RP 80Å analytical column was used. A gradient elution with a solvent system composed of H_2O + 0.1% HCOOH/ MeCN + 0.1% HCOOH was performed for a total run time of 20 min (Table 5.1).

Time (min)	Solvent A (%)	Solvent B (%)	Curvature
0	95	5	0
5	95	5	0
20	0	100	1
25	0	100	0
27	95	5	-3
30	95	5	0

Table 5.1: Flow rate = 1ml/min; Solvent A = H_2O + 0.1% HCOOH; Solvent B = MeCN + 0.1% HCOOH.

Emission Spectra and Lifetime Measurements

Emission spectra and lifetimes were measured on a Fluorolog-3 and a Perkin Elmer LS55 luminescence spectrometer using FL Winlab software. All samples were contained in quartz cuvettes with a path length of 1 cm and measurements obtained relative to a reference of pure solvent contained in a matched cell.

Lifetime measurements were measured by excitation of the sample by a short pulse of light, followed by monitoring the integrated intensity of light (546 nm for terbium) emitted during a fixed gate time and set delay. Measurements were made for at least 20 delay times over a period of three or more lifetimes. A gate time of 0.1 ms was used, and the excitation and emission slits were set to 10 and 2.5 nm respectively. The obtained decay curves were plotted in Microsoft Excel and fit to the equation:

$$I = A_0 + A_1 e^{-kt}$$

where *I* is the intensity at time *t* after the flash

A_0 is the intensity after decay is completed

A_1 is the pre-exponential factor

and *k* is the rate constant for decay of the excited state.

The excited state lifetime, τ, is the inverse of the rate constan

Cell Culture and Cytotoxicity

NIH 3T3 (mouse skin fibroblast) cells were maintained in exponential growth as monolayers in DMEM (Dulbecco's Modified Eagle Medium) supplemented with 10% fetal bovine serum (FBS) and 1% penicillin and streptomycin. Cells were incubated at 37 °C, 20% average humidity and 5% (v/v) CO_2. IC_{50} values were determined using the MTT assay, as described by Carmichael[1], which makes use of the conversion of MTT (3-(4,5-dimethylthiazol-2-yl)-2,5- diphenyltetrazolium bromide) to a purple formazan product by the mitochondrial dehydrogenase of viable cells. This insoluble formazan was quantified spectrophotometrically upon dissolution in DMSO. Approximately 1 x 10^4 NIH-3T3 cells in 100 µL DMEM were seeded into each well of flat-bottomed 96-well plates and allowed to attach overnight. Complex solutions were added to triplicate wells to give final concentrations over at least a 2-log range. Following 24 h incubation, MTT (1.0 mM) was added to each well, and the plates incubated for a further 4 h. The culture medium was removed, and DMSO (150 µL) was added. The plates were shaken for 20 seconds and the absorbance measured immediately at 540 nm in a microplate reader. IC_{50} values were determined as the drug concentration required to reduce the absorbance to 50% of that in the untreated, control wells, and represent the mean for data from at least three independent experiments.

Lipophilicity

Lipophilicity was measured as the relative partitioning of the complex between water and 1-octanol. Water was saturated with 1-octanol, and 1-octanol was saturated with water. Complexes were prepared as 100 µM solutions in water and mixed with 1-octanol in 1:2, 1:1 and 2:1 water:octanol ratios. Mixtures were agitated for twelve hours, after which emission spectra of the water and octanol layers were collected. Emission spectra were measured on an Instruments SA Fluorolog 3-11 spectrometer and DataMax v2.1 for Windows. The complex concentration was calculated at the emission maximum with reference to calibration curves constructed for at least five concentrations between 0 and 100 µM in water and 1-octanol. For each mixture, the logP value was calculated according to the following equation:

$$\log P = \log_{10} \frac{[X]_{1-\text{octanol}}}{[X]_{\text{water}}}$$

Final logP values were calculated as the average of at least two replicates of the three solvent mixtures.

5.2 Synthetic Procedures

1. 2-Chloro-*N*-(2-trifluoromethyl-phenyl)-acetamide

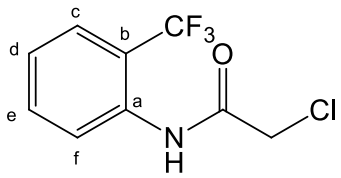

Chloroacetyl chloride (1.68 g, 14.9 mmol) was added dropwise to a solution of 2-aminobenzotrifluoride (2.00 g, 12.4 mmol) and Et_3N (1.51g , 14.9 mmol) in anhydrous CH_2Cl_2 (15 mL) at -4^oC (H_2O / ice) under argon. The reaction was stirred for 7 h, resulting in a pale yellow solution with an off-white precipitate. After filtration, the solution was washed first with dilute HCl (2 x 20 mL), followed by H_2O (2 x 20 mL). The organic phases were combined, dried over Na_2SO_4, and the solvent removed under reduced pressure. The crude product was purified by silica gel column chromatography, eluting with a gradient starting from 100% toluene to 20% CH_2Cl_2/ toluene to yield the *title compound* as a white solid (2.05 g, 69 %); m.p. 99-101^oC; ^1H NMR (700 MHz, $CDCl_3$) δ 4.21 (2H, s, CH_2Cl), 7.27 (1H, t, J= 8 Hz, H^d), 7.57 (1H, t, J= 8 Hz, H^e), 7.64 (1H, d, J= 8 Hz, H^c), 8.20 (1H, d, J= 8 Hz, H^f), 8.73 (1H, s, NH); ^{13}C NMR (176 MHz, $CDCl_3$) δ 43.1 (CH_2Cl), 120.8 (q, $^2J_{CF}$= 30 Hz, C^b), 124.1 (q, $^1J_{CF}$= 271 Hz, CF_3), 124.2 (C^f), 125.5 (C^d), 126.5 (q, $^3J_{CF}$= 5 Hz, C^c), 133.2 (C^e), 134.5 (C^a), 164.5 (CO); ^{19}F NMR (188 MHz, $CDCl_3$) δ -61.16 (CF_3); ESI/MS^- m/z 236.1 $[M–H]^-$; MS Calcd for $C_9H_6NOF_3Cl$ 236.0096. Found 236.0095; Anal Calcd for $C_9H_6NOF_3Cl$ C, 45.49; H, 2.97; N: 5.79%. Found C, 45.29; H, 2.96; N, 5.65%.

2. N-(2-Trifluoromethyl-phenyl)-2-{4,7,10-tris-[(2-trifluoromethylphenyl carbamoyl)-methyl]-1,4,7,10-tetraazacyclododec-1-yl]-acetamide

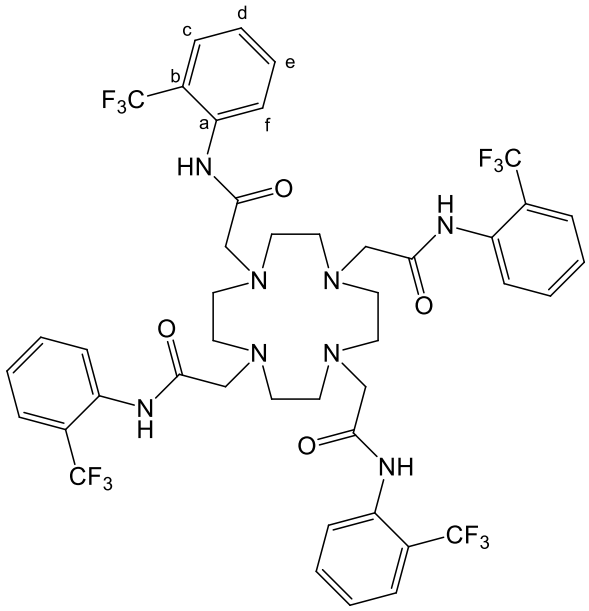

2-Chloro-*N*-(2-trifluoromethyl-phenyl)-acetamide (2.00 g, 8.43 mmol) was added to a stirred solution of 1,4,7,10 – tetraazacyclododecane (0.29 g, 1.68 mmol) and K_2CO_3 (0.23 g, 1.68 mmol) in anhydrous CH_3CN (10mL) at 85^oC under argon. The reaction was left to boil under reflux for 15 h, to give a colourless solution with a pale yellow precipitate. The precipitate was isolated by filtration and dried under reduced pressure yielding a pale yellow solid. The crude product was purified by silica gel column chromatography, eluting with a gradient starting from 100% CH_2Cl_2 to 15% CH_3OH/ CH_2Cl_2 to yield the *title compound* as a white solid (0.77 g, 47 %); m.p. 201-203^oC; ^1H NMR (700 MHz, CD_3OD) δ 2.06 – 3.59 (24H, br. m, CH_2 ring and CH_2CO), 7.14 (4H, t, J= 8 Hz, H^d), 7.46 (4H, t, J= 8 Hz, H^e), 7.52 (4H, d, J= 8 Hz, H^c), 8.20 (4H, d, J= 8Hz, H^f), 9.19 (4H, br. s, NH); ^{13}C NMR (126 MHZ, CD_3OD) δ 52.4 (br., CH_2 ring), 58.5 ($\underline{C}H_2CO$), 122.2 (q, $^2J_{CF}$= 30 Hz, C^b), 124.3 (q, $^1J_{CF}$= 272 Hz, CF_3), 124.9 (C^f), 126.3 (C^d), 126.8 (q, $^3J_{CF}$= 5 Hz, C^c), 133.6 (C^e), 135.9 (C^a), 171.1 (CO); ^{19}F NMR (188 MHz, CD_3OD) δ -60.02 (CF_3); ESI/MS^+ m/z 977.8 $[M + H]^+$.

3. $[Tb.L^1(H_2O)]^{3+}$

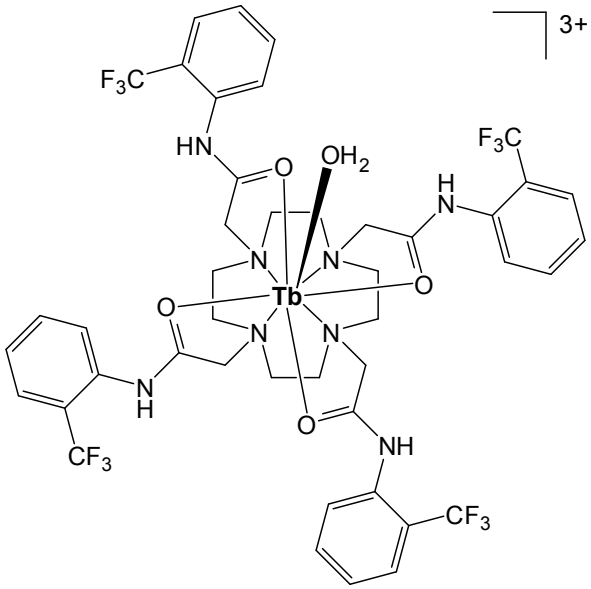

N-(2-Trifluoromethyl-phenyl)-2-{4,7,10-tris-[(2-trifluoromethyl-phenylcarbamoyl)-methyl]-1,4,7,10-tetra-cyclododec-1-yl]-acetamide (11.4 mg, 11.6 µmol) was added to a stirred solution of $Tb^{III}(OTf)_3$ (8.44 mg, 13.9 µmol) in anhydrous CH_3CN (2 mL) under argon at 85^oC. The mixture was left to boil under reflux for 15 h, and the resulting solution was added dropwise into cold Et_2O (3 x 20 mL), generating an off-white precipitate. The precipitate was isolated following centrifugation and dried to give the desired complex as a trifluoroacetate salt. The complex was dissolved in H_2O: CH_3OH (75: 25, 5 mL) and stirred for 2 hours with anion exchange resin (DOWEX 1X8 200-400 MESH Cl, pre-treated with 1M HCl) to give the chloride salt. Following filtration, the water was lyophilized to yield the hydrochloride salt as a white powder (9.22 mg, 70 %); ^1H NMR (500 MHZ, CD_3OD) Peaks range from -81.45 to 185.90. Selected peaks at : -81.45, -75.93, -62.32, -0.53, 25.59, 42.65, 99.30, 129.59, 181.81, 185.90; ^{19}F NMR (470 MHz, CD_3OD) δ -53.89 (CF_3, major species), -42.34, -51.89, -59.56, -63.43 (CF_3, minor species); ESI/MS^+ m/z 378.7 $[M]^{3+}$, 567.3 $[M-H]^{2+}$; MS Calcd for $C_{44}H_{44}N_8O_4F_{12}{}^{159}Tb$ 378.4177. Found 378.4175; τ (H_2O) 1.76 ms, τ (D_2O) 3.18 ms; q= 0.97.

4. $[Ho.L^1(H_2O)]^{3+}$

An analogous procedure to that described for **$[Tb.L^1(H_2O)]^{3+}$** was followed using N-(2-trifluoromethyl-phenyl)-2-{4,7,10-tris-[(2-trifluoromethyl-phenylcarbamoyl)-methyl]-

1,4,7,10-tetra-cyclododec-1-yl]-acetamide (13.1 mg, 13.4 µmol) and $Ho^{III}(OTf)_3$ (9.85 mg, 16.1 µmol) to yield the *title complex* as a white solid (10.4 mg, 68 %); ^{1}H NMR (500 MHZ, CD_3OD) Peaks range from -177.84 to 118.45. Selected peaks at: -177.84, -48.08, -44.00, -0.11, 8.71, 15.70, 17.31, 62.34, 118.45; ^{19}F NMR (470 MHz, CD_3OD) δ -58.97 (CF_3, major species), -47.77, -50.92, -55.66, -61.66 (CF_3, minor species); ESI/MS^+ m/z 380.0 $[M]^{3+}$, 570.9 $[M\text{-}H]^{2+}$; MS Calcd for $C_{44}H_{44}N_8O_4F_{12}{}^{165}Ho$ 380.7538. Found 380.7525; HPLC: t_R = 6.9 min.

6. $[Gd.L^1(H_2O)]^{3+}$

An analogous procedure to that described for **$[Tb.L^1(H_2O)]^{3+}$** was followed using N-(2-trifluoromethyl-phenyl)-2-{4,7,10-tris-[(2-trifluoromethyl-phenylcarbamoyl)-methyl]-1,4,7,10-tetra-cyclododec-1-yl]-acetamide (42.3 mg, 43.3 µmol) and $Gd^{III}(OTf)_3$ (31.4 mg, 51.9 µmol) to yield the *title complex* as a white solid (34.8 mg, 71 %); ^{19}F NMR (188 MHz, CD_3OD) δ -60.04 (CF_3); ESI/MS^+ m/z 566.2 $[M\text{-}H]^{2+}$; MS Calcd for $C_{44}H_{43}N_8O_4F_{12}{}^{158}Gd$ 566.6228. Found 566.6223; r_{1p} = 6.5 $mM^{-1}s^{-1}$ (20 MHz, 298 K); HPLC: t_R = 6.9 min.

7. $[Er.L^1(H_2O)]^{3+}$

An analogous procedure to that described for **$[Tb.L^1(H_2O)]^{3+}$** was followed using N-(2-trifluoromethyl-phenyl)-2-{4,7,10-tris-[(2-trifluoromethyl-phenylcarbamoyl)-methyl]-1,4,7,10-tetra-cyclododec-1-yl]-acetamide (19.4 mg, 19.9 µmol) and $Er^{III}(OTf)_3$ (14.6 mg, 23.8 µmol) to yield the *title complex* as a white solid (18.6 mg, 82 %); ^{1}H NMR (500 MHZ, CD_3OD) Peaks range from -55.76 to 100.31. Selected peaks at: -55.76, -39.03, -33.89, -25.43, -2.05 7.54, 9.32, 10.30, 81.43, 94.56, 100.31; ^{19}F NMR (470 MHz, CD_3OD): δ -63.44 (CF_3, major species), -61.16, -64.46, -68.27 (CF_3, minor species); ESI/MS^+ m/z 571.0 $[M\text{-}H]^{2+}$; MS Calcd for $C_{44}H_{43}N_8O_4{}^{166}ErF_{12}$ 570.6254. Found 570.6255.

8. $[Tm.L^1(H_2O)]^{3+}$

An analogous procedure to that described for **$[Tb.L^1(H_2O)]^{3+}$** was followed using N-(2-trifluoromethyl-phenyl)-2-{4,7,10-tris-[(2-trifluoromethyl-phenylcarbamoyl)-methyl]-1,4,7,10-tetra-cyclododec-1-yl]-acetamide (14.8 mg, 15.1 µmol) and $Tm^{III}(OTf)_3$ (11.2 mg, 18.2 µmol) to yield the *title complex* as a white solid (14.7 mg, 85 %); ^{1}H NMR

(500 MHz, CD_3OD) Peaks range from -153.56 to 100.41. Selected peaks at: -153.56, -87.42, -75.38, -21.31, -18.93, 22.30, 31.45, 42.84, 83.92, 100.41; ^{19}F NMR (470 MHz, CD_3OD) δ -65.09 (CF_3, major species), -64.08, -69.07, -75.93 (CF_3, minor species); ESI/MS^+ m/z 572.4 $[M-H]^{2+}$; MS calcd for $C_{44}H_{43}N_8O_4F_{12}{}^{169}Tm$ 572.174. Found 572.1274.

9. $[Y.L^1(H_2O)]^{3+}$

An analogous procedure to that described for **$[Tb.L^1(H_2O)]^{3+}$** was followed using N-(2-trifluoromethyl-phenyl)-2-{4,7,10-tris-[(2-trifluoromethyl-phenylcarbamoyl)-methyl]-1,4,7,10-tetra-cyclododec-1-yl]-acetamide (10.2 mg, 10.4 µmol) and $Y^{III}(OTf)_3$ (6.7 mg, 12.5 µmol) to yield the *title complex* as a white solid (8.2 mg, 74 %); ^{19}F NMR (188 MHz, CD_3OD) δ -62.51 (CF_3); ESI/MS^+ m/z 532.3 $[M-H]^{2+}$.

10. 2-Chloro-*N*-*o*-tolyl-acetamide

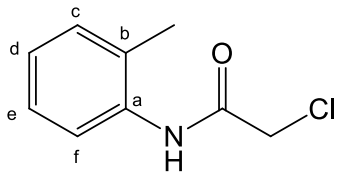

Chloroacetyl chloride (2.53 g, 22.4 mmol) was added dropwise to a solution of o-toluidine (2.0 g, 18.6 mmol) and Et_3N (2.26 g, 22.4 mmol) in anhydrous CH_2Cl_2 (15 mL) at -4°C (water / ice) under argon. The reaction was stirred for 7 h, resulting in a strong orange solution with an off-white precipitate. The precipitate was filtered off and the solution washed first with dilute HCl (2 x 20 mL), followed by H_2O (2 x 20 mL). The organic phases were combined, dried over Na_2SO_4 and the solvent removed under reduced pressure. The crude product was purified by column chromatography over silica gel, eluting with a gradient starting from 100% CH_2Cl_2 to 5% toluene / CH_2Cl_2 to yield the *title compound* as a white solid (2.46 g, 72.3 %); m.p. 109-111°C; ^1H NMR (700 MHz, $CDCl_3$) δ 2.29 (1H, s, CH_3), 4.22 (2H, s, CH_2Cl), 7.11 (1H, t, J= 8 Hz, H^d), 7.20 (1H, t, J = 8 Hz, H^e), 7.21 (1H, d, J= 8 Hz, H^f), 7.87 (1H, d, J= 8 Hz, H^c), 8.21 (1H, s, NH); ^{13}C NMR (176 MHz, $CDCl_3$) δ 17.7 (CH_3), 43.4 (CH_2), 122.6 (C^f), 125.9 (C^e), 127.2 (C^d), 129.2 (C^c), 130.8 (C^b), 134.9 (C^a), 163.9 (CO); EI/MS m/z 183.0; Anal. Calcd for $C_9H_{10}NOCl$ C, 58.86; H, 5.49; N: 7.63%. Found C, 58.59; H, 5.32; N, 7.54%.

11. N-o-Tolyl-2-[4,7,10-tris-(o-tolylcarbamoyl-methyl)1,4,7,10-tetraaza-cyclododec-1-yl]-acetamide

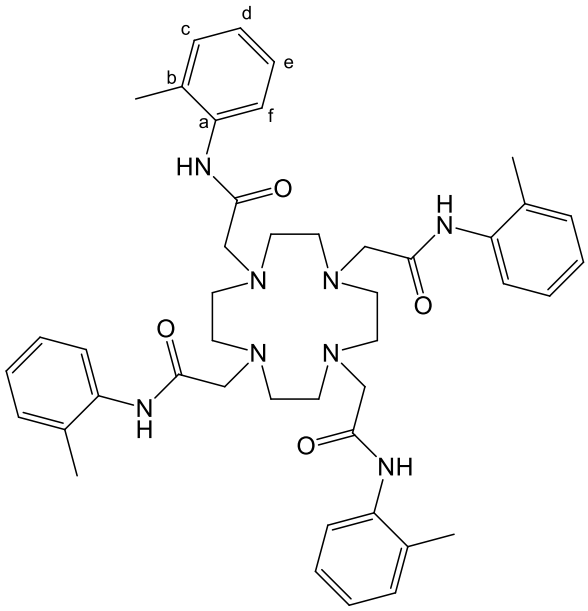

2-Chloro-*N*-*o*-tolyl-acetamide (0.32 g, 1.76 mmol) was added to a stirred solution of 1,4,7,10 – tetraazacyclododecane (0.25 g, 1.4 mmol) and K_2CO_3 (0.20 g, 1.4 mmol) in anhydrous CH_3CN (10mL) at 85^oC under argon. The reaction was left to boil under reflux for 15 h, yielding a colourless solution with a pale yellow precipitate. The precipitate was isolated by filtration, dried under reduced pressure to give the crude product as a pale yellow solid. The crude product was purified by column chromatography over silica gel, eluting with a gradient starting from 100% CH_2Cl_2 to 10% CH_3OH / CH_2Cl_2 to yield the *title compound* as a white solid (0.62 g, 58.3 %): m.p. 206- 208^oC; ^1H NMR (700 MHz, $CDCl_3$) δ 2.14, (12H, CH_3), 2.31-3.80 (24H, br. m, CH_2 ring and CH_2CO), 6.90 (4H, t, J= 8 Hz, H^d), 7.12 (4H, t, J= 8 Hz, H^e), 7.20 (4H, d, J = 8 Hz, H^f), 7.98 (4H, d, J= 8 Hz, H^c), 9.36 (4H, s, NH); ^{13}C NMR (125MHz, $CDCl_3$) δ 18.6 (CH_3), 51.9 (br., CH_2 ring), 57.2 (CH_2O), 125.9 (C^f), 126.4 (C^e), 129.2 (C^d), 130.8 (C^c), 132.5 (C^b), 136.5 (C^a), 170.7 (CO); ESI/MS^+ m/z 783.8 $[M + Na]^+$, 761.2 $[M + H]^+$; MS Calcd for $C_{44}H_{56}O_4N_8Na$ 783.4318. Found 783.4308.

12. $[Tb.L^2(H_2O)]^{3+}$

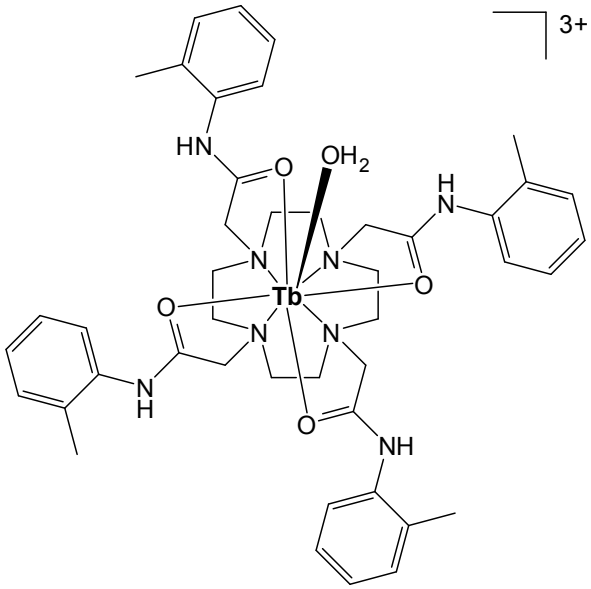

An analogous procedure to that described for **$[Tb.L^1(H_2O)]^{3+}$** was followed using N-o-tolyl-2-[4,7,10-tris-(o-tolylcarbamoyl-methyl)1,4,7,10tetraazacyclododec-1-yl]-acetamide (14.2 mg, 18.7 µmol) and $Tb^{III}(OTf)_3$ (13.6 mg, 22.4 µmol) to yield the *title complex* as a white solid (13.2 mg, 77 %); ^{1}H NMR (200 MHZ, CD_3OD) Peaks range from -130.49 to 100.23. Selected peaks at : -130.49, -92.65, -80.26, -40.56, -30.29, -18.59, -3.20, 20.36, 39.65, 65.42, 92.36, 100.23; ESI/MS$^+$ m/z 306.2 $[M]^{3+}$, 458.8 $[M-H]^{2+}$; MS Calcd for $C_{44}H_{56}O_4N_8{}^{159}Tb$ 306.4553. Found 306.4553; τ (H_2O) 1.65 ms, τ (D_2O) 2.74 ms; q= 0.90.

13. $[Gd.L^2(H_2O)]^{3+}$

An analogous procedure to that described for **$[Tb.L^1(H_2O)]^{3+}$** was followed using N-o-Tolyl-2-[4,7,10-tris-(o-tolylcarbamoyl-methyl)1,4,7,10tetraazacyclododec-1-yl]-acetamide (28.9 mg, 38.0 µmol) and $Gd^{III}(OTf)_3$ (27.6 mg, 45.6 µmol) to yield the *title complex* as a white solid (25.6 mg, 74 %); ESI/MS$^+$ m/z 305.6 $[M]^{3+}$; MS Calcd for $C_{44}H_{56}N_8O_4{}^{155}Gd$ 306.1216. Found 306.1216; r_{1p} = 3.8 $mM^{-1}s^{-1}$ (20 MHz, 298 K); HPLC: t_R = 7.1 min.

14. (4,7-Bis-*tert*-butoxycarbonylmethyl-1,4,7,10tetraaza-cyclododec-1-yl)acetic acid *tert*-butyl ester[2]

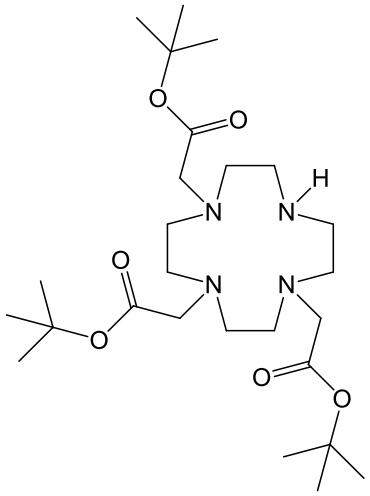

Tert-butylbromoacetate (6.61 g, 33.9 mmol) was added to a stirred solution of 1,4,7,10-tetraazacyclododecane (1.95 g, 11.28 mmol) and $NaHCO_3$ (2.83 g, 33.7 mmol) in anhydrous CH_3CN (75 mL) under argon. The reaction was left stirring overnight at room temperature. The mixture was filtered and the solvent evaporated to give a yellow oil which was purified by silica gel column chromatography, eluting with a gradient starting from 100% CH_2Cl_2 to 5% CH_3OH/ CH_2Cl_2 to yield the *title compound* as a white solid (2.86 g, 49.4 %); m.p. 181-183^oC; ^1H NMR ($CDCl_3$, 400 MHz) δ 1.42 (18H, s, ^tBu), 1.43 (9H, s, ^tBu), 2.80-2.96 (12H, br. m, CH_2 ring), 3.08 (4H, br. s, CH_2 ring), 3.26 (2H, s, CH_2CO), 3.35 (4H, s, CH_2CO), 9.92 (1H, s, NH); ^{13}C NMR ($CDCl_3$, 125 MHz) δ 27.9, 28.3 (^tBu), 47.5, 49.1, 51.2 (br., cyclen CH_2), 55.9, 57.9 (CH_2O), 81.5, 82.1 ($\underline{C}CH_3$), 169.7, 170.5 (CO); ESI/MS^+ 515.4 $[M + H]^+$; MS Calcd for $C_{26}H_{51}O_6N_4$ 515.3803.Found 515.3806.

15. {4,7-Bis-*tert*-butoxycarbonylmethyl-10-[(2-trifluoromethylphenylcarbamoyl)-methyl]-1,4,7,10 tetraaza-cyclododec-1-yl}-acetic acid *tert*-butyl ester

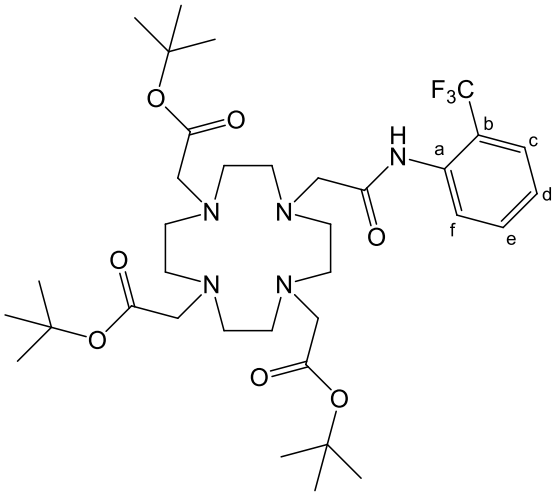

2-Chloro-*N*-(2-trifluoromethyl-phenyl)-acetamide (167 mg, 0.91 mmol) was added to a stirred solution of 1,4,7-tris(tert-butoxycarbonylmethyl)-1,4,7,10-tetraazacyclododecane (300 mg, 0.58 mmol), KI (~10 mg, as catalyst) and K_2CO_3 (0.80 g, 0.58 mmol) in anhydrous CH_3CN (20 mL) at 85^{o}C under argon. The mixture was left to boil under reflux for 15 hours, yielding an orange solution and white precipitate. The precipitate was removed by filtration and the residue washed with CH_2Cl_2 (2 x 30 mL). The solvent was removed under reduced pressure and the resulting oil purified by silica gel column chromatography, eluting with a gradient starting from 100% CH_2Cl_2 to 5% CH_3OH / CH_2Cl_2 to yield the *title compound* as a pale brown oil (254 mg, 61 %); ^{1}H NMR (400 MHz, $CDCl_3$) δ 1.43 (18H, ^{t}Bu), 1.45 (9H, ^{t}Bu), 2.02- 3.66 (24H, br., CH_2 ring and CH_2CO), 7.28 (1H, t, J= 8Hz, H^{d}), 7.43 (1H, t, J= 8Hz, H^{e}), 7.56 (2H, m, H^{c} and H^{f}), 9.97 (1H, s, NH); ^{13}C NMR (125MHz, $CDCl_3$) δ 28.1 (CH_3), 49.0, 53.7 (br., cyclen CH_2), 55.9, 56.7 ($\underline{C}H_2CO$), 82.1 ($\underline{C}CH_3$), 122.7 (q, $^{2}J_{CF}$= 30 Hz, C^{b}), 123.8 (q, $^{1}J_{CF}$= 274 Hz, CF_3), 126.1 (C^{f}), 126.4 (q, $^{3}J_{CF}$= 5 Hz, C^{c}), 129.4 (C^{d}), 132.4 (C^{e}), 135.6 (C^{a}), 172.3 (CO), 172.8 (CO), 173.1 (CO); ^{19}F NMR (188 MHz, $CDCl_3$) δ -60.80 (CF_3); ESI/MS^{+} m/z 716.3 [M + H]$^{+}$; MS Calcd for $C_{35}H_{56}O_7N_5F_3Na$ 738.4024. Found 738.4028.

16. {4,7-Bis-carboxymethyl-10-[(2-trifluoromethyl-phenylcarbamoyl)methyl]-1,4,7,10tetraaza-cyclododec-1-yl}-acetic acid

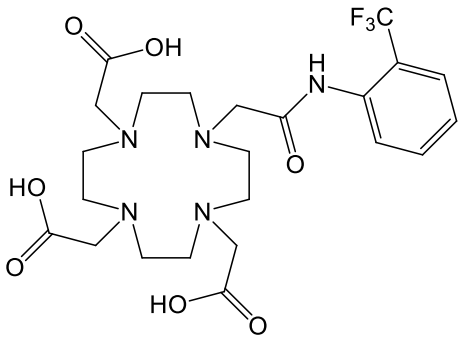

Trifluoroacetic acid (3 mL) was added to a solution of {4,7-bis-*tert*-butoxycarbonylmethyl-10-[(2-trifluoromethyl-phenylcarbamoyl)-methyl]-1,4,7,10 tetraaza-cyclododec-1-yl}-acetic acid *tert*-butyl ester (0.23 g, 0.32 mmol) in CH_2Cl_2 (5 mL). The solution was stirred at room temperature for 2 hours. The solvent was removed under reduced pressure and the resulting solid repeatedly washed with CH_2Cl_2 (5 x 5 mL), yielding the product as a trifluoroacetate salt. The residue was dissolved in H_2O (5 mL) and left to stir for 2 hours with anion exchange resin (DOWEX 1X8 200-400 MESH Cl, pre-treated with 1M HCl) in H_2O to give the chloride salt. The resin was filtered and the solvent removed under reduced pressure to yield the *title compound* as a light yellow oil (0.13 g, 74 %); ^{1}H NMR (400 MHz, D_2O) δ 3.09- 3.60 (16H, br., CH_2 ring), 3.92 (2H, br., CH_2CO), 7.25- 7.94 (4H, br. m, Ar); ^{19}F NMR (188 MHz, $CDCl_3$) δ -62.31 (CF_3); MS (ES^+) m/z 570.4 $[M + Na]^+$.

17. [Tb.L^3(H_2O)]

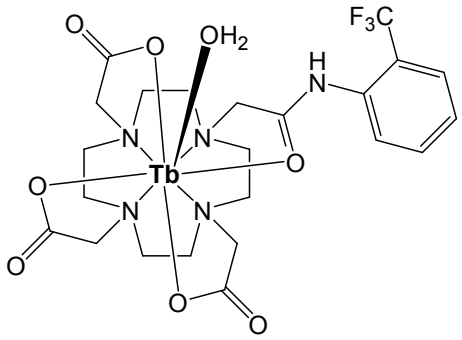

{4,7-Bis-carboxymethyl-10-[(2-trifluoromethyl-phenylcarbamoyl)methyl]-1,4,7,10 tetraaza-cyclododec-1-yl}-acetic acid (45.8 mg, 83.6 µmol) was dissolved in H_2O (3

mL) and the pH adjusted to ~6. $Tb^{III}Cl_3$ (26.6 mg, 0.10 mmol) was added to the solution, which was subsequently left to boil under reflux for 3 h. Once cooled, the solvent was removed under reduced pressure and the complex purified by alumina chromatography, eluting with a gradient starting from 5% MeOH/ CH_2Cl_2 to 20% MeOH/ CH_2Cl_2 (36.4 mg, 62 %); ^{1}H NMR (200 MHZ, D_2O, pD 5.4) Peaks range from -405.23 to 263.19. Selected peaks at: -405.23, -401.36, -371.42, -356.98, -151.46, -132.09, -108.12, -100.04, -83.45, -42.78, 82.33, 118.32, 126.59, 140.23, 223.78, 230.24, 254.00, 263.19; ^{19}F NMR (188 MHz, D_2O, pD 5.4): δ -51.94 (CF_3, major species), -60.18, -44.912, -39.78, -36.68 (CF_3, minor species); ESI/$MS^{+/-}$ m/z 742.1 $[M+K]^+$, 702.2 $[M-H]^-$; MS Calcd for $C_{23}H_{28}O_7N_5F_3{}^{159}Tb$ 702.1198. Found 702.1189; τ (H_2O) 1.76 ms, τ (D_2O) 2.76 ms; q= 0.75; HPLC: t_R = 5.8 min.

18. [Ho.L^3(H_2O)]

An analogous procedure to that described for **[Tb.L^3(H_2O)]** was followed using {4,7-bis-carboxymethyl-10-[(2-trifluoromethyl-phenylcarbamoyl)methyl]-1,4,7,10tetraaza-cyclododec-1-yl}-acetic acid (15.2 mg, 27.7 µmol) and $Ho^{III}(OAc)_3$ (11.4 mg, 33.3 µmol) to yield the *title complex* as a white solid (12.4 mg, 63 %); ^{1}H NMR (200MHz, D_2O, pD 5.4) Peaks range from -93.47 to 92.51. Selected peaks at: -93.47, -79.34, -69.09, -58.23, -47.42, -36.03, -32.12, 14.86, 18.69, 23.04, 28.93, 44.19, 55.31, 86.32, 92.51; ^{19}F NMR (376 MHz, D_2O, pD 5.4) δ -64.24 (CF_3, major species), -62.72, -62.13, -60.45, -57.90, -56.21, -54.20, -50.84 (CF_3, minor species); ESI/$MS^{+/-}$ m/z 732.1 $[M+Na]^+$, 708.2 $[M-H]^-$; MS Calcd for $C_{23}H_{28}O_7N_5F_3{}^{165}Ho$ 708.1250. Found 708.1250.

19. [Gd.L^3(H_2O)]

An analogous procedure to that described for **[Tb.L^3(H_2O)]** was followed using {4,7-bis-carboxymethyl-10-[(2-trifluoromethyl-phenylcarbamoyl)methyl]-1,4,7,10-tetraaza-cyclododec-1-yl}-acetic acid (63.2 mg, 0.12 mmol) and $Gd^{III}(OAc)_3$ (46.3 mg, 0.14 mmol) to yield the *title complex* as a white solid (68.3 mg, 81 %); ^{19}F NMR (376 MHz, D_2O, pD 5.4): δ -62.82 (CF_3); ESI/$MS^{+/-}$ m/z 701.3 $[M-H]^-$, 725.2 $[M+Na]^+$, 741.2 $[M+K]^+$; MS Calcd for $C_{23}H_{28}O_7N_5F_3{}^{155}Gd$ 698.1172. Found 698.1162; r_{1p} = 5.5 $mM^{-1}s^{-1}$ (20 MHz, 298 K).

20. [Er.L^3(H_2O)]

An analogous procedure to that described for **[Tb.L^3(H_2O)]** was followed using {4,7-bis-carboxymethyl-10-[(2-trifluoromethyl-phenylcarbamoyl)methyl]-1,4,7,10-tetraaza-cyclododec-1-yl}-acetic acid (38.7 mg, 70.1 µmol) and $Er^{III}Cl_3$ (23.2 mg, 84.8 µmol) to yield the *title complex* as a white solid (35.4 mg, 71 %); ^{1}H NMR (500 MHz, D_2O, pD 5.4) Peaks range from -101.68 to 164.03. Selected peaks at: -101.68, -89.93, -84.39, -80.42, -71.36, -66.49, -57.56, -56.00, -38.10, -32.14, -29.47, 14.61, 15.95, 18.69, 21.86, 33.45, 128.93, 136.42, 153.89, 164.03; ^{19}F NMR (188 MHz, D_2O, pD 5.4) δ -64.65 (CF_3, major species), -76.21, -70.45, -69.23, -62.72, -61.78, -58.30, -54.81 (CF_3, minor species); ESI/$MS^{+/-}$ m/z 709.3 $[M-H]^-$, 751.2 $[M+K]^+$; MS Calcd for $C_{23}H_{28}O_7N_5{}^{166}ErF_3$ 709.1249. Found 709.1240.

21. [Tm.L^3(H_2O)]

An analogous procedure to that described for **[Tb.L^3(H_2O)]** was followed using {4,7-bis-carboxymethyl-10-[(2-trifluoromethyl-phenylcarbamoyl)methyl]-1,4,7,10-tetraaza-cyclododec-1-yl}-acetic acid (26.0 mg, 47.5 µmol) and $Tm^{III}(OAc)_3$ (19.7 mg, 56.9 µmol) to yield the *title complex* as a white solid (19.3 mg, 57 %); ^{1}H NMR (500 MHz, D_2O, pD 5.4) Peaks range from -246.31 to 380.04. Selected peaks at: -246.31, -215.46, -208.69, -150.69, -142.56, -119.56, -92.58, -80.45, -71.87, -25.31, 18.91, 24.58, 35.89, 40.01, 45.69, 79.35, 320.56, 340.23, 380.04; ^{19}F NMR (188 MHz, D_2O, pD 5.4) δ -75.91 (CF_3, major species), -88.11, -87.34, - 80.77, -77.39, -66.82, -49.54 (CF_3, minor species); ESI/$MS^{+/-}$ m/z 736.2 $[M+Na]^+$, 712.2 $[M-H]^-$; MS Calcd for $C_{23}H_{28}O_7N_5F_3{}^{169}Tm$ 712.1289. Found 712.1278.

22. [Y.L^3(H_2O)]

An analogous procedure to that described for **[Tb.L^3(H_2O)]** was followed using {4,7-bis-carboxymethyl-10-[(2-trifluoromethyl-phenylcarbamoyl)methyl]-1,4,7,10-tetraaza-cyclododec-1-yl}-acetic acid (12.3 mg, 22.4 µmol) and $Y^{III}Cl_3$ (5.3 mg, 26.9 µmol) to yield the *title complex* as a white solid (9.1 mg, 64 %); ^{19}F NMR (188 MHz, D_2O, pD 5.4) δ -61.98 (CF_3); ESI/$MS^{+/-}$ m/z 656.2 $[M+Na]^+$, 632.2 $[M-H]^-$; MS Calcd for $C_{23}H_{29}F_3N_5O_7Na^{89}Y$ 656.0969. Found 656.0970.

23. 1,5-Dimethyl (2*S*)-2-brompentanedioate

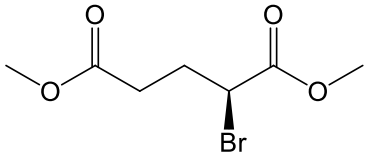

A solution of sodium nitrite (5.50 g, 80.1 mmol) dissolved in H_2O (50mL) was added dropwise to a stirred solution of sodium bromide (16.0 g, 156 mmol) and L-glutaric acid 5 methyl ester (6.41 g, 39.8 mmol) in 1M HBr (250mL), cooled at -5^{o}C. After 18 h, conc. H_2SO_4 (1mL) was added dropwise to the reaction mixture, which was subsequently extracted with diethyl ether (2 x 250 mL). The combined organic extracts were washed with brine (2 x 200 mL), dried over $MgSO_4$, filtered, and the solvent removed under reduced pressure. The crude material was dissolved in anhydrous CH_3OH to which conc. H_2SO_4 (0.5 mL) was added. The solution was left to stir at 50^{o}C under argon for 4 h. Once cooled, the solvent was removed under reduced pressure and the crude material purified by silica gel column chromatography, eluting with a gradient starting from 100 % toluene to 15 % CH_2Cl_2 / toluene to yield the *title compound* as a colourless viscous oil (5.89 g, 62 %); ^{1}H NMR (400 MHz, $CDCl_3$) δ 2.26 (1H, m, C$\underline{H}_2$CHBr), 2.36 (1H, m, C$\underline{H}_2$CHBr), 2.50 (2H, m, C$\underline{H}_2$CH$_2$CHBr), 3.67 (3H, s, CH_3), 3.76 (3H, s, CH_3), 4.36 (1H, dd, = 9, 1 Hz, CH); ^{13}C NMR (126 MHz, $CDCl_3$) δ 29.7 (C$\underline{H}_2$CH$_2$CHBr), 31.2 (C$\underline{H}_2$CHBr), 44.5 (CH), 51.8 (CH_3), 53.0 (CH_3), 169.8 (C=O), 172.4 (C=O); ESI/MS^{+} m/z 239.0 $[M+H]^{+}$; MS Calcd for $C_7H_{12}O_4Br$ 238.9919. Found 238.9914.

24. 2-(1,4,7,10-Tetraazacyclododecane-1-yl)-N-[2-trifluoromethyl) phenyl]acetamide

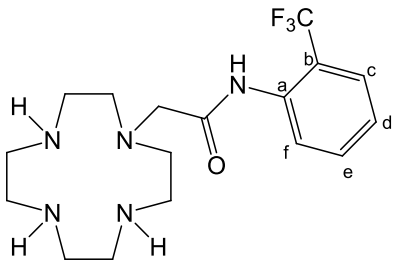

2-Chloro-*N*-(2-trifluoromethyl-phenyl)-acetamide (0.20 g, 0.84 mmol) was added to a stirred solution of 1,4,7,10 – tetraazacyclododecane (1.45 g, 8.43 mmol) and K_2CO_3 (0.12 g, 0.84 mmol) in anhydrous CH_3CN (10mL) at 55^{o}C under argon. After 16 h, the

solvent was removed under reduced pressure and the residue dissolved in CH_2Cl_2 (20 mL). The solution was washed repeatedly with H_2O (4 x 20 mL), dried over $MgSO_4$, and the solvent removed under reduced pressure to yield the *title compound* as a light yellow solid (0.12 g, 38 %); m.p. 123- 125^oC; ^1H NMR (700 MHz, $CDCl_3$) δ 2.62 – 2.77 (18 H, br. m., CH_2 ring and CH_2O), 7.22 (1H, t, J= 8 Hz, H^d), 7.51 (1H, t, J= 8 Hz, H^e), 7.58 (1H, d, J= 8 Hz, H^c), 7.98 (1H, d, J= 8 Hz, H^f), 9.51 (1H, s, NH); ^{13}C NMR (176 MHz, $CDCl_3$) δ 45.9, 46.5, 47.4 (CH_2 ring), 60.9 ($\underline{C}H_2CO$), 122.0 (q, $^2J_{CF}$= 30 Hz, C^b), 124.2 (q, $^1J_{CF}$= 273 Hz, CF_3), 125.3 (C^f), 126.4 (C^d), 126.5 (q, $^3J_{CF}$= 5 Hz, C^c), 132.9 (C^e), 135.3 (C^a), 170.5 (C=O); ^{19}F NMR (188 MHz, $CDCl_3$) δ -60.72 (CF_3); ESI/MS^+ m/z 374.3 $[M+H]^+$; MS Calcd for $C_9H_6NOF_3Cl$ 374.2162. Found 374.2165.

25. 1,5-Dimethyl (2R)-2-{4,7-bis[(2R)-1,5-dioxopentan-2-yl]-10-({[2-(trifluoromethyl)phenyl]carbomyl}methyl)-1,4,7,10-tetraazacyclododecan-1-yl}pentanedioate

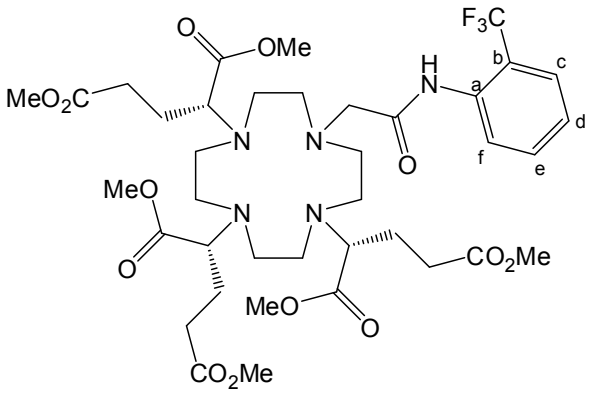

1,5-Dimethyl (2S)-2-bromopentanedioate (0.26 g, 1.11 mmol) was added to a stirred solution of 2-(1,4,7,10-tetraazacyclododecane-1-yl)-N-[2-trifluoromethyl)phenyl] acetamide (0.10 g , 0.28 mmol) and K_2CO_3 (0.15 g, 1.11 mmol) in anhydrous CH_3CN (30 mL) at 85^oC under argon. The mixture was left to boil under reflux for 15 h, yielding an orange solution and white precipitate. The precipitate was removed by filtration and the residue washed with CH_2Cl_2 (2 x 30ml). The solvent was removed under reduced pressure and the resulting oil purified by silica gel column chromatography, eluting with a gradient starting from 100% CH_2Cl_2 to 2 % CH_3OH / CH_2Cl_2 to yield the *title compound* as a colourless viscous oil (0.19 g, 82 %); ^1H NMR (400 MHz, $CDCl_3$) δ 1.78 (6H, m, $CHC\underline{H}_2$), 2.01 (6H, m, $CHCH_2C\underline{H}_2$), 2.44 (6H, m, CH_2

ring), 2.53 – 2.68 (6H, br. m, CH_2 ring), 2.75 – 2.98 (4H, br. m, CH_2 ring), 3.07 (2H, m, CH_2CO), 3.32 (1H, s, CH), 3.36 (2H, s, CH), 3.64 (6H, s, CH_3), 3.66 (12H, s, CH_3), 7.21 (1H, t, J = 8 Hz, H^d), 7.54 (1H, t, J = 8 Hz, H^e), 7.60 (1H, d, J= 8 Hz, H^c), 8.14 (1H, d, J= 8 Hz, H^f), 9.69 (1H, s, NH); ^{13}C NMR (106 MHz, $CDCl_3$) δ 24.8, 25.0 ($CH\underline{C}H_2$), 30.6, 30.8 ($CHCH_2\underline{C}H_2$), 50.0, 50.2 ($\underline{C}H_3$), 51.0, 51.5, 51.8, 52.8, (br., CH_2 ring) 61.3 (CH_2CO), 62.0, 62.6 (CH), 121.3 (q, $^2J_{CF}$ = 30 Hz, C^b), 124.2 (q, $^1J_{CF}$ = 273 Hz, CF_3), 124.5 (C^f), 126.9 (C^d), 127.0 (q, $^3J_{CF}$ = 5 Hz, C^c), 134.6 (C^e), 138.2 (C^a), 168.6 (CONH), 174.3 ($\underline{C}OCH_3$); ^{19}F NMR (376 MHz, $CDCl_3$) δ -60.87 (CF_3); ESI/MS^+ m/z 848.8 $[M+H]^+$; MS Calcd for $C_{38}H_{57}O_{13}N_5F_3$ 848.3900 Found 848.3902.

26. (2R)-2-{4-[(2R)-1-Carboxy-5-methoxy-1,5-dioxopentan-2-yl]-10-[(1R)-1,3 dicarboxypropyl]-7-({[2-(trifluoromethyl)phenyl]carbamoyl}methyl)-1,4,7,10-tetraazacyclododecan-1-yl}pentanedioic acid

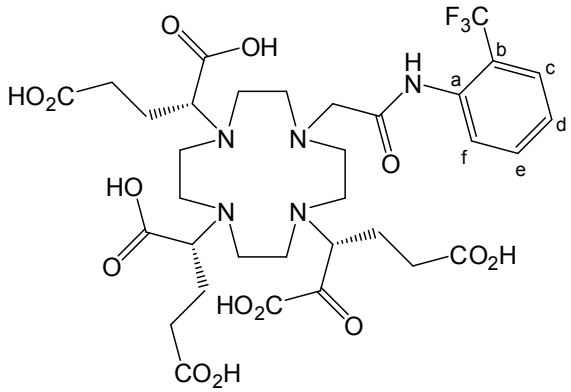

Freshly made aqueous KOD solution (1.0 mL, 0.1 M) was added to 1,5-dimethyl (2R)-2-{4,7-bis[(2R)-1,5-dioxopentan-2-yl]-10-({[2-(trifluoromethyl)phenyl]carbomyl} methyl)-1,4,7,10-tetraazacyclododecan-1-yl}pentanedioate (0.15 g, 0.18 mmol). The reaction was kept under argon at 40^{o}C and monitored by ^{1}H NMR. After 5 h, no ester methyl groups were observed in the ^{1}H NMR spectrum. The pH of the mixture was increased to ~6 and the solution loaded onto a DOWEX strong cation exchange resin. The column was eluted with 100% water to 10% NH_4OH and fractions were analysed by $ESMS^+$. The fractions were combined and lyphilised to yield the *title compound* as a pale yellow oil (0.11 g, 77 %); ^{1}H NMR (400 MHz, D_2O) δ 1.83 (6H, m, $CHC\underline{H}_2$), 2.12 (6H, m, $CHCH_2C\underline{H}_2$), 2.40- 2.73 (12H, br. m, CH_2 ring), 2.80 – 3.04 (4H, br. m, CH_2 ring), 3.12 (2H, br., CH_2CO), 3.38 (3H, s, CH), 7.18 (1H, t, J = 8 Hz, H^d), 7.49 (1H, t, J = 8

Hz, H^e), 7.66 (1H, d, J= 8 Hz, H^c), 8.18 (1H, d, J= 8 Hz, H^f), 10.04 (1H, br. s, NH); ^{19}F NMR (376 MHz, D_2O, pD 5.4) δ -61.23 (CF_3); ESI/MS^+ m/z 806.3 $[M+H]^+$.

27. $[Tb.L^4(H_2O)]^{3-}$

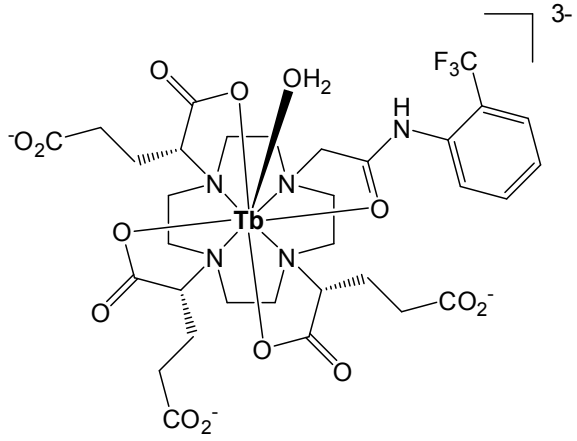

(2R)-2-{4-[(2R)-1-Carboxy-5-methoxy-1,5-dioxopentan-2-yl]-10-[(1R)-1,3 dicarboxypropyl]-7-({[2-(trifluoromethyl)phenyl]carbamoyl}methyl)-1,4,7,10-tetraazacyclododecan-1-yl}pentanedioic acid (23.1 mg, 28.7 µmol) was dissolved in H_2O (3 mL) and the pH adjusted to ~6. $Tb^{III}(OAc)_3$ (11.6 mg, 34.4 µmol) was added to the solution, which was subsequently left to boil under reflux for 3 h. Once cooled, the pH of the solution was increased to ~9.5 resulting in a clear solution and white precipitate. The precipitate was removed by centrifugation. The crude product was purified using benzoylated dialysis tubing (9 mm flat width, MWCO 500) to yield the *title complex* as its sodium salt (17.7 mg, 63 %); ^1H NMR (200 MHZ, D_2O, pD = 5.4) Peaks range from -90.63 to 120.15. Selected peaks at: -90.63, -56.93, -48.91, -35.62, -30.26, -29.35, -18.04, 23.74, 26.98, 28.00, 82.56, 84.03, 94.20, 120.15; ^{19}F NMR (376 MHz, D_2O, pD 5.4) δ –59.1 (CF_3, major species), -67.59, -60.47, -56.76, -51.86, -51.69, -45.36, -42.09 (CF_3, minor species); ESI/MS^+ m/z 958.1 $[M+Na]^+$; τ (H_2O) 1.69 ms, τ (D_2O) 2.86 ms; q= 0.90; HPLC: t_R =7.1 min.

28. $[Gd.L^4(H_2O)]^{3-}$

An analogous procedure to that described for **$[Tb.L^4(H_2O)]^{3-}$** was followed using (2R)-2-{4-[(2R)-1-carboxy-5-methoxy-1,5-dioxopentan-2-yl]-10-[(1R)-1,3dicarboxypropyl]-7-({[2-(trifluoromethyl)phenyl]carbamoyl}methyl)-1,4,7,10-tetraazacyclododecan-1-yl}pentanedioic acid (26.3 mg, 32.6 µmol) and $Gd^{III}(OAc)_3$ (13.1 mg, 39.2 µmol) to

yield the *title complex* as a white solid (26.8 mg, 84 %); ^{19}F NMR (376 MHz, D_2O, pD 5.4) δ –60.96 (CF_3); ESI/MS^+ m/z 972.1 $[M+K]^+$; r_{1p} = 5.92 $mM^{-1}s^{-1}$ (60 MHz, 310 K).

29. $[Er.L^4(H_2O)]^{3-}$

An analogous procedure to that described for **$[Tb.L^4(H_2O)]^{3-}$** was followed using (2R)-2-{4-[(2R)-1-carboxy-5-methoxy-1,5-dioxopentan-2-yl]-10-[(1R)-1,3dicarboxypropyl]-7-({[2-(trifluoromethyl)phenyl]carbamoyl}methyl)-1,4,7,10-tetraazacyclododecan-1-yl}pentanedioic acid (15.9 mg, 19.7 µmol) and $Gd^{III}(OAc)_3$ (8.2 mg, 23.7 µmol) to yield the *title complex* as a white solid (14.8 mg, 76 %); ^{1}H NMR (200 MHZ, D_2O, pD = 5.4) Peaks range from -62.03 to 83.71. Selected peaks at: -62.03, -48.36, -47.03, -52.10, -22.96, 19.04, 22.14, 36.80, 48.02, 83.71; ^{19}F NMR (376 MHz, D_2O, pD 5.4) δ –63.50 (CF_3, major species), -64.82, -62.90, -58.32; ESI/MS^+ m/z 943.8 $[M+H]^+$.

30. $[Tm.L^4(H_2O)]^{3-}$

An analogous procedure to that described for **$[Tb.L^4(H_2O)]^{3-}$** was followed using (2R)-2-{4-[(2R)-1-carboxy-5-methoxy-1,5-dioxopentan-2-yl]-10-[(1R)-1,3dicarboxypropyl]-7-({[2-(trifluoromethyl)phenyl]carbamoyl}methyl)-1,4,7,10-tetraazacyclododecan-1-yl}pentanedioic acid (18.2 mg, 22.6 µmol) and $Tm^{III}(OAc)_3$ (9.4 mg, 27.1 µmol) to yield the *title complex* as a white solid (18.1 mg, 81 %); ^{1}H NMR (200 MHZ, D_2O, pD = 5.4) Peaks range from -128.09 to 150.85. Selected peaks at: -128.09, -99.30, -68.20, -52.90, -48.78, - 24.71, 22.14, 36.99, 50.03, 89.04, 90.52, 109.70, 150.85; ^{19}F NMR (376 MHz, D_2O, pD 5.4) δ –73.9 (CF_3, major species), -70.69, -68.32, -67.51; ESI/MS^+ m/z 984.0 $[M+K]^+$.

31. Ethyl[(4,7-di{[ethoxy(methyl)phoshoryl]methyl}-10-({[2(trifluoromethyl) phenyl]carbamoyl}methyl)-1,4,7,10-tetraazacyclodecan-1-yl)methyl](methyl) phosphinate

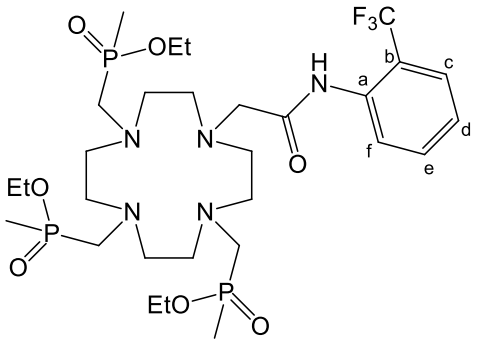

2-(1,4,7,10-Tetraaza-cyclododec-1-yl)-*N*-(2-trifluoromethyl-phenyl)-acetamide (0.72 g, 1.93 mmol) was heated to 80^{o}C in anhydrous tetrahydrofuran under argon. Paraformaldehyde (0.26 g, 8.67 mmol) followed by diethoxymethylphosphine (1.18 g, 8.67 mmol) were added. The solution was boiled at reflux over molecular sieves. After 15 h, the excess paraformaldehyde was removed by filtration and the solvent removed under reduced pressure. The resulting orange oil was purified by alumina gel column chromatography, eluting with a gradient starting from 100% CH_2Cl_2 to 1.7 % CH_3OH / CH_2Cl_2 to yield the *title compound* as a pale yellow oil (0.96 g, 68 %); ^{1}H NMR (400 MHz, $CDCl_3$) δ 1.15 (9H, m, CH_3), 1.36 (9H, m, CH_3), 2.41-3.98 (22H, br. m, CH_2 ring and CH_2P), 3.16 (2H, s, CH_2CO), 3.91 (6H, m, $C\underline{H}_2CH_3$), 7.07 (1H, t, J= 7 Hz, H^{d}), 7.41 (1H, t, J= 8 Hz, H^{e}), 7.46 (1H, d, J = 8 Hz, H^{c}), 8.11 (1H, d, J=7 Hz, H^{f}), 9.61 (1H, s, NH); ^{13}C NMR (176 MHz, $CDCl_3$) δ 13.4 (d, $^{1}J_{CP}$= 90 Hz, PCH_3), 16.95 (CH_3), 53.4 (d, $^{3}J_{CP}$ = 84 Hz, CH_2P), 54.5, 54.6, 55.2 (br., CH_2 ring), 60.5 ($\underline{C}H_2CO$), 62.1 (br., $\underline{C}H_2CH_3$) 121.0 (q, $^{2}J_{CF}$= 30 Hz, C^{b}), 124.2 (q, $^{1}J_{CF}$= 273 Hz, CF_3), 125.4 (C^{f}), 126.4 (C^{d}), 127.6 (q, $^{3}J_{CF}$ = 5 Hz, C^{c}), 133.2 (C^{e}), 135.8 (C^{a}), 169.3 (C=O); ^{31}P NMR (162 MHz, $CDCl_3$) δ 52.33 (1P, s, PCH_3), 52.47 (2P, s, PCH_3); ^{19}F NMR (376 MHz, $CDCl_3$) δ -60.98 (CF_3), -60.94 (CF_3); ESI/MS^{+} m/z 734.3 $[M + H]^{+}$, 756.3 $[M+Na]^{+}$; MS Calcd for $C_{29}H_{54}N_5O_7P_3$ 734.3188. Found 734.3210.

32. [(4,7,-Di{[hydroxyl(methyl)phosphoryl]methyl}-10-({[2-(trifluoromethyl)phenyl] carbamoyl}methyl)-1,4,7,10-tetraazacyclododecan-1-yl)methyl](methyl)phosphinic acid

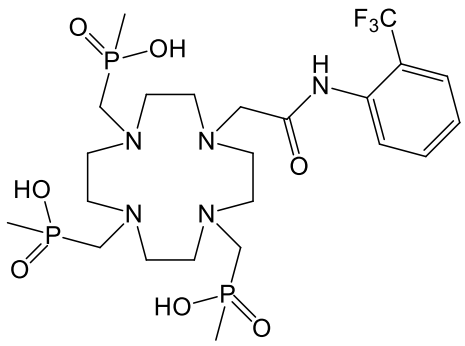

Freshly prepared aqueous KOD solution (5 mL, 0.1 M) was added to ethyl [(4,7-di{[ethoxy(methyl)phoshoryl]methyl}-10-({[2-(trifluoromethyl)phenyl]carbamoyl} methyl)-1,4,7,10-tetraazacyclodecan-1-yl)methyl](methyl)phosphinate (61.0 mg, 83.2 µmol). The solution was left to stir at 40^{o}C under argon and the reaction monitored by ^{1}H and ^{31}P NMR. After 6 h, the pH of the solution was lowered to ~6 by the addition of HCl. The solvent was removed under reduced pressure and the residue washed repeatedly with CH_2Cl_2 (3 x 5 mL). The resulting oil was dissolved in ethanol. The white precipitate was removed by filtration and the solvent removed under reduced pressure to yield the title compound as a pale yellow oil (40.9 mg, 74 %); ^{1}H NMR (400 MHz, D_2O) δ 1.12 (9H, d, J=13 Hz, PCH_3), 2.56-3.83 (22H, br. m, cyclen CH_2 and CH_2P), 3.20 (2H, s, CH_2CO), 7.14 (1H, m, Ar), 7.24 (1H, m, Ar), 7.48 (1H, m, Ar), 7.60 (1H, br. , Ar), 9.50 (1H, s, NH); ^{31}P NMR (162 MHz, D_2O) δ 40.62 (3P, s, PCH_3); ^{19}F NMR (376 MHz, D_2O) δ – 61.28 (CF_3); ESI/MS^{+} m/z 650.9 $[M + H]^{+}$.

33. [Tb.L^5]

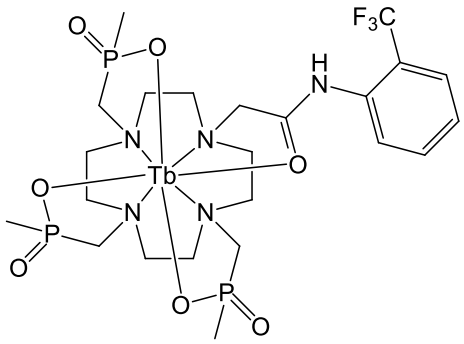

An analogous procedure to that described for **[Tb.L^3(H$_2$O)]** was followed using [(4,7,-di{[hydroxyl(methyl)phosphoryl]methyl}-10-({[2-(trifluoromethyl)phenyl] carbamoyl}methyl)-1,4,7,10-tetraazacyclododecan-1-yl)methyl](methyl)phosphinic acid (0.10 g, 0.15 mmol) and $Tb^{III}(OAc)_3$ (0.06 g, 0.18 mmol) to yield the *title complex* as a white solid (0.10 g, 85 %); ^{1}H NMR (500 MHZ, D_2O, pD= 5.4) Peaks range from -418.56 to 480.02. Selected peaks at : -418.56, -351.48, 225.61, -161.08, -158.47, -136.41, 184.07, -174.08, 81.32, 115.96, 110.41, 138.07, 156.71, 283.67, 383.43, 480.02; ^{19}F NMR (188 MHz, D_2O) δ – 45.89 (CF_3); ESI/MS$^{+/-}$ m/z 828.2 $[M+Na]^+$, 804.2 $[M-H]^-$; MS Calcd for $C_{23}H_{37}O_7N_5F_3P_3{}^{159}Tb$ 804.1111. Found 804.1110; τ (H_2O) 3.13 ms, τ (D_2O) 3.57 ms; q= 0; HPLC: t_R = 9.4 min.

34. [Dy.L^5]

An analogous procedure to that described for **[Tb.L^3(H$_2$O)]** was followed using [(4,7,-di{[hydroxyl(methyl)phosphoryl]methyl}-10-({[2-(trifluoromethyl)phenyl]carbamoyl} methyl)-1,4,7,10-tetraazacyclododecan-1-yl)methyl](methyl)phosphinic acid (0.10 g, 0.15 mmol) and $Dy^{III}(OAc)_3$ (0.06 g, 0.18 mmol) to yield the *title complex* as a white solid (0.10 g, 81 %); ^{1}H NMR (500 MHZ, D_2O, pD = 5.4) Peaks range from -268.12 to 183.70. Selected peaks at : -268.12, -212.04, -187.35, -147.96, -83.45, -49.03, -35.01, -19.63, 40.07, 81.09, 99.68, 116.43, 174.51, 183.70; ^{19}F NMR (188 MHz, D_2O) δ – 63.71 (CF_3); ESI/MS$^-$ m/z 805.1 $[M-H]^-$; MS Calcd for $C_{23}H_{37}O_7N_5F_3P_3{}^{160}Dy$ 805.1110. Found 805.1142.

35. [Ho.L^5]

An analogous procedure to that described for **[Tb.L^3(H$_2$O)]** was followed using [(4,7,-di{[hydroxyl(methyl)phosphoryl]methyl}-10-({[2-(trifluoromethyl)phenyl]carbamoyl} methyl)-1,4,7,10-tetraazacyclododecan-1-yl)methyl](methyl)phosphinic acid (0.10 g, 0.15 mmol) and $Ho^{III}(OAc)_3$ (0.06 g, 0.18 mmol) to yield the *title complex* as a white solid (0.09 g, 71 %); ^{1}H NMR (500 MHZ, D_2O, pD = 5.4) Peaks range from -200.32 to 204.60. Selected peaks at : -200.32, -162.54, -136.20, -117.74, -90.83, -52.19, 50.13, 57.32, 78.48, 99.60, 153.65, 200.32; ^{19}F NMR (188 MHz, D_2O) δ -61.20 (CF_3); ESI/MS$^{+/-}$ m/z 834.2 $[M+Na]^+$, 810.2 $[M-H]^-$; MS Calcd for $C_{23}H_{37}O_7N_5F_3P_3{}^{165}Ho$ 810.1161. Found 810.1136.

36. [Er.L^5]

An analogous procedure to that described for **[Tb.L^3(H$_2$O)]** was followed using [(4,7,-di{[hydroxyl(methyl)phosphoryl]methyl}-10-({[2-(trifluoromethyl)phenyl]carbamoyl} methyl)-1,4,7,10-tetraazacyclododecan-1-yl)methyl](methyl)phosphinic acid (0.10 g, 0.15 mmol) and $Er^{III}(OAc)_3$ (0.06 g, 0.18 mmol) to yield the *title complex* as a white solid (0.06 g, 49 %); ^{1}H NMR (500 MHZ, D_2O, pD= 5.4) Peaks range from -168.09 to 180.65. Selected peaks at : -168.09, -140.26, -132.82, -107.81, -60.5, -45.09, -20.47, 32.17, 45.78, 58.92, 74.18, 107.45, 112.95, 140.85, 172.65, 180.65; ^{19}F NMR (188 MHz, D_2O) δ -72.78 (CF_3); ESI/MS$^+$ m/z 815.1 $[M+H]^+$, 837.1 $[M+Na]^+$; MS Calcd for $C_{23}H_{39}O_7N_5F_3P_3{}^{168}Er$ 815.1445. Found 815.1395.

37. [Tm.L^5]

An analogous procedure to that described for **[Tb.L^3(H$_2$O)]** was followed using [(4,7,-di{[hydroxyl(methyl)phosphoryl]methyl}-10-({[2-(trifluoromethyl)phenyl]carbamoyl} methyl)-1,4,7,10-tetraazacyclododecan-1-yl)methyl](methyl)phosphinic acid (0.10 g, 0.15 mmol) and $Tm^{III}(OAc)_3$ (0.06 g, 0.18 mmol) to yield the *title complex* as a white solid (0.11 g, 89 %); ^{1}H NMR (500 MHZ, D_2O, pD= 5.4) Peaks range from -361.35 to 169.39. Selected peaks at : -361.35, -340.68, -270.63, -230.49, -199.76, -177.18, -161.41, -93.79, -64.16, -40.56, 20.64, 30.09, 40.49, 44.42, 59.16, 93.32, 128.51, 145.28, 157.04, 169.39; ^{19}F NMR (188 MHz, D_2O) δ -90.59 (CF_3); ESI/MS$^+$ m/z 816.1 $[M+H]^+$; MS Calcd for $C_{23}H_{39}O_7N_5F_3P_3{}^{169}Tm$ 816.1357. Found 816.1348.

38. 2-Methyl-7-(trifluoromethyl)quinoline

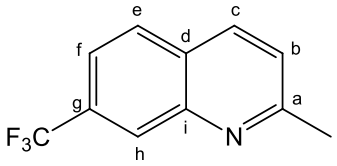

3-(Trifluoromethyl)aniline (2.01 g, 12.4 mmol) and crotonaldehyde (0.87 g, 12.4 mmol) were dissolved in concentrated HCl (6 mL) and the solution was stirred at 90^{o}C. After 18 h, the solution was neutralised carefully with 1 M KOH, keeping the temperature of the solution at 0^{o}C. The crude was extracted into CH_2Cl_2 (2 x 10 mL) and washed repeatedly with H_2O (3 x 10 mL). The organic layer was dried over $MgSO_4$ and the solvent removed under reduced pressure. The crude product was purified by silica gel column chromatography, eluting with a gradient starting from 100% CH_2Cl_2 to 5 % CH_3OH/ CH_2Cl_2 to yield the *title compound* as a viscous dark orange oil (1.10 g, 42 %); ^{1}H NMR (400 MHz, $CDCl_3$) δ 2.66 (3H, CH_3), 7.26 (1H, d, J = 9 Hz, H^{b}), 7.53 (1H, d, J = 8 Hz, H^{f}), 7.73 (1H, d, J = 8 Hz, H^{e}), 7.94 (1H, d, J= 9 Hz, H^{c}), 8.23 (1H, s, H^{h}); ^{13}C NMR (176 MHz, $CDCl_3$) δ 22.6 (CH_3), 121.5 (q, $^{3}J_{CF}$= 4 Hz, C^{f}), 124.1 (C^{d}), 124.2 (q, $^{1}J_{CF}$= 273 Hz, CF_3), 126.8 (q, $^{3}J_{CF}$= 4 Hz, C^{h}), 128.2 (C^{b}), 128.8 (C^{c}), 131.3 (q, $^{2}J_{CF}$= 33 Hz, C^{g}), 136.1 (C^{e}), 147.1 (C^{i}), 160.9 (C^{a}); ^{19}F NMR (188 MHz, $CDCl_3$) δ -63.04 (CF_3); ESI/MS^{+} m/z 212.1 $[M+H]^{+}$; MS Calcd for $C_{11}H_9NF_3$ 212.0687. Found 212.0685.

39. 2-(Dibromomethyl)-7-(trifluoromethyl)quinoline

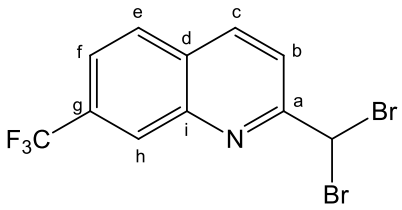

N-bromosuccinimide (0.42 g, 2.3 mmol) and benzoyl peroxide (10.2 g, 0.41 mmol) were added to a solution of 2-methyl-7-(trifluoromethyl)quinoline (0.45 g, 2.1 mmol) in CCl_4 (18 mL) at 80^{o}C under argon. After 15 h, the solvent was removed under reduced pressure and the crude material was purified by silica gel column chromatography, eluting with a gradient starting from 100% hexane to 2% ethyl

acetate/ hexane to yield the title compound as a white solid (0.16 g, 21%); m.p. 138-139^{o}C; ^{1}H NMR (400 MHz, $CDCl_3$) δ 6.80 (1H, CH), 7.76 (1H, d, J = 9 Hz, H^b), 7.97 (1H, d, J = 9 Hz, H^f), 8.09 (1H, d, J = 9 Hz, H^e), 8.33 (1H, d, J= 9 Hz, H^c), 8.36 (1H, s,H^h); ^{13}C NMR (126 MHz, $CDCl_3$) δ 51.2 (CH), 121.8 (C^d), 123.7 (q, $^{3}J_{CF}$= 4 Hz, C^f), 124.0 (q, $^{1}J_{CF}$= 273 Hz, CF_3), 127.7 (q, $^{3}J_{CF}$= 4 Hz, C^h), 128.9 (C^b), 129.0 (C^c), 132.4 (q, $^{2}J_{CF}$= 33 Hz, $\underline{C}CF_3$), 138.3 (C^e), 145.1 (C^i), 160.0 (C^a); ^{19}F NMR (188 MHz, $CDCl_3$) δ -63.20 (CF_3); ESI/MS^{+} m/z 367.9 $[M+H]^{+}$; MS Calcd for $C_{11}H_7NBr_2F_3$ 367.8897. Found 367.8895.

40. 2-(Bromomethyl)-7-(trifluoromethyl)quinoline

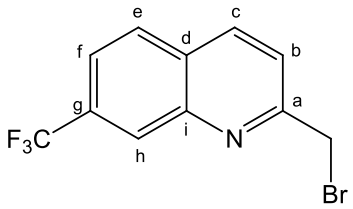

Procedure A:

2-(Dibromomethyl)-7-(trifluoromethyl)quinoline (0.16 g, 0.44 mmol) was added to a mixture of diethylphosphite (0.18 g, 1.3 mmol) and diisopropylamine (0.15 g, 1.5 mmol) in anhydrous THF (5 mL) at 0^{o}C under argon. After 48 h, the crude mixture was slowly poured into ice water (20 mL) and then extracted into CH_2Cl_2 (2 x 20 mL). The combined organic extracts were dried over $MgSO_4$ and the solvent removed under reduced pressure. The crude material was purified by silica gel column chromatography, eluting with a gradient starting from 100% hexane to 2% ethyl acetate/ hexane to yield the title compound as a white solid (0.11 g, 89 %).

Procedure B:

N-bromosuccinimide (0.42 g, 2.3 mmol) and benzoyl peroxide (10.0 mg, 0.41 mmol) were added to a solution of 2-methyl-7-(trifluoromethyl)quinoline (0.45 g, 2.1 mmol) in CCl_4 (18 mL) at 80^{o}C under argon. After 15 h, the solvent was removed under reduced pressure and the crude material was purified by silica gel column chromatography, eluting with a gradient starting from 100% hexane to 2% ethyl acetate/ hexane to yield the title compound as a white solid (0.25 g, 40 %); ^{1}H NMR (700 MHz, $CDCl_3$) δ 4.70 (2H, CH_2), 7.67 (1H, d, J = 8 Hz, H^b), 7.71 (1H, d, J = 8 Hz, H^f), 7.92 (1H, d, J = 8 Hz, H^e), 8.21 (1H, d, J= 8 Hz, H^c), 8.38 (1H, s, H^h); ^{13}C NMR (126 MHz, $CDCl_3$) δ 34.0 (CH_2), 122.9 (q, $^{3}J_{CF}$= 4 Hz, C^f), 123.3 (C^d), 124.0 (q, $^{1}J_{CF}$= 273 Hz, CF_3),

127.40 (q, $^{3}J_{CF}$= 4 Hz, C^{h}), 128.9 (C^{b}), 129.1 (C^{c}), 131.9 (q, $^{2}J_{CF}$= 33 Hz, C^{g}), 137.3 (C^{e}), 146.8 (C^{i}), 158.7 (C^{a}); ^{19}F NMR (376 MHz, $CDCl_3$) δ -63.26 (CF_3); ESI/MS^+ m/z 290.0 $[M+H]^+$; MS Calcd for $C_{11}H_8NBrF_3$ 289.9792. Found 289.9794.

41. 2-(1,4,7,10-Tetraazacyclododecan-1-ylmethyl)-7-(trifluoromethyl)quinoline

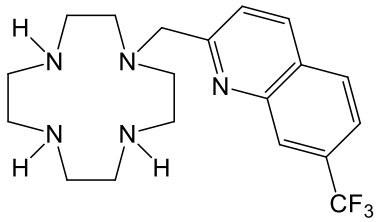

2-(Bromomethyl)-7-(trifluoromethyl)quinoline (0.14 g, 0.48 mmol) was added to a stirred solution of cyclen (0.83 g, 4.8 mmol) in anhydrous CH_3CN at 55^{o}C under argon. After 3 h, the solvent was removed under reduced pressure. The crude residue was dissolved in CH_2Cl_2 (20 mL) and washed repeatedly with H_2O (5 x 30 mL). The organic layer was dried over $MgSO_4$ and the solvent removed under reduced pressure to yield the crude product. This was used without further purification. ESI/MS^+ m/z 382.2 $[M+H]^+$.

42. Ethyl[(4,7-di{[ethoxy(methyl)phosphoryl]methyl}-10-{[7-(trifluoromethyl) quinolin-2-yl]methyl}-1,4,7,10-tetraazacyclododecan-1yl)methyl](methyl) phosphinate

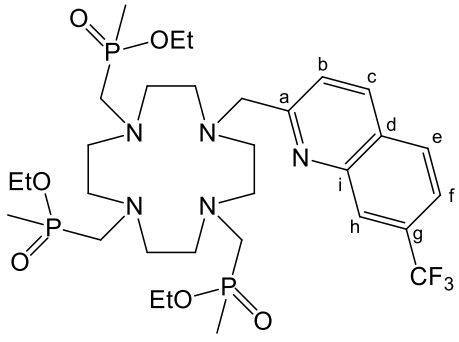

2-(1,4,7,10-Tetraazacyclododecan-1-ylmethyl)-7-(trifluoromethyl)quinoline (0.54 g, 1.41 mmol) was heated to 80^{o}C in anhydrous tetrahydrofuran (10 mL) under argon. Paraformaldehyde (0.19 g, 6.35 mmol) followed by diethoxymethylphosphine (0.85

g, 6.35 mmol) were added. The solution was boiled at reflux over molecular sieves. After 15 h, the excess paraformaldehyde was removed by filtration and the solvent removed under reduced pressure. The resulting orange oil was purified by alumina gel column chromatography, eluting with a gradient starting from 100% CH_2Cl_2 to 0.9 % CH_3OH / CH_2Cl_2 to yield the *title compound* as a pale yellow oil (0.12 g); ^{1}H NMR (400 MHz, $CDCl_3$) δ 1.27 (9H, m, CH_3), 1.43 (9H, m, CH_3), 2.62- 3.18 (22H, br. m, CH_2 ring and CH_2P), 4.04 (6H, m, $C\underline{H}_2CH_3$), 4.21 (2H, CH_2), 7.72 (2H, m, H^b and H^f), 7.90 (1H, d, J = 8 Hz, H^e), 8.19 (1H, d, J = 8 Hz, H^c), 8.32 (1H, s, H^h); ^{13}C NMR (176 MHz, $CDCl_3$) δ 14.2 (d, $^1J_{CP}$= 86 Hz, PCH_3), 16.9 (CH_3), 52.9 (d, $^3J_{CP}$ = 95 Hz, CH_2P), 53.2, 54.6, 54.8 (br., CH_2 ring), 60.7 ($\underline{C}H_2CO$), 61.9 (br., $\underline{C}H_2CH_3$) 121.0 (q, $^3J_{CF}$= 4 Hz, C^f), 122.4 (C^d), 123.6 (q, $^1J_{CF}$= 273 Hz, CF_3), 127.0 (q, $^3J_{CF}$= 4 Hz, C^h), 128.2 (C^b), 129.1 (C^c), 131.6 (q, $^2J_{CF}$= 33 Hz, C^g), 136.7 (C^e), 146.6 (C^i), 174.3 (C^a); ^{31}P NMR (162 MHz, $CDCl_3$) δ 53.48 (2P, s, PCH_3), 53.71 (1P, s, PCH_3); ^{19}F NMR (376 MHz, $CDCl_3$) δ -63.08 (CF_3), -63.03 (CF_3); ESI/MS$^+$ m/z 742.3 $[M+H]^+$; MS Calcd for $C_{31}H_{54}N_5O_6P_3F_3$ 742.3239. Found 742.3235.

43. [(4,7-Di{[hydroxy(methyl)phosphoryl]methyl}-10-{[7-(trifluoromethyl)quinolin-2-yl]methyl}-1,4,7,10-tetraazacyclododecan-1-yl)methyl](methyl)phosphinic acid

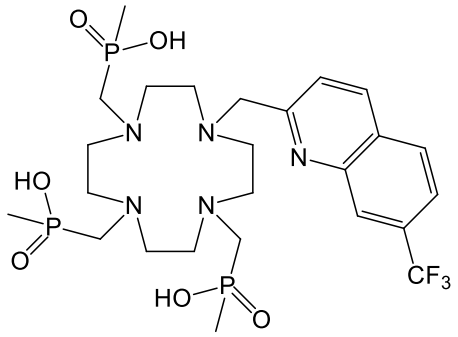

Freshly prepared aqueous KOD solution (5 mL, 0.1 M) was added to ethyl [(4,7-di{[ethoxy(methyl)phosphoryl]methyl}-10-{[7-(trifluoromethyl)quinolin-2-yl]methyl}-1,4,7,10-tetraazacyclododecan-1-yl)methyl](methyl)phosphinate (0.12 g, 0.16mmol). The solution was left to stir at 40^{o}C under argon and the reaction monitored by ^{1}H and ^{31}P NMR. After 24 h, the pH of the solution was lowered to ~6 by addition of HCl. The solvent was removed under reduced pressure and the residue washed

repeatedly with CH_2Cl_2 (3 x 5 mL). The resulting oil was dissolved in ethanol. The white precipitate was removed by filtration and the solvent removed under reduced pressure to yield the title compound as a colourless oil (87.2 mg, 82 %); ^{1}H NMR (400 MHz, D_2O) δ 1.52 (9H, m, CH_3), 2.42- 3.21 (22H, br. m, CH_2 ring and CH_2P), 4.18 (2H, CH_2), 7.80 (1H, d, J = 8 Hz, Ar), 8.04 (2H, m, Ar), 8.19 (1H, d, J = 8 Hz, Ar), 8.20 (1H, s, Ar); ^{31}P NMR (162 MHz, D_2O) δ 40.64 (3P, s, PCH_3); ^{19}F NMR (376 MHz, D_2O, pD = 5.4) δ -62.82 (CF_3); ESI/MS$^{+/-}$ m/z 658.2 $[M+H]^+$.

44. [Tb.L^6]

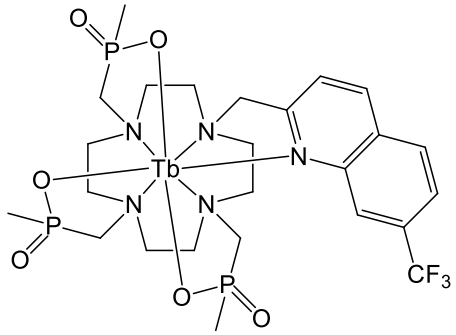

An analogous procedure to that described for **[Tb.L^3(H$_2$O)]** was followed using [(4,7-di{[hydroxy(methyl)phosphoryl]methyl}-10-{[7-(trifluoromethyl)quinolin-2-yl]methyl}-1,4,7,10-tetraazacyclododecan-1-yl)methyl](methyl)phosphinic acid (42 mg, 63.8 µmol) and $Tb^{III}(OAc)_3$ (25.7 mg, 76.6 µmol) to yield the *title complex* as a white solid (43.7 mg, 81 %); ^{1}H NMR (200 MHZ, D_2O, pD= 5.4) Peaks range from -318.12 to 256.01. Selected peaks at : -318.12, -263.12, -220.78, -201.36, -160.47, -102.41, -98.04, -60.12, -40.32, 56.41, 104.32, 112.56, 170.89, 190.45, 200.63, 256.01; ^{19}F NMR (188 MHz, D_2O) δ -180.16 (CF_3); ESI/MS$^{+/-}$ m/z 836.2 $[M+Na]^+$, 853.0 $[M+K]^+$; MS Calcd for $C_{25}H_{38}O_6N_5F_3P_3Na^{159}Tb$ 836.1138. Found 836.1140; τ (H_2O) 2.70 ms, τ (D_2O) 3.57 ms; q= 0.15; HPLC: t_R = 10.6 min.

45. [Tm.L^6]

An analogous procedure to that described for **[Tb.L^3(H$_2$O)]** was followed using [(4,7-di{[hydroxy(methyl)phosphoryl]methyl}-10-{[7-(trifluoromethyl)quinolin-2-yl]methyl}-1,4,7,10-tetraazacyclododecan-1-yl)methyl](methyl)phosphinic acid (30 mg, 45.6 µmol) and $Tm^{III}(OAc)_3$ (18.9 mg, 54.7 µmol) to yield the *title complex* as a white solid (30.1 mg, 77 %); ^{1}H NMR (200 MHZ, D_2O, pD= 5.4) Peaks range from -392.04 to 420.56. Selected peaks at: -392.04, -295.47, -241.18, -190.78, -163.74, -

142.92, -97.41, -41.79, 47.12, 67.51, 121.36, 148.50, 176.98, 369.41, 420.56; ^{19}F NMR (188 MHz, D_2O) δ -64.51 (CF_3); ESI/MS$^{+/-}$ m/z 824.2 $[M+H]^+$; MS Calcd for $C_{25}H_{39}O_6N_5F_3P_3{}^{169}Tm$ 824.1410. Found 824.1411.

46. (±) Dimethyl-2-bromoglutarate[3]

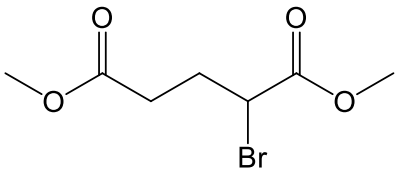

Glutaric acid monomethyl ester (12.0 g, 82.0 mmol) was added to thionyl chloride (25 mL, 0.34 mol) and the mixture was heated at 70^{o}C for 2 h. Molecular bromine (4.7 mL, 0.09 mol) was added dropwise to the solution over a period of 2 h, after which the reaction mixture was allowed to cool to rt. After 14 h, the mixture was poured onto CH_3OH (40 mL) cooled on crushed ice and stirred for a further 3 h. H_2O (40 mL) was added to the reaction mixture and the aqueous phase was extracted with diethyl ether (3 x 40 mL). The combined organic extracts were washed with H_2O (30 mL) followed by 5 % $NaHCO_3$ solution (30 mL). The organic phase was dried over $MgSO_4$, filtered and the solvent removed under reduced pressure. The crude material was placed into a micro distillation apparatus equipped with a Vigreux column (bath temperature 130^{o}C) and the title compound was distilled at 70^{o}C/ 0.1 mm Hg (10.9 g, 55 %); ^{1}H NMR (400 MHz, $CDCl_3$) δ 2.41 (2H, m, C$\underline{H}_2$CH), 2.45 (2H, m, CH_2CO), 3.60 (3H, s, CH_3), 3.71 (3H, s, CH_3), 4.37 (1H, t, J= 8 Hz, CHBr); ^{13}C NMR (125 MHz, $CDCl_3$) δ 29.81 ($\underline{C}H_2$CH), 31.60 ($CH_2\underline{C}$O), 44.91 (CHBr), 52.13, 55.19 (CH_3), 169.9 ($\underline{C}$OCH), 172.69 ($\underline{C}OCH_2$); ESI/MS$^+$ m/z 260.1 $[M + Na]^+$.

47. 1,7-Bis(α-dimethylglutarate)-1,4,7,10-tetraazacyclododecane[4]

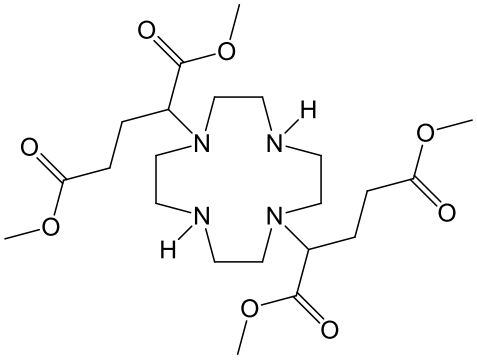

Racemic dimethyl-2-Bromoglutarate (6.10 g, 25.5 mmol) was added to a stirred solution of 1,4,7,10-tetraazacyclododecane (2.02 g, 11.6 mmol) and $NaHCO_3$ (2.14 g, 25.5 mmol) in anhydrous CH_3CN (30 mL) under argon at 55°C. the reaction was monitored by TLC (10% CH_3OH/ CH_2Cl_2). After 5 days the dimethyl-2- bromoglutarate had been consumed. The solvent was removed under reduced pressure and the resulting oil dissolved in CH_2Cl_2. The solution was washed with HCl, dried over $MgSO_4$, and the solvent removed under reduced pressure. The crude product was purified by silica gel column chromatography eluting with a gradient starting from 100% CH_2Cl_2 to 12 % CH_3OH/ CH_2Cl_2 to yield the *title compound* as a pale yellow oil (1.05 g, 18 %); ^{1}H NMR (400 MHz, $CDCl_3$) δ 1.87 (4H, m, CH_2CH), 2.30 (4H, m, CH_2CO), 2.33- 3.10 (16H, br., CH_2 ring), 3.26 (2H, m, CHBr), 3.52 (3H, s, CH_3), 3.68 (3H, CH_3), 7.72 (2H, s, NH); ^{13}C NMR (125 MHz, $CDCl_3$) δ 22.4 ($\underline{C}H_2CH$), 29.8 ($\underline{C}H_2CO$), 46.8, 48.9 (CH_2 ring), 51.7, 51.9 (CH_3), 64.2 (CHBr), 173.0 ($\underline{C}OCH$), 173.4 ($\underline{C}OCH_2$); ESI/MS$^+$ m/z 489.4 $[M + H]^+$.

48. 2-{7-(1,3-Bis-methoxycarbonyl-propyl)-4,10-bis-[(2-trifluoromethyl-phenylcarbamoyl)-methyl]-1,4,7,10-tetraaza-cyclododec-1-yl}-pentanedioic acid dimethyl ester

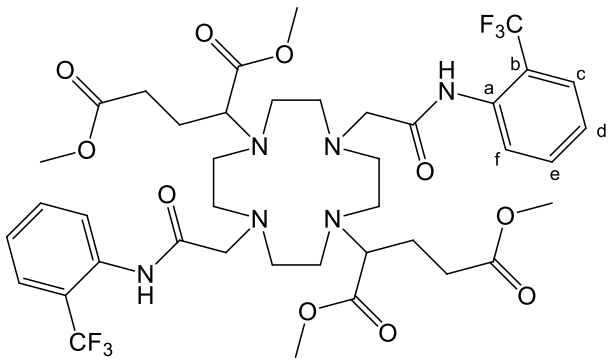

2-Chloro-*N*-(2-trifluoromethyl-phenyl)-acetamide (0.12 g, 0.50 mmol) was added to a stirred solution of 1,7-bis(α-dimethylglutarate)-1,4,7,10-tetraazacyclododecane (0.12 g, 0.25 mmol), KI (~5 mg) and K_2CO_3 (71.2 mg, 0.5 mmol) in anhydrous CH_3CN (10 mL) at 85°C under argon. The mixture was left to boil under reflux for 18 h, yielding a dark orange solution and white precipitate. The precipitate was removed by filtration and the residue washed with CH_2Cl_2 (2 x 30mL). The solvent was removed under reduced pressure and the resulting oil purified by silica gel column

chromatography, eluting with a gradient starting from 100% CH_2Cl_2 to 5 % CH_3OH / CH_2Cl_2 to yield the *title compound* as a pale yellow oil (0.11 g, 55 %); ^{1}H NMR (400 MHz, $CDCl_3$) δ 1.80- 3.41 (30 H, br. m, CH_2 ring, C<u>H</u>CH_2, C<u>H</u>$_2$CH, C<u>H</u>$_2$CH$_2$CH, C<u>H</u>$_2$CO), 3.60 (6H, s, CH_3), 3.63 (6H, s, CH_3), 7.21 (2H, t, J= 8 Hz, H^d), 7.60 (4H, m, H^e and H^c), 8.10 (2H, d, J= 8 Hz, H^f), 9.60 (2H, s, NH); ^{13}C NMR (125 MHz, $CDCl_3$) δ 22.9 (<u>C</u>H$_2$CH), 31.2 (<u>C</u>H$_2$CO), 49.0, 50.1-50.3 (br., CH_2 ring), 51.9, 52.4 (CH_3), 63.7 (CHBr), 120.5 (q, $^2J_{CF}$= 30 Hz, C^b), 122.6 (q, $^1J_{CF}$= 272 Hz, CF_3), 124.8 (C^f), 125.3 (C^d), 126.4 (q, $^3J_{CF}$= 5 Hz, C^c), 133.0 (C^e), 136.9 (C^a), 170.1, 172.5, 174.3 (CO); ^{19}F NMR (188 MHz, $CDCl_3$) δ 60.98 (CF_3), -60.88 (CF_3); ESI/MS$^+$ m/z 891.0 $[M + H]^+$; MS Calcd for $C_{40}H_{53}O_6N_6F_6$ 891.3722. Found 891.3728.

49. 2-{7-(1,3-Dicarboxy-propyl)-4,10-bis-[(2-trifluoromethyl-phenylcarbamoyl)-methyl]-1,4,7,10-tetraaza-cyclododec-1-yl}-pentanedioic acid

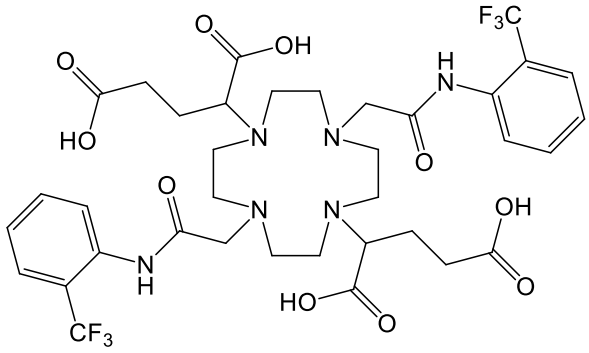

Freshly made aqueous KOD solution (2.5 mL, 0.1 M) was added to 2-{7-(1,3-bis-methoxycarbonyl-propyl)-4,10-bis-[(2-trifluoromethyl-phenylcarbamoyl)-methyl]-1,4,7,10-tetraaza-cyclododec-1-yl}-pentanedioic acid dimethyl ester (0.10 g, 0.11 mmol). The reaction was kept under argon and monitored by ^{1}H NMR. After 5 h, no ester methyl groups were observed in the ^{1}H NMR spectrum. The pH of the mixture was lowered to ~6 and the solution loaded onto a DOWEX strong cation exchange resin. The column was eluted with 100% water to 10% NH_4OH and fractions were analysed by ESMS$^+$. The fractions were combined and lyphilised to yield the title compound as a pale yellow oil (64 mg, 62 %); ^{1}H NMR (400 MHz, D_2O) δ 1.94- 3.40 (30 H, br. m, cyclen CH_2, C<u>H</u>CH_2, C<u>H</u>$_2$CH, C<u>H</u>$_2$CH$_2$CH, C<u>H</u>$_2$CO), 7.09 (2H, t, J= 8 Hz, Ar), 7.66 (4H, m, Ar), 8.08 (2H, m, Ar); ^{19}F NMR (376 MHz, D_2O) δ -61.10 (CF_3), ESI/MS$^+$ m/z 836.4 $[M + H]^+$.

50. $[Tb.L^{7a}(H_2O)]^-$

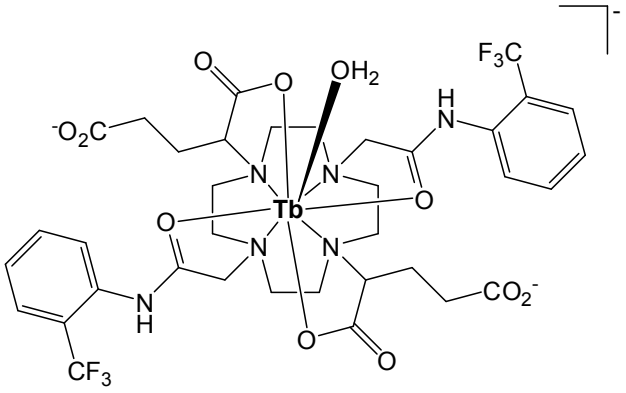

An analogous procedure to that described for **$[Tb.L^4(H_2O)]^{3-}$** was followed using 2-{7-(1,3-dicarboxy-propyl)-4,10-bis-[(2-trifluoromethyl-phenylcarbamoyl)-methyl]-1,4,7,10-tetraaza-cyclododec-1-yl}-pentanedioic acid (20 mg, 23.9 µmol) and $Tb^{III}(OAc)_3$ (10.0 mg, 29.8 µmol) to yield the *title complex* as a white solid (17 mg, 72 %); ^{1}H NMR (200 MHz, D_2O, pD 5.4) Peaks range from -130.45 to 92.30. Selected peaks at: -130.45, -110.24, -90.86, -87.42, -65.32, -61.23, -60.40, -38.07, 31.78, 48.78, 50.14, 51.63, 87.99, 92.30; ^{19}F NMR (188 MHz, D_2O, pD 5.4) δ -58.91 (CF_3, major species), - 57.43, 63.49, 72.10 (CF_3, minor species); ESI/MS$^+$ m/z 1014.2 $[M + Na]^+$; τ (H_2O) 1.78 ms, τ (D_2O) 3.23 ms; q = 0.90; HPLC: t_R = 4.9 min.

51. $[Gd.L^{7a}(H_2O)]^-$

An analogous procedure to that described for **$[Tb.L^4(H_2O)]^{3-}$** was followed using 2-{7-(1,3-dicarboxy-propyl)-4,10-bis-[(2-trifluoromethyl-phenylcarbamoyl)-methyl]-1,4,7,10-tetraaza-cyclododec-1-yl}-pentanedioic acid (40.0 mg, 47.9 µmol) and $Gd^{III}(OAc)_3$ (19.2 mg, 57.3 µmol) to yield the *title complex* as a white solid (32.2 mg, 68 %); ^{19}F NMR (188 MHz, D_2O, pD 5.4) δ -61.42 (CF_3); r_{1p} = 8.0 $mM^{-1}s^{-1}$ (20 MHz, 298 K).

52. N-[2-(Trifluoromethyl)phenyl]-2-[7-({[2-trifluoromethyl)phenyl]carbamoyl} methyl)-1,4,7,10-tetraazacyclododecane-1-yl]acetamide

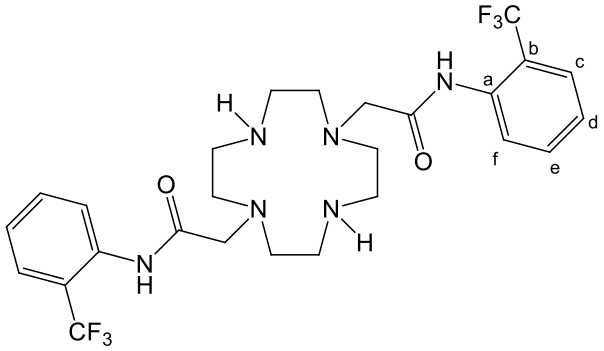

2-Chloro-*N*-(2-trifluoromethyl-phenyl)-acetamide (1.42 g, 5.99 mmol) was added to a stirred solution of 1,4,7,10-Tetraazacyclododecane (0.34 g, 2.0 mmol) and Et_3N (0.61 g, 6.0 mmol) in anhydrous ethanol (20 mL) at 50^{o}C under argon. After 18 h, crude mixture was poured onto 1M HCl (20 mL) and washed with Et_2O (2 x 30 mL). The aqueous layer was neutralised with 1M NaOH and then extracted into CH_2Cl_2 (3 x 30 mL). The organic extracts were combined, dried over $MgSO_4$, and the solvent removed to yield the *title compound* as a light yellow oil (0.43 g, 37 %); ^{1}H NMR (400 MHz, $CDCl_3$) δ 2.79- 2.84 (16H, br. m, CH_2 ring), 2.34 (4H, s, CH_2CO), 7.16 (2H, t, J = 7 Hz, H^{d}), 7.41 (2H, t, J = 7 Hz, H^{e}), 7.51 (2H, d, J= 7 Hz, H^{c}), 7.77 (2H, d, J= 7 Hz, H^{f}), 9.56 (2H, br., NH); ^{13}C NMR (500 MHz, $CDCl_3$) δ 45.1, 51.9 (CH_2 ring), 59.9 ($\underline{C}H_2CO$), 121.0 (q, $^{2}J_{CF}$= 30 Hz, C^{b}), 124.1 (q, $^{1}J_{CF}$= 272 Hz, CF_3), 124.3 (C^{f}), 125.5 (C^{d}), 126.4 (q, $^{3}J_{CF}$= 5 Hz, C^{c}), 132.6 (C^{e}), 133.2 (C^{a}), 171.4 (CO); ^{19}F NMR (376 MHz, D_2O) δ –60.84 (CF_3); ESI/MS^{+} m/z 575.3 $[M+H]^{+}$; MS Calcd for $C_{26}H_{33}O_2N_6F_6$ 575.2563. Found 575.2561.

53. 1,5-Dimethyl (2R)-2-[7-[(2R)-1,5-dimethoxy-1,5-dioxopenta-2-yl]-4,10-bis({[2-(trifluoromethyl)phenyl]carbamoyl}methyl)-1,4,7,10-tetraazacyclododecan-1-yl}pentanedioate

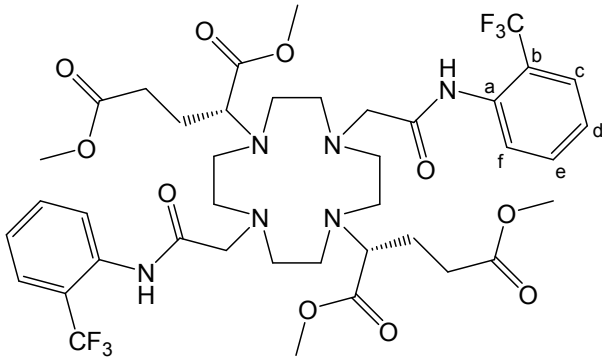

(S)-2-Bromo-pentanedioic acid dimethyl ester (0.42 g, 1.76 mmol) was added to a stirred solution of N-[2-(trifluoromethyl)phenyl]-2-[7-({[2-trifluoromethyl) phenyl]carbamoyl}methyl)-1,4,7,10-tetraazacyclododecane-1-yl]acetamide (0.46 g , 0.80 mmol) and K_2CO_3 (0.24 g, 1.76 mmol) in anhydrous CH_3CN (20 mL) at 85^oC under argon. The mixture was left to boil under reflux for 18 h, yielding a pale yellow solution and white precipitate. The precipitate was removed by filtration and the residue washed with CH_2Cl_2 (2 x 30ml). The solvent was removed under reduced pressure and the resulting oil purified by silica gel column chromatography, eluting with a gradient starting from 100% CH_2Cl_2 to 3.5 % CH_3OH / CH_2Cl_2 to yield the *title compound* as a colourless viscous oil (0.38 g, 54 %); ^{1}H NMR (700 MHz, $CDCl_3$) δ 1.84 (4H, m, CHC$\underline{H}_2$), 2.08 (4H, m, CHCH$_2$C$\underline{H}_2$), 2.39 (6H, m, CH_2 ring), 2.51 (2H, m, CH_2 ring), 2.62 (2H, m, CH_2 ring), 2.73 (2H, m, CH_2 ring), 2.75 – 2.90 (4H, br m, CH_2 ring), 2.98 – 3.21 (4H, br m, CH_2CO), 3.32 (2H, s, CH), 3.58 (6H, s, CH_3), 3.64 (6H, s, CH_3), 7.19 (2H, t, J = 8 Hz, H^d), 7.52 (2H, t, J = 8 Hz, H^e), 7.58 (2H, d, J= 8 Hz, H^c), 8.17 (2H, d, J= 8 Hz, H^f), 9.58 (2H, s, NH); ^{13}C NMR (700 MHz, $CDCl_3$) δ 25.1 (CH$\underline{C}H_2$), 30.8 (CHCH$_2\underline{C}H_2$), 50.3, 50.4 (CH_3), 51.2, 51.3, 51.7, 51.8, 53.5 (CH_2 ring), 60.8 ($\underline{C}H_2CO$), 62.2, 62.8 (CH), 120.4 (q, $^2J_{CF}$= 30 Hz, C^b), 124.6 (q, $^1J_{CF}$= 272 Hz, CF_3), 124.6 (C^f), 126.3 (C^d), 127.7 (q, $^3J_{CF}$= 5 Hz, C^c), 133.1 (C^e), 136.0 (C^a), 170.3 (CONH), 172.9 (CONH), 173.5 ($COCH_3$), 173.6 ($COCH_3$); ^{19}F NMR (376 MHz, $CDCl_3$) δ –60.85 (CF_3); ESI/MS$^+$ m/z 891.0 $[M+H]^+$; MS Calcd for $C_{40}H_{53}O_6N_6F_6$ 891.3722. Found 891.3734.

54. (2R)-2-{7-[(1R)-1,3-Dicarboxypropyl]-4,10-bis({[2-(trifluoromethyl)phenyl] carbamoyl}methyl)-1,4,7,10-tetraazacyclododecan-1-yl}pentanedioic acid

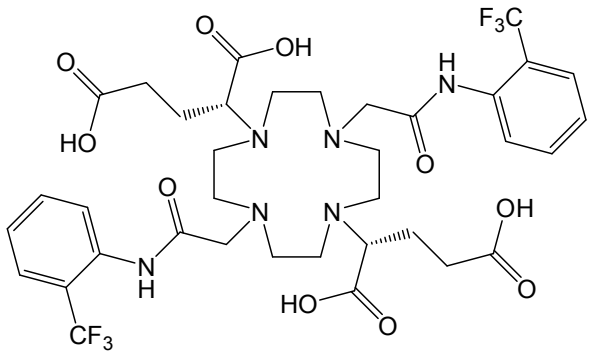

Freshly prepared aqueous KOD solution (5 mL, 0.1 M) was added to 1,5-dimethyl (2R)-2-[7-[(2R)-1,5-dimethoxy-1,5-dioxopenta-2-yl]-4,10-bis({[2-(trifluoromethyl) phenyl]carbamoyl}methyl)-1,4,7,10-tetraazacyclododecan-1-yl}pentanedioate (0.21 g, 0.23 mmol). The solution was left to stir at 40^{o}C under argon and the reaction monitored by ^{1}H NMR spectroscopy. After 4 h, the pH of the mixture was lowered to ~6 and the solution loaded onto a DOWEX strong cation exchange resin. The column was eluted with 100 % water to 10 % NH_4OH to yield the *title compound* as a colourless oil (0.15 g, 78 %); NMR (200 MHz, D_2O) δ 1.62- 2.08 (8H, m, $CHC\underline{H}_2$ and $CHCH_2C\underline{H}_2$), 2.28-3.05 (20H, br m, CH_2 ring and CH_2CO), 3.53 (2H, br s, CH), 7.38 (4H, m, Ar), 7.58 (2H, m, Ar), 7.67 (2H, m, Ar); ^{19}F NMR (376 MHz, D_2O) δ –61.11 (CF_3); ESI/MS^{+} m/z 836.1 $[M + H]^{+}$.

55. $[Tb.L^{7b}(H_2O)]^{-}$

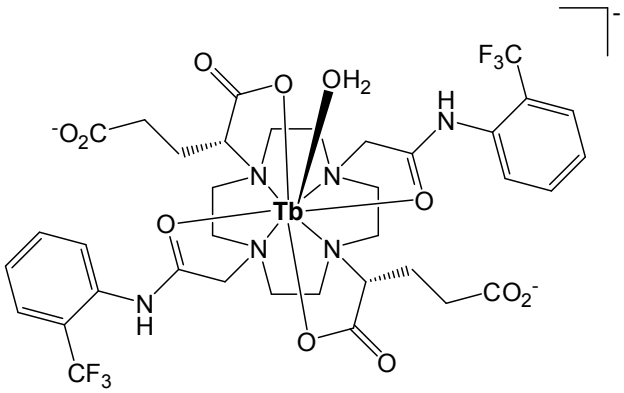

An analogous procedure to that described for **$[Tb.L^{7a}(H_2O)]^{-}$** was followed using (2R)-2-{7-[(1R)-1,3-dicarboxypropyl]-4,10-bis({[2-(trifluoromethyl)phenyl]

carbamoyl}methyl)-1,4,7,10-tetraazacyclododecan-1-yl}pentanedioic acid (0.10 g, 0.12 mmol) and $Tb^{III}(OAc)_3$ (0.05 g, 0.14 mmol) to yield the *title complex* as a white solid (0.06 g, 46%); ^{1}H NMR (200 MHz, D_2O, pD 5.4) Peaks range from -120.47 to 83.93. Selected peaks at: -120.47, -96.23, -80.56, -65.43, -36.89, -20.40, 22.36, 34.09, 50.41, 60.84, 83.93;^{19}F NMR (188 MHz, D_2O, pD 5.4) δ -62.10 (CF_3, major species), -71.82 (CF_3, minor species); τ (H_2O) 1.72 ms, τ (D_2O) 2.94 m; q= 0.90. HPLC: t_R = 5.1 min.

56. [Gd.L^{7b}(H_2O)]$^-$

An analogous procedure to that described for **[Tb.L^{7a}(H_2O)]$^-$** was followed using (2R)-2-{7-[(1R)-1,3-dicarboxypropyl]-4,10-bis({[2-(trifluoromethyl)phenyl] carbamoyl}methyl)-1,4,7,10-tetraazacyclododecan-1-yl}pentanedioic acid (0.05 g, 0.05 mmol) and $Gd^{III}(OAc)_3$ (0.02 g, 0.07mmol) to yield the *title complex* as a white solid (0.08 g, 63 %); ^{19}F NMR (188 MHz, D_2O, pD 5.4) δ -60.20 (CF_3); r_{1p} = 8.1 $mM^{-1}s^{-1}$ (20 MHz, 298 K); HPLC: t_R = 5.2 min.

57. 1,4,7,10-Tetraazacyclododecane-1,7-dicarboxylic acid dibenzyl ester[5]

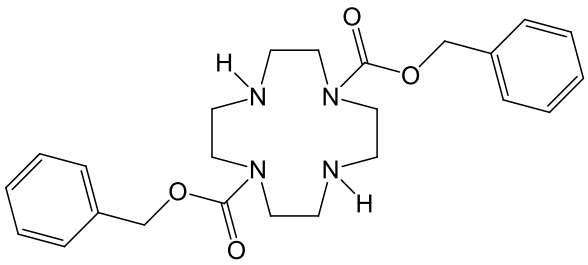

1,4,7,10-Tetraazacyclododecane (5.0 g, 29.0 mmol) was dissolved in a solution of distilled H_2O: dioxane (50:20, 70 mL) , followed by addition of disodium hydrogen phosphate (14.0 g, 98.6 mmol). The pH of the solution was adjusted to 2.7 by careful addition of conc. HCl. Benzyl chloroformate (11.9 mL, 70.0 mmol) in dioxane (~20 mL) was added dropwise over a period of 2 h and the solution left to stir for a further 18 h at room temperature, yielding a colourless solution with a white precipitate. The solvent was evaporated under reduced pressure and the residue dissolved in H_2O (100 mL), followed by adjustment of the pH to 7 by addition of conc. KOH (aq). The aqueous phase was extracted with Et_2O (2 x 100 mL), followed by CH_2Cl_2 (2 x 100

mL). The organic phases were combined, dried over $MgSO_4$, filtered, and the solvent removed under reduced pressure to give a clear oil. The oil was repeatedly washed with Et_2O to yield the *title compound* as a white solid (8.40 g, 64 %); m.p. 115-117^oC; ^1H NMR (500 MHz, $CDCl_3$) δ 2.07 (2H, br. s, NH), 2.80–3.14 (8H, br. m, CH_2 ring), 3.42–3.81 (8H, br. m, CH_2 ring), 5.16 (4H, s, Cbz CH_2), 7.30–7.38 (10H, m, Ar); ^{13}C NMR (125 MHz, $CDCl_3$) δ 48.0, 50.8 (CH_2 ring), 67.4, 68.1 (Cbz CH_2), 128.3, 128.7, 128.9, 129.1, 136.1 ($Ar_{(q)}$), 156.3, 156.4 (CO); ESI/MS^+ m/z 441.1 $[M + H]^+$; MS Calcd for $C_{24}H_{33}O_4N_4$ 441.2496. Found 441.2494.

58. 4,10-Bis-*tert*-butoxycarbonylmethyl-1,4,7,10-tetraazacyclododecane-1,7-dicarboxylic acid dibenzyl ester[6]

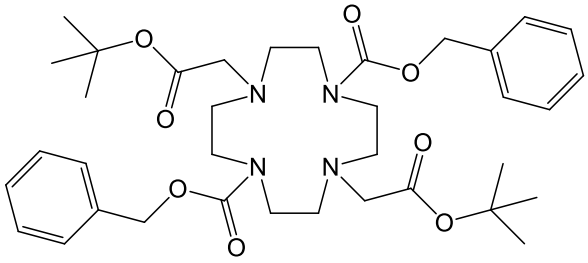

1,4,7,10-Tetraazacyclododecane-1,7-dicarboxylic acid dibenzyl ester (2.0 g, 4.54 mmol) and *tert*-butyl bromoacetate (1.83 g, 9.34 mmol) were dissolved in anhydrous CH_3CN (25 mL) followed by the addition of Cs_2CO_3 (4.0 g, 12.2 mmol). The mixture was left to boil under reflux for 18 h. The caesium salts were filtered off, and the solvent removed under reduced pressure. The resulting dark yellow oil was purified by silica gel chromatography, eluting with a gradient starting from 100% CH_2Cl_2 to 2% CH_3OH/ CH_2Cl_2 to yield the *title compound* as a light yellow oil (2.18 g, 72 %); ^1H NMR (400 MHz, $CDCl_3$) δ 1.39 (18H, s, ^tBu), 2.74- 2.83 (8H, br. s, CH_2 ring), 3.12- 3.42 (12H, CH_2 ring and CH_2CO), 5.08 (4H, s, CH_2Ar), 7.18- 7.29 (10H, m, Ar); ^{13}C NMR ($CDCl_3$, 176 MHz) δ 28.0 (CH_3), 46.7- 46.9 (br., CH_2 ring), 54.2- 54.5 (br., CH_2 ring), 55.9 ($\underline{C}H_2CO$), 66.8 ($\underline{C}H_2Ar$), 80.7 ($\underline{C}CH_3$), 127.7, 127.8, 128.0, 128.3, 128.5 (Ar), 136.8 ($Ar_{(q)}$), 156.3, 170.4 ($\underline{C}O$); ESI/MS^+ m/z 669.4 $[M + H]^+$; MS Calcd for $C_{36}H_{53}O_8N_4$ 669.3858. Found 669.3860.

59. (7-*tert*-Butoxycarbonylmethyl-1,4,7,10-tetraazacyclododec-1-yl)-acetic acid *tert*-butyl ester[6]

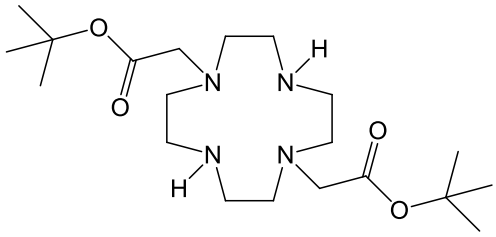

4,10-bis-*tert*-Butoxycarbonylmethyl-1,4,7,10-tetraazacyclododecane-1,7-dicarboxylic acid dibenzyl ester (2.10 g, 3.15 mmol) was dissolved in absolute ethanol (20 mL) to which $Pd(OH)_2/C$ (Pd content 10%, 30 mg) was added. The mixture was hydrogenated in a Parr hydrogenation apparatus (40 psi) for 3 days. The catalyst was removed by filtration and the ethanol removed under reduced pressure to yield the *title compound* as a white solid (1.02 g, 81 % yield); ^{1}H NMR (500 MHz, $CDCl_3$) δ 1.45 (18H, s, ^{t}Bu), 2.71 (8H, br. s, CH_2 ring), 2.82 (8H, br. s, CH_2 ring), 3.31 (4H, s, CH_2CO); ^{13}C NMR (125MHz, $CDCl_3$) δ 27.3 (CH_3), 51.8, 53.4 (CH_2 ring), 82.7 ($\underline{C}CH_3$), 171.9 (CO); ESI/MS$^+$ m/z 401.1 $[M+H]^+$; MS Calcd for $C_{20}H_{41}O_4N_4$ 401.3122. Found 401.3121.

60. {7-*tert*-Butoxycarbonylmethyl-4,10-bis-[(2-trifluoromethyl-phenylcarbamoyl)-methyl]-1,4,7,10tetraaza-cyclododec-1-yl}-acetic acid *tert*-butyl ester

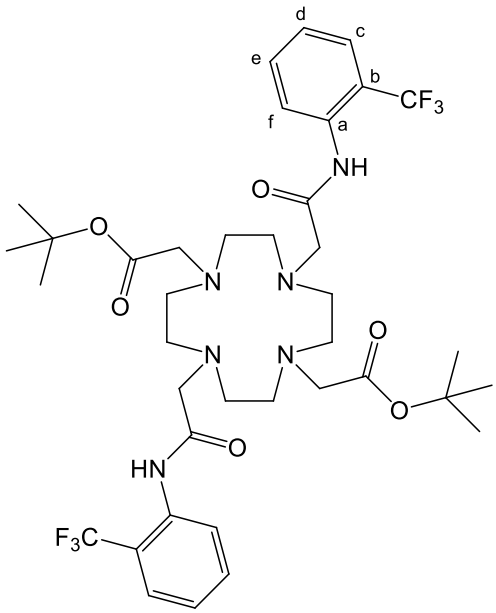

2-Chloro-*N*-(2-trifluoromethyl-phenyl)-acetamide (0.12 g, 0.50 mmol) was added to a stirred solution of (7-*tert*-butoxycarbonylmethyl-1,4,7,10-tetraazacyclododec-1-yl)-

acetic acid *tert*-butyl ester (0.10 g, 0.25 mmol), KI (~5 mg) and K_2CO_3 (72 mg, 0.5 mmol) in anhydrous CH_3CN (10 ml) at 85^oC under argon. The mixture was left to boil under reflux for 18 h, yielding a pale yellow solution and white precipitate. The precipitate was removed by filtration and the residue washed with CH_2Cl_2 (2 x 30mL). The solvent was removed under reduced pressure and the resulting oil purified by silica gel column chromatography, eluting with a gradient starting from 100% CH_2Cl_2 to 2.5% CH_3OH / CH_2Cl_2 to yield the *title compound* as a colourless oil (0.14 g, 52 %); ^1H NMR (400 MHz, $CDCl_3$) δ 1.22 (18H, s, ^tBu), 2.14- 3.70 (24H, br. m, CH_2 ring and CH_2CO), 7.27 (2H, t, J= 8 Hz, H^d), 7.43 (2H, t, J= 8 Hz, H^e), 7.58 (2H, d, J= 8Hz, H^c), 7.80 (2H, d, J=8 Hz, H^f), 8.07 (2H, s, NH); ^{13}C NMR (176 MHz, $CDCl_3$) δ 27.9 (CH_3), 49.0, 52.5 (br. CH_2 ring), 55.8, 57.4 ($\underline{C}H_2CO$), 82.1 ($\underline{C}CH_3$), 121.4 (q, $^2J_{CF}$= 30 Hz, C^b), 123.9 (q, $^1J_{CF}$= 272 Hz, CF_3), 125.8 (C^f), 126.4 (q, $^3J_{CF}$= 5 Hz, C^c), 127.3 (C^d), 132.6 (C^e), 134.9 (C^a), 171.4, 172.56 (CO); ^{19}F NMR (188 MHz, $CDCl_3$) δ -60.84 (CF_3); ESI/MS^+ m/z 803.1 $[M+H]^+$, 825.1 $[M+Na]^+$; MS Calcd for $C_{38}H_{52}O_6N_6F_6Na$ 825.3744. Found 825.3745.

61. {7-Carboxymethyl-4,10-bis-[(2-trifluoromethyl-phenylcarbamoyl)methyl]-1,4,7,10-tetraaza-cyclododec-1-yl}-acetic acid

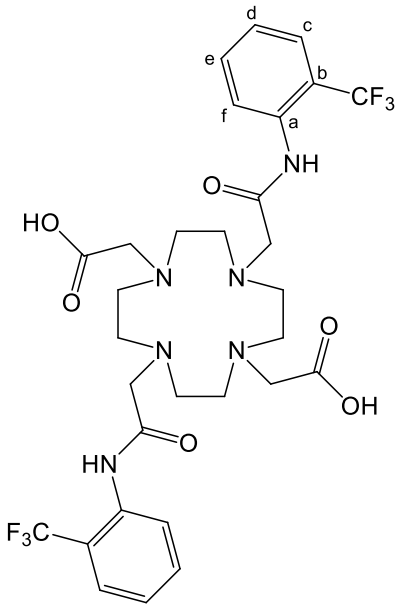

Trifluoroacetic acid (3 mL) was added to a solution of {7-*tert*-butoxycarbonylmethyl-4,10-bis-[(2-trifluoromethyl-phenylcarbamoyl)-methyl]-1,4,7,10tetraaza-cyclododec-1-yl}-acetic acid *tert*-butyl ester (0.12 g, 0.15 mmol) in CH_2Cl_2 (5 mL). The solution was stirred at room temperature for 2 hours. The solvent was removed under

reduced pressure and the resulting solid repeatedly washed with CH_2Cl_2 (5 x 5 mL), yielding the *title compound* as a trifluoroacetate salt (72.3 mg, 70 %); ^{1}H NMR (400 MHz, $CDCl_3$) δ 2.23- 3.65 (24H, br. m, CH_2 ring and CH_2CO), 7.28 (2H, t, J= 15 Hz, H^d), 7.39 (2H, t, J= 15 Hz, H^e), 7.52 (2H, d, J= 8Hz, H^c), 7.83 (2H, d, J=8 Hz, H^f), 8.07 (2H, s, NH); ^{19}F NMR (188 MHz, $CDCl_3$) δ -61.32 (CF_3); MS (ES^+) m/z 691.3 $[M + H]^+$.

62. $[Tb.L^8(H_2O)]^+$

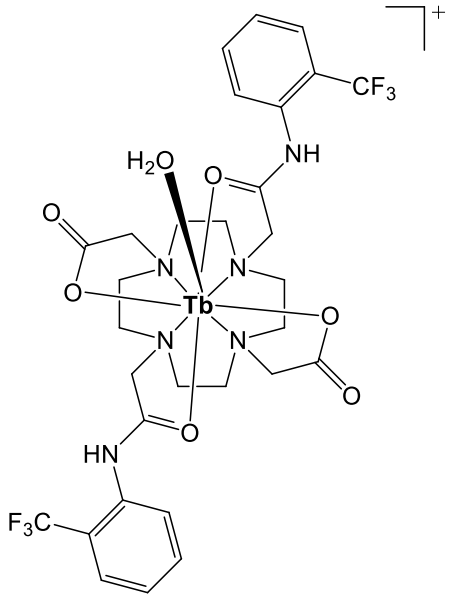

{7-Carboxymethyl-4,10-bis-[(2-trifluoromethyl-phenylcarbamoyl)methyl]-1,4,7,10 tetraaza-cyclododec-1-yl}-acetic acid (16.1 mg, 23.3 µmol) was dissolved in H_2O (3mL) and the pH adjusted to ~6. $Tb^{III}Cl_3$ (7.4 mg, 28.0 µmol) was added to the solution, which was subsequently left to boil under reflux for 3 h. Once cooled, the solvent was removed under reduced pressure. The complex was re-dissolved in H_2O (5 mL) and stirred for 2 h with anion exchange resin (DOWEX 1X8 200-400 MESH Cl, pre-treated with 1M HCl) to give the chloride salt. Following filtration, the water was lyophilized to yield the *title complex* as a white powder (15.9 mg, 81 %); ^{1}H NMR (200 MHz, D_2O, pD 5.4) Peaks range from -80.04 to 109.23. Selected peaks at: -80.04, -64.06, -60.89, -50.42, -30.26, -20.78, 30.14, 32.56, 51.46, 64.69, 82.96, 109.23; ^{19}F NMR (376 MHz, D_2O, pD 5.4) δ -61.9 (CF_3, major species, 87 %), -73.2 (CF_3, minor species); ESI/MS^+ m/z 847.2 $[M]^+$; MS Calcd for $C_{30}H_{34}O_6N_6F_6{}^{159}Tb$ 847.1692. Found 847.1704; τ (H_2O) 1.80 ms, τ (D_2O) 3.18 ms; q= 0.90; HPLC: t_R = 7.9 min.

63. $[Ho.L^8(H_2O)]^+$

An analogous procedure to that described for **$[Tb.L^8(H_2O)]^+$** was followed using {7-carboxymethyl-4,10-bis-[(2-trifluoromethyl-phenylcarbamoyl)methyl]-1,4,7,10 tetraaza-cyclododec-1-yl}-acetic acid (12.7 mg, 18.4 µmol) and $Ho^{III}(OAc)_3$ (7.6 mg, 22.0 µmol) to yield the *title complex* as a white solid (11.1 mg, 71 %); ^{1}H NMR (200 MHz, D_2O, pD 5.4) Peaks range from -104.21 to 87.48. Selected peaks at: -104.23, -73.56, -62.59, -59.63, -40.78, -27.80, 21.47, 30.80, 48.97, 63.00, 70.07, 79.63, 87.48; ^{19}F NMR (376 MHz, D_2O, pD 5.4) δ -57.71 (CF_3, major species, 82 %), -60.63, -61.80, -66.83, -68.21, -71.23 (CF_3, minor species); ESI/MS^+ m/z 853.2 $[M]^+$; MS Calcd for $C_{30}H_{34}O_6N_6F_6{}^{165}Ho$ 853.1747 Found 853.1740.

64. $[Gd.L^8(H_2O)]^+$

An analogous procedure to that described for **$[Tb.L^8(H_2O)]^+$** was followed using {7-carboxymethyl-4,10-bis-[(2-trifluoromethyl-phenylcarbamoyl)methyl]-1,4,7,10 tetraaza-cyclododec-1-yl}-acetic acid (22.1 g, 32.0 µmol) and $Gd^{III}(OAc)_3$ (12.8 mg, 38.4 µmol) to yield the *title complex* as a white solid (21.1 mg, 78 %); ^{19}F NMR (188 MHz, D_2O, pD 5.4) δ -62.41 (CF_3); ESI/MS^+ m/z 846.0 $[M]^+$; MS Calcd for $C_{30}H_{34}O_6N_6F_6{}^{158}Gd$ 846.1685. Found 846.1690; r_{1p} = 6.3 $mM^{-1}s^{-1}$ (20 MHz, 298 K).

65. $[Er.L^8(H_2O)]^+$

An analogous procedure to that described for **$[Tb.L^8(H_2O)]^+$** was followed using {7-carboxymethyl-4,10-bis-[(2-trifluoromethyl-phenylcarbamoyl)methyl]-1,4,7,10 tetraaza-cyclododec-1-yl}-acetic acid (10.4 mg, 15.1 µmol) and $Er^{III}Cl_3$ (4.9 mg, 18.1 µmol) to yield the *title complex* as a white solid (9.4 mg, 73 %); ^{1}H NMR (200 MHz, D_2O, pD 5.4) Peaks range from -139.40 to 182.30. Selected peaks at: -139.40, -100.53, -82.07, -62.89, -60.48, -59.81, 21.03, 37.61, 41.89, 120.13, 170.00, 179.02, 182.30; ^{19}F NMR (376 MHz, D_2O, pD 5.4) δ -58.45 (CF_3, major species, 78 %), -59.80, -61.65 (CF_3, minor species); ESI/MS^+ m/z 855.2 $[M]^+$; MS Calcd for $C_{30}H_{34}O_6N_6F_6{}^{166}Er$ 854.1742. Found 854.1747.

66. $[Tm.L^8(H_2O)]^+$

An analogous procedure to that described for **$[Tb.L^8(H_2O)]^+$** was followed using {7-carboxymethyl-4,10-bis-[(2-trifluoromethyl-phenylcarbamoyl)methyl]-1,4,7,10

tetraaza-cyclododec-1-yl}-acetic acid (11.3 mg, 16.4 µmol) and $Tm^{III}(OAc)_3$ (6.8 mg, 19.6 µmol) to yield the *title complex* as a white solid (8.9 mg, 64 %); ^{1}H NMR (200 MHz, D_2O, pD 5.4) Peaks range from -220.87 to 240.43. Selected peaks at: -220.87, -180.69, -160.45, -89.01, -60.23, -40.56, 38.94, 48.96, 70.51, 92.22, 109.53, 180.78, 240.43; ^{19}F NMR (376 MHz, D_2O, pD 5.4) δ -77.2 (CF_3, major species, 91 %), -62.19, -65.32 (CF_3, minor species); ESI/MS^+ m/z 846.0 $[M]^+$; MS Calcd for $C_{30}H_{34}O_6N_6F_6{}^{169}Tm$ 857.1786. Found 857.1780.

67. Ethyl 4-amino-3-(trifluoromethyl)benzoate

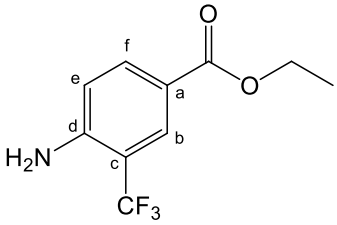

4-Amino-3-(trifluoromethyl)benzonitrile (1.0 g, 5.4 mmol) was added to a stirred solution of H_2SO_4 (1 mL), ethanol (5 mL) and H_2O (0.5 mL). The mixture was stirred at 95^{o}C for 48 h. Once cooled, $CHCl_3$ (20 mL) and H_2O (20 mL) were added and the pH was adjusted to 7 by the careful addition of K_2CO_3. The product was extracted into $CHCl_3$ (3 x 30 mL), dried over $MgSO_4$, and the solvent removed under reduced pressure. The resulting oil was purified by silica gel column chromatography, eluting with a gradient starting from 100 % toluene to 5 % CH_2Cl_2 / toluene to yield the *title compound* as a white solid (0.84 g, 64 %); m.p. 82-84^{o}C; ^{1}H NMR (200 MHz, $CDCl_3$) δ 1.36 (3H, t, J= 7, $C\underline{H}_3$), 4.33 (2H, q, J= 7, $C\underline{H}_2CH_3$), 4.61 (2H, br. s, NH_2), 6.72 (1H, d, J= 9 Hz, H^e), 7.94 (1H, d, J = 9 Hz, H^f), 8.13 (1H, s, H^b), 9.50 (1H, s, NH); ^{13}C NMR (176 MHz, $CDCl_3$) δ 14.5 ($CH_2\underline{C}H_3$), 60.7 ($\underline{C}H_2CH_3$), 112.7 (q, $^2J_{CF}$ = 31 Hz, C^c), 116.3 (C^e), 119.0 (C^a), 125.1 (q, $^1J_{CF}$ = 272 Hz, CF_3), 129.1 (q, $^3J_{CF}$ = 5 Hz, C^b), 134.1 (C^f), 148.6 (C^d), 166.0 (CO); ^{19}F NMR (188 MHz, $CDCl_3$) δ – 63.49 (CF_3); ESI/MS^+ m/z 234.1 $[M+H]^+$; MS Calcd for $C_{10}H_{11}O_2NF_3$ 234.0742. Found 234.0743.

68. 2-Chloro-N-(4-(ethoxycarbonyl)-2-trifluoromethylphenyl)-ethanamide

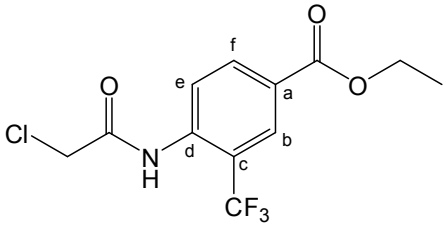

Chloroacetylchloride (0.45 g, 4.0 mmol) was added dropwise to a stirred solution of ethyl 4-amino-3-(trifluoromethyl)benzoate (0.78 g, 3.3 mmol) and Et_3N (0.40 g, 4.0 mmol) in CH_2Cl_2 (15 mL) at 0^oC under argon. After 4 h, the crude mixture was washed with HCl (20 mL, 0.1M), NaOH (20 mL, 0.1 M) and H_2O (20 mL). The combined organic extracts were dried over $MgSO_4$ and the solvent removed under reduced pressue. The resulting residue was purified by recrystallisation from hexane/ Et_2O to yield the title compound as white needles (0.84 g, 82 %); mp 98-101^oC; ^1H NMR (400 MHz, $CDCl_3$) δ 1.39 (3H, t, J= 7 Hz, $C\underline{H}_3$), 4.24 (2H, s, $C\underline{H}_2CO$), 4.39 (2H, q, J = 7 Hz, $C\underline{H}_2CH_3$), 8.21 (1H, dd, J= 8, 1 Hz, H^f), 8.30 (1H, d, J= 1 Hz, H^b), 8.45 (1H, d, J= 8 Hz, H^e), 8.96 (1H, s, NH); ^{13}C NMR (126 MHz, $CDCl_3$) δ 14.6 ($\underline{C}H_3$), 43.2 ($\underline{C}H_2CO$), 61.8 ($\underline{C}H_2CH_3$), 119.8 (q, $^2J_{CF}$ = 30 Hz, C^c), 122.7 (C^e), 123.7 (q, $^1J_{CF}$ = 274 Hz, CF_3), 127.2 (C^a), 128.1 (q, $^3J_{CF}$ = 5 Hz, C^b), 134.6 (C^f), 138.3 (C^d), 164.3 (CONH), 165.1 (COO); ^{19}F NMR (376 MHz, $CDCl_3$) δ – 61.32 (CF_3); ESI/MS^+ m/z 310.0 $[M+H]^+$; MS Calcd for $C_{12}H_{12}ClO_3NF_3$ 310.0458. Found 310.0457.

69. Ethyl-4-[2-(1,4,7,10-tetraazacyclododecan-1-yl)acetamido]-3-(trifluoromethyl) Benzoate

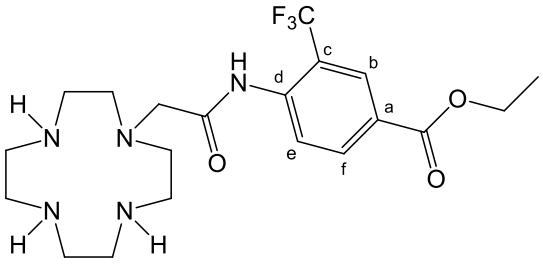

2-Chloro-N-(4-(ethoxycarbonyl)-2-trifluoromethylphenyl)-ethanamide (0.40 g, 1.29 mmol) was added to a stirred solution of 1,4,7,10 – tetraazacyclododecane (2.29 g, 12.9 mmol) in anhydrous CH_3CN (10mL) at 40^oC under argon. After 4 h, the solvent was removed under reduced pressure and the residue dissolved in CH_2Cl_2 (20 mL).

The solution was washed repeatedly with H_2O (4 x 20 mL), dried over $MgSO_4$, and the solvent removed under reduced pressure to yield the *title compound* as a light yellow oil (0.24 g, 43 %); ^{1}H NMR (700 MHz, $CDCl_3$) δ 1.33 (3H, t, J= 7 Hz, CH_3), 2.56 (4H, m, CH_2 ring), 2.64 (4H, m, CH_2 ring), 2.69-2.73 (8H, m, CH_2 ring), 3.28 (2H, s, CH_2CO), 4.32 (2H, q, J= 7 Hz, $C\underline{H}_2CH_3$), 8.12 (1H, dd, J= 8, 1 Hz, 1, H^f), 8.22 (1H, d, J= 1 Hz, H^b), 8.26 (1H, d, J= 8 Hz, H^e), 9.52 (1H, br. s, NH); ^{13}C NMR (176 MHz, $CDCl_3$) δ 14.4 (CH_3), 45.6, 46.3, 47.3 (CH_2 ring), 53.3 ($\underline{C}H_2CO$), 61.3 ($\underline{C}H_2CH_3$), ^{19}F NMR (188 MHz, $CDCl_3$) δ – 60.81 (CF_3); ESI/MS$^+$ m/z 446.2 $[M+H]^+$; MS Calcd for $C_{20}H_{31}O_3N_5F_3$ 446.2379. Found 446.2376.

70. Ethyl-({4-[2-({4-[ethoxy(hydroxy)methyl]-2-(trifluoromethyl)cyclohexyl}amino)-2-hydroxyethyl]-7,10-di{[ethoxy(methyl)phosphoryl]methyl}-1,4,7,10-tetraazacyclododecan-1-yl}methyl)(methyl)phosphinate

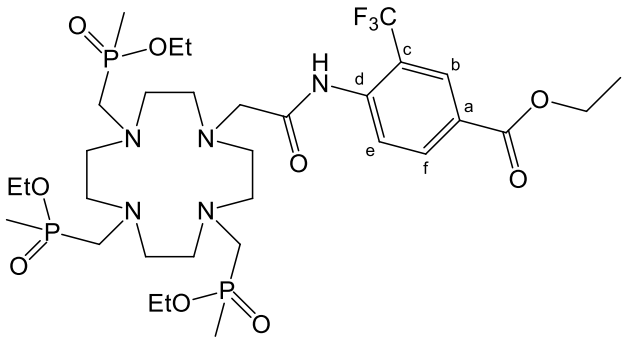

Ethyl-4-[2-(1,4,7,10-tetraazacyclododecan-1-yl)acetamido]-3-(trifluoromethyl) benzoate (1.01 g, 2.5 mmol) was heated to 80^{o}C in anhydrous tetrahydrofuran under argon. Paraformaldehyde (0.33 g, 11.1 mmol) followed by diethoxymethyl phosphine (1.51 g, 11.1 mmol) were added. The solution was boiled at reflux over molecular sieves. After 15 h, the excess paraformaldehyde was removed by filtration and the solvent removed under reduced pressure. The resulting orange oil was purified by alumina gel column chromatography, eluting with a gradient starting from 100% CH_2Cl_2 to 0.6 % CH_3OH / CH_2Cl_2 to yield the *title compound* as a pale yellow oil (1.14 g, 57 %); ^{1}H NMR (200 MHz, $CDCl_3$) δ 1.11-1.21 (9H, m, $^2J_{HP}$ = 14 Hz, $PC\underline{H}_3$), 1.24-1.30 (9H, m, $POCH_2C\underline{H}_3$), 1.43 (3H, t, J=7 Hz, $COCH_2C\underline{H}_3$), 2.62-3.04 (22H, br. m, CH_2 ring and CH_2P), 3.12 (2H, s, CH_2CO), 3.98 (6H, m, $POCH_2$), 4.31 (2H, q, J= 7 Hz, $COCH_2$), 8.14 (2H, m, H^e and H^f), 8.21 (1H, d, J= 1Hz, H^b), 9.52 (1H, br. s, NH); ^{13}C

NMR (126 MHz, $CDCl_3$) δ 14.6 (br. m, $^1J_{CP}$ = 89 Hz, P<u>C</u>H$_3$), 15.0 (OCH$_2$<u>C</u>H$_3$), 16.9 (t, $^3J_{CP}$ = 4 Hz, CH$_2$<u>C</u>H$_3$), 50.4, 51.5, 52.6, 53.9 (br., CH_2 ring), 54.9 (CH_2N), 60.7 (br., m, PCH_2) 61.3 (OCH$_2$<u>C</u>H$_3$), 121.6 (q, $^2J_{CF}$ = 30 Hz, C^c), 124.0 (q, $^1J_{CF}$ = 274, CF_3), 125.7 (C^e), 126.1 (C^a), 129.0 (q, $^3J_{CF}$ = 5 Hz, C^b), 132.8 (C^f), 139.3 (C^d), 168.0 (CONH), 171.0 (COO); ^{31}P NMR (81 MHz, $CDCl_3$) δ -51.84 (2P, s, PCH_3), -52.82 (1P, s, PCH_3); ^{19}F NMR (188 MHz, $CDCl_3$) δ -61.28 (CF_3), -61.26 (CF_3); ESI/MS$^+$ m/z 806.2 $[M + H]^+$; MS Calcd for $C_{32}H_{57}N_5O_9P_3F_3$ 806.3390. Found 806.3383.

71. ({4-[2-({4-[Ethoxy(hydroxy)methyl]-2-(trifluoromethyl)cyclohexyl}amino)-2-hydroxyethyl]-7,10-di{[hydroxy(methyl)phosphoryl]methyl}-1,4,7,10-tetraazacyclododecan-1-yl}methyl)(methyl)phosphinic acid

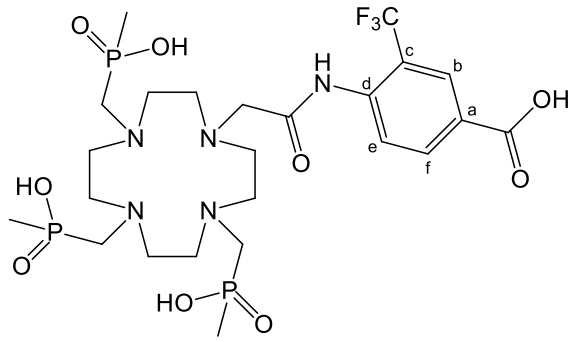

Freshly prepared aqueous KOD solution (5 mL, 0.1 M) was added to ethyl-({4-[2-({4-[ethoxy(hydroxy)methyl]-2-(trifluoromethyl)cyclohexyl}amino)-2-hydroxyethyl]-7,10-di{[ethoxy(methyl)phosphoryl]methyl}-1,4,7,10-tetraazacyclododecan-1-yl}methyl)(methyl)phosphinate (0.30 g, 0.37 mmol). The solution was left to stir at 40^{o}C under argon and the reaction monitored by ^{1}H and ^{31}P NMR. After 72 h, the pH of the solution was lowered to ~6 by the addition of HCl. The solvent was removed under reduced pressure and the residue washed repeatedly with CH_2Cl_2 (3 x 5 mL). The resulting oil was dissolved in ethanol. The white precipitate was removed by filtration and the solvent removed under reduced pressure to yield the title compound as a pale yellow oil (0.21 g, 83%); ^{1}H NMR (400 MHz, D_2O) δ1.03-1.15 (9H, br. m, PCH_3), 2.48- 2.58 (8H, br. m, CH_2 ring), 2.63-2.81 (16H, br. m, CH_2 ring, CH_2P and CH_2CO), 7.42 (1H, dd, J = 8, 1 Hz, H^f), 7.92 (1H, d, J= 8, H^e), 8.05 (1H, s, H^b); ^{31}P NMR (162 MHz, D_2O) δ -40.28 (3P, s, PCH_3); ^{19}F NMR (376 MHz, D_2O) δ – 61.46 (CF_3).

72. [Tb.L^9]

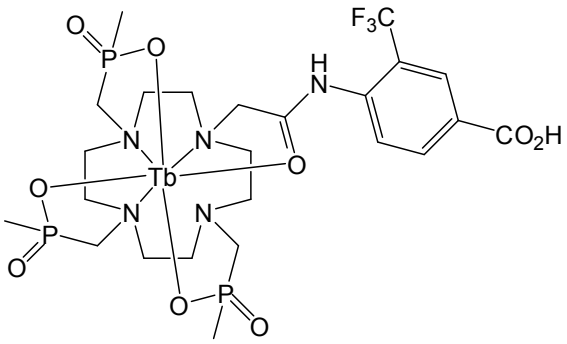

An analogous procedure to that described for **[Tb.L^4(H$_2$O)]$^{3-}$** was followed using ({4-[2-({4-[ethoxy(hydroxy)methyl]-2-(trifluoromethyl)cyclohexyl}amino)-2-hydroxy ethyl]-7,10-di{[hydroxy(methyl)phosphoryl]methyl}-1,4,7,10-tetraazacyclododecan-1-yl}methyl)(methyl)phosphinic acid (0.20 g, 0.28 mmol) and $Tb^{III}(OAc)_3$ (0.11 g, 0.33 mmol) to yield the *title complex* as a white solid (0.17 g, 70 %); ^{19}F NMR (376 MHz, D_2O, pD 5.4) δ –48.43 (CF_3, major species), -52.06, -53.80 (CF_3, minor species); ESI/MS$^+$ m/z 850.1 $[M+H]^+$; MS Calcd for $C_{24}H_{39}O_9N_5P_3F_3{}^{159}Tb$ 850.1161. Found 850.1180; τ (H_2O) 2.56 ms, τ (D_2O) 3.70 ms; q= 0.30; HPLC: t_R = 5.8 min.

73. [Gd.L^9]

An analogous procedure to that described for **[Tb.L^4(H$_2$O)]$^{3-}$** was followed using ({4-[2-({4-[ethoxy(hydroxy)methyl]-2-(trifluoromethyl)cyclohexyl}amino)-2-hydroxy ethyl]-7,10-di{[hydroxy(methyl)phosphoryl]methyl}-1,4,7,10-tetraazacyclododecan-1-yl}methyl)(methyl)phosphinic acid (0.18 g, 0.26 mmol) and $Gd^{III}(OAc)_3$ (0.10 g, 0.31 mmol) to yield the *title complex* as a white solid (0.14 g, 66 %);ESI/MS$^-$ m/z 860.1 $[M-H]^-$; MS Calcd for $C_{24}H_{37}O_9N_5P_3F_3{}^{154}Gd$ 843.0995. Found 843.0965; r_{1p}= 3.3 $mM^{-1}s^{-1}$ (60 MHz, 298 K).

74. [Tm.L^9]

An analogous procedure to that described for **[Tb.L^4(H$_2$O)]$^{3-}$** was followed using ({4-[2-({4-[ethoxy(hydroxy)methyl]-2-(trifluoromethyl)cyclohexyl}amino)-2-hydroxy ethyl]-7,10-di{[hydroxy(methyl)phosphoryl]methyl}-1,4,7,10-tetraazacyclododecan-1-yl}methyl)(methyl)phosphinic acid (0.20 g, 0.28 mmol) and $Tm^{III}(OAc)_3$ (0.12 g, 0.33 mmol) to yield the *title complex* as a white solid (0.13 g, 54 %); ^{19}F NMR (376 MHz, D_2O, pD 5.4) δ –88.90 (CF_3, major species), -90.12, -91.69 (CF_3, minor species);

ESI/MS$^+$ m/z 860.1 $[M+H]^+$; MS Calcd for $C_{24}H_{39}O_9N_5P_3F_3{}^{169}Tm$ 860.1250. Found 860.1255.

75. 2-(2-(2-(2-Methoxyethoxy)ethoxy)ethyl)isoindoline-1,3-dione[7]

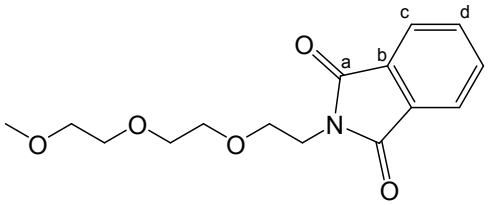

Triethyleneglycol monomethyl ether (3.28 g, 20 mmol) was added to a stirred solution of phthalimide (3.53 g, 24.0 mmol) and triphenylphosphine (6.30 g, 24.0 mmol) in anhydrous THF (100 mL) under argon. After 15 min, diisopropyl azodicarboxylate (4.85 g, 24 mmol) was added. After 24 h, the reaction was quenched by the addition of ethanol (20 mL). The solvent was removed under reduced pressure and the resulting viscous oil dissolved in a petroleum ether: ethyl acetate mixture (1:1, 20 mL). The mixture was stirred at 40^{o}C for 1 h, yielding a white precipitate. The precipitate was removed by filtration and the filtrate evaporated to dryness. The crude material was purified on silica gel colum chromatography, eluting with a gradient starting from Petroleum Ether/ 25 % Ethyl Acetate to Petroleum Ether/ 40 % Ethyl Acetate to yield the *title compound* as a viscous yellow oil (4.98 g, 85 %); ^{1}H NMR (500 MHz, $CDCl_3$) δ 3.31 (3H, s, CH_3), 3.45 (2H, t, J= 7 Hz, CH_2), 3.55-3.99 (6H, m, CH_2), 3.63 (2H, t, J= 7 Hz, $C\underline{H}_2CH_2N$), 3.88 (2H, t, J = 7 Hz, CH_2N), 7.69 (2H, m, Ar), 7.82 (2H, m, Ar); ^{13}C NMR (126 MHz, $CDCl_3$) δ 37.5 (CH_2N), 59.2 (CH_3), 68.11 ($\underline{C}H_2CH_2CN$), 70.3, 70.7, 70.8 (CH_2), 72.1 ($\underline{C}H_2COCH_3$), 123.4 (C^c), 132.3 (C^b), 134.1 (C^d), 168.4 (C^a); ESI/MS$^+$ m/z 294.3 $[M+H]^+$; MS Calcd for $C_{15}H_{20}O_5N$ 294.1336. Found 294.1337.

76. 2-(2-(2-Methoxyethoxy)ethoxy)ethanamine[7]

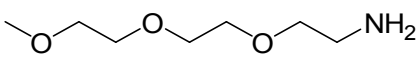

Hydrazine (0.39 g, 12.1 mmol) was added to a stirred solution of 2-(2-(2-(2-methoxyethoxy)ethoxy)ethyl)isoindoline-1,3-dione (3.24 g, 11.0 mmol) in ethanol

(35 mL) at 100°C. After 3 h, the resulting slurry was allowed to cool and the pH was lowered to ~2 by the addition of HCl. The mixture was heated to 100°C for 1h, yielding a colourless solution and white precipitate. The precipitate was removed by filtration and the solvent removed under reduced pressure. H_2O (30 mL) was added to the resulting oil and the pH increased to 11 by the addition of NaOH. The crude material was extracted into CH_2Cl_2 (3 x 30 mL), dried over $MgSO_4$ and the solvent removed under reduced pressure to give the *title compound* as a colourless oil (1.12 g, 62 %); ^{1}H NMR (400 MHz, $CDCl_3$) δ 2.84 (2H, br. s, NH_2), 3.01 (2H, t, J = 7 Hz, CH_2N), 3.34 (3H, s, CH_3), 3.52 (2H, t, J= 7 Hz, CH_2), 3.58 (2H, t, J= 7 Hz, CH_2), 3.59-3.62 (6H, m, CH_2), 3.80 (2H, t, J = 7 Hz, $C\underline{H}_2CH_2N$); ^{13}C NMR (100 MHz, $CDCl_3$) δ 41.7 (CH_2N), 53.6 (CH_3), 67.9 ($\underline{C}H_2CH_2CN$), 69.1, 70.5, 71.9, 73.4 (CH_2); ESI/MS$^+$ m/z 164.3 $[M+H]^+$; MS Calcd for $C_7H_{18}O_3N$ 164.1281. Found 164.12823.

77. 4-Amino-3-(trifluoromethyl)benzoic acid

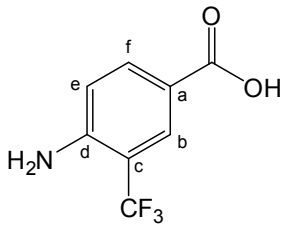

Freshly prepared aqueous KOD solution (5 mL, 0.1 M) was added to ethyl 4-amino-3-(trifluoromethyl)benzoate (2.01 g, 8.6 mmol). The solution was left to stir at 40°C under argon and the reaction monitored by ^{1}H NMR. After 72 h, the pH of the solution was lowered to ~5 by addition of HCl. The resulting white precipitate was filtered and dried under reduced pressure to give the *title compound* as a white solid (1.51 g, 86 %); m.p. = 80– 82°C; ^{1}H NMR (500 MHz, CD_3OD) δ 4.90 (2H, s, NH), 6.84 (1H, d, J = 9 Hz, H^e), 7.93 (1H, d, J= 9 Hz, H^f), 8.05 (1H, s, H^b); ^{13}C NMR (126 MHz, CD_3OD) δ 111.2 (q, $^2J_{CF}$ = 31 Hz, C^c), 115.9 (C^e), 117.4 (C^a), 125.0 (q, $^1J_{CF}$ = 270 Hz, CF_3), 128.9 (q, $^3J_{CF}$ = 5 Hz, C^b), 134.2 (C^f), 150.3 (C^d), 168.1 (CO); ^{19}F NMR (376 MHz, CD_3OD) δ – 65.48 (CF_3); ESI/MS$^-$ m/z 204.1 $[M-H]^-$; MS Calcd for $C_8H_5O_2NF_3$ 204.0278. Found 204.0280.

78. 1H-1,2,3-Benzotriazol-1-yl 4-amino-3-(trifluoromethyl)benzoate

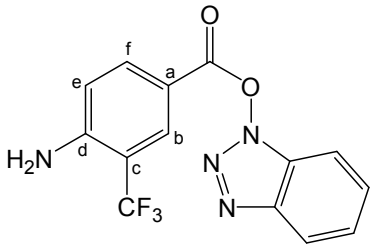

4-Amino-3-(trifluoromethyl)benzoic acid (0.76 g, 3.71 mmol) was dissolved in anhydrous DMF (4 mL) to which N-methylmorphiline (0.45 g, 4.46 mmol) and TBTU (1.43 g, 4.46 mmol) were added. The mixture was left to stir at room temperature for 30 mins after which the solvent was removed under reduced pressure. The crude material was purified by alumina gel column chromatography, eluting with a gradient starting from 100% CH_2Cl_2 to 5.4 % CH_3OH / CH_2Cl_2 to yield the *title compound* as a white solid (0.75 g, 63 %); m.p. 104 -106; ^{1}H NMR (400 MHz, $CDCl_3$) δ 6.88 (1H, d, J = 9 Hz, H^e), 7.46 (2H, m, Ar), 7.57 (1H, t, J = 8 Hz, Ar), 8.11 (1H, d, J=8 Hz, Ar), 8.18 (1H, dd, J = 8, 1 Hz, H^f), 8.40 (1H, d, J = 1 Hz, H^b); ^{13}C NMR (100 MHz, $CDCl_3$) δ 113.0 (q, $^2J_{CF}$ = 31 Hz, C^c), 113.0 (C^e), 117.2 (C^a), 121.9, 123.0, 124.9 (Ar), 125.7 (q, $^1J_{CF}$ = 270 Hz, CF_3), 129.0 (Ar), 129.2 (q, $^3J_{CF}$ = 5 Hz, C^b), 131.3 (C^f), 135.7, 143.7 ($Ar_{(q)}$), 151.3 (C^d), 162.1 (CO); ^{19}F NMR (376 MHz, $CDCl_3$) δ – 63.76 (CF_3); ESI/MS^+ m/z 345.2 $[M+Na]^+$; MS Calcd for $C_{14}H_9O_2N_4F_3Na$ 345.0575. Found 345.0583.

79. 4-Amino-N-{2-[2-(2-methoxyethoxy)ethoxy]ethyl}-3-(trifluoromethyl)-benzamide

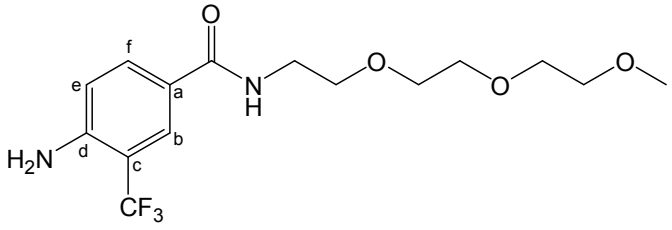

1H-1,2,3-Benzotriazol-1-yl 4-amino-3-(trifluoromethyl)benzoate (0.44 g, 1.37 mmol) was added to a stirred solution of 2-(2-(2-methoxyethoxy)ethoxy)ethanamine (0.29 g, 1.78 mmol) and N-methylmorphiline (0.18 g, 1.78 mmol) in anhydrous DMF (5 mL) under argon at 40^{o}C. After 4 h, the solvent was removed under reduced pressure. The crude material was purified by alumina gel column chromatography, eluting with a gradient starting from 100% CH_2Cl_2 to 4.3 % CH_3OH / CH_2Cl_2 to yield the *title*

compound as a white solid (0.44 g, 91 %); m.p. 124-125^{o}C; ^{1}H NMR (400 MHz, $CDCl_3$) δ 3.30 (3H, s, CH_3), 3.52 (2H, m, CH_2), 3.65 (10H, m, CH_2), 6.41 (1H, d, J= 9 Hz, H^e), 6.84 (2H, NH_2), 7.76 (1H, dd, J = 8, 1 Hz, H^f), 7.92 (1H, s, H^b), 7.99 (1H, br. s, NH); ^{13}C NMR (100 MHz, $CDCl_3$) δ 40.9 (CH_2N), 57.8 (CH_3), 69.3, 70.1, 70.4, 72.1, 73.0 (CH_2), 113.5 (q, $^{2}J_{CF}$ = 31 Hz, C^c), 114.5 (C^e), 119.6 (C^a), 124.7 (q, $^{1}J_{CF}$ = 270 Hz, CF_3), 128.0 (q, $^{3}J_{CF}$ = 5 Hz, C^b), 133.4 (C^f), 147.0 (C^d), 170.4 (CO); ^{19}F NMR (376 MHz, $CDCl_3$) δ – 63.48 (CF_3); ESI/MS$^+$ m/z 351.3 $[M+H]^+$; MS Calcd for $C_{15}H_{22}O_4N_2F_3$ 351.1526. Found 351.1530.

80. 4-(2-chloroacetamido)-N-{2-[2-(2-methoxyethoxy)ethoxy]ethyl}-3-(trifluoromethyl)benzamide

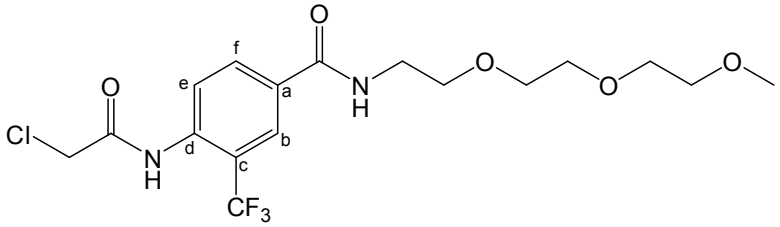

Chloroacetyl chloride (0.17 g, 1.55 mmol) was added dropwise to a solution of 4-amino-N-{2-[2-(2-methoxyethoxy)ethoxy]ethyl}-3-(trifluoromethyl)benzamide (0.42 g, 1.18 mmol) and Et_3N (0.15 g, 1.53 mmol) in anhydrous CH_2Cl_2 (10 mL) at -4^{o}C (H_2O / ice) under argon. After 4 h, the solvent was removed under reduced pressure. The crude material was purified by alumina gel column chromatography, eluting with a gradient starting from 100% CH_2Cl_2 to 1.8 % CH_3OH / CH_2Cl_2 to yield the *title compound* as a viscous colourless oil (0.36 g, 72 %); ^{1}H NMR (500 MHz, $CDCl_3$) δ 3.32 (3H, s, CH_3), 3.54 (2H, m, CH_2), 3.67 (10H, m, CH_2), 4.26 (2H, s, CH_2Cl), 7.16 (1H, br. s, NH), 8.03 (1H, dd, J = 8, 1 Hz, H^f), 8.20 (1H, dd, J = 1 Hz, H^b), 8.43 (1H, d, J= 9 Hz, H^e), 8.91 (1H, br. s, NH); ^{13}C NMR (126 MHz, $CDCl_3$) δ 40.2 (CH_2N), 43.1 (CH_2Cl), 59.1 (CH_3), 69.9, 70.5, 70.7, 70.8, 72.1 (CH_2), 119.9 (q, $^{2}J_{CF}$ = 30 Hz, C^c), 123.0 (C^e), 123.8 (q, $^{1}J_{CF}$ = 270 Hz, CF_3), 126.1 (q, $^{3}J_{CF}$ = 5 Hz, C^b), 131.3 (C^a), 131.8 (C^f), 137.0 (C^d), 164.5 (CO), 165.6 (CO); ^{19}F NMR (376 MHz, $CDCl_3$) δ – 61.21 (CF_3); ESI/MS$^+$ m/z 449.3 $[M+Na]^+$; MS Calcd for $C_{17}H_{22}O_5N_2F_3ClNa$ 449.1067. Found 449.1052.

81. (S)-2-Bromo-pentanedioic acid 5-benzyl ester[8]

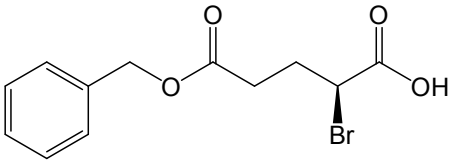

A solution of sodium nitrite (5.51 g, 80.1 mmol) dissolved in H_2O (50mL) was added dropwise to a stirred solution of sodium bromide (16.03 g, 116 mmol) in 1M HBr (250 mL), cooled at -5^{o}C. After 18 h, conc. H_2SO_4 (1 mL) was added dropwise to the reaction mixture, which was subsequently extracted with diethyl ether (2 x 250 mL). The combined organic extracts were washed with brine (2 x 200 mL), dried over $MgSO_4$, filtered and the solvent removed under reduced pressure. The crude material was purified by silica gel column chromatography, eluting with a gradient starting from 100% hexane to 20% ethyl acetate / hexane to yield the *title compound* as a pale yellow oil (6.82 g, 53 %); ^{1}H NMR (400 MHz, $CDCl_3$) 2.34 (1H, m, C$\underline{H}_2$CHBr), 2.45 (1H, m, C$\underline{H}_2$CHBr), 2.61 (2H, m, C$\underline{H}_2$CH$_2$CHBr) 4.41 (1H, m, CH), 5.15 (2H, s, C$\underline{H}_2$Ar), 7.34-7.38 (5H, m, Ph); ^{13}C NMR (126 MHz, $CDCl_3$) 29.7 (C$\underline{H}_2$CH$_2$CHBr), 31.8 (C$\underline{H}_2$CHBr), 44.5 (CH), 67.1 (C$\underline{H}_2$Ar), 128.6, 128.7, 128.8, 129.1 (Ar$_{(o/m)}$), 129.6 (Ar$_{(p)}$), 135.8 (Ar$_{(q)}$), 172.5 (C$\underline{O}$OCH$_2$), 174.9 (C$\underline{O}$OH); ESI/MS^{+} m/z 323.1 [M+Na]$^{+}$; MS Calcd for $C_{12}H_{13}O_4BrNa$ 322.9889. Found 322.9892.

82. (S)-2-Bromo-pentanedioic acid 5-benzyl ester 1-*tert*-butyl ester[8]

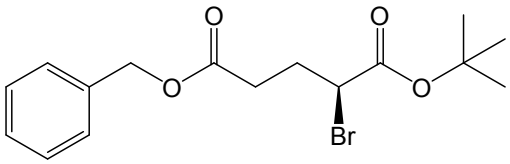

A solution of (S)-2-bromo-pentanedioic acid -5-benzyl ester (1.02g, 3.43 mmol) in tert-butyl acetate (15 mL) and $HClO_4$ in H_2O (70 %, 0.20 mmol) was stirred at room temperature. After 16 h, H_2O was added to the reaction mixture, and the organic phase separated. The organic phase was washed firstly with H_2O (2x 25mL), and then 5% Na_2CO_3 (2 x 25mL). The solvent was removed under reduced pressure to yield the title compound as a pale yellow oil (0.923 g, 81%); ^{1}H NMR (400 MHz, $CDCl_3$) 1.47 (9H, s, CH_3), 2.30 (1H, m, C$\underline{H}_2$CHBr), 2.37 (1H, m, C$\underline{H}_2$CHBr), 2.60 (2H, m, C$\underline{H}_2$CH$_2$CHBr), 4.30 (1H, d, J = 8, 6 Hz, CH), 5.11 (2H, s, CH$_2$Ar), 7.30-7.41 (5H, m, Ar);

^{13}C NMR ($CDCl_3$, 126 MHz) δ 27.8 (CH_3), 30.0 ($\underline{C}H_2CH$), 31.8 ($\underline{C}H_2CH_2$), 47.1 (CH), 66.9 ($\underline{C}H_2Ar$), 82.8 ($\underline{C}CH_3$), 128.3, 129.5, 128.7 ($Ar_{(o/m)}$), 128.8 ($Ar_{(o/m)}$), 128.9 ($Ar_{(p)}$), 136.2 ($Ar_{(q)}$), 169.5 (CO), 173.1 (CO). ESI/MS$^+$ m/z 379.2 $[M+Na]^+$; MS Calcd for $C_{16}H_{21}O_4BrNa$ 379.0521. Found 379.0529.

83. 5-Benzyl-1-tert-butyl (2R)-2-{4,10-bis[2-(tert-butoxy)-2-oxoethyl]-1,4,7,10-tetraazacyclododecan-1-yl}pentanedioate

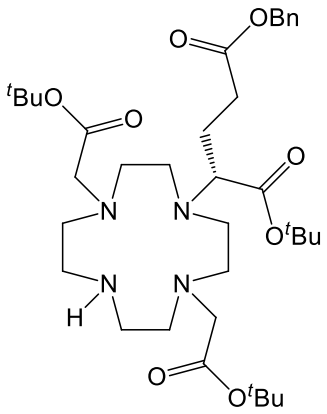

(7-*tert*-Butoxycarbonylmethyl-1,4,7,10-tetraazacyclododec-1-yl)-acetic acid *tert*-butyl ester (1.21 g, 3.03 mmol) and $NaHCO_3$ (0.23 g, 2.7 mmol) were dissolved in anhydrous CH_3CN (40 mL). After stirring at room temperature under argon for 15 mins, (S)-2-Bromo-pentanedioic acid 5-benzyl ester 1-*tert*-butyl ester (0.96 g, 2.7 mmol) dissolved in anhydrous CH_3CN (10 mL) was added dropwise. After 18 h, the resulting mixture was filtered and the solvent removed under reduced pressure to give a dark orange oil. The crude material was purified by silica gel column chromatography, eluting with a gradient starting from 100 % CH_2Cl_2 to 5 % CH_3OH/ CH_2Cl_2 to give the *title compound* as a pale yellow viscous oil (1.00 g, 55 %); ^{1}H NMR (500 MHz, $CDCl_3$) δ 1.21 (27H, s, CH_3), 1.83 (2H, m, $CHC\underline{H}_2$), 2.24 (2H, m, $CHCH_2C\underline{H}_2$), 2.45-2.98 (16H, br. m, CH_2 ring), 3.04 (2H, $C\underline{H}_2CO^tBu$), 3.15 (1H, s, CH), 4.98 (2H, CH_2Ar), 7.08 (5H, br. s, Ar), 9.02 (1H, br. s., NH); ^{13}C NMR (126 MHz, $CDCl_3$) δ 24.9 ($CH\underline{C}H_2CH_2$), 28.2 (CH_3), 30.8 ($CHCH_2\underline{C}H_2$), 46.2, 49.3, 50.2, 51.0 (CH_2 ring), 60.6 (CH), 66.4 ($\underline{C}H_2Ar$), 81.3 ($CH_2CO_2\underline{C}CH_3$), 81.9 ($CHCO_2\underline{C}CH_3$), 128.2, 128.3, 128.6 (Ar), 135.9 ($Ar_{(q)}$), 170.3 ($CH\underline{C}O_2tBu$), 171.3 ($CH_2\underline{C}O_2{}^tBu$), 172.7 ($\underline{C}O_2CBz$); ESI/MS$^+$ m/z 677.1 $[M+H]^+$; MS Calcd for $C_{36}H_{61}O_8N_4$ 677.4487. Found 677.4491.

84. 5-Benzyl-1-tert-butyl (2R)-2-{4,10-bis[2-(tert-butoxy)-2-oxoethyl]-7-{3-[4-({2-[2-(2-methoxyethoxy)ethoxy]ethyl}carbamoyl)-2-(trifluoromethyl)phenyl]-2-oxopropyl}-1,4,7,10-tetraazacyclododecan-1-yl}pentanedioate

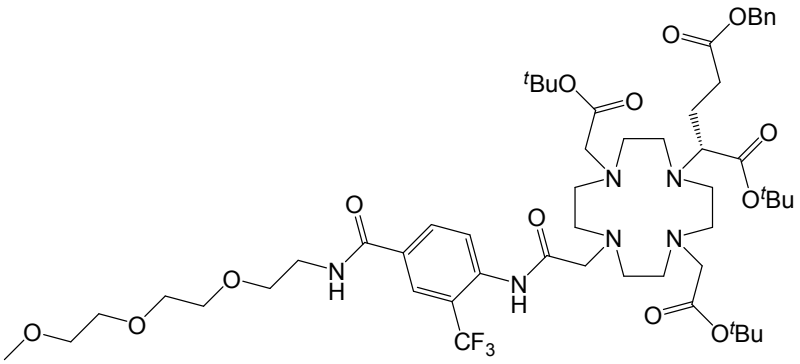

4-(2-Chloroacetamido)-N-{2-[2-(2-methoxyethoxy)ethoxy]ethyl}-3-(trifluoromethyl)benzamide (0.36 g, 0.84 mmol) was added to a stirred solution of 5-benzyl-1-tert-butyl(2R)-2-{4,10-bis[2-(tert-butoxy)-2-oxoethyl]-1,4,7,10-tetraazacyclododecan-1-yl}pentanedioate (0.48 g, 0.70 mmol) and K_2CO_3 (1.16 g, 0.84 mmol) in anhydrous CH_3CN (30 mL) at 80^{o}C. After 15 h, the resulting mixture was filtered and the solvent removed under reduced pressure. The crude product was purified by silica gel column chromatography, eluting with a gradient starting from 100 % CH_2Cl_2 to 2.5 % CH_3OH/ CH_2Cl_2 to give the *title compound* as an orange oil (0.48 g, 65 %); ^{1}H NMR (400 MHz, $CDCl_3$) δ 1.20 (9H, s, CCH_3), 1.40 (18H, s, CCH_3), 1.98 (2H, m, $CHC\underline{H}_2$), 2.20 (2H, m, $CHCH_2C\underline{H}_2$), 2.28-2.84 (20H, m, CH_2 ring and CH_2CO), 3.28 (3H, s, CH_3), 3.24 (1H, s, CH), 3.62 (12H, CH_2), 5.04 (2H, s, CH_2Ph), 7.21 (5H, m, Ph), 7.70 (1H, br., Ar), 7.98 (1H, d, J= 8 Hz, Ar), 8.11 (1H, s, Ar), 9.23 (1H, br. s., NH); ^{13}C NMR (100 MHz, $CDCl_3$) δ 22.4 ($CH\underline{C}H_2CH_2$), 27.8, 28.1, 28.2 (^{t}Bu), 32.2 ($CHCH_2\underline{C}H_2$), 40.0 ($\underline{C}H_2NHCO$), 44.0, 45.8, 46.2, 47.4, 51.0 (br., CH_2 ring), 54.3, 58.2 (CH_2), 59.0 ($O\underline{C}H_3$), 60.6 (CH), 66.6 ($\underline{C}H_2Ph$), 70.0, 70.3, 70.5, 70.6, 72.0 (CH_2), 82.1, 82.3, 82.7 (CCH_3), 121.0 (q, $^{2}J_{CF}$ = 30 Hz, Ar), 123.2 (Ar), 124.9 (q, $^{1}J_{CF}$ = 270 Hz, CF_3), 127.0 (Ar), 128.4, 128.6, 128.8 (Ph), 131.8, 132.2, 135.7 (Ar), 137.9 (Ph), 166.1, 172.3, 172.8, 173.1, 175.0 (CO); ^{19}F NMR (376 MHz, $CDCl_3$) δ – 63.19 (CF_3); ESI/MS^{+} m/z 1089.9 $[M+H]^{+}$; MS Calcd for $C_{53}H_{82}O_{13}N_6F_3$ 1067.5890. Found 1067.5900.

85. (2R)-2-[4,10-Bis(carboxymethyl)-7-{3-[4-({2-[2-(2-methoxyethoxy)ethoxy]ethyl} carbamoyl)-2-(trifluoromethyl)phenyl]-2-oxopropyl}-1,4,7,10-tetraazacyclo-dodecan-1-yl]pentanedioic acid

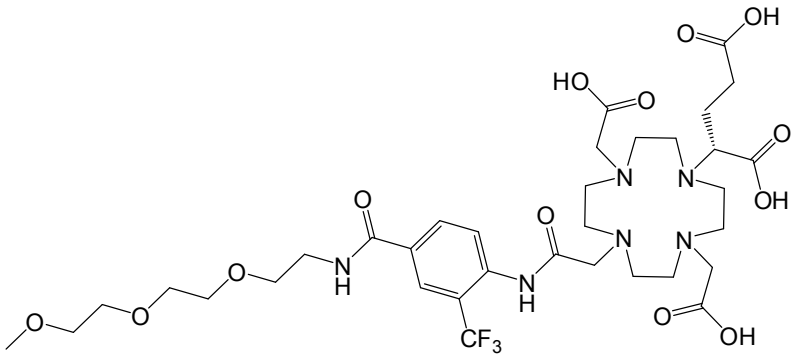

5-Benzyl-1-tert-butyl (2R)-2-{4,10-bis[2-(tert-butoxy)-2-oxoethyl]-7-{3-[4-({2-[2-(2-methoxyethoxy)ethoxy]ethyl}carbamoyl)-2-(trifluoromethyl)phenyl]-2-oxopropyl}-1,4,7,10-tetraazacyclododecan-1-yl}pentanedioate (240 mg, 0.23 mmol) was dissolved in HBr (48 % in acetic acid, 5 mL). The reaction was monitored by ^{1}H NMR. After 1 h, the solution was diluted with H_2O (30 mL) and then dialysed (MWCO 500D) against purite water until the pH of the tube contents reached neutral (48 h). Lyphilisation yielded a white solid (129 mg, 71 %); m.p. 229-230^{o}C (dec); ^{1}H NMR (400 MHz, D_2O) δ 1.20 (9H, s, CCH_3), 1.40 (18H, s, CCH_3), 1.98 (2H, m, $CHC\underline{H}_2$), 2.20 (2H, m, $CHCH_2C\underline{H}_2$), 2.28-2.84 (20H, m, CH_2 ring and CH_2CO), 3.28 (3H, s, CH_3), 3.24 (1H, s, CH), 3.62 (12H, CH_2), 5.04 (2H, s, CH_2Ph), 7.21 (5H, m, Ph), 7.70 (1H, br., Ar), 7.98 (1H, d, J= 8 Hz, Ar), 8.11 (1H, s, Ar), 9.23 (1H, br. s., NH); ^{19}F NMR (376 MHz, $CDCl_3$) δ – 63.04 (CF_3); ESI/MS^{+} m/z 847.8 $[M+K]^{+}$.

86. $[Tb.L^{12}(H_2O)]^{-}$

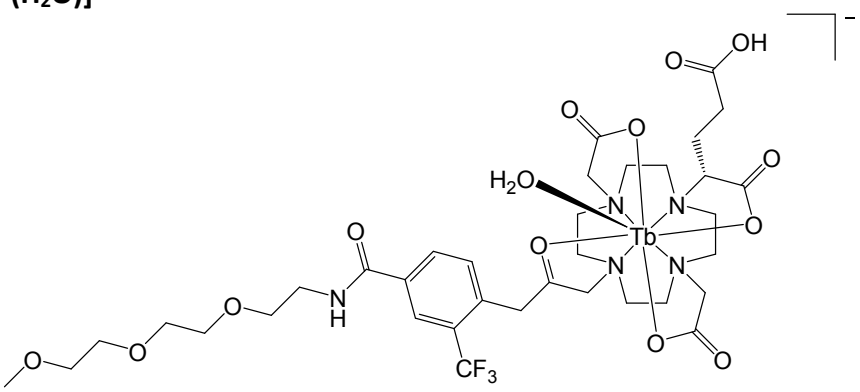

An analogous procedure to that described for **$[Tb.L^{4}(H_2O)]^{3-}$** was followed using (2R)-2-[4,10-bis(carboxymethyl)-7-{3-[4-({2-[2-(2-methoxyethoxy)ethoxy]ethyl}

carbamoyl)-2-(trifluoromethyl)phenyl]-2-oxopropyl}-1,4,7,10-tetraazacyclo-dodecan-1-yl]pentanedioic acid (129 mg, 0.16 mmol) and $Tb^{III}(OAc)_3$ (65.2 mg, 0.19 mmol) to yield the *title complex* as a white solid (124.6 mg, 82 %); ^{19}F NMR (376 MHz, D_2O, pD 5.4) δ –45.12 (CF_3, major species), -42.06, -43.98, -49.78. -50.10, -50.14, 56.98 (CF_3, minor species); ESI/MS^+ m/z 1003.6 $[M+Na]^+$; τ (H_2O) 1.68 ms, τ (D_2O) 2.77 ms; q= 0.90; HPLC: t_R = 8.2 min.

87. [(Tm.L^9).Cyclodextrin]

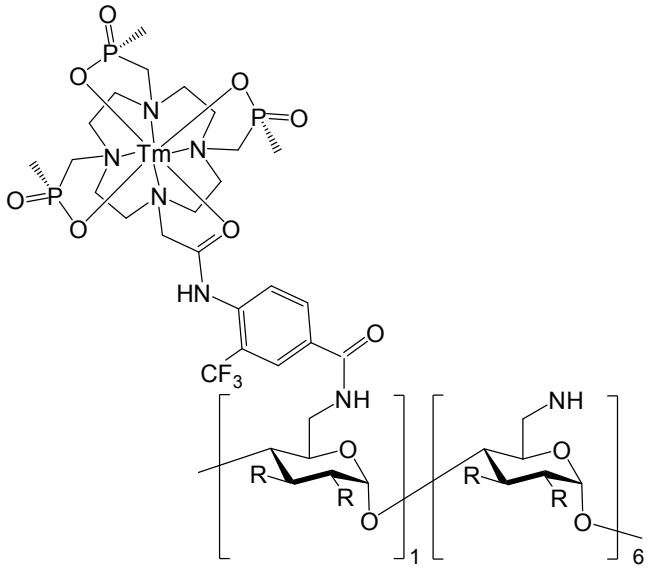

Procedure A

[Tm.L^9] (109.1 mg, 127.1 μmol), was dissolved in anhydrous DMF (2 mL) to which N-methylmorpholine (13.0 mg, 128.5 μmol) and TBTU (41.5 mg, 128.5 μmol) were added. The mixture was left to stir for 30 min, under argon, at room temperature then β-cyclodextrin (16.4 mg, 12.8 μmol), dissolved in 1 mL H_2O was added. The mixture was left stirring overnight at 40^{o}C. The crude product was diluted with H_2O (10 mL) and dialysed against Purite water over 48 h (MWCO 1000 D). The solution was lyophilised to yield the *title compound* as a white solid (82.0 mg, 89 %); ^{19}F NMR (376 MHz, D_2O, pD 5.4) δ –89.23 (CF_3); MALDI$^+$ 7242 $[M+Na]^+$; Anal Found Tm, 2.1 %; HPLC: t_R = 9.6 min.

Procedure B

An analogous procedure to that described for **[(Tm.L^9).Cyclodextrin]** *Procedure A* was followed, using **[Tm.L^9]** (130.6 mg, 152.0 μmol), N-methylmorpholine (19.4 mg,

193.2 µmol), TBTU (63.0 mg, 196.3 µmol) and β-cyclodextrin (16.2 mg, 12.3 µmol) to yield the *title compound* as a white solid (62.9 mg, 71 %); ^{19}F NMR (376 MHz, D_2O, pD 5.4) δ –90.04 (CF_3); MALDI$^+$ 7219 $[M+H]^+$; Anal Found Tm, 2.6 %; HPLC: t_R = 9.6 min.

Procedure C

Cumene (6.9 mg, 58.2 µmol) was dissolved in anhydrous DMF (2 mL) to which N-methylmorpholine (5.9 mg, 58.4 µmol) and TBTU (18.9 mg, 59.0 µmol) were added. The mixture was left to stir for 30 mins, under argon, at room temperature then β-cyclodextrin (7.4 mg, 5.6 µmol) and **[Tm.L^9]** (49.7 mg, 57.9 µmol) dissolved in 1 mL H_2O were added. The mixture was left stirring overnight at 40^{o}C. The crude product was diluted with H_2O (10 mL) and dialysed against Purite water over 48 h (MWCO 1000 D). The solution was lyophilised to yield the *title compound* as a white solid (62.9 mg, 71 %); ^{19}F NMR (376 MHz, D_2O, pD 5.4) δ –89.05 (CF_3); MALDI$^+$ 7219 $[M+H]^+$; Anal Found Tm, 2.4 %; HPLC: t_R = 9.6 min.

88. [(Tm.L^9).Silsesquioxane]

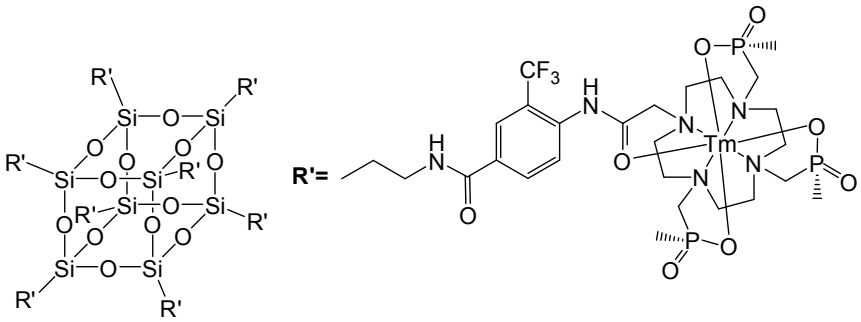

[Tm.L^9] (108 mg, 125.7 µmol), was dissolved in anhydrous DMSO (2 mL) to which N,N-diisopropylethylamine (16.2 mg, 125.8 µmol) and TBTU (40.9 mg, 127.4 µmol) were added. The mixture was left to stir for 20 mins at room temperature, under argon, and then T_8-silsesquioxane (10.7 mg, 12.0 µmol) was added. After 3 h the reaction mixture was dropped slowly into diethyl ether. The resulting precipitate was filtered, dissolved in H_2O (10 mL) and dialysed against Purite water over 48 h (MWCO 1000 D). The solution was lyophilised to yield the *title compound* as a white solid (62.9 mg, 71 %); ^{19}F NMR (376 MHz, CD_3OD:D_2O (50: 50), pD 5.4) δ –89.23 (CF_3); ^{19}F

NMR (139 MHz, CD_3OD:D_2O (50: 50), pD 5.4) δ –65.8 (SiO); Anal Found Tm, 17.4 %; HPLC: t_R = 4.8 min.

89. [(Tb.L^{10}(H_2O)).Silsesquioxane]

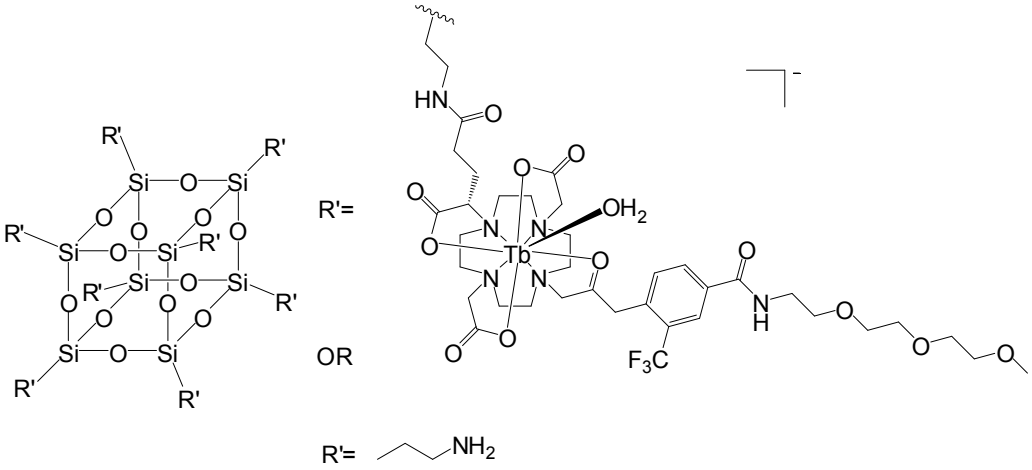

An analogous procedure to that described for **[(Tm.L^9).Silsesquioxane]** was followed, using **[Tb.L^{12}(H_2O)]$^-$** (124.6 mg, 127.5 µmol), N,N-diisopropylethylamine (16.5 mg, 128.0 µmol), TBTU (41.1 mg, 127.9 µmol) and T_8-silsesquioxane (11.4 mg, 12.8 µmol) to yield the *title compound* as a light brown solid (51 mg); ^{19}F NMR (376 MHz, CD_3OD:D_2O (20: 80), pD 5.4) δ –45.39 (CF_3); ^{29}S NMR (139 MHz, CD_3OD:D_2O (20: 80), pD 5.4) δ –66.9 (SiO); Anal Found Tb, 4.1 %; HPLC: t_R = 5.9, 7.9, 8.5, 9.1 min.

90. [(Tb.L^9).Chitosan]

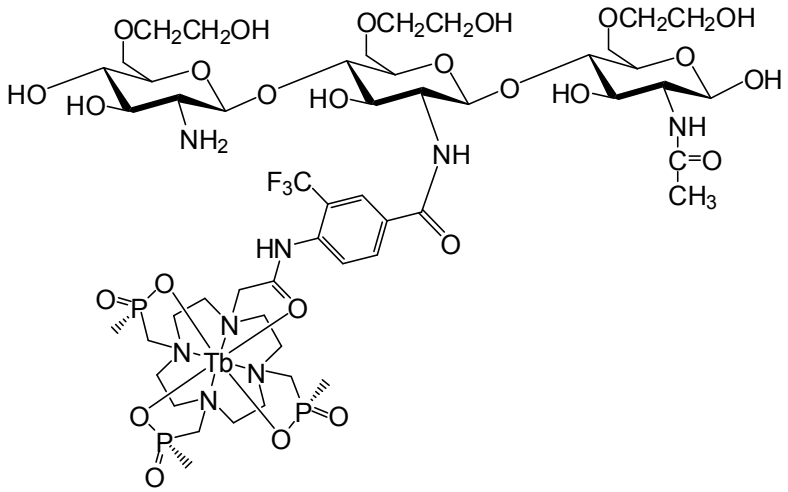

An analogous procedure to that described for **[(Tm.L^9).Silsesquioxane]** was followed, using **[Tb.L^6]** (220.1 mg, 258.9 µmol), N-methylmorpholine (26.3 mg, 260.1 µmol),

TBTU (83.6 mg, 260.5 µM) and chitosan (40 mg, MW ~ 6500) to yield the *title compound* as a white solid (83 mg); ^{19}F NMR (376 MHz, D_2O, pD 5.4) δ -58.46 (CF_3); For GCP analysis refer to Table 5.2.

91. [(Gd.L^9).Chitosan]

An analogous procedure to that described for **[(Gd.L^9).Silsesquioxane]** was followed, using **[Gd.L^6]** (223.9 mg, 260.3 µmol), N-methylmorpholine (26.1 mg, 258.0 µmol), TBTU (82.9 mg, 26.6 µM) and chitosan (40 mg, MW ~ 6500) to yield the *title compound* as a white solid (91 mg); r_{1p}= 12.4 $mM^{-1}s^{-1}$ (60 MHz, 298 K); For GCP analysis refer to Table 5.2.

Sample	M_w [a]	M_n [b]	PDI [c]
Chitosan	6,590	2,250	2.9
[(Gd.L^9).Chitosan]	16,500	8,565	1.9
[(Tb.L^9).Chitosan]	16,300	8,615	1.9

Table 5.2: Gel permeation chromatography (GPC) data for the starting glycol chitosan sample and the corresponding Tb and Gd conjugates. Mean values obtained from two successive scans. [a] calculated molecular weight averages expressed as the pullulan polysaccaride equivalent molecular weights; [b] number average molecular weights; [c] polydispersity (Mw/Mn).

5.3 References

1) J. Carmichael, W. G. DeGraff, A. F. Gazdar, J. D. Minna, J. B. Mitchell, *Cancer Res.*, **1987**, *47*, 936

2) O. Reany, T. Gunnlaugsson, D. Parker, *J. Chem. Soc.-Perkin Trans. 2*, **2000**, 1819.

3) H. Reinheckel, *Alfa-Bromo Esters*, **1965**.

4) M. P. Lowe, D. Parker, *Inorg. Chim. Acta.*, **2001**, *317*, 163.

5) Z. Kovacs, A. D. Sherry, *J. Chem. Soc., Chem. Commun*., **1995**, *2*, 185.

6) Z. Kovacs, A. D. Sherry, *Synthesis*, **1997**, *7*, 759.

7) K. L. Dombi, N. Griesang, C. Richert, *Synthesis*, **2002**, 816.

8) K. P. Eisenweiner, P. Powell, H. R. Macke, *Bioorg. Med. Chem. Lett.*, **2000**, *10*, 2133.